Micro Scale Sediment - Fluid Interactions

Dissertation

zur Erlangung des Doktorgrades der Naturwissenschaften am Fachbereich Geowissenschaften der Universität Bremen

submitted in fulfillment of the requirements for the doctoral degree in natural sciences at the Faculty of Geosciences of the University of Bremen

vorgelegt von

by

Gerhard Bartzke

Bremen,
Dezember / December 2012

Gutachter / Reviewers

Prof. Dr. Katrin Huhn, Universität Bremen

Dr. Karin Bryan, University of Waikato

Declaration

Name: Gerhard Bartzke
Address: Hemelingerstraße 60, 28205 Bremen

Herewith I declare that

I. This document and the accompanying data have been composed by myself and describes my own work.

II. Material from the published or unpublished work of others, which is referred to in this dissertation, is credited to the author in the text.

III. This work has not been submitted for any other degree.

Gerhard Bartzke
20th of December 2012
University of Bremen, Germany

Abstract

This thesis was inspired by the inherent limitations in the quantification of the physical parameters (e.g. flow speed, grain size and density) controlling sediment-fluid interactions in the direct vicinity of the sediment water interface of a seabed. In marine environments it is widely accepted that mix-grain size sediment beds have a higher erosion resistance than sediment beds composed of a single grain size. This phenomenon of sediment bed stabilization can be explained by textural in-homogeneities and density differences within the sediment body. With a focus on the physical features, i.e., cage like structures and density related differences, the overall goal of this dissertation was to identify and quantify their role in the transport behavior and the erosion resistance of sediments beds.

To investigate these aspects, the effects of a fine fraction on the entrainment and transport characteristics of a coarser sand bed were explored. For this, the transport behaviour of layered - and mixed sediment beds consisting of a simplified two-grain fraction distribution (silt and sand) was tested in an analogue laboratory-based annular flume. Two suites of experiments were designed: (1) "The Layering Experiment" in which a sandy bed was covered by a thin layer of silt of varying thickness; and (2) "The Mixing Experiment", where sand beds were homogenously mixed with increasing amounts of silt. To initiate erosion and to detect a possible stabilizing effect, the flow speeds were incrementally increased in 2.5 cm/s steps up to 30 cm/s.

The results showed that the sediment bed (or the underlying sand bed in the case of the layered experiments) stabilized with increasing silt composition. Both cases showed that small amounts of fine sediment fractions can completely change the erosion characteristics of a seabed. By this approach it was possible to formulate the hypothesis that textural caging structures made of fine silt particles encompass the coarse sand particles like a cage (i.e., pore space plugging) and prevent erosion successively. However, as the caging effects occur within sediment beds, direct observation and quantification of the textural in-homogeneities are limited using only analogue techniques, and, hence, previous studies on this topic are not comprehensive.

In order to investigate this effect in more detail, a high resolution 3D numerical model was designed for the simulation of sediment transport by a fluid by coupling two numerical techniques. The two coupled techniques were the Finite Difference Method (FDM) and the Distinct Element Method (DEM). The 3D model was given settings that correspond generally to previous flume tank studies. The model domain focused on a small-scale 'cut-out' of a sediment bed. For the quantification of the physical parameters controlling bed stabilization by caging effects in the direct vicinity of the sediment water interface, graded and mixed sediment beds were generated numerically and tested under predefined flow speeds.

The results indicated that textural caging structures developed between sand pores causing bed stabilization. It was shown that with increasing amounts of silt, inflow was increasingly blocked causing an increase in the internal compaction and, ultimately, a decrease in the flow available to entrain particles

located in the deeper parts of a bed. Using this approach, it was possible to verify that in the case of the deposition of fine particles on top of, or mixed into, a coarse matrix, the bed stability increased significantly. These findings allowed for quantification and validation of the hypothesis of texture induced bed stabilization.

The same 3D numerical model was also used to examine the role of grain density variations on the threshold conditions and erosion behavior of sediment beds. In order to quantify the process of heavy mineral enrichment and to understand the depositional history in various depositional environments, a range of numerical sediment beds were generated and tested under predefined flow speeds. Overall, the results showed that a larger lighter Quartz grain was entrained earlier and at lower flow speeds than smaller heavier Magnetite particles. The experiments showed that bed stability increased when the heavy mineral concentrations were increased, which validated heavy mineral enrichment.

The findings of this research represent a significant advancement in the field of grain-scale sediment bed transport processes because traditional methods are limited to mainly qualitative measurements. Application of the 'numerical' flume tank allowed for direct quantification of physical parameters that influence grain movements, in combination with fluid motions, in the vicinity of the sediment-water interface of the bed, but is also capable for numerous applications in the field of geoscientific research. This approach has significant potential for future research on sediment fluid interactions, a topic that is currently under-represented in the body of knowledge.

At the same time this thesis provides significant innovations for ongoing research in the field of sediment transport and may have further relevance in the fields of applied sciences and the industry. The finding that bed stabilization is highly sensitive to small silt concentrations could be a useful tool for the dredging and sea-bed structure industry in order to stabilize dumped sediment at the seafloor. Also, the influence of grain density differences on the erosion behavior of sediment beds shows implications on the prediction of sediment transport processes. The result that differing grain densities influence on the erosion behavior of sediment beds shows implications the position and distribution of heavy minerals placers for the heavy mineral industry.

Zusammenfassung

Hauptaugenmerk der vorliegenden Arbeit lag auf der Quantifizierung der physikalischen Parameter, wie beispielsweise Fließgeschwindigkeit, Korngröße und Dichte, die das Zusammenspiel von Fluid und Sediment am Meeresboden steuern. Im marinen Milieu, ist diese Quantifizierung limitiert, da es sich um einen schwer zu untersuchenden Bereich in unmittelbarer Nähe der Sediment-Fluid Grenze handelt. Generell gilt, dass ein Sedimentbett bestehend aus unterschiedlich großen einzelnen Körnern eine höhere Erosionsbeständigkeit aufweist, als ein gleichkörniges Sedimentbett. Dieses Phänomen der Sedimentbettstabilisierung kann durch texturbedingte Inhomogenitäten als auch durch Dichteunterschiede im Sedimentkörper erklärt werden.

Mit dem Fokus auf die physikalischen Besonderheiten von käfigartigen Strukturen und Dichteunterschieden, lag das Ziel der Dissertation darin, den Einfluss auf das Transportverhalten und die Erosionsbeständigkeit von Sedimentbetten zu beschreiben als auch zu quantifizieren. Um diese Aspekte im großskalierten Bereich zu untersuchen, wurde mit Hilfe eines Rund-Strömungskanals im Labor der Einfluss einer Feinfraktion auf das Bewegungs- und Erosionsverhalten eines groben sandigen Sedimentbettes untersucht. Dabei wurde das Transportverhalten von abgelagerten als auch gemischten Sedimenten, aus einer vereinfachten bimodalen Korngrößenverteilung (Silt und Sand), getestet. Zwei Experimentreihen wurden entworfen und durchgeführt: (1) „Das Schichtungsexperiment“, in diesem wurde ein Sedimentbett bestehend aus Sand und einer dünnen Deckschicht Silt mit ansteigender Mächtigkeit getestet; und (2) „Das Mischungsexperiment“, in diesem wurden Sandbetten mit ansteigenden Anteilen an Silt homogen vermischt. In beiden Experimentreihen wurden die Strömungsgeschwindigkeiten schrittweise (in 2,5 cm/s Schritten) auf 30 cm/s erhöht, um Erosion herbeizuführen und um Stabilisierungseffekte identifizieren zu können.

Die Ergebnisse aus beiden Experimentreihen zeigen, dass zunehmende Siltkonzentrationen zur Stabilisierung des Sedimentbettes führen. Darüber hinaus wird deutlich, dass eine bereits geringe Menge Silt die Erosionscharakteristika stark beeinflussen. Dieser Ansatz lieferte die Grundlage zur Hypothese der texturbedingten, käfigartigen Strukturen: in diesem Fall umschließen feinere Siltpartikel größere Sandpartikel ähnlich eines Käfigs (Porenraumverstopfung) und schwächen somit die Erosion ab. Diese Effekte treten im Inneren von Sedimentbetten auf. Folglich ist eine direkte Beobachtung dieser texturellen Inhomogenitäten mittels analoger Techniken weitestgehend nicht möglich und die Ergebnisse vorheriger Studien daher größtenteils auf Oberflächenprozesse beschränkt.

Um diesen Effekt besser untersuchen und quantifizieren zu können, wurde ein hochauflösendes drei dimensionales numerisches Modell zur Simulation von Sedimenttransportprozessen mittels Fluiden entwickelt. Hierfür wurden zwei unabhängige numerische Simulationstechniken miteinander gekoppelt, die Finite Differenzen Methode (FDM) und die Diskrete Elemente Methode (DEM). Dieses 3D-Modell parametrisiert die allgemeinen Bedingungen der analogen vorher durchgeführten Strömungskanalstudien

und fokussiert auf einen kleinskalierten Ausschnitt des Sedimentbettes. Zur Quantifizierung der physikalischen Parameter, die bei der Sedimentbettstabilisierung wirken und zu käfigartigen Strukturen an der unmittelbaren Oberfläche und an der Sediment-Wasser-Grenze führen, wurden gradierte als auch gemischte Sedimentbetten numerisch modelliert und unter den analogen Strömungsgeschwindigkeiten getestet. Die Ergebnisse bestätigten, dass sich Käfigstrukturen im Porenraum des Sandes entwickeln und zur Bettstabilisierung führen. Weiterhin wird deutlich, dass mit zunehmenden Anteilen an Silt der Einstrom in das Sedimentbett blockiert und somit ein Anstieg der internen Kompaktion verursacht wird. Folglich wird der Einstrom um die Partikel reduziert, die im tieferen Bereich des Bettes liegen. Dieser Ansatz stützt die Hypothese, dass im Fall von abgelagerten feinen Partikeln oder gemischten Sedimentbetten die Bettstabilität deutlich ansteigt. Diese Ergebnisse erlauben die Quantifizierung und Validierung der Hypothese texturbedingter, käfigartiger Strukturen.

Der gleiche Ansatz wurde verwendet, um die Rolle der Korndichte auf die Bewegungen und Erosionsbedingungen von Sedimentbetten zu untersuchen. Um den Prozess der Schwermineralanreicherung zu quantifizieren und die Prozesse in unterschiedlichen Ablagerungsbereichen zu ergründen, wurde eine Reihe von numerischen Sedimentbetten erstellt und unter vorgegeben Fließgeschwindigkeiten getestet. Die Resultate zeigen, dass ein größeres Quarzkorn mit einer geringeren Dichte bei langsamen Fließgeschwindigkeiten früher bewegt wird als ein kleineres Magnetitpartikel mit einer höheren Dichte. Dies ermöglichte die Validierung des Prozesses der Magnetitanreicherung. Darüber hinaus wird deutlich, dass die die Bettstabilität ansteigt wenn die Schwermineralkonzentration erhöht ist.

Da vorherige Methoden weitestgehend auf qualitative Messungen beschränkt sind, zeigen die Ergebnisse dieser Studie eine bedeutende Verbesserung unseres Verständnisses von Sedimenttransportprozessen. Die Anwendung des numerischen Strömungskanals ermöglicht eine direkte Quantifizierung der physikalischen Parameter, welche die Kornbewegung in Verbindung mit Fluidbewegungen in der unmittelbaren Nähe der Sediment-Fluid Grenze als auch im Inneren eines Bettes bestimmen. Weitere Anwendungsmöglichkeiten des numerischen Strömungskanals finden sich auch den unterschiedlichen geowissenschaftlichen Forschungsbereichen. Dieser Ansatz hat ein bedeutendes Potential für zukünftige Forschung im kleinskalierten Sediment-Fluid-Interaktionsbereich, ein Thema das derzeit noch unzulänglich erkundet ist. Gleichzeitig weist diese Arbeit signifikante Erkenntnisse im Bereich des Sediment Transports auf, die Anwendung in den angewandten Wissenschaften als auch in der Industrie finden können. Das Ergebnis, dass die Sedimentbettstabilisierung sehr sensibel auf geringste Siltbeimengungen reagiert ist ein nützliches Werkzeug für die Baggerindustrie, um Sediment am Meeresboden zu stabilisieren. Ebenso zeigt das Ergebnis, dass unterschiedliche Dichten das Erosionsverhalten von Sedimentbetten beeinflussen können, wichtige Anwendungen zur Vorhersage, Position und Verteilung von Schwermineral Lagerstätten für die Schwermineralindustrie.

Contents

Chapter I - Outline and Objectives

Sediment erosion is understood as the initiation of motion of single grains by a hydrodynamic driving force. Most classical studies have attempted to predict sediment erosion as a function of single grain size at a defined flow force, e.g., Shields (1936) and Hjulstroem (1935). However, at present, it is understood that the erosion behavior of sediments is also controlled by additional factors that shift the initial erosion conditions towards higher regimes. This increase in the erosion resistance of a sediment bed is termed as 'sediment bed stabilization' and is controlled by: (1) biostabilization, (2) cohesion, and (3) textural caging structures. (1) Biostabilization, i.e., biological activity of the micro and macro fauna, can increase the stability of sediment by binding sediment particles together (Paterson, 1994; Paterson et al., 1990; Paterson and Hagerthey, 2001; Young and Southard, 1978). (2) Small clay minerals in a sediment bed have the ability to bind each other forming larger aggregates due to electrostatic forces (cohesive forces) that can increase the erosion resistance significantly (Alvarez-Hernandez, 1990; Dyer, 1989; Hir et al., 2008; Hir et al., 2011; Kamphuis, 1990; Murray, 1977; Panagiotopoulos et al., 1997; van Ledden et al., 2004). (3) Erosion resistance can also be increased by texture related caging structures. In such a case, fine particles encompassing coarse particles, like a cage, prevent erosion successively (Hir et al., 2008; Torfs, 1997; van Ledden et al., 2004; Whitehouse et al., 2000).

An additional factor controlling the erosion behavior in sediment beds is related to the differing densities of the mineral grains forming the bed (Li and Komar, 1992; Middleton, 2003). Due to their higher density, magnetite particles are heavier and are therefore, more resistant to erosion than the light quartz particles (Komar, 1987; Komar, 2007). Hence, the density distribution of particles in sediment beds also plays a major role in erosion characteristics. Therefore the following overall research questions were addressed:

- What is the influence of current velocities on the sediment erosion behavior?
- What factors cause variations in the erosion behavior?
- How to quantify the controlling factors that influence sediment erosion?

Traditionally, for the investigation of sediment erosion and transport processes, analogue laboratory based flume or *in situ* field investigations are used (Amos et al., 1992; Black and Paterson, 1997; Komar, 2007). However, analogue approaches are limited in their ability, e.g., due to the low resolution of the sensors, to resolve and quantify the physical processes at the sediment surface and in the interior of the bed (Komar, 1987; Komar, 2007). In order to quantify the processes controlling sediment transport and bed stabilization, such as inflow rates, particle transport rates, and porosity changes, in the sediment beds, numerical models are required. Thus, numerical modeling approaches can quantify previous assumptions

and conceptual approaches shown by flume tank experiments and further explain transport behavior and textural changes in sediment beds during fluid flow.

With a focus on the physical parameters, i.e., cage like structures and density related effects, the overall goal of this dissertation was to identify and quantify their role of erosion resistance of sediment beds and transport behavior. In order to identify these effects influencing sediment movement at a bed laboratory-based annular flume tank experiments were undertaken. These experiments focus on the effects caused by non-cohesive silt and sand grains on erosion resistance and the transport behaviour of layered - and mixed sediment beds consisting of a simplified two-grain fraction (silt and sand). To mimic layered and mixed sediment beds, two suites of experiments were designed: (1) "The Layering Experiment": in which a sandy bed was covered by a thin layer of silt of varying thickness; and (2) "The Mixing Experiment" where sand beds were homogenously mixed with increasing amounts of silt. To initiate erosion and to detect bed stabilization effects within both set-ups, the flow speeds were increased in increments of 2.5 cm/s up to 30 cm/s.

For the quantification of the processes occurring between individual particles in the direct vicinity of the sediment-water interface and in the interior of sediment bed, a 3D high resolution numerical model was developed and simulations were undertaken (Chapter IV - VII). The 3D numerical model was designed for the simulation of sediment transport by a fluid by coupling two numerical simulation techniques. This 3D model was given settings that correspond generally to previous flume tank studies. These experiments are able to validate the most fundamental questions on sediment transport; for example:

- How far is a particle transported at a certain flow speed?
- How deep is the infiltration of the water flow into of a sediment bed?
- How does the porosity in the bed change at a certain flow speed?

In the following text, the structure and content of each Chapter are described. The individual thesis objectives of each study, comprising Chapters III-VII are detailed within this structure.

Chapter II introduces the topic of sediment transport. A review of the fundamental concepts of sediment and fluid interactions is necessary to place this thesis into a wider framework beyond the scope of a single manuscript.

Chapter III investigates the parameters, controlling the erodibility of sediment beds, and explores effects of a fine fraction on the entrainment and transport characteristics of a coarser sand bed. In this study the following research questions were addressed:

- How does a fine fraction (silt) influence the erosion behavior of a sand bed?
- How do different current velocities influence the sediment stabilization and re-mobilization of a sand bed?
- What factor causes sediment stabilization in silt and sand beds?

The manuscript entitled, 'ON THE STABILIZATION INFLUENCE OF SILT ON SAND BEDS' has been accepted (with major revisions) for publication in the *Journal of Sedimentary Research* and was recently resubmitted.

All experimental work and data has been composed by myself. The Co-authors provided comments and edits on the manuscript.

Chapter IV & V were inspired by the inherent limitations in quantification of the physical parameters controlling sediment- fluid interactions in the direct vicinity of the sediment water interface, and in the interior of a sediment bed. Therefore, both chapters focus on the validation of the hypothesis of bed stabilization by textural caging structures, proposed in Chapter III, in graded (Chapter IV), and mixed sediment beds (Chapter V). Therefore, the following research questions were addressed:

- How do textural caging structures increase bed stability on a grain-scale level?
- How do textural caging structures control sediment stability in graded and mixed sediment beds?

The manuscript presented in Chapter IV: 'THE ROLE OF GRADED SEDIMENT BEDS ON THE EROSION BEHAVIOR', is ready for submission to the *Journal of Sedimentary Geology*.
The manuscript presented in Chapter V: 'HOW IS MIXED SEDIMENT PROTECTED FROM EROSION? USING A NUMERICAL APPROACH' is in preparation for submission to *Earth Surface Processes and Landforms*.

All experimental work and data presented in Chapters IV and V were composed by myself. The Co-authors provided comments and edits on the manuscript.

Chapter VI & VII focus on the effect of variations in grain densities in sediment beds on threshold conditions and the erosion behavior of sediment beds. Heavy mineral grains have different hydrodynamic properties in comparison to light minerals, e.g., Quartz and Feldspar (Gallaway et al., 2012). Due to their higher densities, heavy minerals are more resistant to erosion by flowing water (Komar, 2007; Komar and Wang, 1984). Light minerals can be preferentially 'washed out' from the heavy fractions based on their differing threshold conditions (Li and Komar, 1992). This process of selective grain entrainment can lead to the formation of economically valuable placers (Komar, 2007). However, as yet, the understanding of the physical processes of heavy mineral enrichment has been limited to theoretical approaches and conceptual models of a more descriptive manner. Hence, there is a fundamental need for quantification of the physical processes of selective grain entrainment to predict the formation of heavy mineral placers. The studies presented in Chapter VI and VII focus on the quantification of the physical processes controlling selective grain entrainment. Therein, the following research question was addressed:

- How do density-related effects influence the erosion behavior of sediment beds?

The manuscript presented in Chapter VI: 'A NUMERICAL APPROACH TO QUANTIFY SELECTIVE SORTING OF HEAVY MINERALS' is currently in review for the conference proceedings *Special Volume EST 2012, Houston, USA June 25-29, 2012*.

All experimental work and data was composed by myself. The Co-authors provided comments and edits on the manuscript.

The manuscript presented in Chapter VII: 'SELECTIVE TRANSPORT AND FRACTIONATION OF MAGNETIC PARTICLES IN A TRANSIENT COASTAL ENVIRONMENT (TAURANGA HARBOUR AND BAY OF PLENTY, NEW ZEALAND)' is in preparation for submission to *Sedimentology*.

All numerical work and data has been composed by myself. I also contributed to the writing of the manuscript (esp. the discussion), production of the figures, and interpretation of the findings.

Chapter VIII summarizes the results and conclusions of the previous chapters. Connections are drawn between the findings of the studies to give the global context within the collection of previous work. Suggestions are also made for future work that could enhance the findings presented herein.

Note on INTERCOAST

This thesis was established within the DFG-International Research Training Group INTERCOAST– 'Integrated Coastal Zone and Shelf-Sea Research'. INTERCOAST is a PhD graduate school, which is the product of a collaboration between the Universities of Bremen, Germany and Waikato, New Zealand, that is funded by the German Research Foundation (DFG). INTERCOAST focuses on the impacts of global, climate, and environmental changes in coastal and shelf-sea areas. Within INTERCOAST, PhD students with backgrounds in marine geosciences, marine biology, social sciences, or law have the opportunity to work in an interdisciplinary setting. Further, each PhD student undertakes a one year research stay at the partner University. Consequently, the findings presented in this thesis were established both at the University of Waikato (Chapter III) and the University of Bremen (Chapter IV - VII).

Chapter II - Background

2.1 Sediment transport

Imagine water flowing over fine sand. You will observe, if the flow speed is large enough, that single grains are moved and transported (Leeder, 1999). This natural process is understood as sediment erosion and transport and is the result of the mechanical interaction of two components: water and sand. In aquatic environments, these processes have been active throughout geological time and have shaped the present landscape of our world (Allen, 1970; Leeder, 1999).

Physically, sediment motion is caused by the interaction of a liquid, i.e., water, and a solid phase i.e., sediment particles, such as quartz grains. The liquid phase embodies the hydrodynamic driving force, as well as the transport medium e.g., river currents, waves, and tides (Allen, 1970). The solid phase on the other hand, is characterized by solid particles, i.e., sediment particles, such as sands, silt and clay. The threshold at the sediment surface, beyond which particles move, is reached when the hydrodynamic driving force, i.e. shear stress, is larger than the resistance force of each grain (Figure 2.1) (Allen, 1970; Komar, 1987; Rijn, 2007). The relationship between fluid flow and grain size causing sediment transport is termed 'initiation of motion' was shown by classical, empirical studies e.g. (Hjulstroem, 1935; Miller et al., 1977; Shields, 1936). For the formulation of a universal predictor of sediment transport, researchers have commonly tested the transport behavior of single grains of various sizes under several flow speeds using analogue techniques, i.e. laboratory, flume studies but also with *in situ* field investigations (Amos et al., 1992; Black and Paterson, 1997). This predictor has been proposed for the purposes of engineers working in hydro-marine environments requiring detailed information on the initiation of motion of sediments for maintenance of navigational routes and shipping channels. At present, it is understood that the erosion characteristics of sediment beds are influenced by processes that shift the conditions of the initial threshold towards higher regimes (Whitehouse et al., 2000), in other words, to conditions where higher flow speeds are required to initiate sediment erosion.

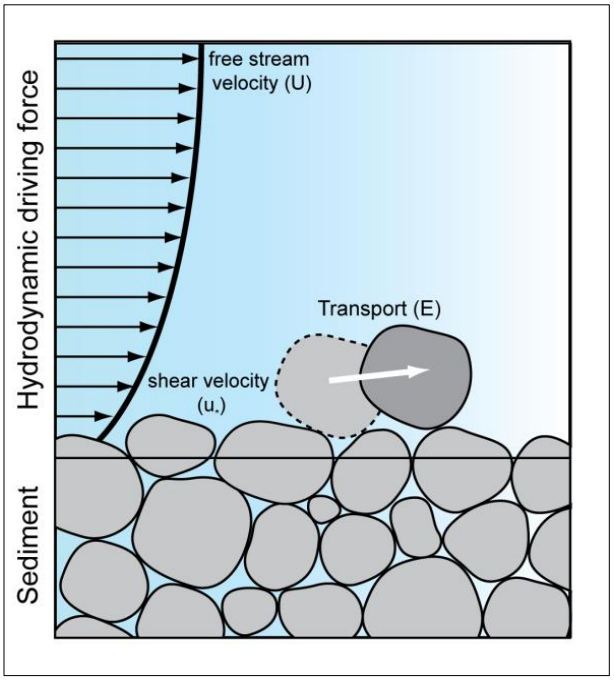

Figure 2.1: Principle of sediment transport.

This increase in erosion resistance is termed as 'sediment bed stabilization' and is influenced by such processes as biological production in the sediment bed (Paterson, 1994), electrostatic forces between particles (Mitchener and Torfs, 1996),

as well as by textural related in - homogeneities i.e., the occurrence of cage-like structures in the sediment bed (Hir et al., 2008; Torfs, 1997; Whitehouse et al., 2000) (section 2.5.3, and Chapter III, IV, and V). Additionally, variations in the grain mineralogy (Hatfield et al., 2010; Komar, 2007), and, hence, densities within the sediment beds, also influence the erosion behavior of sediment beds (Chapter VI and VII).

Sediment transport in most aquatic environments is highly dynamic (Leeder, 1999). Rivers transport sediments from the hinterland towards the sea, which is usually trapped in the floodplains of rivers, or accumulates in estuaries (Dyer, 1994). Tidal currents and superimposed waves also supply sediment from the sea. During storm events, floodwaters carry new sediment as plumes into the estuary and previously deposited estuarine sediments are mixed and dispersed throughout the estuary (Healy, 2002). In deep marine environments sediment drifts transport sediments along the continental shelf (Leeder, 1999). This continuous re-erosion and deposition of sediments causes problems, e.g. for maintenance of navigational routes and shipping channels or harbour basins (Essink, 1999). Therefore, the prediction of the entrainment thresholds and erosion rates for these sediments lies at the heart of understanding sediment transport dynamics. In particular, coastal engineers and managers rely on these predictions to manage port developments (drilling and dredging activities) and maintain navigation routes. In addition, such predictions are widely used across a number of scientific fields ranging from the ability, e.g. to reconstruct past sedimentary environments of the deep sea, or to understanding the impact of sediments on benthic communities following large storm events (Essink, 1999; Leys and Mulligan, 2011; Thrush et al., 2004; Zajac et al., 1998). For the formulation of a universal predictor of sediment transport, for commercial and scientific application, researchers have commonly tested the transport behaviour of single grains of various sizes under several flow speeds using analogue techniques, i.e. laboratory, flume studies but also *in situ* field investigations (Amos et al., 1992; Black and Paterson, 1997).

The empirically-derived Shields curve (Shields, 1936) predicts the initiation of motion as when the bed-shear stress exceeds the critical threshold for that particle size. The Shields curve was derived for uniform, homogeneous, non-cohesive sediments of the same grain size (Soulsby, 1997) and it is less accurate for finer grained beds (Hir et al., 2008; Mehta and Lee, 1994). Thus Hjulstroem (1935, 1939) used observations in an attempt to develop a universal predictor of the critical erosion of sediments of a wide range of sizes (the “Hjulstroem Diagram”). This predictor indicated that fine sediments, in particular mud, are much harder to erode than sand. In the last decades, many studies (Allen, 1970; Mc Cave, 1984; Miller et al., 1977; Rijn, 2007; Soulsby, 1997; Winterwerp and Van Kesteren, 2004; Young and Southard, 1978) focused their research on the development of a universal predictor of the erosion of sediments in various grain sizes following the classical approaches of Shields and Hjulstroem (Hjulstroem, 1935; Shields, 1936).

At present, it is widely accepted that the erosion behaviour of a sediment bed is controlled by biostabilization (Whitehouse et al., 2000), cohesion (Sutherland, 1987), textural induced caging structures (Hir et al., 2008; Mitchener and Torfs, 1996; van Ledden, 2002) and grain density variations (Baba and Komar, 1981; Komar, 2007). (1) Biostabilization (Paterson, 1994; Paterson et al., 1990; Paterson and Hagerthey, 2001; Young and Southard, 1978) is the influence of the activity of the micro- (bacteria, microalgae, fungi) and macro- (worms, molluscs, crustaceans) organisms which can alter the sediment stability by binding sediment particles together. As shown by many studies on muddy, clay rich sediments, (2) cohesion (caused by electrostatic forces) binds together the clay minerals and increases the erosion resistance significantly (Alvarez-Hernandez, 1990; Dyer, 1989; Hir et al., 2008; Hir et al., 2011; Jacobs et al., 2011; Kamphuis, 1990; Murray, 1977; Panagiotopoulos et al., 1997; van Ledden et al., 2004). Additionally, the entrainment characteristics of beds can be altered by (3) texture induced caging structures, which develop when fine particles encompass coarse grains as a cage (Whitehouse et al., 2000). This phenomenon has been shown in various studies, e.g. Whitehouse (2000), Torfs (1997), van Ledden et al., (2004) and Hir et al., (2008) on mud (i.e., cohesive clay and sand) using laboratory based analogue flume studies. Mitchener and Torfs (1996) showed that a similar effect is caused when fine clays are deposited on top of a sand bed. They concluded that the generation of cage-like networks encompassing the sand grains increases the density of the matrix and the additional cohesive forces bind clay particles, thus raising the erosion resistance. This was also observed in various experiments, e.g. Panagiotopoulos et al., (1997), Wiberg and Smith (1987), and Torfs et al. (2000), which showed that sediment stability is increased by clay in-filled pockets within the sand bed. Further, variations in grain densities (4) in sediment beds can influence threshold conditions and the erosion behavior of sediment beds. Heavy mineral grains have different hydrodynamic properties in comparison to light minerals, e.g., Quartz and Feldspar. Due to their higher densities, heavy minerals are more resistant to erosion by flowing water (Komar 1989). Light minerals can be preferentially ‘washed out’ from the heavy fractions based on their differing threshold conditions. This process of selective grain entrainment can lead to the formation of economically valuable placers (Komar, 1987; Komar, 2007).

In the past, this textural caging effect has been mainly investigated in the context of clay-sand mixtures (Hir et al., 2008; Hir et al., 2011; Torfs, 1997; van Ledden et al., 2004; Whitehouse et al., 2000). The effect would therefore also be expected with other fine fractions, e.g. silt, which are very common in many sandy coastal environments, however, until now this has not been considered. Also, the effects of denser grains on a sediment bed are merely reported in a descriptive manner. Both silt, sand and heavy minerals (e.g., Magnetite) are very common in New Zealand in the region ‘Bay of Plenty’ (Badesab et al., 2012; De Lange, 1991). This area serves as an excellent study site to investigate the effects of textural caging structures by silt and the effect of denser grains on the sediment transport behavior. However, as caging

effects and density variations occur within the sediment beds, direct observation and quantification are limited when only analogue techniques such as laboratory flume studies (e.g., (Black and Paterson, 1997) or *in situ* field studies (Soulsby, 1997)) are employed, and hence previous studies are not comprehensive. Consequently, there is a need for validation of previous conceptual models describing the influence of textural-caging structure and the effect of density variations in the bed that allow the investigation of related physical processes to predict the erosion behavior of sediments.

Numerical simulations are tools that can satisfy this need. Most of the numerical approaches are excellent tools for simulation of the hydrodynamic drivers (e.g. river flow, waves, tidal currents) and the subsequent sediment transport. In recent years, many 3D hydrodynamic models have been developed to evaluate the hydrodynamic and sediment transport characteristics on a large scaled level, such as the Princeton Ocean Model (POM) (Blumberg and Mellor, 1999), the Regional Ocean Modeling System (ROMS) (Shchepetkin and McWilliams, 2004), MIKE 3 (DHI Water and Environment, 2003), and Delft3D by WL Delft Hydraulics. All models aim at modeling marine, coastal to basin-scale problems and solve the primitive equations based on numerical grids. These approaches are widely used to study morphological effects of large scale sediment processes e.g. the simulation of sediment transport and deposition within fluvial, costal and deep marine sedimentary environments (Lesser et al., 2004; Tonnon et al., 2007; van Maren, 2007)

All large scale models use grid based calculation schemes and calculate sediment transport based on empirically developed transport equations (e.g., (Lesser et al., 2004; Rijn, 2007; van Rijn, 1993)). Therefore, these averaged sediment transport models are inadequate to describe the highly variable nature of particle motion during sediment transport (Schmeeckle and Nelson, 2003). Consequently, processes occurring at the direct vicinity of a sediment bed such as the initiation of motion are not representable by these approaches. Further, high resolution measurements of fluid flow, particle transport rates, and porosity differences at the direct vicinity of sediment beds are limited. Therefore, 3D high resolution grain scaled numerical models that focus on textural caging effects and density variations in sediment beds to quantify their influence on sediment erosion are required.

Discrete element method (DEM) models provide an important tool in the field of sediment transport by illuminating behavior at the grain scale leading to understanding and evaluation of behavior at the macroscopic level (Heald et al., 2004). DEM modeling was initiated by Cundall & Strack (1979) and the continuing evolution of computing resources has led to increasingly complex simulations. In the field of sediment transport Schmeeckle and Nelson (2003) presented a DEM model on bedload transport. The sediment particles were represented by smooth spheres, which move under the drag forces of a simulated

fluid flow. Hodge et al., (2007) used the DEM method to investigate grain-scale processes in sediment beds. This involved simulation of each grain explicitly, to investigate their behavior during multi-point collisions while undergoing transport. The model was initialized by creating a numerical sediment bed in that the requisite number of the grains had a specified size and density. The model was then run by calculating the forces acting on each grain, and using the resultant of these to calculate the grain velocities, and hence the future positions of the grains. Further, Heald (2004) presented a DEM model that explored bedload transport over a flat bed of a unimodal mixed-sized distribution of particles. The authors directly applied physical rules to large numbers of discrete sediment grains moving within a unidirectional flow. Equation of motion for sediment grains, collisions between grains, grain-flow momentum exchange and flow exposure were all accounted in their model.

These studies simulate sediment transport and hence particle transport by an applied averaged shear stress above the bed. Therefore, the individual particles are driven by the averaged forces, and hence, particle transport is physically limited to the DEM models. A coupling of a DEM model with a grid based FDM (Finite Difference Method) model to simulate particle transport by fluid flow, without using an averaged shear stress formula (Lesser et al., 2004; van Rijn, 1993), has not been shown yet. Additionally, the role of textural caging structures and density variations in sediment beds has not been investigated yet.
However, these studies reveal that large scaled models, such as Delft 3D or ROMS (Lesser et al., 2004; Shchepetkin and McWilliams, 2004), could be able of predicting sediment transport at the direct vicinity of a sediment bed, but would also be capable to predict sediment transport processes based on a better mathematical description to simulate sediment transport by particles (Lesser et al., 2004; Rijn, 2007). Therefore, the 3D high resolution models presented in this thesis show a new step in the evolution of sediment transport models to predict sediment transport on a large scale level.

The main aim of this thesis is to understand, analyze, and quantify the physical factors controlling sediment erosion and their influence in increasing erosion resistance. In particular, the effects on erosion behavior caused by texture related inhomogeneities and density differences occurring at the sediment water interface and also in the interior of the sediment bed were investigated. Analogue, laboratory-based flume studies (Chapter III) as well as numerical simulation techniques (Chapter IV - V) were used.
Due to the fact that sediment transport processes are based on physical laws it is first necessary to provide a background in the principles of sediment transport processes that will be given in the following sections.

2.2 Sediment and fluid properties

In principle, sediment transport is the result of the interaction between two physical phases, i.e. a liquid phase (e.g., water, ice, or air) and a solid phase (e.g., mineral grains). Within aquatic environments, the solid phase is represented by sediment grains, whereas the liquid phase is represented by water. For the understanding of the associated transport behavior, the physical properties of both sediment grains and water need to be introduced.

Sediment grains differ in mineralogical composition, size, and shape. Some of these grains were detached during weathering processes on rocks exposed at the earth surface, others were formed by organisms that manufacture hard tissues, and still others were formed through the precipitation of salts from natural waters, e.g., evaporation (Allen, 1982). Due to the huge variety of different sediment grains, sediments are classified according to their mineralogical composition, density, size, and shape (Allen, 1970). Natural sediment is defined as an aggregate of particles that vary in mineralogical composition, grain size range, and in textural composition (Allen, 1982). These attributes contribute to the configuration of the sediment bed. However, on a macro-scale, sediment bed configuration is also influenced by the internal packing and porosity (Middleton, 2003). All of these factors contribute to site specific sediment transport processes.

2.2.1 Mineralogical composition and density

All sediment grains found in the sedimentary environment, differ from each other according to their mineralogical composition, and hence, in density (Table 2.1). From a sedimentological perspective, minerals are classified in to three groups: common minerals, clay minerals, and heavy minerals (Allen, 1982; Komar and Wang, 1984; Leeder, 1999).

The most abundant mineral grains found in the sedimentary environment are termed as ‘common minerals’ (Table 2.1). The most ubiquitous in this group are quartz, feldspars (orthoclase, microcline, and the plagioclase series), and also calcite and aragonite, which are typically found in large quantities within beach sands (Allen, 1982; Pettijohn et al., 1972). Their density ranges between 2 - 3 g/cm³.

The second group is termed as ‘clay minerals’. Minerals of the clay group form the fine grained blackish muds that are found in estuaries or tidal flats, e.g., at the North Sea (Allen, 1982; Tucker, 1981). According to their density, clay minerals are comparable with quartz, feldspar, and carbonates. However, some of these minerals, such as small clay minerals that have the ability to stick together, generate powerful aggregates ((Whitehouse et al., 2000); section 2.5.2). Such clays are able to trap fluid into their structure and flocculate even when only a small amount of water is present (Whitehouse et al., 2000).

In contrast heavy minerals differ from common and clay groups due to their higher densities, (3.5 – 19.3 g/cm³) (Table 2.1, Chapter VI and VII). This higher density attribute plays a major role when considering

erosion behavior. Additionally, due to their relative seldom occurrences and unique mineralogical compositions, some heavy minerals are highly economically valuable (Komar, 1987).

Table 2.1: Physical properties of minerals found in sediments (modified from Allen, 1982).

Mineral	Formula	Density [kg/m³]
	Common Minerals	
Aragonite	$CaCO_3$	2930
Biotite	$K(Mg,Fe)_3(AlSi_3O_{10})(OH)_2$	2800-3400
Calcite	$CaCO_3$	2710
Dolomite	$CaMg(CO_3)2$	2870
Gypsum	$CaSO_4 \cdot 2H_2O$	2320
Microcline	$KAlSi_3O_8$	2560
Muscovite	$KAl_2(AlSi_3O10)(OH_2)$	2800-2900
Orthoclase	$KAlSi_3O_8$	2550
Plagioclase	$(Na,Ca)(Al,Si)AlSiO_2O_8$	2620-2760
Quartz	SiO_2	2650
	Clay Minerals	
Kaolinite	$Al_4Si_2O_5(OH)_4$	2600
Illite	$KAl(AlSi_3O_{10})(OH)_2$	2800-2900
Chlorite	$(Mg,Fe,Al)_6(Al,Si)_4O_{10}(OH)_8$	2600-3300
Smectite	$Al_2Si_4O_{10}(OH)_2 \cdot nH_2O$	2000-2700
	Heavy Minerals	
Magnetite	Fe_3O_4	5100-5180
Ilmenite	$FeTiO_4$	4500-5000
Zircon	$ZrSiO_4$	4500-4700
Garnet	$(Fe,Al,Mg,Mn,Ca,Cr)_5(SiO_4)_3$	3500-4500

2.2.2 Grain size and shape

When examining various sediment types by hand, e.g., different beach sands, it is not difficult to observe that sediment grains have highly variable sizes (Allen, 1982; Middleton, 2003). In sedimentology, a widely used classification scheme to determine the exact grain size of a sediments is the Wentworth`s ratio scale (Pettijohn et al., 1972; Wright et al., 1999) (Figure 2.2). This method classifies sediments based on the particle diameter (D) of individual grains. Hence, the grain-size scale classifies sediments ranging from fine to very coarse into five groups: clay, silt, sand, gravel, and boulders (Figure 2.2).

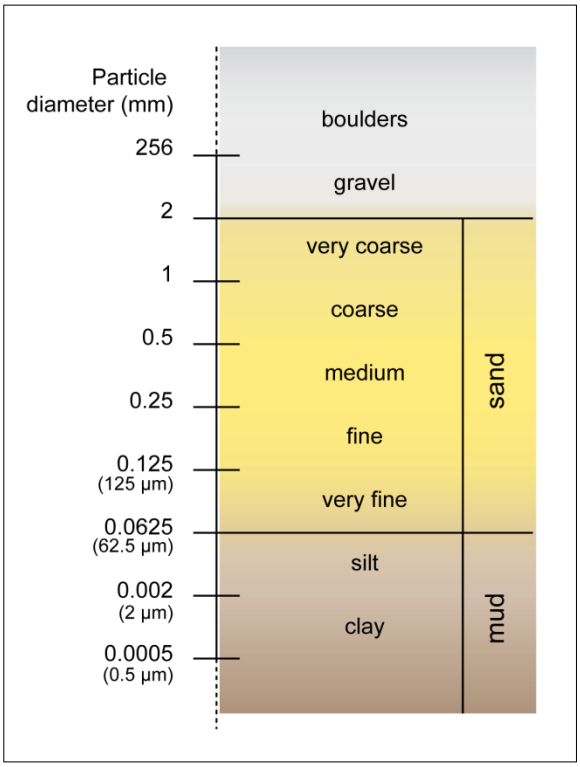

Figure 2.2: Wentworth`s ratio scale, divides sediments ranging from fine to very coarse into five grades: clay, silt, sand, gravel and boulders (modified from Wright et al., 1999).

A standardized method to determine the grain size distribution of a certain sediment sample is called test sieve analysis (Chapter III). Therein, the bulk sediment sample, e.g., 100g of beach sand, is shaken through a column of stacked test sieves with upward increasing mesh sizes, following the Wentworth scale so that the grains become separated into their respective size classes (Leeder, 1999; Middleton, 2003). The weight percentage of the total sample left in each sieve represents the frequency in the sample of the grains ranging in size between the mesh size of the sieve and that of the next coarsest (Allen, 1970; Allen, 1982). The resultant particle size distribution is graphically represented in the form of a frequency distribution versus grain size curve (Chapter III). A more recent technique to determine the particle size of a sediment sample is achieved using laser particle size analysis (Middleton, 2003). Therein, a representative amount of particles passes through a broadened beam of laser light that scatters the incident light onto a Fourier lens. This lens focuses the scattered light onto a detector array. The resultant particle size distribution is inferred from the collected diffracted light data using a specific inversion algorithm (Middleton, 2003). Similar to the sieve analysis, the measured particle size distribution can then be graphically represented in the form of a frequency distribution versus grain size curve (Tucker, 1981). Both sieve analyses, and laser particle analyses were used in this study to determine the exact grain size classes of the sediment samples tested in the flume experiments (Chapter III).

As mentioned above some natural sediments show a broad variety in their size and shape. In particular, biogenic particles, e.g., fragments of cockle shells or coral fragments, have the most extreme shape variations ranging from spherical, plate-like, and tabular, to elongated, and even needle shaped (Tucker, 1981). In contrast, non-biogenic particles, which are found in many aquatic environments, are usually more spherical-shaped due to natural rounding processes. The rounding is caused by fluvial processes, such as the abrasion within a river bed or from tidal currents (Allen, 1982; Wright et al., 1999). Consequently, the shape of sand grains ranges from angular to well-rounded minerals grains. Silts can consist of many minerals, but, by far, the most common is quartz followed by small amounts of feldspar. Similar to quartz grains, but in contrast to clay minerals, minerals of the silt group exhibit shapes ranging from angular to spherical and from rounded to well-rounded (Soulsby, 1997). Sediments consisting of significant amounts of minerals within the silt and clay range are termed as 'mud' or 'muddy sediments' (Figure 2.2). The shape of clay minerals highly depends on the mineralogical composition leading to some variability in shape, but with most having elongated or tabular aggregates (Torfs, 1997; Whitehouse et al., 2000).

2.2.3 Packing and porosity

An important factor controlling sediment transport processes is the sediment bed configuration of which packing is highly influential. A sediment bed is defined as an aggregation of multiple particles (Leeder, 1999), whereby all the grains support each other against the gravity field and define the inter-particle voids (Leeder, 1999). A measurement of the textural composition and, hence, textural density, of the bed is porosity. Porosity (Φ) describes the relationship of voids with the number of particles in the bed. Therefore, porosity (Φ) is defined by the ratio (Leeder, 1999; Middleton, 2003):

$$\Phi = \frac{V_V}{V_T} \qquad (1)$$

where V_V is the volume of the void-space between the particles and V_T is the total volume, including particles and void-space. Fine sands, for example, found at beaches or river banks, show a relatively close packing, and therefore, low porosity values of about 33 % (Soulsby, 1997; Tucker, 1981). In contrast, sediment beds composed of coarse gravels, characterized by a relatively loose packing, have high porosity values of roughly 45 % (Allen, 1982). An additional variable describing the textural composition of a sediment bed is the coordination number (Allen, 1970). This number expresses the amount of particles in contact with each other. This property is not easily measured in field experiments or laboratory based flow channel experiments (Komar, 2007).

2.2.4 Fluid properties - water

The second physical component that needs to be introduced for the understanding of sediment transport processes is the fluid phase, e.g. ice, water, and air. Physically, a fluid is defined as a substance that continually deforms under applied stress (Leeder, 1999). In aquatic environments, liquid is the hydrodynamic driver of sediment transport processes and is physically distinct from solid particles by its viscosity.

2.2.5 Viscosity of water

Generally speaking, viscosity is the resistance of a liquid to flow and is understood by its density (Munson et al., 2002). For example, water has a relatively low viscosity, whereas honey or oil are much denser, and, thus, have higher viscosities. Therefore, it is generally understood that the less viscous a substance, the greater the ease of fluidity. Expressly, the viscosity is a measure of the resistance of a fluid that is deformed by an applied stress (Allen, 1982; Munson et al., 2002).

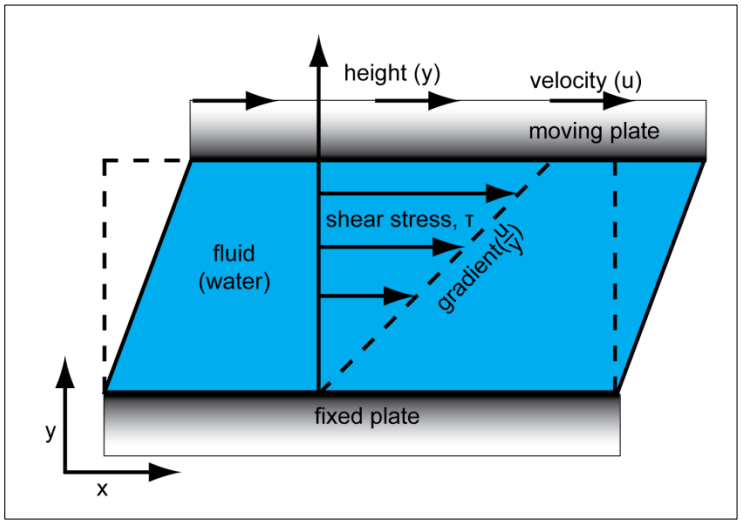

Figure 2.3: Schematic X, Y profile describing a physical approach to measure the viscosity (modified from Munson et al., 2002).

A simple physical experiment (Munson et al., 2002) to determine the viscosity is shown in Figure 2.3. Consider two plates: one lower and one upper (fixed plate and moving plate; Figure 2.3) with close vertical spacing (y). Between the plates, any physical substance, e.g., water, ice, or even solid materials can be placed. For example, if water is filled between both plates and the upper plate is moved the applied stress will easily move the water. This required force or shear stress, to move the water is a measure of the fluid viscosity and is also known as the 'viscous force'. Physically, the water between both plates undergoes a shear flow and develops a velocity gradient (du/dy). Therein, viscosity represents the

momentum that flow loses in order to sustain a velocity gradient. The applied force, resulting in a shear stress (τ), is proportional to the velocity gradient (du/dy) in the fluid and can be written:

$$\tau = \mu \frac{du}{dy} \qquad (2)$$

where μ is the proportionality factor called viscosity (Munson et al., 2002). The SI units of viscosity are Newton seconds per square meter (N s/m²). Water, for example, has a viscosity of 1.06 x 10^{-3} N s/m² at 18°C (Middleton, 2003), whereas air has a viscosity of 1.8 x 10^{-5} N s/m² (Munson et al., 2002; Soulsby, 1997). Additionally, the viscosity of water is influenced by salinity and water temperature where, for example, the viscosity increases when salinity increases or the water temperature decreases (Leeder, 1999). Salinity is defined as the amount of dissolved salts (e.g. magnesium, sodium chloride) in a body of water and is measured as per mil, ‰ (parts per thousand). Salinity values of our modern oceans have, on average a salinity of with 35 ‰ (Leeder, 1999). As an example, seawater is slightly more viscous than freshwater and is, therefore, more resistant to flow. Temperature also influences the flow resistance of water and is, in fact, more important for viscosity than salinity (Middleton, 2003).

2.3 Fluid flow behavior

Following the description of the physical properties of sediments and water, it is prudent to review, the physical characteristics of the fluid flow, the flow velocity distribution, and the behavior of the fluid forcing, for a more complete background of the mechanisms influencing sediment transport.

2.3.1 Laminar and turbulent flow behavior

Flow can be laminar or turbulent in the fluid phase. This phenomenon is best visualized by looking at the tip of a burning cigarette (Leeder, 1999). At the tip, the smoke is rises perpendicular to the cigarette with parallel streamlines exemplifying laminar behavior. After the smoke reaches a certain speed, the rising filament breaks and begins to form large eddies at which point laminar flow transitions into turbulent flow behavior (Leeder, 1999). In water, this phenomenon can be also visualized when introducing dye into a flow channel, whereby large eddies also linear streamlines can be observed (Allen, 1982). A schematic of laminar and turbulent fluid behavior is presented in Figure 2.4. Laminar flow is defined by parallel unidirectional streamlines that follow parallel paths with constant velocities along the streamlines. With increasing distance from the seabed, these streamlines tend to flow at successively higher speeds creating a velocity gradient (compare section 2.2.5). Laminar flow occurs at low flow speeds over smooth sediment beds and is assumed for the most subsurface flows or at the sediment water interface close to the bottom of the boundary layer (Allen, 1982; Wright et al., 1999). In contrast, turbulent flow is characterized by flow as a series of constantly changing and deforming masses (eddies) that superimpose the mean motion. Turbulent flow behavior occurs in the higher parts of a water body (Wright et al., 1999).

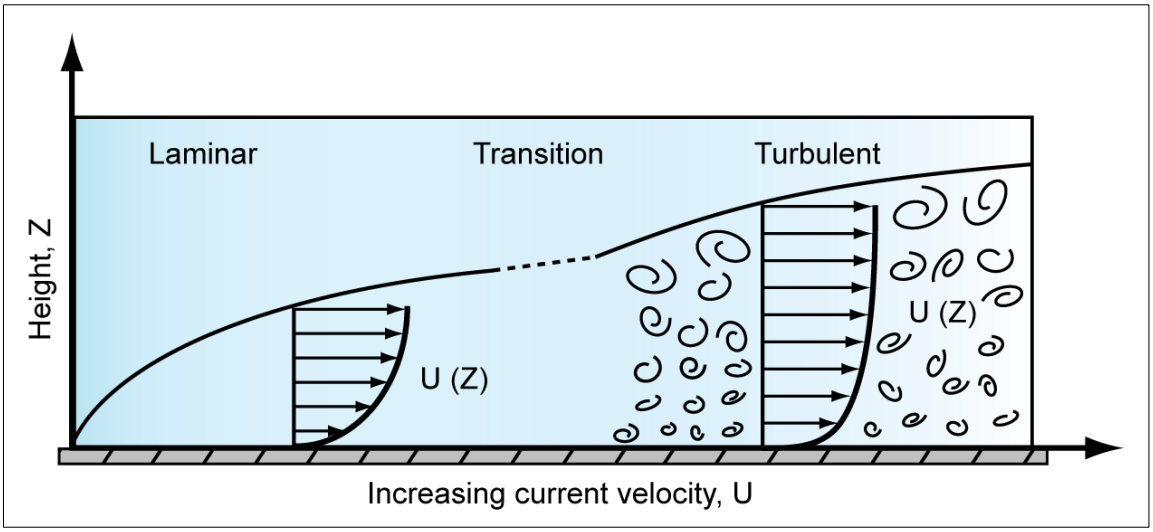

Figure 2.4: Laminar and turbulent fluid flow behavior (modified from Allen, 1982).

The transition from laminar to turbulent flows is described by the Reynolds number (Re). Osborne Reynolds, a British 19th century physicist, realized from his classic Reynolds apparatus experiments, the transition from laminar to turbulent fluid flow (Leeder, 1999). This transition is expressed by:

$$Re = \frac{Uh}{\nu} \qquad (3)$$

where Re is the dimensionless Reynolds number, U is the flow velocity (m/s), h the flow depth (m), and ν (N s/m²) the fluid viscosity (Wright et al., 1999). Reynolds showed that a fluid flow becomes turbulent when Re exceeds about 500 – 2000. Free-surface flows are laminar at Reynolds numbers less than Re 500 and at Reynolds numbers larger than Re 2000, flows are fully turbulent (Leeder, 1999; Wright et al., 1999).

2.3.2 The boundary layer

Consider a fluid is running near a solid surface. Due to the friction of the surface the fluid flow experiences a current shear and is slowed down along that boundary. This area of flow retardation caused by friction is called the "boundary layer". Boundary layers develop wherever fluids moves over a surface, e.g., wind over a dune, or water over a sediment bed (Wright et al., 1999). Due to the decreasing flow velocities with proximity to the surface, the flow velocity profile in the boundary layer exhibits a logarithmic pattern (Figure 2.5). The development of the boundary layer was initially described by Ludwig Prandtl, who worked in the field of aerodynamics in 1904 (Schlichting and Klaus, 2004). Most sediment transport processes, whether it is the erosion of a single sediment grain, or large scale effects, such as bed form development, occurs within this layer. (Leeder, 1999).

Above the boundary layer, the flow field is characterized by more or less constant flow velocities with no velocity gradient. Therefore, flow velocities in this area are defined as the free stream velocity U (m/s) (equal length flow vectors in Figure 2.5). The fluid flow behavior in this area is considered to be fully turbulent (see section 2.3.1).

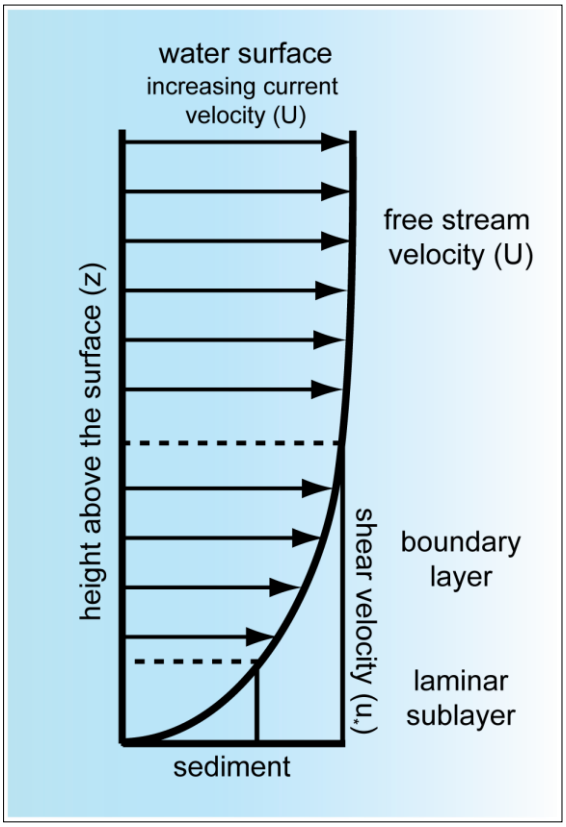

Figure 2.5: Schematic of the boundary layer (modified from Wright et al., 1999).

With depth, where the flow is influenced by the proximity of the surface (e.g. sediment surface), friction causes a current shear and, hence, the decrease in flow speeds along that boundary (Wright et al., 1999). Within this layer, flow velocities decrease logarithmically with decreasing height (z), at a measurable gradient (dU/dz) (see section 2.5). The fluid flow behavior in this area is transitional and ranges from turbulent to laminar fluid behavior, and is defined as the transitional zone (see section 2.3.1). Within the boundary layer, due to a friction related reduction in flow speed, the flow velocity can be characterized by the friction velocity or shear velocity, u_* (m/s). The shear velocity (u_*) at the sediment bed is generally about an order of a magnitude smaller as compared to the mean free stream velocity (U). A good approximation of the shear velocity (u_*) can be derived as (Allen, 1970; Wright et al., 1999):

$$u_* = \frac{1}{5.75} \cdot \frac{du}{dlogz} \qquad (4)$$

A more accurate way to determine the flow velocity is a measurement of the shear velocity in the lower boundary layer directly above the sediment bed (see Chapter III). From the measured shear velocity, u_*, the shear stress τ_b (N/m²) at the sediment bed, i.e., bed shear stress, can be readily calculated. Both shear velocity and bed shear stress are important parameters required to determine the erosion of sediment bed (Allen, 1970):

$$u_* = \sqrt{\frac{\tau_b}{\rho_w}} \qquad \tau_b = \rho_w {u_*}^2 \quad (5)$$

where ρ_w is the density of water.

2.3.3 The laminar sublayer

Due to the fact that friction from the sediment causes a current shear and a decrease in flow speeds, the flow is not turbulent throughout the whole thickness of the boundary layer (Leeder, 1999; Wright et al., 1999). At the bottom of the boundary layer near the bed, a sheet in which the flow is fundamentally laminar can develop (Leeder, 1999; Wright et al., 1999). This area is defined as the laminar or the viscous sublayer (Figure 2.6). However, the laminar sublayer develops when the currents are low in flow speed and the sediment bed is essentially flat (Figure 2.6). Within the sublayer, the velocity gradient is constant, and the shear stress is dominated by the viscous forces (see section 2.2.5). The thickness of the sublayer is considered to be only a few millimeters thick (Wright et al., 1999). The existence of the laminar sublayer is particularly important in the study of sediment transport processes of fine grain size distributions, which is one of the major objectives of this thesis (Chapter III - VII). The vertical development of the laminar sublayer is highly dependent on the sediment bed configuration, i.e., fine grain size distribution, and the

absence of bed features, such as bed forms or ripples (Wright et al., 1999). At a sediment bed surface with high proportion of fine sediment, all grains are immersed in the laminar sublayer (Figure 2.6). The laminar sublayer can remain intact when the average grain diameter is less than one third of the thickness of the sublayer (Wright et al., 1999). If the grain diameters are seven times or more the notional thickness of the sublayer, e.g., in gravel river beds, the grains protrude so far into the turbulent layer and the viscous layer becomes compressed or even breaks leading to fully turbulent fluid behavior (Leeder, 1999; Wright et al., 1999). In this case, development of the laminar sublayer would not to be expected (Figure 2.6). However, towards the top of viscous sublayer, the layers of water move successively faster as the effects of friction decrease and turbulence starts to develop. This zone of turbulence development in the boundary layer is also referred as the transition zone (Schlichting and Klaus, 2004; Wright et al., 1999) (Figure 2.6).

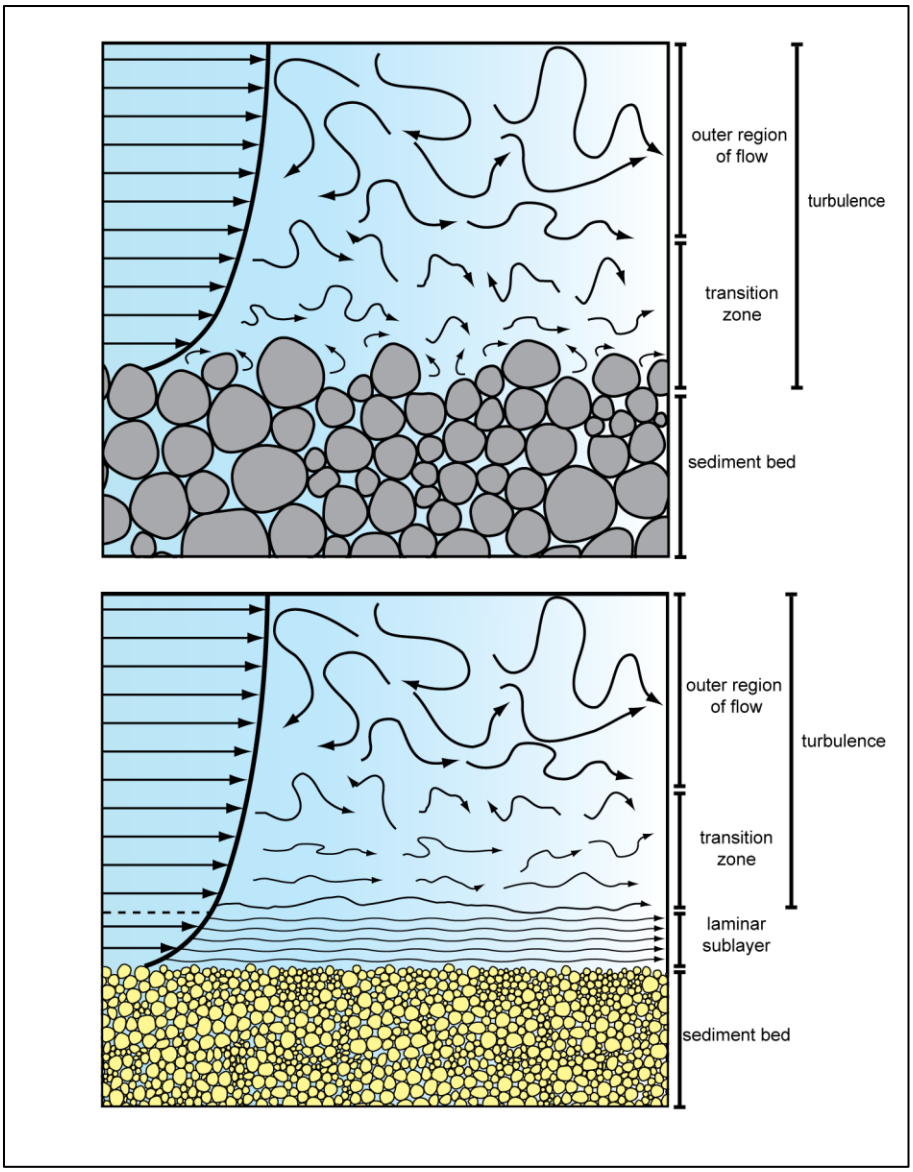

Figure 2.6: Schematic of the fluid behavior above fine and coarse sediment beds.
(modified from Wright et al., 1999).

2.4 Sediment erosion, transport and deposition

The following section introduces the processes of sediment erosion, transport, and deposition. A brief overview on the prediction of sediment erosion is also included.

2.4.1 The initiation of motion

The initiation of sediment motion occurs if: "the aqueous discharge is gradually increased over a plane sand bed; a fairly definite flow condition is reached when grains begin to be entrained" (Allen, 1970; Rijn, 2007). This condition marking the start of sediment transport, is called the plane-bed threshold for particle motion (Figure 2.7). From a grain scale perspective, the threshold beyond which particles move is reached when the instantaneous fluid force (FF) is larger than the resistance force (FR) of the grain, which is a function of the particle weight (FG), the pivoting angle (φ), the lift force (FL), and the drag force (FD) (Allen, 1970; Miller et al., 1977; Rijn, 2007). This relationship is schematized in Figure 2.7.

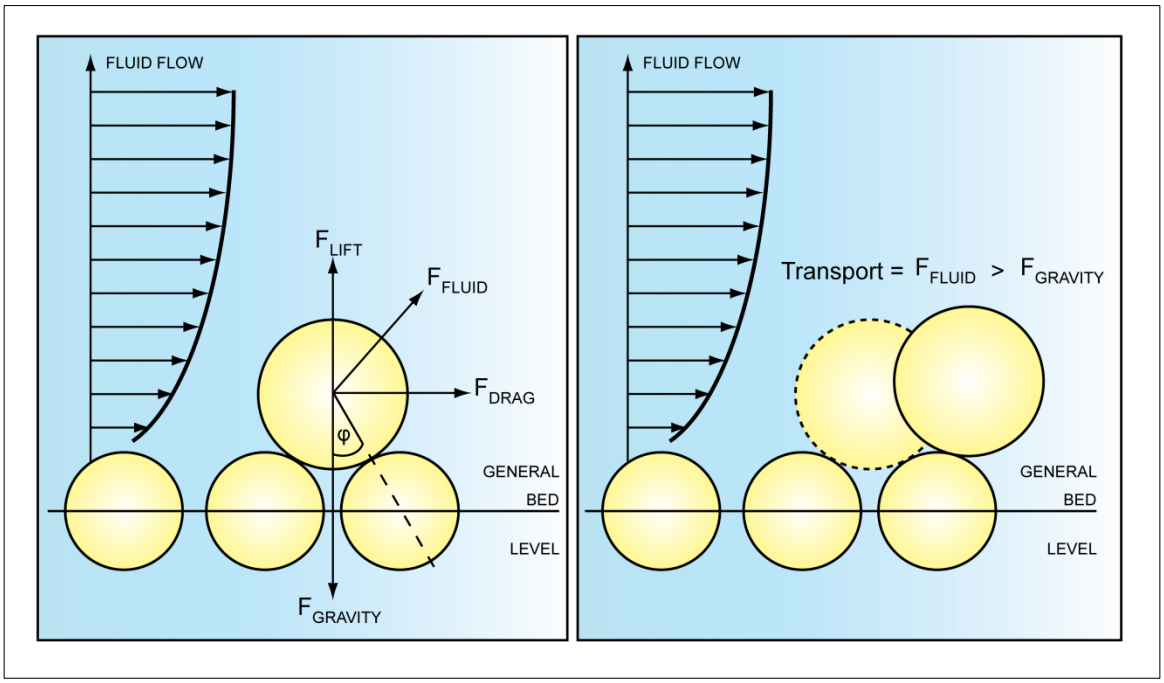

Figure 2.7: Initiation of motion of a single particle on top of a sediment bed (modified from Allen, 1982).

The pivoting angle (φ) describes the geometric relation of the center between two grains at a sediment bed surface. In order to determine the angle the Pythagoras relationship is used (Miller et al., 1977):

$$\tan\varphi = \frac{\sqrt{\Delta x + \Delta y}}{\Delta z} \qquad (6)$$

where x, y, and z are the 3-dimensional coordinates. A small pivot angle implies that a grain sits, with a high degree of stacking above the underlying grain and, thus, is more exposed to flow and entrainment

compared to a grain with a large pivot angle (Middleton, 2003). These governing forces only apply to non-cohesive grains, such as sand and silt (Miller et al., 1977; Soulsby, 1997).

2.4.2 Prediction and the modes of sediment transport

In order to predict sediment transport for engineering purposes, e.g., for the prediction of coastal erosion, various studies have used empirical approaches, such as laboratory based flume tanks (Amos et al., 1992; Black and Paterson, 1997; Hir et al., 2011; Mehta and Lee, 1994; Torfs, 1997). The two most classic approaches for the prediction of sediment erosion are: the Shields diagram (Figure 2.8), and the Hjulstroem diagram (Figure 2.9). Slightly modified versions (Mc Cave, 1984; Shields, 1936; Soulsby, 1997) of both curves are still used today for the prediction of sediment erosion. The Shields diagram (Shields, 1936) presented in Figure 2.8, has been modified more recently by Soulsby et al., (1997). The diagram explores sediment erosion by the dimensionless Shields parameter (Θ) as a function of the dimensionless grain size (D_*). The Shields diagram is divided into an area of sediment erosion (blue area; Figure 2.8) and no erosion (red area; Figure 2.8).

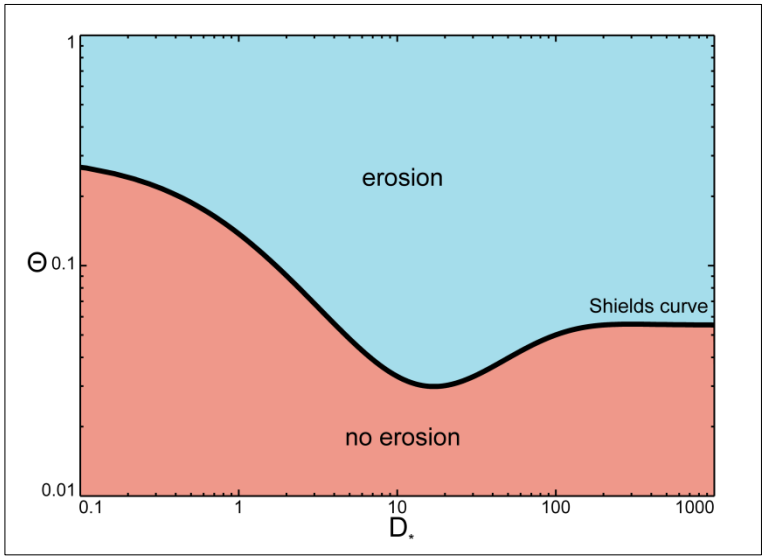

Figure 2.8: Shields diagram (modified from Soulsby et al., 1997).

As sediment erosion is also dependent on the viscosity the fluid (ν), grain diameter (d), gravity (g), grain density (ρ_s) and water density (ρ_f), the diagram is represented with dimensionless variables as (Shields, 1936; Soulsby, 1997):

$$\Theta_{cr} = \frac{\tau_{cr}}{g(\rho_s - \rho)d} \quad D_* = \left[\frac{g(s-1)}{\nu^2}\right]^{1/3} \quad s = \rho_s/\rho_f \qquad (7)$$

where D_* is the dimensionless grain diameter and Θ is the dimensionless Shields parameter representing the critical shear stress (τ_{cr}) i.e. that required to entrain particles. A rough conversion of the dimensionless grain diameter to measured grain diameters in (d) is: $D_* < 1.2$ ~ silt; $1.2 < D_* < 40$ ~ sand; and $D_* > 40$ ~ gravel (Soulsby et al.1997).

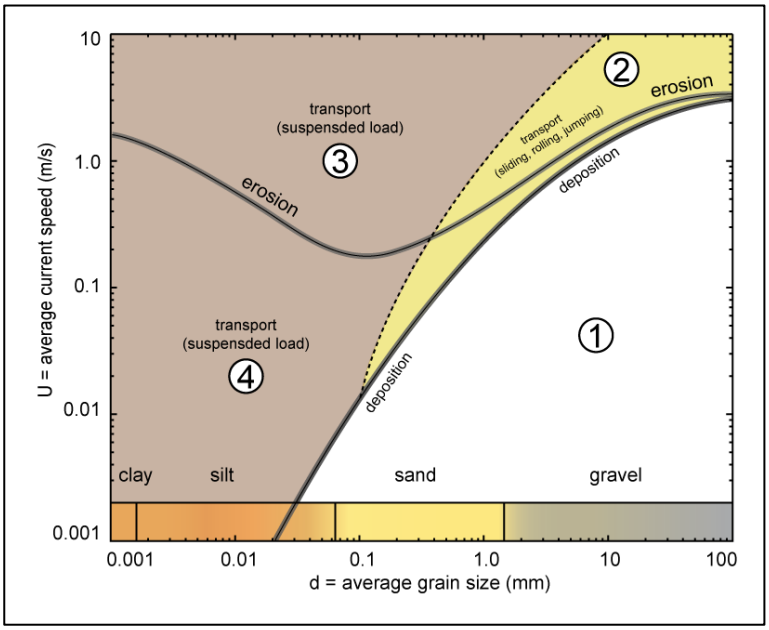

Figure 2.9: Hjulstroem diagram, 1 - 4 indicate the modes of erosion (modified from Wright et al., 1999).

The second important predictor for sediment transport was introduced by Hjulstroem in 1938 (Figure 2.9). In contrast to the Shields approach, Hjulstroem did not convert to dimensionless variables. However, he classified sediment transport into four different modes represented as four different regions in the diagram:

1) flow velocities are too low to erode particles; 2) particles ranging from 0.02 mm to 2.0 mm are eroded and are transported as bed load; 3) grain transport in suspension load; 4) particles of the silt and clay fraction are eroded and are transported directly into suspension. The modes of sediment transport occurring at the surface of a sediment bed described by Hjulstroem (1938) are illustrated in Figure 2.10. Sediment transport at the surface of a sediment bed can occur as bed load transport and suspended load. Bedload transport is characterized by grains that move by sliding (1), rolling (2), or even jumping (3) over the sediment bed. Eventually, when the flow force is large enough, particles begin to be transported in the suspension mode (4), where they lose traction with the sediment bed completely. Smaller grains are mostly carried directly in suspension, i.e., silt and clay. Particles that remain in the deposition mode are not transported at all.

It should be highlighted that the horizontal erosion curves within both the Shields and the Hjulstroem diagrams show an increase in threshold conditions in the silt and clay range (Figure 2.8 and 2.9). Both researchers observed that much higher shear stresses are required to entrain these very fine particles compared to sands (Figure 2.8 and 2.9). Consequently, the relation of grain size and shear stress is not a straightforward linear one (Allen, 1982; Mc Cave, 1984; Whitehouse et al., 2000).

The non-linear relationship has been explained by the additional influence of such factors as, matrix composition, the presence of benthic communities, cohesion, textural caging structures, and density differences (see section 2.5). All of these factors may enhance the erosion resistance and, thereby, pushing the sediment bed towards higher threshold conditions especially in beds with a large fine component.

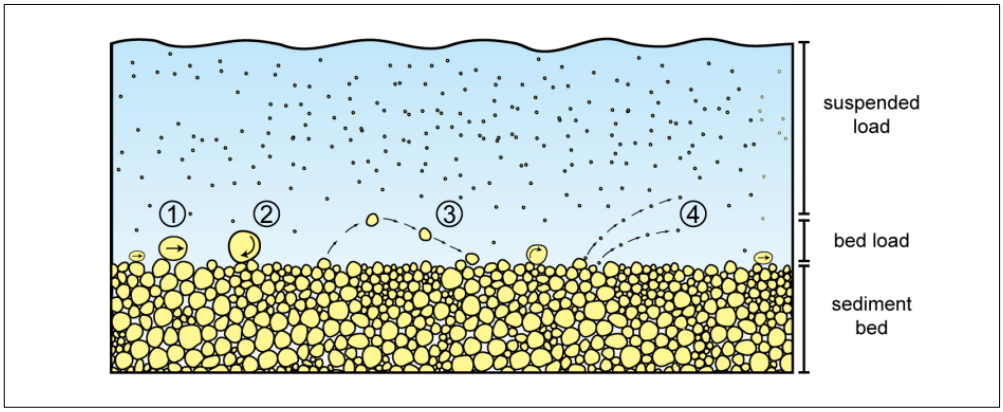

Figure 2.10: Schematic showing the modes of erosion
(modified from Wright et al., 1999).

2.5 Additional factors controlling sediment transport

At present, it is generally accepted that the erosion behavior of sediments is highly influenced by the 1) biological processes, 2) chemical processes, 3) textural caging structures, and/or 4) density related effects (Komar, 1987; Paterson, 1994; Torfs, 1997; van Ledden et al., 2004; Whitehouse et al., 2000). All of these factors have the potential to alter the erosion behavior towards higher threshold conditions and increase the bed stability. An overview of these factors is given in the following sections as well as in Chapters III - VII.

2.5.1 Biogenic factors

Due to the fact that marine environments are ecologically active zones, some natural sediments are home to significant amounts of biota, which can influence the erosion behavior of the sediment beds (Paterson, 1994; Whitehouse et al., 2000; Widdows et al., 1998; Young and Southard, 1978). Their presence and activity at the sediment surface and also in the interior of the bed can affect the sediment erosion behavior through both biostabilizing and biodestabilizing processes (Whitehouse et al., 2000). One factor causing sediment biostabilization is the presence of EPS (extracellular polymeric substances), which is secreted by many micro- (bacteria, microalgae, fungi) and macro- (worms, mollusks, crustaceans) faunal species (Whitehouse et al., 2000). Additionally, the formation of biological network structures, such as algae mats, provide additional strength on and within the sediment bed for resistance to fluid flow. In contrast, the activity of digging and burrowing organisms can weaken the sediment bed structure (Whitehouse et al., 2000). This process termed bioturbation, is one example of biological destabilization of the sediment bed. Further examples are reviewed in Whitehouse et al. (2000).

2.5.2 Cohesion

Sand grains are commonly composed of quartz minerals making them chemically hard and stable. In contrast, minerals of the clay group, i.e., kaolinite, illite, chlorite, and montmorillonite, are cohesive (latin cohaerere means stick together) (Middleton, 2003). These minerals are mostly found in muddy sediments and possess inherent ionic charges that can undergo chemical changes in their elemental makeup (Whitehouse et al., 2000; Winterwerp and Van Kesteren, 2004). If sediments contain a significant amount of these minerals the erosion resistance is usually high (Torfs, 1997). Within aquatic environments, these minerals typically occur in plate-like aggregates and are less than < 2 µm in size (Allen, 1982). The reason why sediments containing clay minerals are more resistant to erosion is due to the occurrence of chemical forces acting between the grains (Whitehouse et al., 2000). Clay minerals are characterized by negatively charged faces and positively charged edges (Winterwerp and Van Kesteren, 2004). The opposing charges from neighboring grains can cause adhesion between them. This electrostatic force leads to the binding of clay particles and causes the cohesive or sticky nature of clay rich sediments (Whitehouse et al., 2000; Winterwerp and Van Kesteren, 2004). Further literature on cohesive sediments is given in e.g., Whitehouse et al. (2000) and Mitchener and Torfs (1996).

2.5.3 Sediment bed composition and textural-related processes

The composition of a sediment bed, whether it is composed of a single grain size or broad spectrum of particle sizes, plays a significant role in erosion behavior. Due to the fact that natural sediments show a broad spectrum of grain sizes, i.e., coarse and fine particles, the different entrainment properties of the component particles cause variable erosion behaviour compared to what would occur over a uniform grain size bed (van Ledden, 2002). Therefore, sediments beds composed of multiple grain sizes have different erosion behaviour than those single-grained beds assumed for the classical relationships described by Shields (1936) and Hjulstroem (1935).

For mixed grain beds, textural in-homogeneities and the grain size differences can result in the development of structures within the sediment beds which can further increase the erosion resistance.
At present, a well understood effect is that sediment beds composed of fine particles are stabilized by overlying coarse particles (Middleton, 2003; Sutherland, 1987). This effect of sediment bed stabilization is termed as ‘armouring’. Such an upward coarsening graded bed is formed through selective entrainment (i.e., wash out of the fine fraction and retention of the coarser fraction), where coarse grains protect and armour the underlying material resulting in a more stable sediment bed (Middleton, 2003; Sutherland, 1987; Tucker, 1981) this stabilization raises the erosion threshold, which, in turn, reduces the transport rate.

It is widely accepted that the erosion resistance of a sediment bed can be controlled by textural induced caging structures (Hir et al., 2008; Hir et al., 2011; van Ledden, 2002). These texture induced caging structures develop when fine particles encompass coarse grains as a cage, whereby the sand pore space is filled with smaller clay particles (Mitchener and Torfs, 1996). These structures stabilize the sediment bed and increase the critical threshold conditions (Whitehouse et al., 2000). Raster electron microscope pictures of this effect are shown in, e.g., in Whitehouse et al. (2000). Mitchener and Torfs (1996) showed that a similar effect is caused when fine clays are deposited on top or mixed into a sand bed. They concluded that the generation of the cage-like network, while increasing the density of the matrix, also introduces additional cohesive forces, which together act to raise the erosion resistance. This was also observed in various experiments, e.g., Panagiotopoulos et al. (1997), Wiberg and Smith (1987), and Torfs et al. (2000), which showed that sediment stability is increased by clay in-filled pockets within the sand bed. This textural caging effect was mainly investigated using clay-sand mixtures. However, it was shown in this thesis (Chapter III - V) that other fine fractions, e.g., silt, which is very common in many sandy coastal environments (Healy, 2002), can cause similar texture related stabilization.

2.5.4 Density-related effects

An additional factor controlling the sediment erosion behavior is related to density differences of the minerals forming the sediment bed (see section 2.2.1). Density differences between the individual grains in sediment beds play a major role in the erosion characteristics, e.g., lighter grains are transported faster compared to the heavier denser particles (Badesab et al., 2012; Bryan et al., 2007; Komar, 1987) (Chapter VI and VII).The light mineral fractions can be ‘washed-out’ more easily due to the lower density-related threshold condition. This process of hydrodynamic sorting is understood as selective grain entrainment (Komar, 2007). If the light mineral fraction is washed out, then the heavier mineral fraction can accumulate faster than the light fraction (Komar, 1987; Li and Komar, 1992). These accumulations of heavy minerals are defined as deposits of residual or detrital mineral grains and are termed as ‘placers’. Placers are an interesting natural phenomenon as they represent a potentially valuable economic resource (Komar, 1987; Peterson et al., 1989).

2.6 Methods

2.6.1 Analogue flume tank experiments

All macro-scaled experiments presented in Chapter III were carried out using an annular laboratory flume (Figure 2.11). The circular channel was 10 cm wide and bounded by an outer (63 cm) and inner (43 cm) rim resulting in a bed area of 1700 cm². At the maximum water level of 25 cm, 40 litres of seawater (Salinity = 30 ppt) were accommodated in the flume. A removable, rotating lid (45 cm diameter) driven by a 12 V motor was mounted on top of the flume, which caused a current motion of up to 30 cm/s (55 rotations per minute (RPM); 1RPM is 0.526 cm/s (Jones et al., 2011)). The motor speed was controlled by a computer with Labview-based software which allowed the controlled variation of flow speeds. Suspended particulate matter concentration (SPM) in the water column was recorded by an optical back scatter-sensor (Seapoint turbidity meter; Seapoint sensors inc.) positioned 7.5 cm above the sediment bed (Figure 2.11). To parameterize the bed shear stress and shear velocity, a downward looking SonTek Micro Acoustic Doppler Velocimeter (ADV) was used. The ADV was mounted onto a vertical racking system through the base plate into the middle of the channel (Jones et al., 2011).

To investigate the influence of silt controlling the stability of a sandy sediment bed, both fractions were sampled in New Zealand. Both silt and sand are very common in New Zealand in particular in the region 'Bay of Plenty' (Healy, 2002). The sand used in the experiments (sampled from Pauanui Beach, New Zealand, 37°0'41.48"S 175°51'58.03"E) was dry sieved to 300 µm (D50, average grain diameter) ranging from 210 µm – 310 µm; using an Endecott's sieve-shaker, whereas the silt (sampled from Waikareao Estuary, Tauranga Harbour, New Zealand, 37°41'42.98"S 176°9'11.80"E) component was extracted from the bulk sample by wet sieving to D50 = 55 µm. Wet sieving had only limited ability to constrain the size fraction, and the grain size distribution of the silt fraction ranged from 0.8 µm – 200 µm (determined using a Laser Particle analyser.

In order to investigate the parameters controlling the stability of a sediment bed two suites of experiments were designed. One in which a sandy bed was covered by a thin layer of silt of varying thickness ((1) "The Layering Experiment") and one in which the bed was composed of sand mixed with small amounts of silt ((2) "The Mixing Experiment"). Both experiments consisted of two phases. In Phase I the bed was allowed to settle and consolidate and in Phase II, the velocity in the annular flume was increased to cause erosion. In each experiment the bed was prepared by creating a 5 cm thick sediment bed in the flume (sand in experiment 1, sand-silt mixture in experiment 2). After filling the channel with sediment, the bed was saturated with saltwater and flattened by a scraper which fitted exactly into the channel. A sheet of bubble-wrap plastic, cut to the dimensions of the channel, was placed on top of the sediment to ensure the bed was not disturbed by the inflow as the tank was filled. Subsequently, the motor, the OBS and the rotating lid were installed. Within experiment (1) the Layering suites were made up of 6 runs with 29; 118; 235; 353; 471 and 941 g/m² of silt deposited in a thin layer on the bed ranging from 0.2; 0.6; 1.1; 1.8;

2.2 and 3 mm. The ranges were chosen so that the lower levels (29; 118 g silt/m²) would fill the pore spaces but not cover the surface. To achieve the best possible dispersion in the flume, the silt mixture was poured gently into the flume with the motor running at 5 cm/s for 5 min. The material was allowed to settle for 4 h by decreasing the velocity to 2.5 cm/s. Within the erosion Phase II the current velocity was increased in steps of 2.5 cm/s ranging from 2.5 - 30 cm/s with the exception of the change between 20 and 25 cm/s, which was undertaken in one 5 cm/s increment. Each velocity increment was 15 min in length. The "Mixing" suite of experiments was made up of 4 runs, each with increasing quantities of silt added to the bed (120 g/m³; 300 g/m³; 600 g/m³; 1200 g/m³). Similar to the Layering experiments, the Mixing experiments were divided into two phases. In Phase I, the mixed sand and silt were added to the flume then allowed the bed to settle under no flow for 12 h. Phase II was the same as in the Layering experiments. All data was processed using Matlab 2011.

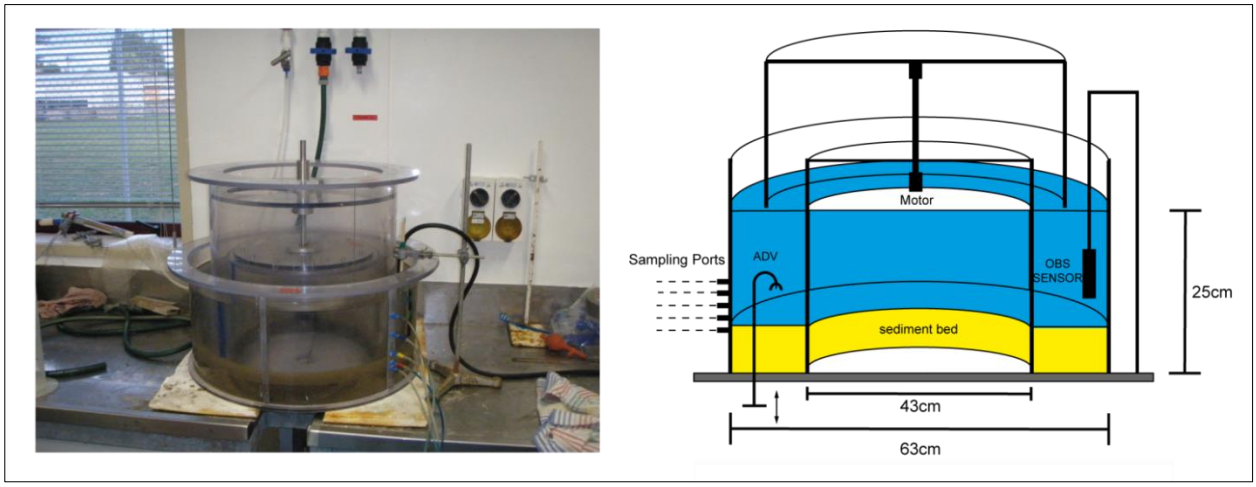

Figure 2.11: Photograph and schematic of the annular flume (Aquatic Research Centre, University of Waikato, New Zealand).

2.6.2 Numerical methods

In order to quantify the physical parameters (see section 2.5 and 2.6) controlling sediment- fluid interactions, in particular sediment erosion and transport, at the direct vicinity of sediment water interface an in the interior of a sediment bed a high resolution 3D numerical flume tank was developed (Chapters IV - VII). Therefore, two independent numerical simulation techniques: the Finite Difference Method (FDM) and the Distinct Element Method (DEM) were coupled. Therein, the FDM model calculates the flow conditions (Fluid model, Figure 2.12) and the DEM model simulates the 'sediment' matrix (Sediment matrix model, Figure 2.12).

The 3D FDM Fluid model was generated using the commercial software FLAC 3D (Fast Ligurian Analysis of Continua; (Itasca, 2004b). This technique is based on the spatial discretization of the study domain into a grid of a finite number of three dimensional rectangular polyhedral elements (Figure 2.12 (Itasca, 2004b)). The software allows the assignment of physical material properties (i.e. fluid parameters) to each cell in the grid (e.g. fluid density and viscosity) in order to mimic natural conditions. In addition, boundary conditions (e.g. boundary inflow velocities and fluid sources) were designated to the model. Consequently, the FDM model calculates flow velocities in each grid cell, based on the applied boundary conditions and approximations of the differential flow equations through numerical differentiation at defined time steps (Itasca, 2004b).

At the same time, a DEM model was used to mimic 'sediment beds' numerically. These were simulated as a particle assembly consisting of multiple, ideal and spherical particles (i.e. numerical 'silt' and 'sand' grains (Figure 2.12)). The software, (PFC 3D, (Particle Flow Code; (Itasca, 2004a)), is based on the DEM theory by Cundall and Strack (1979), which describes the mechanical behavior of particle assemblages based, on physical contact laws. In order to mimic natural conditions, physical properties, such as density, friction, and hardness were assigned to each particle. Similar to FDM, boundary conditions must be designated (e.g. gravity and ball acceleration). The resultant particle assemblages, or the 'sediment body', respectively, are deformable by these applied forces. Consequently, DEM allows the simulation of sediment particles, sediment particle interactions, internal structures, and also porosities. Thus, the method simulates the physical behavior of the particle assemblages during deformation processes, such as the initiation of motion of single spherical grains driven by defined boundary conditions, (e.g. fluid forcing (Figure 2.12)). A complete description of the numerical procedure of the FDM code can be found e.g., in Itasca (2004a). Further descriptions of the numerical DEM code can be found in e.g., Cundall and Hart (1989), Cundall and Strack (1979, 1983), Itasca (Itasca, 2004a), and Kock and Huhn (2007).

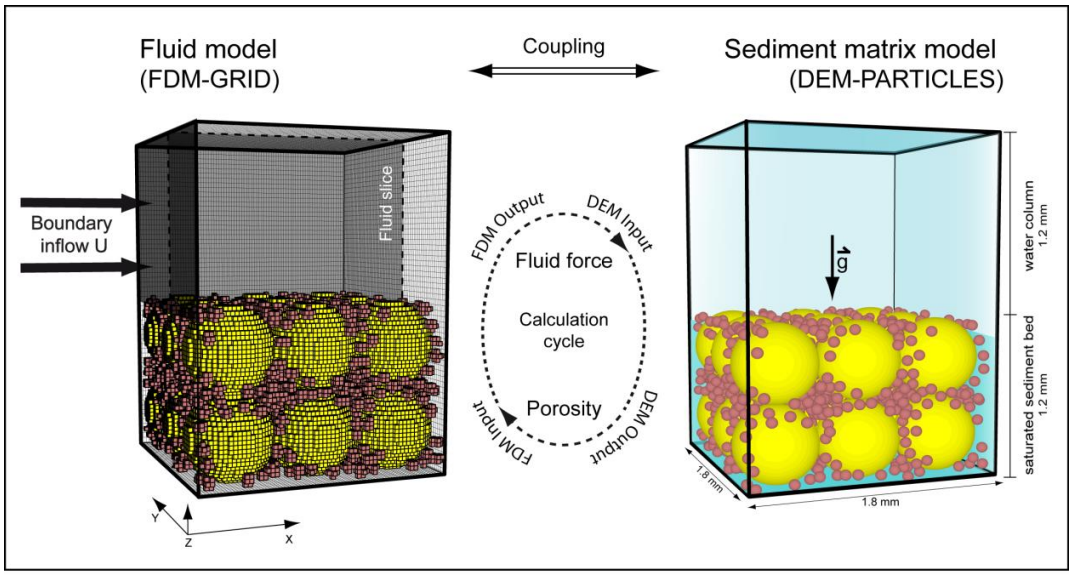

Figure 2.12: Schematic of the coupled sediment matrix model (DEM - discrete elements method) and fluid model (FDM - finite difference method).

In order to quantify the influence of caging structures (Chapter IV and V) and density related effects (Chapter VI and VII) various sediment beds were generated numerically on grain scaled level. At the beginning of the simulation, the grain or sediment model was generated, in order to mimic an isolated section of a sediment surface in a flume tank on the grain-scaled level. Therein, 5 stiff un-deformable box walls were created. To mimic the sediment beds numerically, a sample box was generated which was filled with the numerical sediment. However, the composition of the sediment beds and hence physical parameters of the particles were varied according to the objectives of each study (Chapters IV - VII). In the following step, each sediment bed was tested on erosion behavior by using predefined flow speeds.

Coupling of both models was undertaken after generation of the above described initial model configurations. In the first step, all information from the sediment matrix, such as the spatial parameters x, y, and z coordinates and the radii of all particles, were sent from the DEM to the FDM model. Based on these data representing the grain distribution within the DEM model, the FDM grid elements are defined as either fluid cells or sediment cells. The resulting FDM model grid consists of elements where fluid streaming was allowed (fluid zones) or not allowed (solid matrix zones).
After the grid was classified, a constant boundary inflow above the fully saturated bed field was applied in X-direction at the left box wall and outflow boundary condition at the right box wall (Figure 2.12). Starting with these initial stable conditions, a constant stream in the positive x-direction above the sediment bed evolved. All flow velocities were calculated from cell to cell throughout the whole model (in the water column and the saturated matrix area) based on the initial porosity distribution. After the flow field reached stable conditions, all flow velocities were extracted. These flow velocities were transformed into forces according to the Stokes velocity law (Miller et al., 1977). These fluid forces were sent to the sediment matrix model at their corresponding X,-Y, and Z coordinates and applied to their positioned particles. The velocity parameters then served as boundary conditions for the Sediment matrix model. Based on this forcing, new particle contact forces and the resulting particle displacements were calculated in the DEM model. If the added fluid forces were larger than the resisting force of the particles, the particle contacts broke up and the grains were transported (Cundall and Strack, 1979). This caused new porosities within the DEM model and new particle configurations, respectively. Hence, sediment transport and / or grain re-assembly was initiated. In the cases of grains that were eroded from the matrix, they were transported by the stream. The resultant new porosities (Sediment matrix model) were sent back to the Fluid model and, subsequently, a re-meshing of the FDM model grid was initiated starting a new calculation cycle. The calculation cycle between both models was repeated until constant flow and transport conditions were reached. Hence, high resolution information about, e.g., particle distribution, porosity, texture, and fluid velocities at the sediment surface, as well as in the interior of the sediment matrix was available in space and time.

To quantify the differences on the erosion behavior, variations in fluid velocities, particle positions, and particle displacement at each time step were analyzed in each study. All data was processed using programmed routines in FLAC 3D, PFC 3D, and Matlab 2011 environments. These analyses revealed high resolution data of velocities in the flow field, transport distances, and porosity changes in the sediment bed, which are presented in the following Chapters.

Chapter III

ON THE STABILIZING INFLUENCE OF SILT ON SAND BEDS

Gerhard Bartzke[AC], Karin R. Bryan[A], Conrad A. Pilditch[B] AND Katrin Huhn[C]

[A]Department of Earth and Ocean Sciences, University of Waikato, Private Bag 3105, Hamilton 3240, New Zealand

[B]Department of Biological Sciences, University of Waikato, Private Bag 3105, Hamilton 3240, New Zealand

[C]MARUM – Center for Marine Environmental Sciences, University of Bremen, Leobener Straße, D-28359 Bremen, Germany

Abstract

Within marine environments, sediments from different sources are stirred and dispersed, generating beds that are composed of mixed and layered sediments of differing grain sizes. Traditional engineering formulations used to predict erosion thresholds are however generally for uni-modal sediment distributions, and so may be inadequate for commonly-occurring coastal sediments. We tested the transport behaviour of deposited- and mixed sediment beds consisting of a simplified two-grain fraction (silt (D50=55 µm) and sand (D50=300 µm)) in a laboratory-based annular flume with the objective of investigating the parameters controlling the stability of a sediment bed. To mimic recent deposition of particles following large storm events and the longer term result of the incorporation of fines in coarse sediment, we designed two suites of experiments: (1) "The Layering Experiment": in which a sandy bed was covered by a thin layer of silt of varying thickness (0.2 mm – 3 mm; 0.5 – 3.7 wt %, dry weight in a 10 cm deep layer); and (2) "The Mixing Experiment" where the bed was composed of sand homogenously mixed with small amounts of silt (0.07 – 0.7 wt %, dry weight). To initiate erosion and to detect a possible stabilizing effect within both settings, we increased the flow speeds in increments up to 0.30 m/s. Results showed that the sediment bed (or the underlying sand bed in the case of the "Layering experiment") stabilized with increasing silt composition. The increasing sediment stability was defined by a shift of the initial threshold conditions towards higher flow speeds, combined with, in the case of the mixed bed, decreasing erosion rates. Our results show that even extremely low concentrations of silt play a stabilizing role (1.4 % silt (wt %) on a layered sediment bed of 10 cm thickness). In the case of a mixed sediment bed, 0.18 % silt (wt %, in a sample of 10cm depth) stabilized the bed. Both cases show that the depositional history of the sediment fractions can change the erosion characteristics of the seabed. These observations are summarized in a conceptual model that suggests that, in addition to the effect on surface roughness, silt stabilizes the sand bed by pore space plugging and reducing the inflow in the bed, and hence increases the bed stability. Hydraulic conductivity measurements on similar bed assemblages qualitatively supported this conclusion by showing that silt could decrease the permeability by up to 22 % in the case of a layered bed and by up to 70 % in the case of a mixed bed.

Keywords: sediment mixtures; stabilization; annular-flume; pore space plugging; inflow blocking

3.1 Introduction

Estuaries are well known as highly-dynamic coastal environments surrounded by vastly populated areas and act as a filtering link on the sediment input brought by rivers and the sea. During fluvial sediment transport towards the sea, coarse grained sediment fractions are usually trapped in the floodplains of rivers, while the fine fractions accumulate in the estuaries (Dyer, 1994). Tidal currents and superimposed waves also supply sediment from the sea. During storm events, floodwaters carry new sediment as plumes into the estuary and previously deposited estuarine sediments are mixed and dispersed throughout the estuary. Differential settling rates create mixed- and layered sediment beds of fine and coarse materials (Torfs, 1997; Williamson, 1991). Time varying currents such as those caused by tides can also result in layered sediments, as fine materials are deposited over coarser compositions (Mitchener and Torfs, 1996) during slack tide. Moreover, the sediments mobilised by dredging activities can often cause thin veneers of non-native sediment both as part of the dredging activity and also as part of the process of dredge spoil dumping. Predicting the entrainment thresholds and erosion rates for these mixed sediment beds lies at the heart of understanding estuarine sediment dynamics and such predictions are widely used across a number of fields ranging from our ability to reconstruct past sedimentary environments to understanding the impact of sediments on benthic communities following large storm events (Essink, 1999; Leys and Mulligan, 2011; Thrush et al., 2004; Zajac et al., 1998). In more applied cases, coastal engineers and managers rely on these predictions to, manage port developments (drilling and dredging activities) and maintain navigation routes.

The threshold beyond which particles move is reached when the instantaneous fluid force (F_F) is larger than the resistance force (F_R) of the grain, which is a function of the particle weight (F_G), the particle angle of repose (φ), the lift force (F_L), and the drag force (F_D) (Allen, 1970; Komar, 1987; Rijn, 2007). This "initiation of motion" is classically defined by the empirically-derived Shields curve (Shields, 1936) as when the bed-shear stress exceeds the critical threshold for that particle size. The Shields curve was derived for uniform, homogeneous, non-cohesive sediments of the same grain size (Soulsby, 1997); it is less accurate for finer grained beds (Hir et al., 2008; Mehta and Lee, 1994). Thus Hjulstroem (1935, 1939) used observations in an attempt to develop a universal predictor of the critical erosion of sediments of a wide range of sizes (the "Hjulstroem Diagram"). This predictor indicated that fine sediments, in particular mud, are much harder to erode than sand. The common occurrence of muddy sediments in estuaries, which are typically composed of 60 % silts (2 – 63 µm diameter) and 40 % cohesive clays (< 2 µm diameter) (Manning et al., 2010; Winterwerp and Van Kesteren, 2004) has focused research on developing critical threshold formulations for very fine grained, cohesive, clay-rich sediment compositions after removal of the sand fraction (Torfs, 1997).The cause of these changes in entrainment characteristics towards higher bed stability in finer fractions is the influence of cohesion and biostabilization

(Whitehouse et al., 2000). As shown by many studies on muddy, clay rich sediments, cohesion (caused by electrostatic forces) binds together the clay minerals and increases the erosion resistance significantly (Alvarez-Hernandez, 1990; Dyer, 1989; Hir et al., 2008; Hir et al., 2011; Jacobs et al., 2011; Kamphuis, 1990; Murray, 1977; Panagiotopoulos et al., 1997; van Ledden et al., 2004). Biostabilization (Paterson, 1994; Paterson et al., 1990; Paterson and Hagerthey, 2001; Young and Southard, 1978) is the influence of the activity of the micro- (bacteria, microalgae, fungi) and macro- (worms, molluscs, crustaceans) organisms which can influence the sediment stability by binding sediment particles together increasing erosion resistance or breakdown sedimentary structure via bioturbation decreasing erosion resistance (Karl and Novitsky, 1988). An overview of the erosion formulations for estuarine mud can be found in Whitehouse et al., (2000) and Winterwerp and Van Kesteren (2004).

Many experiments on sand- and mud beds have investigated these components separately to improve the understanding of the erosion behaviour (van Ledden et al., 2004) both in laboratory flumes flume (Black and Paterson, 1997) and *in situ* (Amos et al., 1992; Whitehouse et al., 2000), yet natural estuarine sediments, which consist of both non-cohesive (sand and coarser silt) and cohesive fractions (finer silts and clay) in various combinations, may behave quite differently than their component fractions. The different entrainment properties of the component particles cause different sediment fluxes relative to what would occur over uniform sediment beds of the component fractions (van Ledden, 2002). Therefore mixtures may behave in ways not covered by the traditional relationships derived by Shields (1936) and Hjulstroem (1935, 1939). Recent studies on the threshold conditions of such mixed sediments so far have focused on the erosion behaviour of sand and mud mixtures where the mud was composed of cohesive clay rich compositions (van Ledden et al., 2004; Whitehouse et al., 2000). Laboratory experiments have shown a transition from non-cohesive to muddy cohesive sediment with higher clay concentrations in the sediment beds (Alvarez and Hernandez, 1990; Kamphuis, 1990; Murray, 1977). For example, Panagiotopoulos et al., (1997) identified, by progressively adding clay to sand, a critical clay content of 5 – 10 % (by weight) significantly increased the erosion threshold. Others have observed a similar transition at a clay content of 5 - 15 % (by weight) (van Ledden et al., 2004) while Torfs (1997) showed that adding 20 - 30 % clay (by weight) to pure sand caused an order of magnitude increase of the critical bed-shear stress. In general, the maximum value for increasing the critical bed-shear stress depends on the grain size, porosity and density of the sand (reviewed by Whitehouse et al., (2000)).

It is not only the cohesive properties of the finer fraction in mixed grain beds that causes the change in erosion behavior of the bed, but also the construction and packing of the bed and the existence of "network structures" (Whitehouse et al., 2000). At the surface of the sediment, fine grains can rest in the interstitial spaces of the rougher coarse grains, and thus be protected from erosion by the coarser grains (Komar, 1989). This effect has been shown to be enhanced with increasing difference between the grain size of the two size fractions (Nino et al., (2003)). However, most research has focused on the influence of

the finer fraction on the erosion properties of coarser fraction. Mitchner and Torfs (1996) showed that sand stability increased when adding clay because the binding between the clay particles causes a denser matrix composition which raises the erosion resistance. They demonstrated that the clay particles generated a cage-like network fully encompassing the sand grains. Consequently, the increased erosion resistance was a result of the binding influence and the developed clay cage. Panagiotopoulos et al., (1997) concluded that if the clay content exceeds 11 - 14 %, the sand grains are no longer in contact with each other, which changes the particle angles of repose and therefore erosion resistance of the mixture is controlled by the clay characteristics. Van Ledden et al. (2004) reanalyzed the experiments of Panagiotopoulos et al., (1997) and Torfs et al., (1996) and supported the idea that network structures influence the erosion resistance. Also, Hir et al., (2011) supported the concept that these network structures increase the erosion resistance. Furthermore, several theories have suggested that this texture phenomenon causes a reduction of the intergranular friction due to partial filling of the pore space (Hir et al., 2008; Panagiotopoulos et al., 1997; Torfs et al., 2000). However, the influences of sediment texture and, respectively, the pore space filling network ("network structures") on the entrainment behavior of the sediments are not fully understood.

The literature on mixed sediments (sand and mud) suggests that clays are thought to be the only relevant factor in increasing the erosion resistance and hence the bed stability, due their cohesive properties and the ability to generate "network structures". For example, Jacobs et al., (2011) eroded artificially-generated sand, mud and silt mixtures and postulated that cohesiveness is more important to surface erosion and sediment strength, than packing density and drainage. However silt is also a major part of the mud fraction in natural sediments. Silt is commonly found in many coastal environments of the world (e.g., along estuarine basins, estuarial river channels and mouths, artificial harbor basins (docks), navigational channels and coastal shorelines and shelves (Dolphin and Green, 2009 ; Healy, 2002; Rijn, 2005; Winterwerp and Van Kesteren, 2004). Further, Meta and Lee (1994) showed that cohesion is only important for silt particles of less than 20 micron and cohesion is unlikely to play a role in silt-sand mixtures, suggesting that the role of other mechanisms such as the development of network structures might play a greater role in bed stability.

In contrast to previous studies which have been limited to sand and clay dominated mixtures, this paper explores effects of small amounts of non-cohesive silt in a predominantly sandy bed on entrainment and transport and the potential role of silt in creating network structures and blocking the inflow of porewater. We use laboratory experiments in a small-scale annular flume to test the role of thin layers of silt blanketing the fine sand bed and the more common case of homogeneously mixed beds. These treatments were chosen to imitate respectively, the recent deposition of particles following large storm events and the

longer term result of the incorporation of fines. Two suites of experiments were designed: (1) "The Layering Experiment": in which a layer of silt was deposited in increasing quantities on top of a homogenous sand bed; and (2) "The Mixing Experiment": which used a mixed sediment bed consisting of sand and increasing amounts of silt. The stability of each bed was tested, using a unidirectional flow where the mean flows conditions were increased incrementally.

3.2 Methods

3.2.1 Sediments

All sand used in the experiments (sampled from Pauanui Beach, New Zealand, 37°0'41.48"S 175°51'58.03"E) was dry sieved to 300 µm (D50, average grain diameter) ranging from 210 µm – 310 µm; using an Endecott's sieve-shaker, whereas the silt (sampled from Waikareao Estuary, Tauranga Harbour, New Zealand, 37°41'42.98"S 176°9'11.80"E) component was extracted from the bulk sample by wet sieving to D50 = 55 µm. Wet sieving had only a limited ability to constrain the size fraction, and the grain size distribution of the silt fraction ranged from 0.8 µm – 200 µm (determined using a Laser Particle analyser (Malvern Mastersizer 2000; Figure 3.1)). Note, the cohesive clay particles (< 2 µm) in the "silt" fraction comprised < 1.2 % by volume and the cohesive silt particles (< 20 µm) were¸ < 1.9 % by volume.

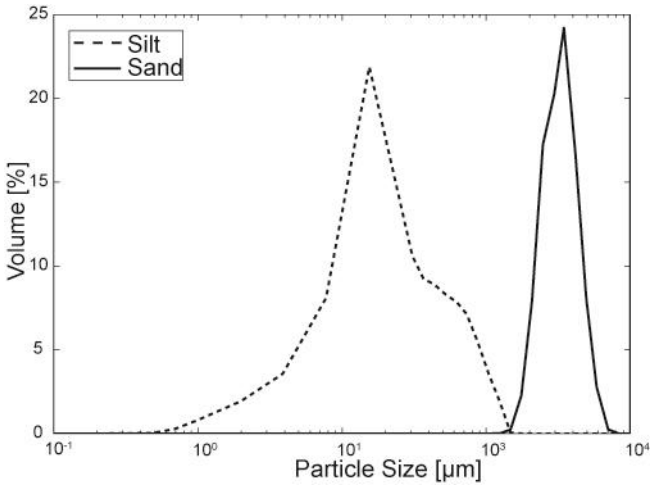

Figure 3.1: Grain size distribution of the extracted sand (D50, 235 µm) and silt (D50, 55 µm) components.

3.2.2 Annular flumes

The experiments were carried out using an annular laboratory flume (Figure 3.2). This was constructed with dimensions according to Widdows et al., (1998). The circular channel was 10 cm wide and bounded by an outer (63 cm) and inner (43 cm) rim resulting in a bed area of 0.17 m². At the maximum water level of 25 cm, 40 litres of artificial seawater (S = 30) were accommodated in the flume. A removable, rotating lid (45 cm diameter) driven by a 12 V motor was mounted on top of the flume, which caused a current

motion of up to 0.30 m/s (55 rotations per minute (RPM); 1RPM is 0.00526 m/s (Jones et al., 2011)) The motor speed was controlled by a computer with Labview-based software which allowed the controlled variation of the flume flow speeds.

Suspended particulate matter concentration (SPM) in the water column was recorded in millivolts by an optical back scatter-sensor (Seapoint turbidity meter; Seapoint Sensors Inc.) positioned 7.5 cm above the sediment bed (Figure 3.2) and was logged on a computer at 1 Hz. In mixed-grain suspensions, the OBS sensor preferentially senses the silt fraction (Green and Black, 1999) and so the sensor was calibrated for each run individually. Water samples were extracted by suction through a sampling port (2 mm dia.) 7.5 cm above the sediment surface in order to calibrate the OBS sensor and to provide absolute measurements of the suspended load (following Widdows et al., (1998). The port was closed by a directional blocked centre valve and connected by a plastic tube to a 50 ml Luer-Lok syringe (BD Plastipak). Samples for calibrating the OBS (for each run at each flow speed tested) were filtered through pre-weighed glass microfiber filters (GF/C 45 mm, Whatman) using a vacuum pump. The filters were prewashed in milli-q water to dissolve salts, then dried at 105 °C for 24 h and weighed.

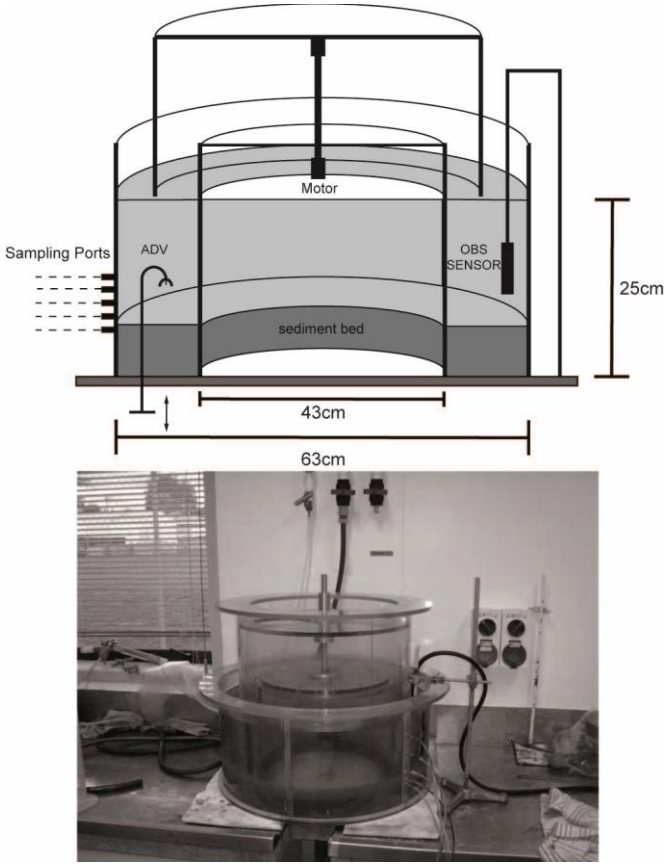

Figure 3.2: Schematic and photograph of the annular flume (Aquatic Research Centre, University of Waikato, New Zealand).

3.2.3 Experimental procedure

We designed two suites of experiments (summarized in Table 3.1). One in which a sandy bed was covered by a thin layer of silt of varying thickness ("1. The Layering Experiment") and one in which the bed was composed of sand mixed with small amounts of silt ("2. The Mixing Experiment"). Both experiments consisted of two phases. In Phase I the bed was allowed to settle and consolidate and in Phase II, the velocity in the annular flume was increased to cause erosion. In each experiment the bed was prepared by creating a 5 cm thick sediment bed in the flume (sand in experiment 1, sand-silt mixture in experiment 2). After filling the channel with sediment, the bed was saturated with saltwater.To minimise any variations in surface elevation which may promote the onset of erosion and add variability to the experiments the bed was flattened by a scraper (sand bed in experiment 1, sand-silt mixture in experiment 2) before filling the flume. In the "Layering experiment" the sand bed was scraped smooth prior to the sedimentation of the silt layer and in the "mixed" treatments bed flattening occurred immediately after the sediment was placed in the flume. A sheet of bubble-wrap plastic, cut to the dimensions of the channel, was placed on top of the sediment to ensure the bed was not disturbed by the inflow as the tank was filled. Subsequently, the motor, the OBS and the rotating lid were installed.

During Phase I of each of the "Layering experiments", the 6 bed treatments were constructed by allowing 29; 118; 235; 353; 471 and 941 g/m² of silt to deposit in a thin layer on the bed ranging from 0.2; 0.6; 1.1; 1.8; 2.2 and 3 mm respectively. The ranges were chosen so that the lower levels (29; 118 g silt/m²) would fill the pore spaces but not cover the surface. The conversion to weight percentage (wt %) was calculated by considering a surface grab sample of 10 cm depth where the composition of the sample would correspond to 0.9; 1.4; 1.8; 3.7 and 7.3 % (dry weight) silt. The silt was deposited to the sand bed by initially mixing it with 2 L of saltwater and by shaking the container for a minute. To achieve the best possible dispersion in the flume, the silt mixture was poured gently into the flume with the motor running at 0.05 m/s for 5 min. The material was allowed to settle for 4 h by decreasing the flume flow velocity to 0.025 m/s. One run was undertaken with a 24 h settling time. It could be shown that after 4 h 99 % of all silt which would have settled in 24 h was deposited, indicating that 4 h settling time was adequate. Within the erosion Phase II the flume flow velocity was increased in steps of 0.025 m/s ranging from 0.025 – 0.30 m/s with the exception of the change between 0.2 and 0.25 m/s, which was undertaken in one 0.05 m/s increment. Each flume flow velocity increment was 15 min in length (Table 3.1). OBS calibration water samples were taken every 15 min. These flow speeds were chosen to characterise the environment on tidal sand flats (Leeder, 1999; Wright et al., 1999) and were strong enough to initiate sediment transport in all treatments.

The "Mixing" suite of experiments was made up of 4 runs, each with increasing quantities of silt added to the bed (120 g/m³; 300 g/m³; 600 g/m³; 1200 g/m³). Considering a surface grab sample of 10 cm depth of the sediment beds, these concentrations correspond to 0.74; 1.8; 3.7; and 7.4 % (dry weight) silt. Similar

to the "Layering experiments", the "Mixing experiments" were divided into two phases. In Phase I, we added the mixed sand and silt to the flume then allowed the bed to settle under no flow for 12 h. Phase II was the identical to that done in the "Layering experiments".

Photographs were taken at the beginning and end of the experiment, and video footage was collected during each experiment. This allowed qualitative observations of the erosion state of the bed, the formation of bedforms (the destabilisation of the bed), the time that the surface silt layer was completely eroded and the time at which the sand was first entrained from the bed. In these visual observations we defined "stable" as a bed in which the sand fraction was not mobilised at the highest flume flow velocity tested (0.30 m/s).

3.2.4 Near-bed hydrodynamics

We mapped the boundary layer dynamics of three of the "Layering experiments" (pure sand; 29 and 941 g/m²) at flow speeds up to 0.20 m/s. To parameterize the bed-shear stress (τ_0), we used a downward looking SonTek MicroAcoustic Doppler Velocimeter (ADV). The ADV (Figure 3.2) was mounted onto a vertical racking system through the base plate into the middle of the channel (Jones et al., 2011). Because of this arrangement flow speeds higher than 0.2 m/s caused scour around the ADV and bed profiles were not measured. The spatial dimensions for a precise positioning near the bed was identified following Finelli et al., (1999). Each velocity profile was recorded at 25 Hz at 15 elevations from 0.5 cm up to 2.69 cm above the bed. The bed-shear stress was calculated by using the turbulent kinetic energy (TKE) method (summarized in (Kim et al., 2000; Pope et al., 2006)). TKE describes the product of the absolute intensity of velocity fluctuations from the mean flume flow velocity and depends on the fluid density (ρ):

$$\mathrm{TKE} = \frac{1}{2}\rho\left(\overline{u'^2} + \overline{v'^2} + \overline{w'^2}\right)$$

$$\tau_0 = C_1 \times \mathrm{TKE}$$

$$C_1 = 0.19$$

where *u*' represents the fluctuating part of the flow in steam-wise direction and *v*' and *w*' the cross channel and vertical components of the flow. The ratio of bed shear stress (τ_0) to TKE is constant and C_1 is the proportionality constant (Pope et al., 2006). The relationship between flow velocity and bed shear stress for the three treatments (pure sand, 29 and 914 g/m^2 silt) was linear (r^2 = 0.85-0.90; n=7-9) and an analysis of covariance revealed no significant treatment effect (homogeneity of slopes p = 0.35; treatment p = 0.88) on boundary layer flow characteristics. Consequently data from all three treatments were pooled to provide a single conversion formula for all treatments given by τ_0 (N/m^2) = 0.355×*U* (m/s) (r^2 = 0.88), where *U* is the depth integrated flow speed in the flume.

In small annular flumes such as those used in these experiments secondary flows are generated. The magnitude of the cross-stream flows in our flume are between 14 and 17 % of the along channel component (C. Pilditch unpubl. data). Note that this proportion does not vary with height above the bed or with along channel flow speeds up to 0.45 m s^{-1}. Although the sediment transport dynamics are likely to be affected by these secondary flows, these were consistent across all treatments and consequently comparisons between each experimental treatments are possible.

3.2.5 Hydraulic conductivity

A constant head permeameter was used (Klute and Dirksen, 1986) to measure the hydraulic conductivity (*k*, m/s) of sediments in both the mixed and layered experiments. In cores (0.052 m dia.) a sediment column of 0.11 m was prepared in the same manner as the erosion experiment (allowing different amounts of silt to settle to the sand bed under gravity or being mixed into the bed) to mimic the range of bed compositions created in the flume. *k* can be estimated from the height of the water column above the core (which remains constant), bed area and depth and the time taken to collect a known volume of water passing through the bed. We constructed one example of each treatment and averaged several reading per core to estimate *k*.

3.2.6 Data analysis

The stabilizing influence of silt on sand beds was analyzed by comparing the relationships between the suspended particulate matter concentrations (SPM), erosion rates and critical bed-shear stresses. OBS (mV) was converted to SMP (mg/l) using empirically derived relationships for each experiment. The coefficient of determination (R^2) ranged from 0.91 - 0.96. The SPM time series following a step change in flow speed was well described by a hyperbolic tangent. Therefore, the sediment erosion rate (E) i.e. rate of change of suspended load in the water column was modeled by the initial slope a·b of the least square fit of the hyperbolic tangent model $y = a \cdot \tanh(b \cdot t)$ fitted to each 10 minute segment of SPM data (with constant velocity), where y is SPM concentration and t is time. The determination coefficients (R^2) of all experiments varied between 0.89 – 0.99, which was higher than the usually implemented linear regression analysis used by, for example, Widdows et al., (1998). With this model, the initial concentration reduces simply to y=a·b·t, where the initial erosion rate (a·b) and sediment concentration at large t asymptotes to y=a. The velocity needed to initiate sand and/or silt transport at the sediment surface or destabilize the bed (as determined from video footage) was defined as the 'critical velocity'. The quantification of the critical bed-shear stress (τ_c), was parameterized following Riethmüller et al. (1998) by using the relationship between the applied bed-shear stress (τ_b) and sediment erosion rate. Fitting a linear regression line to these data at the first significant increase in erosion rate (> 35 mg/m²/s), allowed τ_c to be calculated as the intersection of regression line (R^2 = 0.97 – 0.99) with the x axis (bed-shear stress).

3.3 Results

Overall, the results show that silt increased the erosion resistance of the underlying sand ("Layering Experiment" 1) or mixed-grain bed ("Mixing Experiment" 2) and maintained the stability of the bed. In "Low" silt concentration treatments (the "Layering experiments": 29 g/m²; 118 g/m²; 235 g/m² and the "Mixing experiment": 120 g/m³), no stabilization was observed, instead sand bedforms were generated at higher flow speeds (0.15 m/s; 0.20 m/s; 0.25 m/s) than in the pure sand case. In contrast, in "high" silt concentration treatments (the "Layering Experiments": 351 g/m²; 471 g/m²; 941 g/m² and the "Mixing experiment": 300 g/m³; 600 g/m³; 1200 g/m³) the underlying sand or mixed-sediment bed stabilized and no bedforms were observed. Furthermore, the hydraulic conductivity measurements showed that with increasing silt content, the hydraulic conductivity (*k*) decreased. Table 3.2 provides an overview of the sediment behaviour derived from the flume experiments and the corresponding hydraulic conductivity values. Additionally, photos showing one low and one high silt concentration run, of both experiments are provided in Figure 3.3.

3.3.1 Hydraulic conductivity

In both the "Layering" and "Mixing experiments", the hydraulic conductivity decreased with increasing silt quantities but the effect was greater in the mixed treatments (Table 3.2). For the "Layering experiments" hydraulic conductivity decreased by 22 % from 0.00064 m/s for pure sand to 0.00045 m/s for the 9.5 g/m^2 treatment but note there was little detectable effect of silt on hydraulic conductivity in the range 0.3-2.0 g/m^2. In contrast silt mixed into the sediment produced a 70 % reduction in hydraulic conductivity at 1200 g/m^3 and at 300 g/m^3 the reduction was comparable to that observed at the highest silt concentration used in the "Layering experiment".

3.3.2 "The Layering Experiments"

The change in suspended sediment concentrations observed throughout the "Layering experiments" as the flow speed increased (Phase II) are presented in Figure 3.4A. SPM concentrations decreased slightly below < 0.15 m/s because silt particles were still depositing. At 0.15 m/s silt began to erode in all treatments (Figure 3.4A). After this critical threshold for initiation of silt erosion was exceeded, two classes of erosion behaviour at silt concentrations < 235 g/m² (low) and > 352 g/m² (high) could be identified. Following each incremental change in flow speed, initial erosion was identified by a steep change in sediment concentration followed by an asymptotic decrease in the rate of change to constant concentration. The experiments with low levels of silt showed that the silt increased the threshold where the underlying sand began to move significantly (yellow, blue and black lines in Figure 3.4A and Table 3.2). Visual observations indicated that the thicker the layer of deposited silt, the higher the threshold for sand movement. Therefore, the threshold for initial sand erosion was shifted to higher flow speeds (0.20 –

0.275 m/s) with increasing silt concentration (Figure 3.4A). Furthermore, visual observations indicated that this occurred when the layer of silt protecting the bed was eroded and the sand grains appeared to be exposed (thin silt layer in Figure 3.3, 1A). At higher flume flow velocities (> 0.275 m/s) the sand bed failed with the establishment of 2 - 5 cm wavelength bed forms (Figure 3.3, 1B). In these cases, silt and sand erosion were observed at the same time (Figure 3.4A). This sand and silt continued to suspend and accounts for the steep rise in suspended sediment concentration (from 50 to 150 mg/l) in Figure 3.4A towards the end of the experiments.

The erosion rates of the low-silt layering runs have three stages (Figure 3.5A). Note that the erosion rates have been plotted against applied bed-shear stress rather than flow speed, where 0.01 N/m² corresponds to a 0.05 m/s interval. In stage 1 there was no erosion until the initial silt erosion at 0.04 N/m². Then there was a gradual increase in erosion rate up to about 100 mg/m²/s (stage 2). The erosion rates increased up to a factor of 3, depending on initial silt concentration and then declined, presumably as the surface layer of silt was depleted, and only sand grains were left to be suspended. In the last stage (3), when the bed shear stress reached 0.09 N/m², a strong increase of the erosion rates to 400 mg/m²/s for the low silt treatments occurred, which is related to continuous sand suspension in combination with the growth of bed-forms (Table 3.2; Figure 3.3, 1B).

In contrast, the high silt concentrations (Figure 3.4A, brown, red and green lines) stabilised the sand bed and no bedforms were observed (Table 3.2; Figure 3.3, 2B). The transition from a bed that becomes unstable at high flow speeds (low silt) and the ones that remain stable (high silt) corresponded to a silt concentration between 235 g/m² and 353 g/m². Similar to experiments with “low” concentrations, silt erosion was initiated at 0.15 m/s. As the flow speed increased, there was a continuous increase in SPM and visually a decrease in the thickness of the silt layer on the bed surface was observed (compare Figure 3.3, 2A and 2 B). Visual observations also revealed that silt was transported also as bed load on top of the sand bed. Even if all silt layering on the sediment appeared to be eroded (which only occurred at the highest flume flow velocity tested) and the sand surface was exposed, the remaining sand bed still stayed stable (compare Figure 3.3, 2A and 2 B). In the final stages, the SPM concentration did not equilibrate as quickly after each change in velocity, and the erosion rate did not reach an asymptotic steady state within the 15-minute time frame. The transition to this decreasing erosion rate pattern occurred at a lower flow speed (0.15 m/s) for the 471 g/m² and 941 g/m² experiments. At the highest flow speeds (> 0.275 m/s) and highest silt-layer thicknesses (the 471 g/m² and 941 g/m² runs), 0.5 - 1 cm wavelength silt bed-forms appeared on top of the stable but partially-exposed sand bed. The SPM concentration differences between the 353 g/m²; 471 g/m² and 941 g/m² experiments did not follow a consistent pattern. The SPM concentrations for the 471 g/m² experiments were always higher than the 941 g/m² experiments. The divergence in the erosion behaviour of the 471 g/m² run occurs at the lower flow regimes (< 0.20 m/s) where only the silt is mobilised (Figure 3.4A).

The erosion rates for the "high" (353 g/m²; 471 g/m² and 941 g/m²; brown, red and green lines) silt layering runs differ from the pattern of the erosion rates for "low" silt concentrations in that the previously-defined erosion stage (3) was not observed (Figure 3.5A). Following a steep increase which corresponds to the erosion of the silt layer at 0.04 – 0.05 N/m² (which occurred in all treatments, 100 – 1000 mg/m²/s), a trend towards a constant erosion rate or decreasing erosion rate seems to evolve at higher flow speeds. The flow speed where this flatting trend emerges is higher (> 0.07 N/m²) for larger silt amounts (compare yellow line and red line in Figure 3.5A). This flattening becomes particularly clear while considering the 118 g silt/m² curve (orange line). At this stage visual observation indicated that all silt was suspended, whereas the sand bed remained intact (Figure 3.3; 2B). The 353 g silt/m² (brown line) and 471 g silt/m² (red line) also follow the trend towards decreasing erosion rates because increasing the silt concentration extended the velocity range over which the silt layer was eroded. The last data point could not be collected due to a limited OBS sensor sensitivity range.

From visual observations it was determined that in case of the pure sand bed the tested bed shear stresses resulted in primarily bed load transport. In this case, the sand was not re-suspended to the height of the sensor in sufficient quantities for detection (Figure 3.4). Therefore, the derived erosion rate change resulting from increased bed-shear stresses were compared with the predicted erosion behavior of pure silt (black dashed line in Figure 3.5) and pure sand (black dashed and dotted line in Figure 3.5) based on the erosion rates estimated from published relationships. The erosion functions of pure silt and sand were derived based on the formulations described by Hir (2008) and Mehta and Parchure (2000):

$$E = M\left(\frac{\tau_b - \tau_c}{\tau_c}\right)^n,$$

where E corresponds to the erosion rate (mg/m²/s), M and n are erosion rate constants which were optimized from calibration (M-sand = 20; M-silt = 500; n = 1.5 i.e. van Rijn (2007)) whereas τ_c represents the critical bed-shear stress (N/m²) respectively. The critical bed-shear stress for silt is 0.03 N/m² and was derived from the erosion rate plots following Riethmüller et al. (1998) and was found to be equal for the initial silt erosion for all experiments. In contrast, the critical bed shear stress of sand 0.05 N/m² was derived by the Shields curve found in Soulsby et al., (1997). Our experimental results indicate that the erosion characteristics of the layered bed lie between these two extremes, as expected.

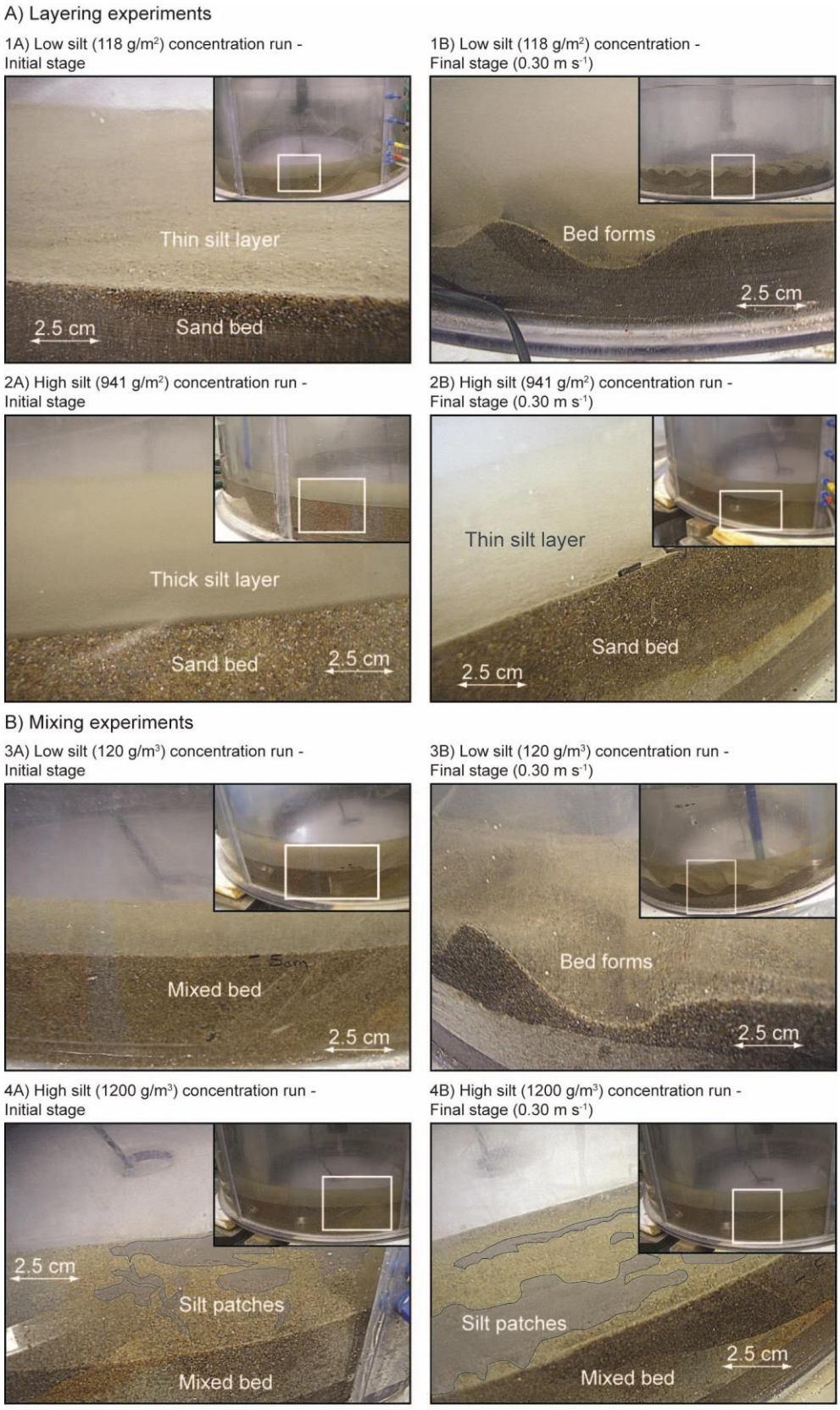

Figure 3.3: A) Photos showing the results of one "Low" (118 g/m²) and one "High" (941 g/m²) silt concentration run from the "Layering Experiments" and B) one "Low" (120 g/m³) and one "High" (1200 g/m³) run of the" Mixing Experiments".

3.3.3 "The Mixing Experiments"

The SPM recordings taken at different flow speeds collected throughout the "Mixing Experiments" are illustrated in Figure 3.4B. Both visual observations and the SPM measurements confirmed that silt erosion took place only when the flow speed exceeded 0.15 cm/s. Experiments with "low" silt concentrations in the bed (120 g/m³; black line in Figure 3.4B) differ from experiments with "high" silt concentrations (> 300 g/m³; blue, yellow and brown lines in Figure 3.4B). The low bed silt concentration run did not asymptote to a constant suspended sediment concentration, instead it was characterised by a steep increase up to 180 mg/l, which occurred at relatively high flow speeds (0.20 m/s – 0.30 m/s). Visual observation showed that sand erosion was initiated at 0.20 m/s and was immediately accompanied by the appearance of 2 – 3 cm wavelength bed forms which were fully established during the 0.30 m/s flow interval (compare Figure 3.3; 3A and 3B). During the "high" silt concentration runs (blue, yellow and brown lines in Figure 3.4B), the sediment bed remained stable and no generation of sand bedforms could be observed (compare Figure 3.3; 4A and 4B). In contrast to the "Layering Experiments", visual observations indicated that silt was suspended directly out of the sand bed. Moreover, SPM increased less with increasing flow speed. Therefore the erosion rate (Figure 3.5B) decreased when there were increased levels of silt mixed into the bed. In particular, the transition between higher erosion rates and lower erosion rates (Figure 3.5B) occurred at different flow speeds (0.15 – 0.175 m/s) in the 300 and 600 g/m³ experiments. In contrast, the 1200 g/m³ runs were characterised by a low erosion rate and minor changes in SPM.

The erosion rates calculated from the "Mixing experiments" (Figure 3.5B) highlight the effect of a decreasing erosion potential during higher current velocities by increasing silt concentrations in the bed. Experiments with "low" silt concentrations (Figure 3.5B black line) are characterised by a continuous rise of the erosion rates. Silt eroded at 0.04 N/m² and was followed by sand erosion beginning at 0.08 N/m². In comparison, in "high" bed silt concentrations (Figure 3.5B, blue, yellow and brown lines), the erosion rate of the 300 and 600 g/m³ experiments peaked between 0.04 N/m² and 0.06 N/m², followed by a decline towards zero. Visual observations indicated at this stage that no more additional silt was suspended. Suprisingly, even up to bed-shear stesses of 0.1 N/m², the erosion rates for the highest bed silt concentrations (1200 g/m³) show only a minor increase in SPM. Further, the erosion rates of the "Mixing experiments" are compared with the predicted erosion behavior of pure silt (black dashed line in Figure 3.5B) and sand (black dashed and dotted line). The results show that the erosion characteristics of the mixed bed lie approximately between the predicted erosion rates for pure sand (dashed line, Figure 3.5) and pure silt (dash-dot line in Figure 3.5). At high bed-shear stresses, the mixed sediment bed erodes at a lower rate than expected for a pure sand bed.

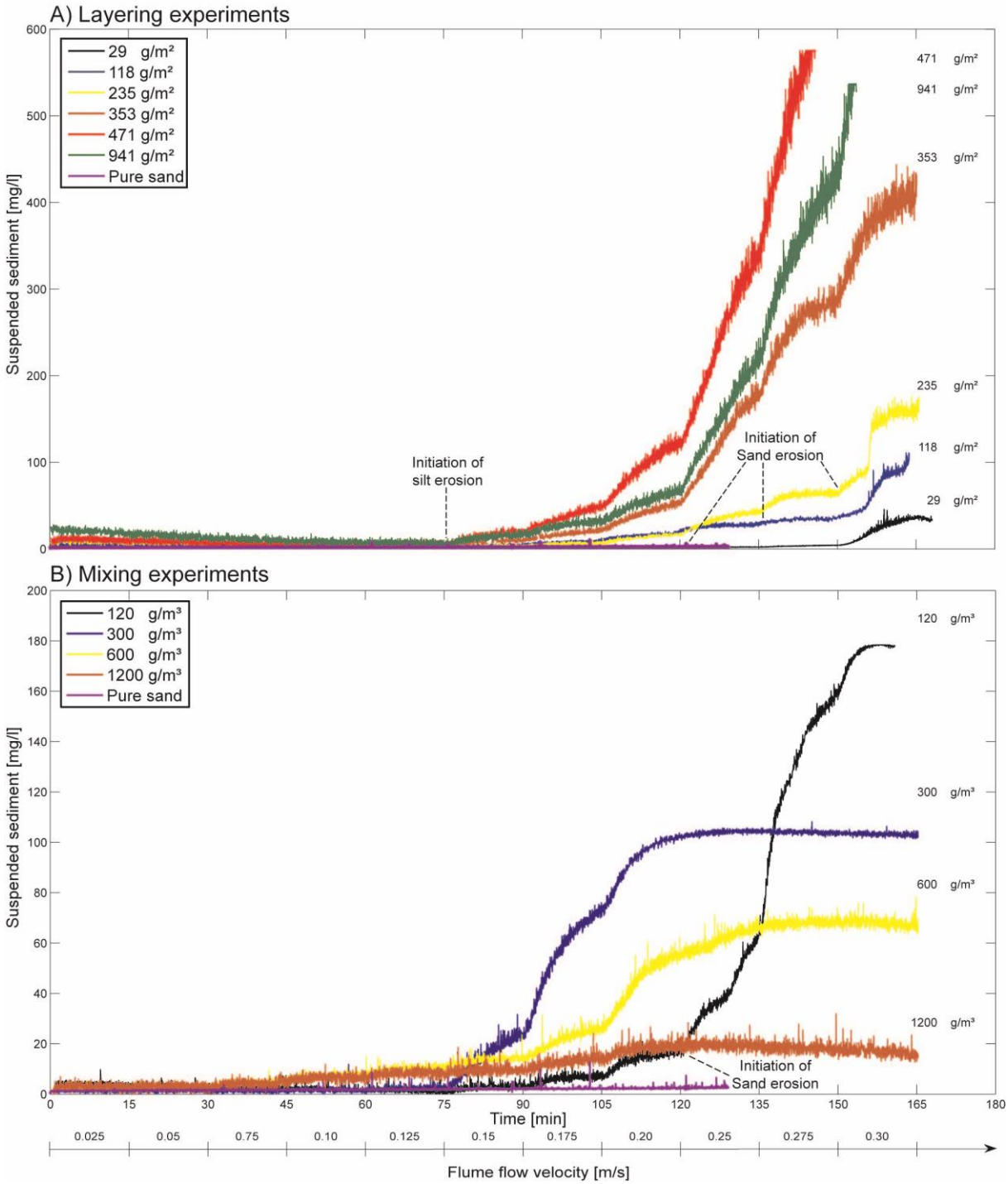

Figure 3.4: Time series of the suspended sediment concentrations (mg/l). A) Silt erosion during the "Layering Experiment" that occurred following 11 incremental changes in flume flow speed up to 0.30 m/s. Note that the flow speed was increased from 0.20 – 0.25 m/s in one increment, all other increments were 0.025 m/s. The size coloured lines correspond to Pure sand, "Low" 29, 118 and 235 g/m² and "High" silt (353, 471 and 941 g/m²) concentrations. The initiation of sand - and silt erosion is highlighted by dashed black lines. B) Silt erosion during the "Mixing Experiment" that occurred following 11 incremental changes in flow speed up to 0.30 m/s. The initiation of sand erosion is highlighted by a dashed black line. Note that the flow speed was increased from 0.20 – 0.25 m/s.

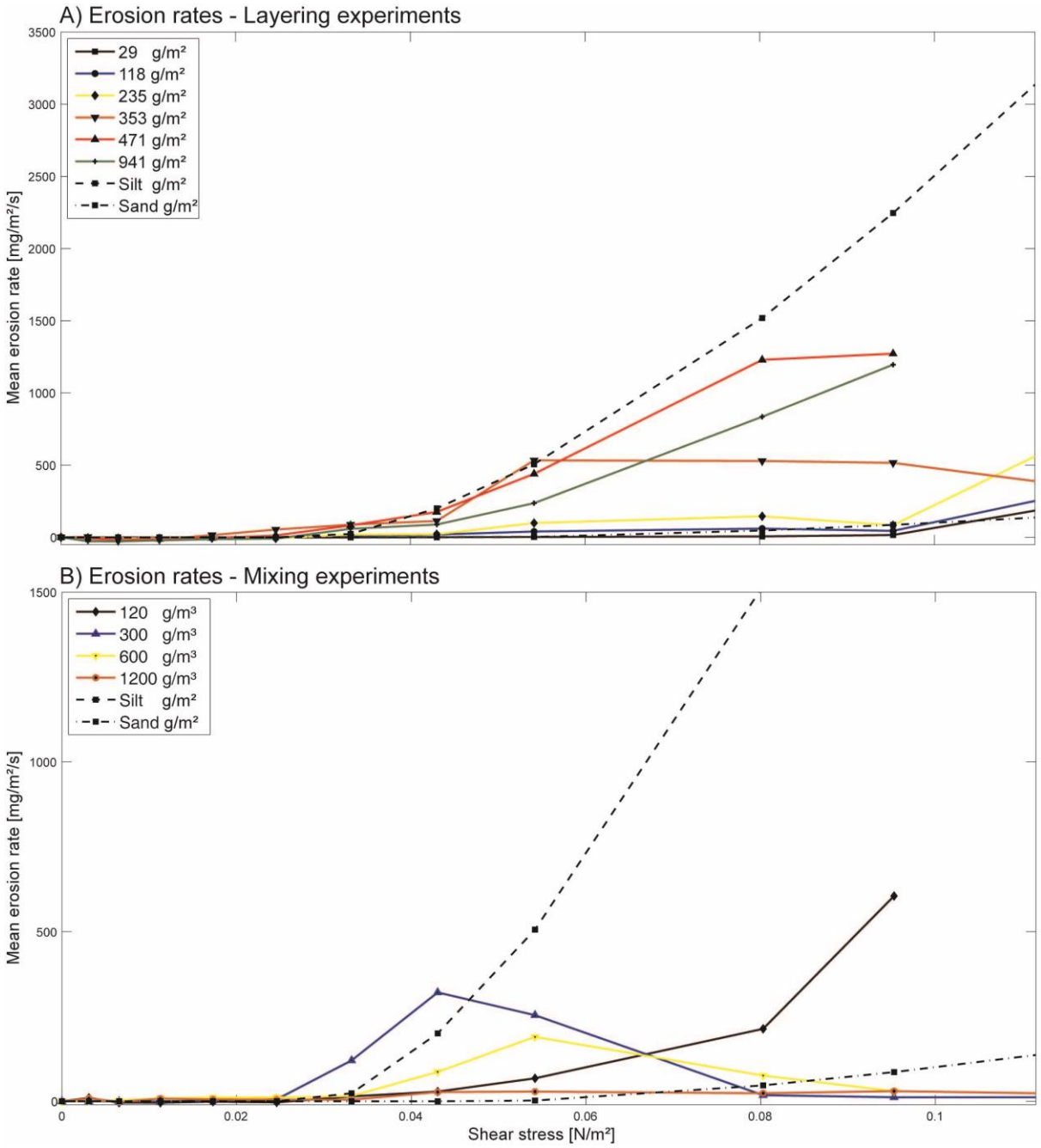

Figure 3.5: Mean erosion rates (mg/m²/s) against bed-shear stress (N/m²) calculated as the initial slope of the hyperbolic tangent fit to the observations in Figure 3.4. A) "Layering Experiments" (Experiment 1) B) "Mixing experiments" (Experiment 2). The erosion behavior of pure silt and sand to silt is compared to layered sediment beds. Note that the flow speed was increased from 20 – 25 cm/s. Further explanations see text.

3.4 Discussion

The annular flume experiments show that silt either deposited on top or mixed into a sand bed has a stabilizing effect on the sand bed. The threshold conditions for initiation of motion of sand were shifted to higher flow speeds for beds containing silts compared initial threshold conditions for a pure sand bed. Even a relatively small amount of silt either deposited out of suspension (1.4 silt wt %) or mixed into the sediment bed (0.18 silt wt %) induced sediment stabilization. Furthermore, the hydraulic conductivity measurements showed a significant decrease in permeability in mixed sand-silt beds (Table 3.2). Therefore, our results show that even minor changes to the silt composition of the bed, and the distribution of the silt within the bed, can cause dramatic changes to the erosion rates, to the hydraulic conductivity, and hence, increase the bed stability. These changes to erosion rates encompass the entire range between predicted rates for pure sand and pure silt.

All studies so far which focused on mud and sand mixtures, (Alvarez-Hernandez, 1990; Dyer, 1989; Kamphuis, 1990; Mitchener and Torfs, 1996; Murray, 1977; Panagiotopoulos et al., 1997; Raudkivi A.J., 1990; Torfs et al., 2001; van Ledden et al., 2004) have noted an increased erosion resistance (compared to pure sand) when treating sand (non cohesive) with mud (in particular cohesive clays) in various compositions. The transition from sandy (non cohesive) to more stable muddy (cohesive) erosion behaviour occurs at clay contents ranging between 3 – 15 % (reviewed in Whitehouse et al., 2000). However, our results also show that silt layered on top of a sand bed ("Layering Experiments") stabilized the sediment with a minimum silt concentration of 353 g silt/m² which corresponds to only 1.4 % silt (wt %), (considering comparable bed samples of 10 cm depth). This is comparable to previous mud experiments. Moreover, when silt was mixed into sand ("Mixing Experiments"), the sediment was stabilized at a minimum concentration of 300 g/m³ i.e., 0.18 % silt (wt %), which is much lower than previous findings (see above, albeit for mud). Our results clearly demonstrate that lower non cohesive silt concentrations are required to increase the erosion resistance than in the case of cohesive mud.

Prior studies which have shown that the main physical controls on the erosion of sediments are the mineralogy, grain size distribution, density and cohesion (Allen, 1970; Hir et al., 2008; Mc Cave, 1984) as well as "network structures" (Whitehouse et al., 2000). Due to the fact that our samples have been separated from the cohesive clay fraction by sieving, cohesion is unlikely to influence the stabilization behavior of our silt-sand treated sediment-beds (Winterwerp and Van Kesteren, 2004). Furthermore, Meta and Lee (1994) showed that the cohesion of silt is only significant for particles smaller than 20 microns, whereas our samples have a median diameter of 55 □m. The cohesive silt particles < 20 □m (1.9 vol. %) and cohesive clays < 2 □m (1.2 vol. %) were only a minor part of the total volume fraction of our silt component and are unlikely to have caused a cohesive influence on the erosion behavior.

Following the hypothesis that a texture induced sand bed stabilization, where the clay particles fill the pore spaces between the sand grains can create a "cage-like" structure (Hir et al., 2008; Hir et al., 2011;

Mitchener and Torfs, 1996; Panagiotopoulos et al., 1997; van Ledden et al., 2004; Whitehouse et al., 2000), we postulate that the non cohesive silt in our treatments is filling the sand matrix. We have not measured these structures directly, but the hydraulic conductivity measurements decreased with added silt, and thus, also possibly a decrease in permeability, in both experimental setups (Table 3.2). This indicates that the quantity of silt particles controls the blockage of the flow through the sediment bed and may explain the increase in sediment stability caused by added silt in the flume experiments. Furthermore, there was a larger decrease in hydraulic conductivity in the case of the mixed sediment cores as compared to the layered cores with increasing silt content. This also corresponds with the findings of the flume experiments, which showed that silt mixed into the sediment beds appeared to cause more stability than layered sediment beds. This effect may reduce the pore water inflow as indicated by the hydraulic conductivity measurements, but also minimizes changes in the pore water pressure, and hence, reduces the effective stress in the bed (Eisbacher, 1996).

Panagiotopoulos et al., (1997) suggested that the erosion resistance is increased by in-filled pockets increasing the internal particle angles of repose between fines and sand. In a sediment bed composed of coarse sand particles, all sand particles are more or less connected to each other. When fine clay particles are mixed into the matrix of the coarse sand bed, the distances between the coarser grains is increased due to the filling of the pore space with finer particles slightly increasing the pivoting characteristics i.e. particle angle of repose. So when finer particles were included in the pore spaces, the bed was more resistant to erosion. In addition, we suggested that the filling would also decrease the surface roughness of the bed by filling in the hollows between grains. Nino et al., (2003) show that fine grained particles are less easily entrained when they are hidden in the pore spaces between coarser particles, and thus the roughness of the coarse bed can reduce the erosion rate of fine particles in a mixed grain bed. Although we have measured erosion rates and not directly measured entrainment thresholds, our results suggest that the change in erosion thresholds caused by mixed grains size beds (shown in Nino et al., 2003) is entirely dependent on the quantity of fine grain sediment relative to coarse, and the erosion rates can range from erosion rates of a pure silt bed to much lower values.

A conceptual model that highlights our understanding of the stabilizing influence of silt on sand bed is presented in Figure 3.6. This is based on former studies which suggested that fine particles fill the voids between large grains to generate a denser packed matrix affecting the erosion threshold. Our experiments can be analyzed in more detail within the framework of this conceptual model.

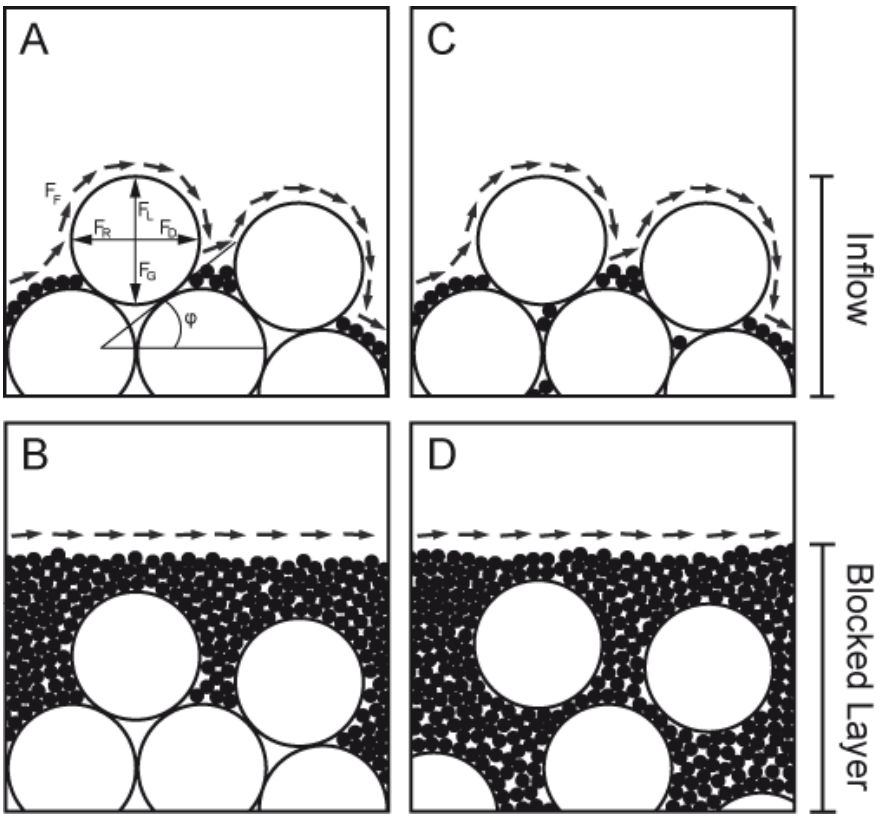

Figure 3.6: Conceptual model of the stabilization process. Large, white particles represent sand and small, black particles correspond to silt. (A-B) silt deposited on top of a sand bed. (A) The sediment bed was not stabilized allowing inflow into the sand bed due to "undersaturated" pore space. (B) Stable case, the pore space was filled by silt causing a blocked inflow "Blocked Layer". (C-D) silt mixed into a sand bed. (C) The sediment bed was not stabilized allowing inflow into the sand bed due to "undersaturated" pore space. (D) Stable case, the pore space was filled by silt throughout the whole sediment bed causing a blocked inflow "Blocked Layer".

3.4.1 Initial response

The initial response of the bed to increasing flow speeds was the removal of the surface silt layer in the case of the "Layering experiments", and removal of the easily available surface silt in case of the "Mixing experiments". In the case of the "Layering experiments", this corresponds to entrainment of grains for a bed of the same grain size, and so the roughness elements of the sand should have no effect on the entrainment process (Nino et al., 2003). It is possible to determine when the surface layer is removed, when the erosion rate curves deviate from the pure-silt case (dashed black line on Figures 3.5A and B). Before this point, the silt eroded following the theoretical curve for non cohesive silt. This provides some confirmation of our assumption that the silt is not cohesive. In the case of layers of silt of 235 g/m^2 or less, this silt layer was removed immediately.

Initial erosion of the silt in the "Mixing experiments" varied depending on treatment. The silt was most easily eroded in the 300 g/m^3 case but not the cases with higher silt fractions. Erosion from the mixed bed would depend on the surface roughness and the flow through the pore spaces (Figure 3.3; 4A and Figure 3.6C). Roughness influences entrainment by changing the particle angle of repose, changing the bed shear

stress, and degree to which the fine particles can be hidden by the coarser particles (Nino et al., 2003). The 300 g/m^3 may cause the most rough bed, yet large enough separation between sand grains that hiding is less important (Figure 3.6C). When the bed silt concentration increases even more, the separation between grains becomes greater, which may reduce the roughness and decrease the particle angle of repose of the sand grains, and cause the erosion rate to drop (Panagiotopoulos et al., (1997); Wiberg and Smith, (1987)). The influence of pore-space blocking, which inhibits flow through the bed may also influence these higher bed-silt concentration more. This is supported by the dramatic drop in hydraulic conductivity at these silt concentrations (Table 3.2). However, we do not have direct evidence of the effect of silt on bed roughness so this interpretation remains conjecture at this point.

3.4.2 Blocked pore spaces

When the easily-available silt was eroded from the bed (either from the surface layer, or between the surface grains), the erosion characteristics depended on how the silt was incorporated into the bed. In this case, the bed was stable when silt was contained within the pore spaces of the sand (Figure 3.3; 2B and 4B), and the flow that normally occurs between the sand grains (and helps the entrainment processes) was blocked. This occurred during both experiments, either when the surface layer of silt had been removed, or when there was sufficient silt incorporated within the bed. With respect to our conceptual model (Figure 3.6), we assume that bed stabilization (Figure 3.3; 2B and 4B) occurs when a "blocked layer" in Figures 3.6B and D evolved. Whereby the smaller, denser silt particles filled the pore spaces between sand grains either by deposition or mixing until a stage of saturation was achieved, i.e. pore space plugging caused a blockage of the inflow (flow vectors in Figure 3.6B and D). This occurred during both experiments, either when the surface layer of silt had been removed (Figure 3.3; 2B), or when there was sufficient silt incorporated within the bed (Figure 3.3; 4B), which was also indicated by the decrease in hydraulic conductivity. Consequently, this would take place in the experiments with significant silt coverage of 353 g/m² (brown line in Figure 3.5A) and 300 g/m³ silt content (blue line in Figure 3.5B) for the mixed case. Furthermore, this filling of the surface pore space and coating of sand particles (Mitchener and Torfs, 1996; Panagiotopoulos et al., 1997) maintains smoother surface conditions (Figure 3.3; 2B and 4B), which, in turn, would also cause a blockage of the inflow (flow vectors in Figure 3.6B and D) and hence, reduce erosion rates. Moreover, this is accompanied by the reduction of the drag and lift forces acting on the sand particles as suggested by (Komar, 1987; Panagiotopoulos et al., 1997).

In terms of the "Layering experiments", a possible evidence for the existence of the blocked inflow is that when the surface layer of silt is removed (compare Figure 3.3; 2A and 2B), the erosion rate does not immediately return to the erosion rate of pure sand, but instead depended on the initial depth of the layer of silt (note the difference in erosion rate between the brown line 353 g/m² and yellow line 235 g/m² in Figure 3.5A). This increase in the effectiveness of the blocked layer may be due to the internal compaction

within the pockets, which may have more of an effect when the initial silt layer is thicker. It could also be that the underlying sand bed is exposed at higher flow speeds when the initial silt layer is thicker, and so the higher flow speeds might cause structural strengthening of the blocked layer. Therefore, a possible explanation could be that the "blocked layer" either becomes thicker or increases in depth and so is more pronounced causing a higher stability due to denser network structures (Torfs, 1997).

The SPM concentration differences between the 471 g/m² and 941 g/m² runs (Figure 3.4A) of the "Layering experiments" could be explained by the evolution of a blocked layer. We assume that at higher flow speeds, the hydrodynamic pressure on the layer forced the silt particles to migrate in the pore space of the underlying sand bed. In the case of an initial thicker silt layer, i.e. 941 g/m² run, (Figure 3.3; 2A) additional sediment loading might enhance this effect, and hence, could cause structural strengthening. A possible explanation could therefore be that the "blocked layer" either becomes thicker causing a higher stability due to denser network structures (Torfs, 1997), similar to self-weight consolidation processes, which have been observed to decrease erosion potential (Whitehouse et al., 2000). It is interesting to note that a surface silt layer only caused a small decrease in hydraulic conductivity (Table 3.2) compared to the case of a mixed bed. This might be, because without the dynamic pressure caused by the overlying flow, silt is not forced into the underlying sand bed. In the case of the Mixed experiments, the blocked layer is not limited to the surface (Figure 3.6D), which may explain why erosion rates were generally lower relative to the layered experiments.

3.4.3 Bed destabilization - "undersaturated" pore space

In cases when a very thin layer of silt is deposited on top of a sand bed (Figure 3.3; 1A), and also when only a small amount of silt is incorporated into the bed (Figure 3.3; 2A), the bed destabilizes and eroded at the higher flow speeds (compare with bed forms in Figure 3.3; 1B, 2B). This could be caused by an "undersaturated" pore space (Figure 3.6A) where silt was deposited or mixed (Figure 3.6C) in too small concentrations to be able to fill the pore space of the sand bed. Consequently, silt was immediately eroded and not able to protect the exposed sand grains from inflow (deep flow vectors in Figure 3.6A and 6C). Moreover, the sand grains were more exposed to the flow (i.e. surface appears rougher in Figure 3.3; 1A and 3A), which would cause rougher surface texture, which in turn, would enhance inflow into the sediment bed and increase the likelihood of sand erosion (Figure 3.6A and 6C). This was also supported by relatively high hydraulic conductivity measurements. It is interesting to note that when silt has been removed (yellow, blue and black lines in Figure 3.5A; and black line in Figure 3.5B), the sand bed erodes approximately like a pure sand bed, indicating that the pore space blockage was either non-existent, or very shallow and easily flushed out under increasing flow speeds. Our flume experiments ceased at 0.30 m/s, so it is possible that the thicker layer treatments and the sediment beds with mixed with greater fractions of silt, might eventually also become unblocked and begin to erode.

Secondary currents are nearly always present in small annular flumes due to the geometry and methods used to generate the flow. Although our results are affected by these flow patterns and may not be comparable to results from the field and other flumes, these flow patterns are not dependent on treatment, and so our results should be comparable between treatments. Pope et al., (2006) used a similar setup and compared *in situ* field data collected on intertidal flats with their annular flume results. The authors showed that the findings derived with their annular flume were environmentally realistic and representative of the dynamic sediment conditions observed in the field. There are limitations to this study, e.g. the difficulty in resolving flows in a compressed laboratory boundary layer, the inability to differentiate between suspended sand and silt by the OBS and the difficulty in resolving the behaviour of the "blocked layer", and the evolution of surface roughness during the bed stabilization process on a grain-scale level. A combined ABS-OBS (where ABS is an acoustic – backscatter sensor) in the flume channel may give considerable added insight into the processes of erosion and suspension in these type of experiments the (Green and Black, 1999). Despite these shortcomings, our study shows clear evidence of the effect of non-cohesive fine particles on sand bed stabilization, and provides possible explanations for our observations which can guide future studies.

3.5 Conclusions and outlook

We designed two suites of experiments to investigate the influence of silt stabilization on a sand bed: (1) "The Layering Experiment" where a sandy bed was covered by a thin layer of silt of varying thickness; (2) "The Mixing Experiment" where the bed was composed of sand mixed with small amounts of silt. All samples were tested in an annular flume for their stability effects using incrementally increasing flow speeds up to 0.30 m/s. Our results show that a silt layer deposited on top of a sand bed stabilized the bed when the concentration was less than 353 g/m² which corresponds to 1.4 % silt (wt %). In contrast, a silt mixed sediment bed was stabilized within a minimum concentration of 300 g/m³ i.e. 0.18 % silt (wt %). Therefore, the stabilization behaviour is sensitive to how the silt is distributed within the bed. Furthermore, we could show that much lower silt concentrations are required to stabilize a sand bed in comparison to studies on muddy cohesive sediments. We suggest that the bed stabilization is controlled by the amount of silt which was filling the pore space i.e. "pore space blocking" of the sand bed and the influence of silt on bed roughness. The pore space blocking effect could possibly be caused the development of a horizon the "blocked layer" which blocked the inflow into the sediment bed, maintained smooth surface conditions, and hence caused sediment stabilization. However, more research on the stabilizing process of silt and sand compositions and establishment of the "blocked layer" needs to be undertaken especially on micro scale level which could be accomplished by high resolution, 3D numerical 'flume tank' models adopting the general settings of the empirical experiments. For example, two

independent numerical simulation techniques can be coupled, using the Finite Difference Method (FDM) and the Distinct Element Method (DEM) to simulate sediment transport processes on a grain by grain basis in aquatic environments. (e.g. Cundall and Hart (1989), Cundall and Strack (1979; 1983), Itasca (Itasca, 2004a), and Kock and Huhn (2007)).

Given that the bed stabilization is highly sensitive to small silt concentrations, manipulating the layering structure may be a useful tool for the dredging and sea-bed structure industry in order to stabilize dumped sediment at the seafloor. Often when obtaining bed samples in the field (e.g. from grab samples or even short cores), the surface structure is destroyed and even homogenised during sampling. If we were to take a surface grab sample of 10 cm depth of a sediment bed and measure the composition of the disturbed sample (in which the original structure was destroyed) this minimum condition for stabilization in each case would correspond to 1.4 silt (wt %) for a layered sediment bed and 0.18 % silt (wt %) for a mixed composition. An understanding of the layering structure and its role in controlling sediment stabilisation not only has engineering applications, but many benthic fauna rely on the ability to access water column nutrients and remove excreted material through movement of water through pore spaces, and the pivotal role of silt in blocking this process highlights the danger of natural and anthropogenically-driven shifts to the particle size distribution of terrestrial sediment inputs to estuaries.

3.6 Acknowledgments

This work has been funded through DFG-International Research Training Group “INTERCOAST “. We thank Dr. Christian Winter, Dr. Willem de Lange, Annette Rodgers, Rafael Guedes, Hannah Jones, Hazel Needham, Lina Podszun, Jannis Kuhlmann, Linda Wenk, Lutz Torbahn, Christopher Daily, Dr. Giovanni Coco, Prof. Dr. Burghard Flemming and the INTERCOAST research student Antonia Ruppel who freely shared their expertise. We also acknowledge the constructive comments of two anonymous reviewers which greatly improved the manuscript. The Hanse Wissenschaftskolleg supported a research stay of Dr. Karin R. Bryan at Bremen University.

3.7 References

Allen, J.R.L., 1970, Physical processes of sedimentation: London, Unwin University Books, 248 p.

Alvarez-Hernandez, E.M., 1990, The influence of cohesion on sediment movement in channels of circular cross-section, New Castle upon Tyne, UK.

Amos, C.L., Grant, J., Daborn, G.R., and Black, K., 1992, Sea Carousel--A benthic, annular flume: Estuarine, Coastal and Shelf Science, v. 34, p. 557-577.

Black, K., and Paterson, D.M., 1997, Measurement of the erosion potential of cohesive marine sediment: A review of current in situ technology: J. Mar Environ. Eng, v. 4, p. 43-83.

Dolphin, T.J., and Green, M., 2009 Patterns of wave-orbital speed and skin friction under estuarine (fetch-limited) waves: Jornal of Costal Research, p. 178-182.

Dyer, K.R., 1989, Sediment processes in estuaries: future research requirements: Journal of Geophysical Research, v. 94 (C10), p. 14327-14339.

Dyer, K.R., 1994, Estuarine sediment transport and deposition *in* Pye, K., ed., Sediment Transport and Depositional Processes: Oxford, Blackwell Scientific Publications, p. 193-218.

Eisbacher, G.H., 1996, Einführung in die Tektonik: Stuttgart, Spektrum Akademischer Verlag; Thieme; Enke, 374 p.

Essink, K., 1999, Ecological effects of dumping of dredged sediments; options for management: Journal of Coastal Conservation, v. 5, p. 69-80.

Finelli, C.M., Hart, D.D., and Fonseca, D.M., 1999, Evaluating the spatial resolution of an acoustic doppler velocimeter and the consequences for measuring near-bed flows: Limnol. Oceanogr., v. 44 (7), p. 1793–1801.

Green, M.O., and Black, K.P., 1999, Suspended-sediment reference concentration under waves: field observations and critical analysis of two predictive models: Coastal Engineering, v. 38, p. 115-141.

Healy, T., 2002, Chapter Fourteen Muddy coasts of mid-latitude oceanic islands on an active plate margin--New Zealand, *in* Terry Healy, Y.W., and Judy-Ann, H., eds., Proceedings in Marine Science, Volume Volume 4, Elsevier, p. 347-374.

Hir, P.L., Cann, P., Waeles, B., Jestin, H., and Bassoullet, P., 2008, Chapter 11 Erodibility of natural sediments: experiments on sand/mud mixtures from laboratory and field erosion tests, *in* Tetsuya Kusuda, H.Y.J.S., and Joseph, Z.G., eds., Proceedings in Marine Science, Volume Volume 9, Elsevier, p. 137-153.

Hir, P.L., Cayoccaa, F., and Waeles, B., 2011, Dynamics of sand and mud mixtures: A multiprocess-based modelling strategy: Continental Shelf Research, v. 31, p. 135-149.

Hjulstroem, F., 1935, Studies in the morphological activity of rivers as illustrated by the River Fyris: Bulletin of the Geological Institute of Uppsala, v. 25, p. 221–527.

Hjulstroem, F., 1939, Transport of detritus by moving water recent marine sediments, *in* Trask, P.D., ed., Recent Marine Sediments; a symposium, Tulsa Oklakoma: American Association of Petroleum Geologists: New York, London, T.Murby & Co., Reprinted 1968 by Dover Publications p. 3-31.

Jacobs, W., Le Hir, P., Van Kesteren, W., and Cann, P., 2011, Erosion threshold of sand-mud mixtures: Continental Shelf Research, v. 31, p. S14-S25.

Jones, H.F.E., Pilditch, C.A., Bryan, K.R., and Hamilton, D.P., 2011, Effects of infaunal bivalve density and flow speed on clearance rates and near-bed hydrodynamics: Journal of Experimental Marine Biology and Ecology, v. 401, p. 20-28.

Kamphuis, J.W., 1990, Influence of sand or gravel on the erosion of cohesive sediment: Journal of Hydraulic Research, v. 28, p. 43-53.

Karl, D.M., and Novitsky, J.A., 1988, Dynamics of microbial growth in surface layers of a coastal marine sediment ecosystem: Marine Ecology Progress Series, v. 50, p. 169-176.

Kim, S.C., Friedrichs, C.T., Maa, J.P.Y., and Wright, L.D., 2000, Estimating bottomstress in tidal boundary layer from Acoustic Doppler Velocimeter data: J. Hydraul. Eng. Asce, v. 126 (6), p. 399–406.

Klute, A., and Dirksen, C., 1986, Hydraulic conductivity and diffusivity: laboratory methods, *in* Klute, A., ed., Methods of Soil Analysis, Part 1 - Physical and Mineralogical Methods. Agronomy Monograph, Volume 9: Madison, WI., American Society of Agronomy-Soil Science Society of America, p. 687-734.

Komar, P.D., 1987, Selective grain entrainment by a current from a bed of mixed sizes: a reanalysis: J. Sediment. Petrol., v. 57(2), p. 203-211.

Leeder, M.R., 1999, Sedimentology and Sedimentary Basins: From Turbulence to Tectonics Oxford, Blackwell Science, 608 p.

Leys, V., and Mulligan, R.P., 2011, Modelling Coastal Sediment Transport for Harbour Planning: Selected Case Studies *in* Ginsberg, S.S., ed., Sediment Transport, http://www.intechopen.com/articles/show/title/modelling-coastal-sediment-transport-for-harbour-planning-selected-case-studies.

Manning, A.J., Baugh, J.V., Spearman, J.R., and Whitehouse, R.J.S., 2010, Flocculation settling characteristics of mud: sand mixtures: Ocean Dynamics, v. 60, p. 237-253.

Mc Cave, 1984, Erosion, transport and deposition of fine-grained marine sediments: Geological Society, London, Special Publications, v. 15, p. 35-69.

Mehta, A.J., and Lee, S.-C., 1994, Problems in linking the threshold condition for the transport of cohesionless and cohesive sediment grain: Journal of Coastal Research, v. 10(1), p. 170-177.

Mehta, A.J., and Parchure, T.M., 2000, Surface erosion of fine-grained sediment revisited, *in* B.W. Flemming, M.T.D., and Liebezeit, G., eds., Proceedings in Marine Science, Volume Volume 2, Elsevier, p. 55-74.

Mitchener, H., and Torfs, H., 1996, Erosion of mud/sand mixtures: Coastal Engineering, v. 29, p. 1-25.

Murray, W.A., 1977, Erosion of coarse sand-clayey silt mixtures: Journal of Hydraulic Division, v. 103 (HY10), p. 1222-1227.

Panagiotopoulos, I., Voulgaris, G., and Collins, M.B., 1997, The influence of clay on the threshold of movement of fine sandy beds: Coastal Engineering, v. 32, p. 19-43.

Paterson, D.M., 1994, Biological mediation of sediment erodibility: ecology and physical dynamics: In Cohesive sediments, p. 215-229.

Paterson, D.M., Crawford, R.M., and Little, C., 1990, Subaerial exposure and changes in the stability of intertidal estuarine sediments: Estuarine Coastal and Shelf Science, v. 30, p. 541-556.

Paterson, D.M., and Hagerthey, S.E., 2001, Microphytobenthos in contrasting coastal ecosystems: biology and dynamics: Ecological comparisons of sedimentary shores. Ecological studies, p. 105-125.
Pope, N.D., Widdows, J., and Brinsley, M.D., 2006, Estimation of bed shear stress using the turbulent kinetic energy approach--A comparison of annular flume and field data: Continental Shelf Research, v. 26, p. 959-970.
Raudkivi A.J., 1990, Loose boundary hydraulics, Pergamon Oxford
Riethmüller, R., Hakvoort, J.H.M., Heineke, M., Heymann, K., Kühl, H., and Witte, G., 1998, Relating erosion shear stress to tidal flat surface colour: Geological Society, London, Special Publications, v. 139, p. 283-293.
Rijn, L.C.v., 2005, ESTUARINE AND COASTAL SEDIMENTATION PROBLEMS: International Journal of Sediment Research, v. 20, p. 39-51.
Rijn, L.C.v., 2007, Unified view of sediment transport by currents and waves. I: Initiation of motion, bed roughness, and bed-load transport: Journal of hydraulic engineering, v. 133, p. 649-667.
Shields, A., 1936, Anwendung der Ähnlichkeitsmechanik und der Turbulenz- forschung auf die Geschiebebewegung: Mitteilungen der Preußischen Versuchsanstalt für Wasserbau und Schiffbau, v. NW 87.
Soulsby, R., 1997, Dynamics of Marine Sands. A Manual for Practical Applications: London, Thomas Telford Publishing.
Thrush, S.F., Hewitt, J.E., Cummings, V.J., Ellis, J.I., Hatton, C., Lohrer, A., and Norkko, A., 2004, Muddy waters: elevating sediment input to coastal and estuarine habitats: Frontiers in Ecology and the Environment, v. 2, p. 299-306.
Torfs, H., 1997, Erosion of mixed cohesive/non cohesive sediments in uniform flow: Cohesive Sediments, p. 245-252.
Torfs, H., Jiang, J., and Mehta, A.J., 2000, Assessment of the erodibility of fine/coarse sediment mixtures, *in* William, H.M., and Ashish, J.M., eds., Proceedings in Marine Science, Volume Volume 3, Elsevier, p. 109-123.
Torfs, H., Jiang, J., and Mehta, A.J., 2001, Assessment of the erodibility of fine/coarse sediment mixtures: Coastal and Estuarine Sediment Processes, v. 3, p. 109-123.
van Ledden, M., 2002, A process-based sand-mud model, *in* Johan, C.W., and Cees, K., eds., Proceedings in Marine Science, Volume Volume 5, Elsevier, p. 577-594.
van Ledden, M., van Kesteren, W.G.M., and Winterwerp, J.C., 2004, A conceptual framework for the erosion behaviour of sand-mud mixtures: Continental Shelf Research, v. 24, p. 1-11.
Whitehouse, R., Soulsby, R., Roberts, W., and Mitchener, H., 2000, Dynamics of estuarine muds. A manual for practical applications: London, Thomas Telford Publishing, 210 p.
Wiberg, P.L., and Smith, J.D., 1987, Calculations of the Critical Shear Stress for Motion of Uniform and Heterogenious Sediments: Water Resources Research, v. 23, p. 1471-1480.
Widdows, J., Brinsley, M.D., Bowley, N., and Barrett, C., 1998, A benthic annular flume for in situ measurement of suspension feeding/biodeposition rates and erosion potential of intertidal cohesive sediments: Estuar Coast Shelf, v. Sci 46, p. 27-38
Williamson, H.J., 1991, Tidal transport of mud/sand mixtures - a literature review: Sediment distributions Report, v. SR 286.
Winterwerp, J.C., and Van Kesteren, W.G.M., 2004, Introduction to the physics of cohesive sediment in the marine environment, Elsevier B.V., 466 p.
Wright, J., Colling, A., and Park, D., 1999, Waves, Tides and Shallow-Water Processes: Oxford, Butterworth Heinemann.
Young, R.N., and Southard, J.B., 1978, Erosion of fine-grained marine sediments: Sea-floor and laboratory experiments GSA Bulletin, v. 89, p. 663-672.
Zajac, R., Whitlatch, R., and Thrush, S., 1998, Recolonization and succession in soft-sediment infaunal communities:the spatial scale of controlling factors: Hydrobiologia, v. 375-376.

Table 3.1: Overview of the experiments

	Duration [h:min]	Sediment type [mm]		Silt concentration	Velocity range [m/s]
"1.The Layering Experiment"					
Phase I deposition	04:00	Sand 0.03	Silt 0.0055	29, 118, 235, 353, 471, 941g/m²	0.025
Phase II-erosion	02:45	Sand 0.03	Silt 0.0055	29, 118, 235, 353, 471, 941g/m²	0.025-0.300
"2. The Mixing Experiment"					
Phase I consolidation	12:00	Sand 0.03	Silt 0.0055	120, 300, 600, 1200 g/m³	0.000
Phase II-erosion	02:45	Sand 0.03	Silt 0.0055	120, 300, 600, 1200 g/m³	0.025-0.300

Table 3.2: Overview of the sediment behavior derived from flume experiments

"1. The Layering Experiments"

Silt concentration [g/m²]	Critical velocity for silt [m/s]	Critical velocity for sand [m/s]	Maximal erosion rate [mg/m²/s]	Hydraulic conductivity [m/s]
0.0	0.15	0.15	not measured	0.00064
0.3	0.15	0.15	185	0.00063
1.0	0.15	0.2	252	0.00064
2.0	0.15	0.25	561	0.00061
3.5	0.15	> 0.30	533	0.00058
5.0	0.15	> 0.30	1272	0.00056
9.5	0.15	> 0.30	1196	0.00045

"2. The Mixing Experiments"

Silt concentration [g/m³]	Critical velocity for silt [m/s]	Critical velocity for sand [m/s]	Maximal erosion rate [mg/m²/s]	Hydraulic conductivity [m/s]
0	0.15	0.15	not measured	0.00064
120	0.15	0.15	605	0.00062
300	0.15	> 0.30	321	0.00049
600	0.15	> 0.30	190	0.00034
1200	0.15	> 0.30	30	0.00019

Chapter IV

THE ROLE OF GRADED SEDIMENT BEDS ON THE EROSION BEHAVIOR

Gerhard Bartzke[A], Katrin Huhn[A] and Karin R. Bryan[B]

[A]MARUM – Center for Marine Environmental Sciences, University of Bremen, Leobener Straße, D-28359 Bremen, Germany

[B] Department of Earth and Ocean Sciences, University of Waikato, Private Bag 3105, Hamilton 3240, New Zealand

Abstract

Within marine environments, it is widely accepted that alternately graded sediment beds have a higher erosion resistance compared to sediment beds composed of a single grain size. This phenomenon of sediment bed stabilization is explained through textural in-homogeneities within the sediment body. For example, a well understood process causing bed stabilization, termed as armouring occurs when a fine sediment base is sealed by a coarse surface layer. Erosion resistance can also be increased by texture related caging structures. In such a case, fine particles encompassing coarse particles, like a cage, prevent erosion successively. This conceptual model was postulated based on analogue flume tank experiments in combination with theoretical assumptions. However, as caging effects form within the sediment beds, direct observation and quantification of the textural in-homogeneities are limited when only analogue techniques are employed, and hence previous studies are not comprehensive. Consequently, to gain a deeper insight into the effect of texture related caging structures and to validate of previous conceptual models numerical simulations are required.

We developed, a high resolution, 3D numerical ‘flume tank’ model adopting the general settings of analogue experiments. Therein, a Finite Difference Model (FDM) was coupled with a Distinct Element Model (DEM). The major aim was to investigate the physical processes occurring during the initiation of motion at the surface of graded sediment beds under different boundary inflow velocities. Four suites of experiments were designed, whereby numerical fine ‘silty’ particles with increasing thicknesses (0.004, 0.3, 0.5, and 0.7 mm) were deposited incrementally on top of a coarse ‘sand’ matrix to simulate graded ‘sediment beds’. All numerical ‘sediment beds’ were tested for their erosion behavior at predefined boundary inflow velocities (U = 10, 15, 20, 25 and 30 cm/s). We measured the inflow behavior, transport rates, and porosity differences during fluid streaming. The results show that with increasing silt layer thickness, textural caging structures developed between sand pores causing bed stabilization. It was shown that with increasing layer thickness, inflow was increasingly blocked, which caused an increase in the internal compaction and, ultimately, a decrease in the flow available to entrain particles located in the deeper parts of a bed.

Keywords: sediment stability; inflow blocking; graded sediments; DEM; FDM

4.1 Introduction

Numerous studies within aquatic environments have shown that the threshold beyond which particles move is reached when the instantaneous fluid force (F_F) is larger than the resistant force (F_R) of the grain, which is related to the ratio of the particle weight (F_G), the particle angle of response (φ), the lift force (F_L), and the drag force (F_D) (e.g., (Allen, 1970; Rijn, 2007; Soulsby, 1997)). To understand the processes that cause this initiation of sediment transport, and the identification of specific critical threshold values, researchers have commonly focused on the transport behavior of homogeneous sediment beds under differing flow conditions. This approach has been undertaken in various studies using analogue techniques (e.g., (Shields, 1936; Soulsby, 1997; Whitehouse et al., 2000) such as laboratory flume studies (e.g., (Black and Paterson, 1997) or *in situ* field studies (Soulsby, 1997)). However, studies testing e.g. heterogeneous beds (Torfs, 1997; Tucker, 1981), revealed that, additional parameters that modify the erosion characteristics of sediment beds shift the theoretical initial sediment threshold towards higher regimes, thus, causing sediment bed stabilization (Whitehouse et al., 2000).

At present, it is generally accepted that sediment beds of fine particles are stabilized by coarse particles deposited on top (Sutherland, 1987). This effect of sediment bed stabilization was observed in numerous experiments and is termed as armouring. Such an upward coarsening graded bed is formed through selective entrainment (i.e. wash out of the fine fraction and retention of the coarser fraction), where coarse grains protect and armour the underlying material resulting in an more stable sediment bed (Sutherland, 1987; Tucker, 1981). In summary, armouring stabilizes a sediment bed by raising the erosion threshold, which reduces the transport rate.

Today, it is widely accepted that the erosion resistance of a sediment bed is controlled by biostabilization (Whitehouse et al., 2000), cohesion (Sutherland, 1987), and textural induced caging structures (van Ledden et al., (2004) and Hir et al., (2008)). In particular, the entrainment characteristics of beds can be altered by texture induced caging structures, which develop when fine particles encompass coarse grains as a cage (Whitehouse et al., 2000). This phenomenon has been shown in various studies, e.g. Whitehouse (2000), Torfs (1997), van Ledden et al., (2004) and Hir et al., (2008) on mud (i.e., cohesive clay and sand) using laboratory based analog flume studies. Mitchener and Torfs (1996) showed that a similar effect is caused when fine clays are deposited on top of a sand bed. They concluded that the generation of the cage-like network encompassing the sand grains increases the density of the matrix and the additional cohesive forces bind the clay particles further raises the erosion resistance. This was also observed in various experiments, e.g. Panagiotopoulos et al., (1997), Wiberg and Smith (1987), and Torfs et al. (2000), which showed that sediment stability is increased by clay in-filled pockets within the sand bed. These observations support the conceptual model by Panagiotopoulos et al., (1997) that bed stabilization occurs when clay particles surround coarser sand grains.

In the past, this textural caging effect has been mainly investigated in the context of clay-sand mixtures. The effect would therefore also be expected with other fine fractions, e.g. silt, which are very common in many sandy coastal environments, however, until now this has not been considered yet. Accordingly, extensive analogue flumes experiments could be undertaken to examine the effect with silt, similar to previous works, but specific quantification of the textural effects on the grain scaled level at sediment-fluid interface can-not be extracted in such laboratory studies. The spatial and temporal evolution of caging structures in alternately stratified sand and silt bed cannot be examined due to spatial restrictions and limitations of the sensors of traditional analogue flume techniques. Hence, there is a need for validation of caging effects in silt-sand beds using other techniques that allow the investigation of textural related physical processes.

Numerical models are tools that can satisfy this need. Most of the numerical approaches are excellent tools for simulation of the hydrodynamic drivers and the subsequent sediment transport (e.g. Delft 3D, WL Delft Hydraulics). However, most of these models are limited in their ability to quantify textural effects and inflow processes in the sediment bed. As there is need to focus to textural changes in sediment beds and their influence on sediment stabilization, we developed a new modeling approach that allows for the simulation of the initiation of motion in graded sediment beds under different flow conditions.

Two independent numerical simulation techniques were coupled. (1) the Finite Difference Method (FDM) and (2) the Distinct Element Method (DEM) for simulation of sediment transport processes in aquatic environments the major aim was to study the evolution of caging structures in graded sediment beds and their influence on sediment stability. The FDM model simulates the inflow conditions and velocities and, simultaneously, the DEM model simulates the numerical ‘sediment’ bed. This 3D model parameterized general settings of laboratory flume tanks. In order to quantify the effect of a stratified sediment bed on the erosion behavior and bed stabilization, four suites of experiments were designed. A coarse ‘sand’ bed was covered by layers of fine ‘silt’ particles with increasing thickness (S = 1.24 mm, M = 1.54 mm, L = 1.74 mm, to XL = 1.94 mm). For the quantification of bed stabilization by textural caging, fluid profiles, transport distances, and porosity variations were extracted from the models at the sediment surface and in the deeper parts of the bed. All beds were tested under predefined, constant boundary inflow velocities, using values of U = 10 cm/s, 15 cm/s, 20 cm/s, 25 cm/s, and 30 cm/s. These flow velocities, as well as ‘sediment’ configurations, were chosen to mimic the environment of tidal sand flats (Allen, 1970).

Analyses of these experiments indicated, that a layer of fine particles has the ability to change the inflow properties of a sediment bed through the generation of textural caging structures and the increase of packing density. This confirmed the conceptual model that was developed based on previous flume tank experiments and in-situ measurements. In addition, our experiments provide further information that the

'silt' cages block the inflow into the deeper horizons of the bed through pore space plugging. This process influences the inflow characteristics and, subsequently, reduces the shear stress conditions with increasing layer thickness, thus, increasing the bed stability. It was also found that these processes also contributed to increases in the particle packing density of the bed. Consequently, we postulate that textural caging effects could be another major player that can shift the initial sediment threshold towards higher regimens. In this way, smaller fractions fill the pore spaces between the larger particles, and protect the coarse fraction by blocking the inflow into the sediment preventing the bed from re-erosion. The resultant higher bed stability suggests that higher flow velocities would be required to erode the deeper, coarser horizons.
This new model approach provides a deeper insight in to the mechanics and physical processes that occur during bed failure evolution on a grain scaled level.

4.2 Methods

A high resolution 3D numerical flume tank was developed for the quantification of the physical processes at the surface of an alternately graded sediment bed in aquatic environments. In order to simulate sediment transport by a moving fluid, we combined two independent numerical simulation techniques: the Finite Difference Method (FDM) and the Distinct Element Method (DEM). Therein, the FDM model calculates the flow conditions (Fluid model, Figure 4.1) and the DEM model simulates the 'sediment' matrix (Sediment matrix model, Figure 4.1). Both models were coupled via an Input Output routine, which will be described in section 4.2.1.

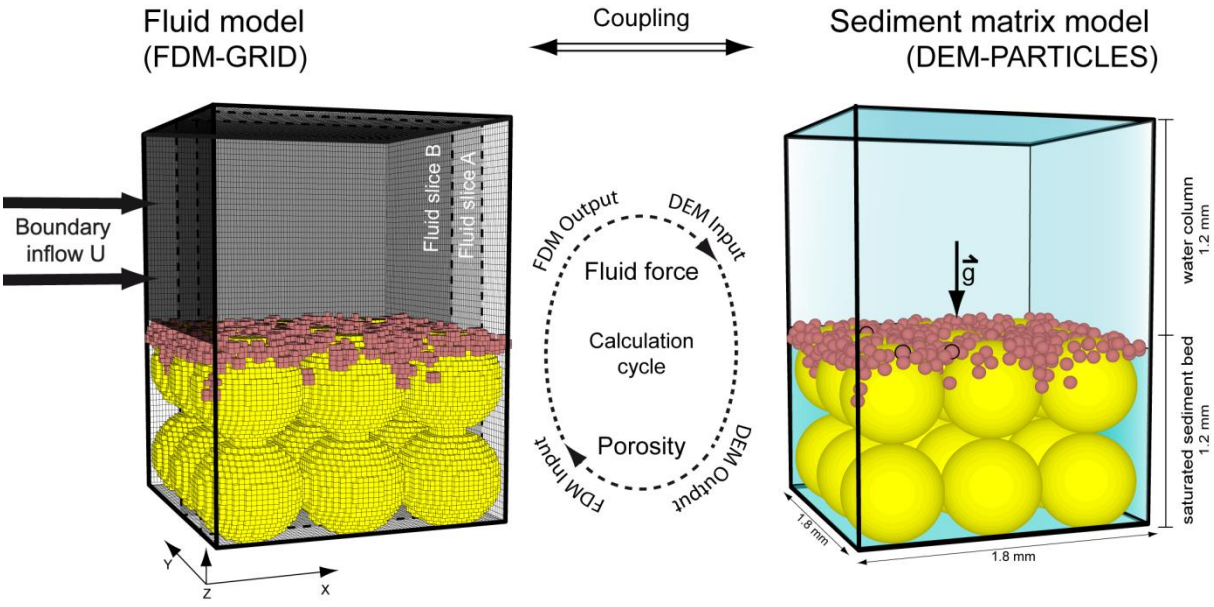

Figure 4.1: Sketch of the coupled Sediment matrix model (DEM - discrete element method) and the Fluid model (FDM finite difference method). In the Fluid model, the positions of the two vertical cross sections (A, B), from which the profiles presented in Figure 4.4 were extracted.

The 3D FDM Fluid model was generated using the commercial software FLAC 3D (Fast Ligurian Analysis of Continua; (Itasca, 2004b). This technique is based on the spatial discretization of the study domain into a grid of a finite number of three dimensional rectangular polyhedral elements (Figure 4.1 (Itasca, 2004b)). The software allows the assignment of physical material properties (i.e. fluid parameters) to each cell in the grid (e.g. fluid density and viscosity) in order to mimic natural conditions. In addition, boundary conditions (e.g. boundary inflow velocities and fluid sources) were designated to the model. Consequently, the FDM model calculates flow velocities in each grid cell, based on the applied boundary conditions and approximations of the differential flow equations through numerical differentiation at defined time steps (Itasca, 2004b).

At the same time, a DEM model was used to mimic 'sediment beds' numerically. These were simulated as a particle assembly consisting of multiple, ideal and spherical particles (i.e. numerical 'silt' and 'sand' grains (Figure 4.1)). The software, (PFC 3D, (Particle Flow Code; (Itasca, 2004a)), is based on the DEM theory by Cundall and Strack (1979), which describes the mechanical behavior of particle assemblages based, on physical contact laws. In order to mimic natural conditions, physical properties, such as density, friction, and hardness were assigned to each particle (Table 4.1). Similar to FDM, boundary conditions must be designated (e.g. gravity and ball acceleration). The resultant particle assemblages, or the 'sediment body', respectively, are deformable by these applied forces. Consequently, DEM allows the simulation of sediment particles, sediment particle interactions, internal structures, and also porosities. Thus, the method simulates the physical behavior of the particle assemblages during deformation processes, such as the initiation of motion of single spherical grains driven by defined boundary conditions, (e.g. fluid forcing (Figure 4.1)).

A more detailed review of the involved algorithms of the FDM and DEM exceeds the scope of this paper. A complete description of the numerical procedure of the FDM code can be found e.g., in Itasca (2004a). Further descriptions of the numerical DEM code can be found in e.g., Cundall and Hart (1989), Cundall and Strack (1979, 1983), Itasca (Itasca, 2004a), and Kock and Huhn (2007).

Please note that hereafter, the term 'grains', as well as 'sediment' will be used, regardless of whether the context is related to numerical or real grains. The same applies to sand and silt, respectively.

4.2.1 Model configuration

Alternately graded numeric sediment beds were generated in order to quantify the influence of fine particles deposited on top of a coarse matrix with respect to erosion behavior, inflow properties, and bed stability. In the following, all sediment beds were exposed to a range of boundary inflow velocities. For

simulation of fluid motion and particle transport with the 3D numerical flume tank, both the DEM and the FDM models had identical dimensions (1.8 x 1.8 x 2.4 mm), geometries, material properties as well as boundary conditions (Figure 4.1).

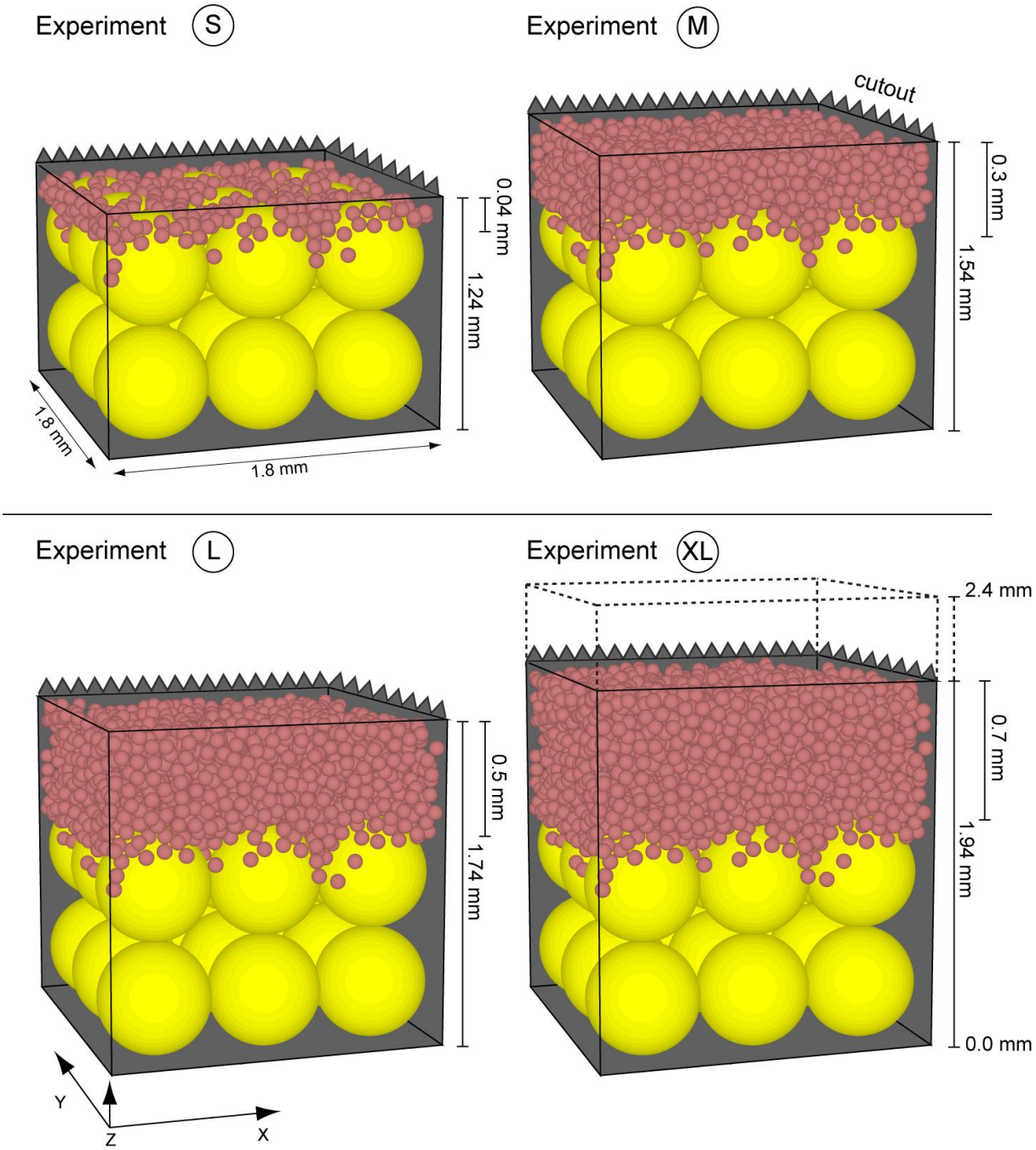

Figure 4.2: Schematic of the four suites of experiments highlighting a cut out of the sediment matrixes from the DEM models S - XL. Silt (brown particles) was deposited under applied gravity on top of a sand bed (yellow particles). The layer thickness was increased incrementally from S) 1.24 mm to XL) 1.94 mm.

At the beginning of the simulation, the grain or sediment model was generated, in order to mimic an isolated section of a sediment surface in a flume tank on the grain-scaled level. In order to mimic this

sediment bed numerically, a sample box was generated with the dimensions of 1.8 mm x 1.8 mm, and 1.2 mm in height, which was filled with the numerical sediment. Therein, 5 stiff un-deformable box walls were created (Table 4.1). For the generation of the graded sediment beds, two end members were used as a simplified treatment of fine grains (i.e., numerical silt (D_{50} = 0.08 mm)) and coarse particles (i.e., numerical sand (D_{50} = 0.6mm)). The numeric sediment beds were composed of a lower coarse-grained layer with a constant thickness (1.2 mm, Figure 4.2). This layer was composed of 18 spherical sand particles deposited in a cubic assembly under applied gravity always filling half of the box (Figure 4.1, 4.2). This geometry having the largest pore volume compared to that of a randomly packed bed was chosen as the aim was to investigate processes that occur in the pore-space between the sand particles. All sand particles were fixed to ensure open pockets enabling quantification of the erosion behavior of the graded bed in more detail. Physical properties (density, friction, normal stiffness, and shear stiffness (Table 4.1)) were assigned to each particle to mimic the natural properties of coastal sands.

In the next step, a finer silt cover layer was deposited on top of the coarse matrix. The thickness of this layer was varied in the experiments (S = 0.004 mm, M = 0.3 mm, L = 0.5 mm, and XL = 0.7 mm) by depositing increasing amounts of smaller silt grains (S = 463, M = 1740, L= 2597 and XL = 3472 particles). The grains were randomly distributed across the entire box and settled under gravity on top of the sand bed. This ensured that natural depositional conditions and packing was induced in the simulations. Physical properties were also assigned to each silt particle with respect to natural conditions (Table 4.1).

The total height of the resulting four numerical sediment beds were: S = 1.24 mm, M = 1.54 mm, L = 1.74 mm and XL = 1.94 mm (Figure 4.2). For the simulation of a flow field, the Fluid model was generated by using the FDM model (Figure 4.1). The spatial extensions of this Fluid model were assigned identical dimensions to the Sediment matrix model. In order to simulate flow fields in highest resolution, the FDM grid was discretized into 288,000 elements (60x60x80 in X, Y and Z directions) with a uniform axes lengths of 0.03 mm (Figure 4.1). Hence, the smallest DEM grains were represented by at least 6 elements to ensure stable coupling between FDM – DEM model (see below). The corresponding fluid properties were applied to the Fluid model (Table 4.1) to simulate natural coastal conditions based on the literature (Allen, 1970; Eisbacher, 1996) and to exclude any scalar discrepancies. The entire box model was flooded to generate a fully saturated sediment bed.

Coupling of both models was undertaken after generation of the above described initial model configurations. In the first step, all information from the sediment matrix, such as the spatial parameters x, y, and z coordinates and the radii of all particles, were sent from the DEM to the FDM model. Based on these data representing the grain distribution within the DEM model, the FDM grid elements are defined

as either fluid cells or sediment cells. The resulting FDM model grid consists of elements where fluid streaming was allowed (fluid zones) or not allowed (solid matrix zones).

After the grid was classified, a constant boundary inflow above the fully saturated bed field was applied in X-direction at the left box wall and outflow boundary condition at the right box wall (Figure 4.1). Starting with these initial stable conditions, a constant stream in the positive x-direction above the sediment bed evolved. All flow velocities were calculated from cell to cell throughout the whole model (in the water column and the saturated matrix area) based on the initial porosity distribution. After the flow field reached stable conditions, all flow velocities were extracted. These flow velocities were transformed into forces according to the Stokes velocity law (Miller et al., 1977). These fluid forces were sent to the sediment matrix model at their corresponding X, Y, and Z coordinates and applied to their positioned particles. The velocity parameters then served as boundary conditions for the Sediment matrix model. Based on this forcing, new particle contact forces and the resulting particle displacements were calculated in the DEM model. If the added fluid forces were larger than the resisting force of the particles, the particle contacts broke up and the grains were transported (Cundall and Strack, 1979). This caused new porosities within the DEM model and new particle configurations, respectively. Hence, sediment transport and / or grain re-assembly was initiated. In the cases of grains that were eroded from the matrix, they were transported by the stream. The resultant new porosities (Sediment matrix model) were sent back to the Fluid model and, subsequently, a re-meshing of the FDM model grid was initiated starting a new calculation cycle.

The calculation cycle between both models was repeated until constant flow and transport conditions were reached. For consistency each model was coupled 40 times to ensure that the results were statistically stable and analyzable. Hence, high resolution information about, e.g., particle distribution, porosity, texture, and fluid velocities at the sediment surface, as well as in the interior of the sediment matrix was available in space and time.

The applied boundary inflow velocities were stepwise increased from U = 10 cm/s, in 5 cm/s increments to 30 cm/s to mimic the environment of tidal sand flats (Allen, 1970).

4.2.2 Measurements and data statistics

To quantify the influence of graded sediment beds on the erosion behavior, we analyzed variations in fluid velocities, particle positions, and particle displacement at each time step. All data was processed using programmed routines in FLAC 3D, PFC 3D, and Matlab 2011 environments. These analyses revealed high resolution data of velocities in the flow field, transport distances, and porosity changes in the sediment bed.

4.2.2.1 Fluid profiles

Two vertical slices in the X-Z direction were extracted from the Fluid model, after reaching steady state flow conditions, to monitor the velocities in the water column, as well as the velocity gradient at the sediment-water interface and within the sediment bed. These sections intersected the entire box at the locations Y = 0.003 mm and Y = 0.006 mm (Figure 4.1 and 4.3). An example is shown for Model M in Figure 4.3A and B. This data allows for the monitoring of along stream variations through the whole Fluid model. Due to the large amount of data (288,000 velocities at 4e10 time steps for 4 model setting times and 40 model runs), single 2D vertical fluid profiles were extracted, that allowed for a direct comparison of the four Experiments (S – XL) at different boundary inflow velocities and a better visualization of our modeling results. These fluid profiles were processed at four positions. Exemplarily locations were chosen to intersect the pore space between the sand particles as we were aiming to extract as much flow data as possible along the vertical cross sections (Figure 4.4). In the cases where the velocity profile intersected a particle (i.e. cell with no flow data), the velocity profile was interpolated using a cubic spline function (Mathworks, 2011). Therein, a linear regression analysis was undertaken. Following extraction, a complete velocity profile was obtained including the water column and the complete thickness of the fully saturated sediment bed. This profile was based on the results of 40 model iteration steps ensuring statistically significant results.

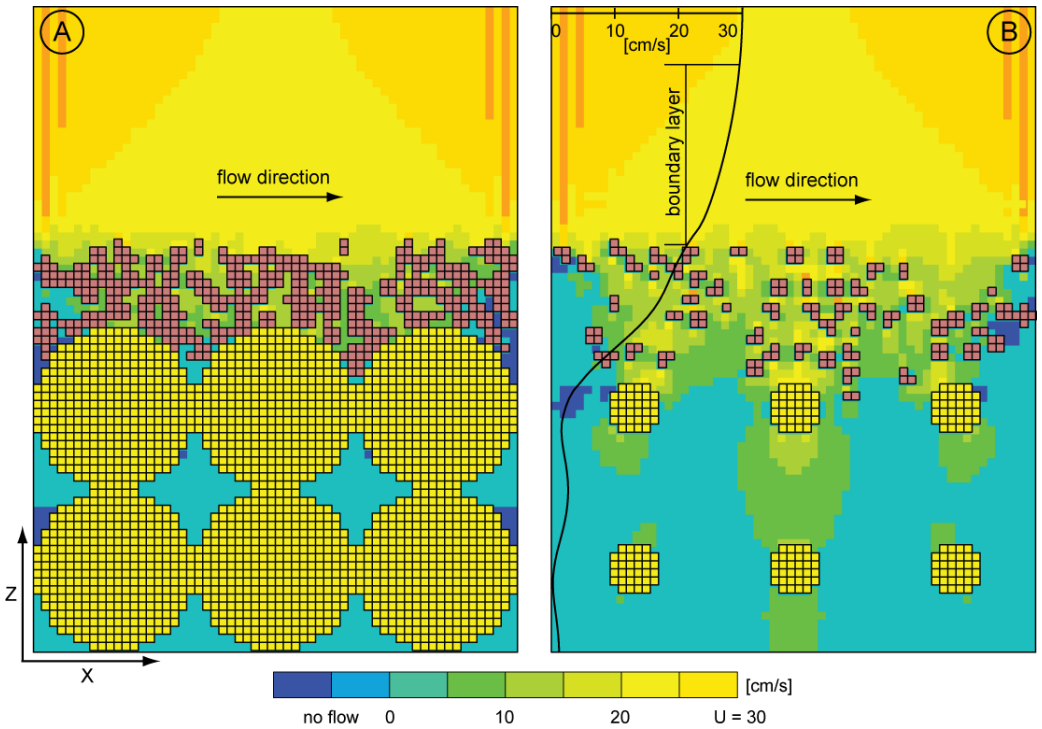

Figure 4.3: A) and B) represent flow velocities along vertical slices through the Fluid model from Experiment - L at a U = 30 cm/s boundary inflow velocity after reaching steady state conditions. The locations of these vertical slices are shown in Figure 4.1 in the FDM grid (A) X-Z slice at Y = 0.3 mm and B) X-Z slice at Y = 0.6 mm). Silt and sand zones have been colored to brown and yellow, respectively (porosity = zero, no flow). A single vertical fluid profile measured at the position of X = 0.6 mm and Y = 0.6 mm is shown in B as example of the profiles plotted in Figure 4.4.

4.2.2.2 Transport distances and porosities

Due to large data volumes, as with the fluid profiles (e.g., 3,472 particle positions at 4e10 calculation steps at 5 predefined boundary inflow velocities and 40 model runs), the total transport distance of singles grains was calculated within each Sediment matrix model as the difference between the initial and the final position after reaching steady state flow conditions. For further analyses, only particles transported a distance exceeding their own radius, were considered. This criterion represented the assumed threshold for particle transport in all experiments. Particle transport and porosity changes were extracted from a horizontal volume at the interface between sand and silt (0.9 mm $\leq z \leq$ 1.1 mm; Base Slice in Figure 4.5). A similar procedure was undertaken for the uppermost sediment portion (0.9 mm $\leq z \leq$ top of sediment bed; Top Slice in Figure 4.5). To make these data comparable between the Experiments (S – XL), which contain differing quantities of silt particles, the ratio of transported particles was calculated.

The porosities (Φ) were also quantified in the two analytical sections (Top Slice and Bottom Slice in Figure 4.5). In each slice, the porosity was calculated by determining the ratio between the total particle volumes (V_T) and the bulk volume of the void space (V_V). In the cases of particles bisected by the designated boundary of the analytical sections grains, lying outside this given area, was subtracted using a spherical cap formulation (Harris and Stöcker, 1998). Consequently, the volume of the remaining hemispheres was considered in the total particle volume calculation (V_T).

The data presented represents a statistically significant average from 40 model runs of each experimental setting.

4.3 Results

In order to quantify the erosion behavior of graded sediment beds, where fine silts are deposited on top of a coarse sand bed, four numerical experiments were undertaken (Figure 4.2). The thickness of the silt layer was increased incrementally (S, M, L and XL) and tested under the predefined boundary inflow velocities (U = 10, 15, 20, 25, and 30 cm/s). Fluid profiles, transport distances, as well as porosities were extracted and analyzed as explained above.

4.3.1 Fluid profiles

All experiments showed a constant flow pattern above the sediment surface in the X – direction at all tested boundary inflow velocities, which indicates uniform flows over the beds (Figure 4.3 and 4.4). In addition, all experiments showed that in the vicinity of the sediment bed, a layer evolved where flow velocities decreased logarithmically towards the sediment - water interface. For example, the vertical velocity profile of the Experiment - M (extracted at U = 30 cm/s boundary inflow velocity) showed a decline from 30 cm/s free stream velocity to 7.6 cm/s within the lowermost 1.5 mm above the bed (Figure

4.4 and Table 4.2). Furthermore, a significant decrease in the flow velocities occurred just below the sediment surface in the uppermost part of the sediment beds in all experiments. However, the magnitudes of the velocities in the sediment bed increased to a lesser extent compared to flow velocities measured in the water column (Table 4.2). The flow velocities approached zero in the deeper parts of the bed. However, a slight increase in the flow speeds was measured between the larger sand grains, e.g., 1.0 cm/s in case of the Experiment - M (Figure 4.3).

This general vertical fluid profile was modified by applied boundary inflow velocities and silt layer thickness.

An increase of the applied boundary inflow velocities caused an increase of the flow velocities in the water column above the sediments bed in all experiments (Figure 4.4). For example, the free stream velocities of the Experiment - S increased from 10 cm/s to 30 cm/s with respect to the applied boundary inflow velocities and at the same time, the thickness of the boundary layer increased (e.g., Experiment series S (Figure 4.4)). Consequently, the velocities measured in the vicinity of sediment bed were constant for all Experiments S – XL at identical boundary inflow velocities (Figure 4.4; Table 4.2).

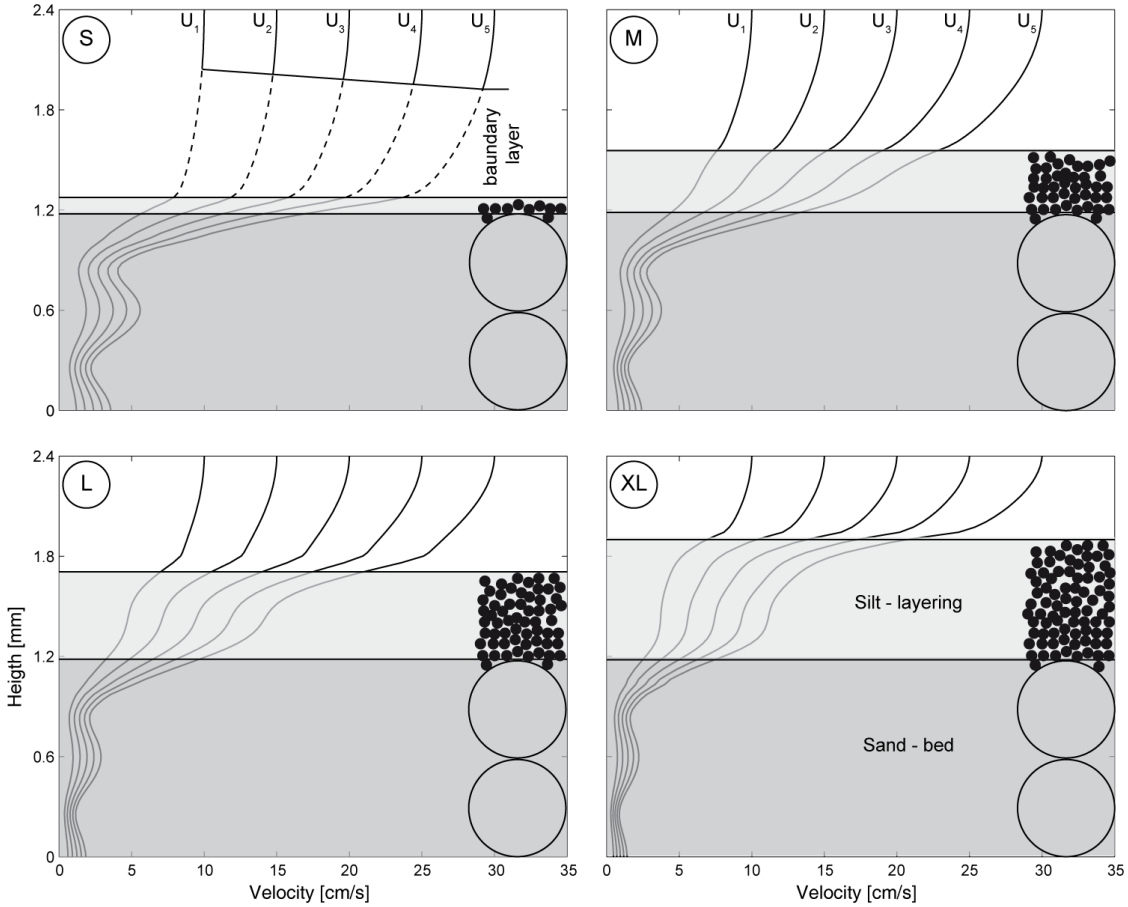

Figure 4.4: Fluid profiles derived from simulations implementing S) 1.24 mm, M) 1.54 mm, L) 1.74, and XL) 1.94 mm thick layered sediment beds at increasing boundary inflow velocities (U_1 = 10, U_2 = 15, U_3 = 20, U_4 = 25, and U_5 = 30 cm/s). Silt and sand horizons have been color coded to light and dark gray, respectively. The developed boundary layer above the sediment surface is indicated in the Experiment – S by dashed lines.

However, the thickness of the boundary layer decreased in Experiments L and XL indicated by a logarithmic increase (Figure 4.4). Additionally it was observed, in all experiments, that the flow velocities measured in the sediment beds increased when the boundary inflow velocities increased. The flow gradients within the silt layers varied in each individual Experiment S – XL (Figure 4.4). The results showed that in case of the thin silt layer sediment bed (Experiment - S), the flow velocities consistently decreased into the deeper parts of the sediment bed (Figure 4.4). Additionally, in the same experiment, the inflow gradient increased with increasing applied flow velocity. For example, at U = 10 cm/s, the decreasing velocity profile had a gradient of 2.4° within the silt layer and that at U = 30 cm/s was 4.5°.
In contrast to this linear flow decrease pattern, the decreasing velocity profile within the silt layers transitioned into a convex shape with increasing silt layer thickness (compare Experiments - M, L and XL in Figure 4.4). In summary, the velocities decreased significantly with increasing silt layer thicknesses. This transition is evident from the more moderate gradients of the velocity profiles in Experiment - L and XL compared to Experiment - S and M. Hence, only deeper parts of the sediment bed are protected from inflow. Furthermore, the, flow velocities at the top of the sand bed were comparable in Experiment - L and XL, whereas they were significantly, higher in Experiments - S and M. Consequently, flow velocities in the deeper sediment bed increased with increasing boundary inflow velocity, but to a lesser extent in Experiment S.

4.3.2 Sediment transport

Our results showed that in all experiments silt particle transport at the sediment surface was initiated immediately at a velocity of 10 cm/s, whereas the sand bed always stayed stable. The number of grains transported at the sediment surface remained relatively constant throughout all experiments (Table 4.3). In all experiments the transport rates measured of the sediment top indicated high transport distances, and thus, continuous erosion, with increased with increasing boundary inflow velocities (Figure 4.5). Values ranged from 70 % transport at U = 10 cm/s at the beginning, to 90 % at 30 cm/s at the end of fluid streaming for all experiments (Figure 4.5 and Table 4.3).

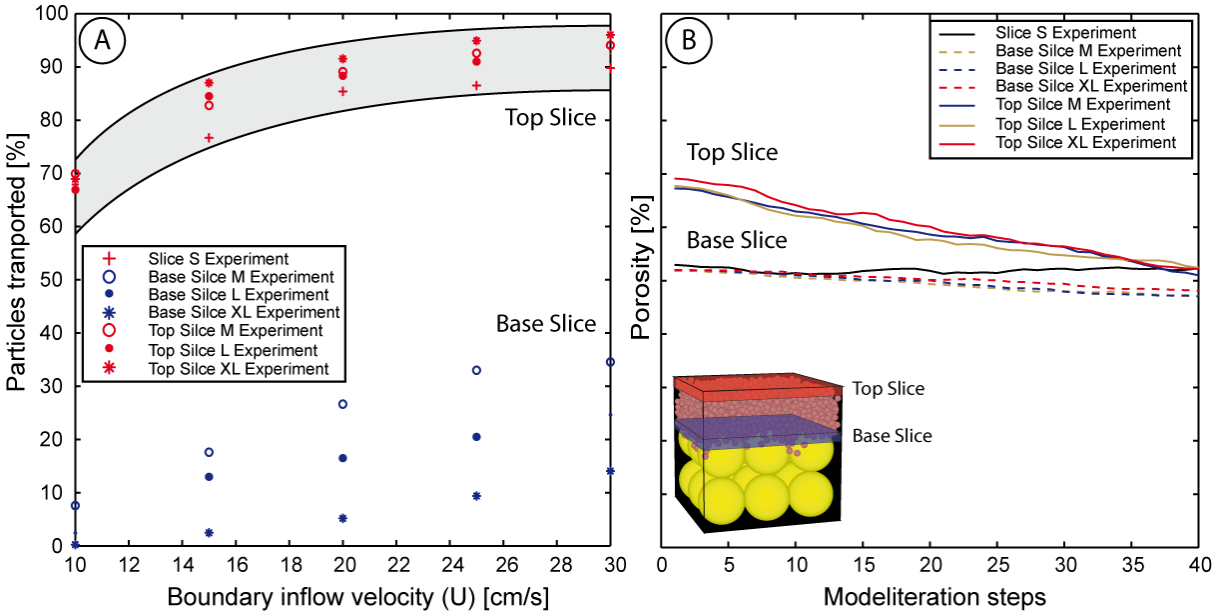

Figure 4.5: A) Mean transport distance of the transported silt particles normalized to the absolute amount of silt at increasing boundary inflow velocities of M) 1.54 mm and XL) 1.94 mm thick sediment bed. The red box in (B) show the transport distances at the top – surface of the silt layering, whereas the blue markers indicate the transport distances at the base of the silt layering. B) Porosity measurements derived from M) 1.54 mm, L) 1.74 mm, and XL) 1.94 mm thick sediment bed at U = 20 cm/s boundary inflow velocity, either taken at the top / surface of the silt layering (blue, red and green lines) or at the bottom of the layering (yellow, blue and red lines).

In the deeper parts of the layers, the transport of particles declined with depth in Experiments -M - XL (Base Slice in Figure 4.5), but similar to the top slice the number of transported particles increased with increasing velocity from 0 – 9 % in the case of U = 10 cm/s to 15 – 35 % at U = 30 cm/s. The results of a deeper positioned base layer were not considered in the Experiment - S because the silt layer was too thin to obtain usable results. Grain transport numbers indicate that more particles were transported at the sediment surface when the silt layer was thicker and the flow velocity higher.

For example, 92 % of particles were transported in case of the Experiment - M at a 30 cm/s boundary inflow velocity at the surface (Top Slice, Figure 4.5), whereas only 30 % of the particles were transported in the deeper parts of the layer (Base Slice, Figure 4.5). For the case of the thicker Experiment – XL, at a 30 cm/s boundary inflow velocity, 90 % of the particles were transported at the surface (Top Slice, Figure 4.5) compared to only 13% in the interior of the silt layer (Base Slice, Figure 4.5).

4.3.3 Porosity differences

Based on the low silt amount in Experiment - S, porosity values from the Experiments - M, L, and XL were processed (Figure 4.5 and Table 4.4). All values were compared and for boundary inflow conditions but only those from U = 20 cm/s are presented here as an example case to highlight general observations. For analyses, porosities were extracted following the onset of stable flow conditions in the water column and sediment bed. For consistency, porosity extraction was always undertaken at time step 4e10.

The porosity measurements of all Experiments - M - XL indicated that the porosities at the top of the silt layer were generally higher compared to those at the base. The top layer showed a stronger porosity decrease with depth compared to those derived at the base of the silt layer. So, with increasing fluid streaming time, porosity values revealed two different trends. The porosity values extracted from the sediment surface showed a strong decrease, with values that ranged from 70 % to 55 %. In contrast, porosities extracted from the lower parts of the layer decreased to a lesser extent (54 % to 43 %, in Figure 4.5) and were almost uniform with respect to fluid streaming time. This mirrors the transition from a highly dynamic surface to a more stable bed.

4.4 Discussion

The results showed that our new numerical approach reproducing a 3D numerical flume tank was capable of simulating sediment transport processes of graded sediment beds. Four suites of experiments were designed (S – XL; Figure 4.2), whereby numerical fine silt particles with increasing thicknesses were deposited incrementally on top of a coarse sand matrix to simulate graded sediment beds. All numerical sediment beds were tested for their erosion behavior at predefined boundary inflow velocities (U = 10, 15, 20, 25, and 30 cm/s). We were able to process high resolution 3D flow velocity data, particle transport rates, and porosity changes for the quantification of the physical processes occurring in the water column, at the sediment surface, and in the interior of sediment beds. The experiments showed that with increasing layer thickness, the inflow into the sediment bed decreased. Consequently, a lower number of particles were exposed to critical flow speeds. This resulted in a decreasing transport potential with depth (Figure 4.5). The above findings verify the hypothesis that the generation of cage-like structures is a major player in bed stabilization (Figure 4.3). We observed that cages were created by finer silt particles which were originally deposited on top of a coarse sand matrix, and subsequently filled the pore spaces between the sand grains. Hence, these cage-like structures increase the bed stability significantly in graded sediment beds. This observation was also supported by high resolution porosity measurements enabled by our new simulations, which show a decrease in porosity that was larger at the surface of the silt layer, but also apparent at depth.

Detailed analyses of our numerical results revealed that the fluid profiles decreased logarithmically from the water column towards the sediment surface (Figure 4.4), which corresponds to data recorded during field campaigns, as well as in laboratory experiments, e.g., ADCP, ADV data (Wright et al., 1999). Furthermore, this logarithmic velocity decrease indicates that a boundary layer developed above the sediment surface. With increasing boundary inflow velocities the boundary layer became compressed with a larger velocity profile gradient (Figure 4.4), which agrees with prior studies using analogue techniques to measure the boundary layer development above sediment beds (Munson et al., 2002; Peterson et al.,

1989). However, with increasing silt layer thickness, the flow velocities measured at the sediment surface (u_*) were in the same range for all Experiments - S - XL (Table 4.3; Figure 4.4). This finding corresponds with the boundary layer theory development theory (Leeder, 1999) that suggests that the surface velocities (u_*) are independent of bed roughness at similar free stream velocities. Smaller variations in the flow velocities may have been related to the local irregularities in surface roughness caused by the unique particle distributions of each experiment. Regardless, the flow velocities (u_*) that cause particle erosion at the sediment surface were not influenced by the height variations in the model set-ups (Figure 4.2). Additionally, it was shown that erosion of the silt particles was initiated and perpetuated within the logarithmic boundary layer. This corresponds with previous studies, that suggest that sediment transport of particles (< 200 µm) occurs in the boundary layer (Leeder, 1999).

In deeper parts of the silt layers, the experiments showed that with increasing silt layer thickness above the sand, the inflow depth into the sediment bed and the overall flow velocity decreased as indicated by the shift from a linear to an increasingly steep convex flow velocity profile shape (S – XL; Figure 4.4). That indicates, that the thickness of the silt layer controls the flow profile in the sediment bed, and hence, the flow environment required to entrain particles in the deeper parts of the bed. This finding demonstrates the significant influence of the silt layer on bed stabilization, which is the focus of our study.

The particle transport measurements showed that sediment transport at the surface in each experiment was initiated at 10 cm/s. This finding corresponds to the Shields criterion for initiation of sediment motion for the grain diameter tested (Shields, 1936; Soulsby, 1997). Similarity in transport rates at the sediment surface of all experiments indicates that erosion conditions at the sediment surface (Figure 4.5) were comparable as would be expected from the consistent flow velocities measured at the sediment surface in all experiments (Figure 4.4 and Table 4.2). Accordingly, the number of transported particles at the top of the silt layer of all experiments was in the same ranges, regardless of the thickness of the silt layering, or the thickness of the boundary layer.

However, in the deeper parts of the sediment beds particle transport decreased with increasing silt layer thickness (Table 4.4), a trend that corresponded to the fluid measurements (Figure 4.4). The model results showed an inflow decrease with increasing layer thickness, indicating that, with increasing silt layer thickness, the erosion threshold velocities deceased with depth and successively lost their ability to transport particles. Based on this, we postulate that there may also be a decrease in particle washout and, subsequently, less sorting effects. As shown by the particle transport measurements, higher numbers of particles were eroded at the sediment surface due to higher flow velocities at the sediment surface (Figure 4.5).

The occurrence of decreased flow velocities and particle transport rates with depth is also supported by the porosity measurements. The strong decrease in the porosity values at the sediment surface is related to the

high particle transport rates (Figure 4.5) and indicates a high compaction rate at the sediment surface (Figure 4.5) caused by migration of the particles into the deeper parts of the bed. However, the porosity values in the deeper parts of the bed showed only a moderate decrease with increasing silt layer thickness towards deeper parts of the sediment beds, which corresponds with the lower particle transport rates, and thus, indicating lower compaction rates in the deeper parts of the layer.

Traditionally, for the investigation of sediment erosion and transport phenomena analogue techniques (laboratory flume tanks or *in-situ* experiments) are used. However, direct comparison and therewith validation of our data with field/lab data was difficult as the quantification of flow velocities, transport rates, and porosity changes in the interior of a sediment bed is highly limited using analogue techniques (Komar, 2007). Analogue tools are typically used for measuring flow speeds at the sediment surface and are limited in their ability to measure flow speeds in high resolution on micro scaled level due to the low resolution of the sensors. For example, flow data measured by ADV (e.g., Sontec Micro ADV) above a flat sand bed allowed for measurement of the flow speeds to only 0.3 mm above the sediment bed (Bartzke et al., 2012 unpublished data). However, in order to quantify processes in sediment beds, other studies used analogue techniques, such as x-rays of the sediment bed ((Mitchener and Torfs, 1996; Whitehouse et al., 2000)) for fluid flow quantification, or colored particles to measure transport rates (Komar, 2007; Leeder, 1999). These studies serve as a basis for our new conceptual model of bed stabilization.

As these *in-situ* techniques are limited in their ability to quantify the dynamical processes of the highest resolution during fluid streaming, our experiments represent a new step forward for overcoming the limitations of the quantification of flow velocities, particle transport changes, and porosity changes that occur in the direct vicinity of the sediment surface and in the sediment beds.

4.4.1 Conceptual model and sediment bed stabilization

As a result of the detailed analysis of the fluid behavior and particle transport as well as porosity changes, a quantification of the effect of texture induced caging structures on the bed stability was possible. This effect was already postulated for clay–sand sediments by various authors e.g.

(Hir et al., 2008; Mitchener and Torfs, 1996; Panagiotopoulos et al., 1997; van Ledden et al., 2004; Whitehouse et al., 2000). These researchers assumed that cohesive clay network structures, surrounding the coarser sand grains caused the development of caging structures which increases the erosion resistance. This conceptual model is based on analogue flume experiments and was introduced in more detail by Panagiotopoulos et al. (1997).They concluded that in sediment beds composed of coarse sand particles, all particles are more or less connected to each other, indicating a relatively easy erosion of the bed. After mixing fine clay particles into the matrix of the coarse sand bed the authors suggested that

increase in the bed, stability occurred through the development of cage like structures around the sand particles. However, the theory and the quantification of bed internal processes are extremely difficult by analogue flume studies and could not be verified due to limitations of analogue studies (Komar, 2007).

Based on these previous analogue flume studies e.g. (Hir et al., 2008; Mitchener and Torfs, 1996; Panagiotopoulos et al., 1997; van Ledden et al., 2004; Whitehouse et al., 2000) our numerical results quantified the generation of textural caging structures and their potential for increasing the bed stability of graded sediment beds. We adapted the previous theoretical model in clay-sand sediments to develop a new conceptual model on the patterns of texture induced bed stabilization in silt-sand graded beds (Figure 4.6). Our model results highlight an improved understanding of the mechanisms for the generation of caging structures and bed stabilization by inflow blockage and internal compaction, which act to increase the erosion resistance of coarse particles overlain by a fine sediment layer. The cases for thin (Experiment – S) and thick graded beds (Experiment – XL) are shown in Figure 4.6A and 4.6B (see Figure 4.6C and 4.6D for a close-up view). To the best of our knowledge, this is the first study that directly simulates the generation of textural caging structures and their influence on changes in inflow velocities, particle transport rates, and porosities in graded sediment beds.

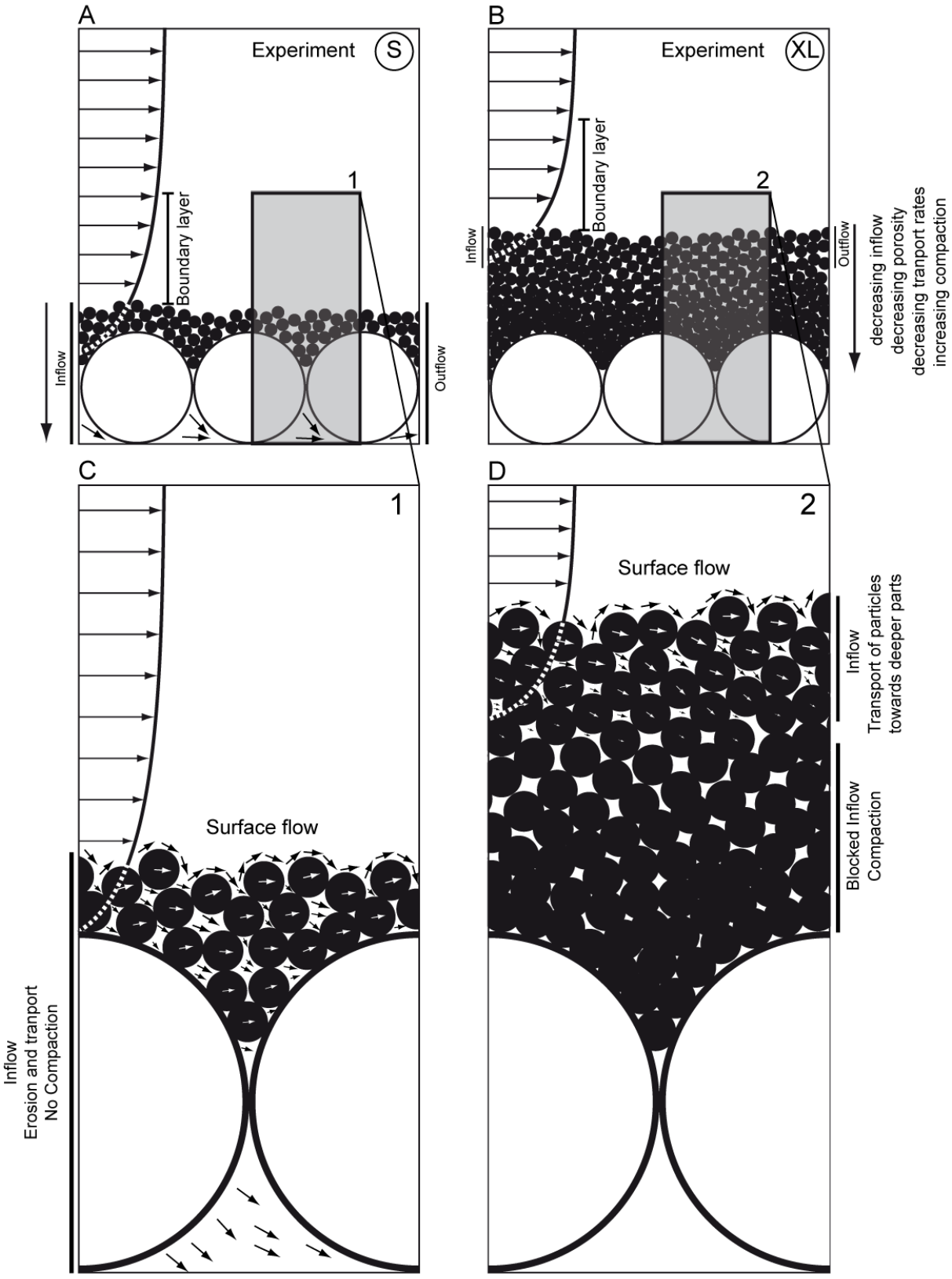

Figure 4.6: Conceptual model of the processes of the thin layer Experiment – S, and thick layer Experiment - XL.

As shown by the fluid profiles in all experiments (Figure 4.4), a bed boundary layer developed, which corresponds to the theory of (Munson et al., 2002; Peterson et al., 1989). This boundary layer is illustrated by the flow vectors in Figure 4.6. At the top of the bed, the flow infiltrated and entrained the particles there (Figure 4.6), which was also shown by the decreasing inflow rates into the silt layering (compare with section 4.3.1).

The results showed that with increasing silt layer thickness, inflow decreased (Figure 4.4), with the case of a very thin layer (Experiment – S; Figure 4.6A), it was shown that the fluid migrates through the pore space of the fine fraction and flows through the whole sediment bed allowing erosion of the underlying coarse particles (Figure 4.6C). In case of a thick layer (Experiment – XL; Figure 4.6B), the fluid flow infiltrated the sediment bed (compare fluid velocities of the Experiment - S and XL); however, due to the additional thickness and the development of caging structures surrounding the coarse grains (Figure 4.3), the flow did not penetrate into the deeper parts of the bed. This resulted in a decrease in fluid velocities, thus, and the transport potential in the deeper horizons of the bed (i.e. blocked inflow).

The experiments also showed that a downward directed bed internal flow developed (arrows in Figure 4.6B and 4.6D) causing particle transport into the deeper parts (Figure 4.6).This process led to an increasing compaction rate with depth (compare section 4.3.2 and 4.3.3) as shown by the significant decline in the porosity values and the decreasing transport distances in the deeper parts of the coarse matrix.

This suggests that the presence of, a thick layer on top of a coarse matrix increases the erosion resistance through the process of inflow blockage and internal texture induced compaction. Therein, the threshold velocities are lowered in the interior of the sediment bed and the entrainment of coarser particles located in the deeper parts of the bed, is prevented, which together contribute an increased stability of the whole sediment bed (Figure 4.6).

In summary, following former studies and pre-existing existing conceptual models on the key role of textural induced sediment stabilization, our results confirm the theory of texture induced bed stabilization for graded sediment beds. Our new model approach confirms that sediments beds are stabilized through the generation of cage like structures or rather an inflow protection caused by pore space filling and/or porosity decrease (Figure 4.3), brought about by the incorporation of fine silt particles in the pore spaces of the coarse sand fractions. In contrast to the armouring effect, where the coarse fractions stabilize the fine fractions (Sutherland, 1987), textural caging structures are the mode for bed stabilization in graded sediment beds. This can be initiated when the coarse fraction is protected by finer sediment, even if it is a non-cohesive silt layer as shown here. Therefore, bed stabilization in graded sediment beds is induced by the development of a protective silt layer that blocks the inflow and results in increased erosion resistance of particles located in the deeper parts of the bed.

4.5 Conclusions and outlook

To investigate the effect of sediment grading, whereby a layer of fine particles overlies a coarse matrix, on the inflow behavior and the threshold conditions of underlying particles, we used a 3D high resolution numerical flume tank. Using this approach, we were able to quantify processes controlling texture induced bed stabilization caused by the development of cage like structures in a graded sediment bed. Four suites of experiments were designed by generating a coarse matrix, (i.e., numerical sand) and depositing increasing quantities of numerical silt on top to establish graded sediment beds. All numerical sediment samples were tested for erosion resistance and bed stability with respect to predefined boundary inflow velocities. The results showed that with increasing layer thickness, inflow into the sediment bed decreased, causing a decrease in erosion potential in the deeper parts of the bed. Measurements in the layering showed lower transport rates in the deeper parts of the bed compared to those at the sediment surface. Porosity measurements in the beds showed that with an increase in layer thickness, compaction was also increased. Therefore, we conclude that a layer of fine particles can cause an inflow blockage into the sediment bed, thereby increasing the sediment stability. Furthermore, the effect of texture induced caging structures caused structural compaction towards deeper parts of the layer and a complete blockage of the flow, which protected the underneath lying coarser fractions and increased the stability of the bed under higher flow regimes.

There are, however, some limitations to this study, such as the difficulty in generating larger sediment beds or multiple grain spectra, due to an extreme calculation effort, e.g. an exponential increase in calculation time even on faster supercomputers. Regardless, this new approach allowed for the development of an improved conceptual model through the testing of a general hypothesis. Flowing the analogue history, future research will focus on multiple particle spectra and density compositions, as well as the implementation of cohesive clay aggregates e.g., through the stacking of elongated particles to quantify cohesion related bed stability processes (Kock and Huhn, 2007). Further, a validation of the armouring effect is planned. It is anticipated that that these added model features will assist in improved quantification of internal threshold conditions, further explain internal grain entrainment, and allow for the development of sediment bed forms within the continuum. In order to increase the complexity of our models, we are also aiming to implement more complex flow conditions and also a larger amount of particles in the numerical sediments beds. Therefore we will use faster supercomputers.

4.6 Acknowledgments

This work has been funded through the DFG-International Research Training Group INTERCOAST.

We thank Lina Podszun, Jannis Kuhlmann, Bryna Flaim, Melanie Schäfer, Linda Wenk, Firoz Badesab, and the INTERCOAST research student Leonard Rossmann for discussion and comments on the manuscript.

4.7 References

Allen, J.R.L., 1970. Physical processes of sedimentation. Unwin University Books, London, 248 pp.
Black, K. and Paterson, D.M., 1997. Measurement of the erosion potential of cohesive marine sediment: A review of current in situ technology. J. Mar Environ. Eng, 4: 43-83.
Coleman, S., E. and Eling, B., 2000. Sand wavelets in laminar open-channel flows. Journal of Hydraulic research, 38: 331-338.
Cundall, P.A. and Hart, R.D., 1989. Numerical modeling of discontinua. In Keynote address in Proceedings of the 1st US conference on discrete element methods Golden Colorado, p.^pp. 1–17.
Cundall, P.A. and Strack, O.D.L., 1979. A discrete numerical model for granular assemblies. Geotechniqe, 29(1): 47-65.
Cundall, P.A. and Strack, O.D.L., 1983. Modeling of microscopicmechanisms in granularmaterial. Proceedings of the US-Japan Seminar on New Models and Constitutive Relations in The Mechanics of Granular Materials: 137-149.
Cunningham, E., 1910. On the velocity of steady fall of spherical particles through fluid medium. Proceedings of the Royal Society of London, Series A, Containing Papers of a Mathematical and Physical Character, 83(563): 357-365.
Eisbacher, G.H., 1996. Einführung in die tektonik. Spektrum Akademischer Verlag; Thieme; Enke, Stuttgart, 374 pp.
Harris, J. and Stöcker, H., 1998. Handbook of mathematics and computational science. Springer, New York, 1028 pp.
Hir, P.L., Cann, P., Waeles, B., Jestin, H. and Bassoullet, P., 2008. Chapter 11 erodibility of natural sediments: Experiments on sand/mud mixtures from laboratory and field erosion tests. In: H.Y.J.S. Tetsuya Kusuda and Z.G. Joseph (Editors), Proceedings in marine science. Elsevier, pp. 137-153.
Itasca, 2004a. Pfc 3d 3.1 manual. Itasca Consulting Group, Inc., Minneapolis.
Itasca, 2004b. Flac 3d 3.1 manual. Itasca Consulting Group, Inc., Minneapolis.
Kock, I. and Huhn, K., 2007. Influence of particle shape on the frictional strength of sediments — a numerical case study. Sedimentary Geology, 196(1–4): 217-233.
Komar, P.D., 2007. Chapter 1 the entrainment, transport and sorting of heavy minerals by waves and currents. In: A.M. Maria and T.W. David (Editors), Developments in sedimentology. Elsevier, pp. 3-48.
Leeder, M.R., 1999 Sedimentology and sedimentary basins: From turbulence to tectonics 1. Blackwell Science, Oxford, 608 pp.
Mitchener, H. and Torfs, H., 1996. Erosion of mud/sand mixtures. Coastal Engineering, 29(1-2): 1-25.
Panagiotopoulos, I., Voulgaris, G. and Collins, M.B., 1997. The influence of clay on the threshold of movement of fine sandy beds. Coastal Engineering, 32(1): 19-43.
Rijn, L.C.v., 2007. Unified view of sediment transport by currents and waves. I: Initiation of motion, bed roughness, and bed-load transport. Journal of hydraulic engineering, 133(6): 649-667.
Schlichting, H. and Klaus, G., 2004. Boundary-layer theory. Springer, Berlin-Heidelberg, 811 pp.
Shields, A., 1936. Anwendung der ähnlichkeitsmechanik und der turbulenz- forschung auf die geschiebebewegung. Mitteilungen der Preußischen Versuchsanstalt für Wasserbau und Schiffbau, NW 87.
Soulsby, R., 1997. Dynamics of marine sands. A manual for practical applications. Thomas Telford Publishing, London.
Sutherland, A., 1987. Static armour layers by selective erosion. In: C.R. Thorne, Bathurst, J.C., and Hey, R.D. (Editor), Sediment transport in gravel-bed rivers. Wiley, London, pp. 141-169.
Torfs, H., 1997. Erosion of mixed cohesive/non cohesive sediments in uniform flow. Cohesive Sediments: 245-252.
Torfs, H., Jiang, J. and Mehta, A.J., 2000. Assessment of the erodibility of fine/coarse sediment mixtures. In: H.M. William and J.M. Ashish (Editors), Proceedings in marine science. Elsevier, pp. 109-123.
Tucker, M.E., 1981. Sedimentary petrology. Geoscience texts, 3. Blackwell Scientific Publications, Oxford, 252 pp.
van Ledden, M., van Kesteren, W.G.M. and Winterwerp, J.C., 2004. A conceptual framework for the erosion behaviour of sand-mud mixtures. Continental Shelf Research, 24(1): 1-11.
Whitehouse, R., Soulsby, R., Roberts, W. and Mitchener, H., 2000. Dynamics of estuarine muds. A manual for practical applications. Thomas Telford Publishing, London, 210 pp.
Wiberg, P.L. and Smith, J.D., 1987. Calculations of the critical shear stress for motion of uniform and heterogenious sediments. Water Resources Research, 23(8): 1471-1480.
Wright, J., Colling, A. and Park, D., 1999. Waves, tides and shallow-water processes. Butterworth Heinemann, Oxford.

Table 4.1: Properties and configurations of the numerical experiments.

Sediment Matrix Model	Experiment - S	Experiment - M	Experiment - L	Experiment - XL
Length [mm]	1.8	1.8	1.8	1.8
Width [mm]	1.8	1.8	1.8	1.8
Height [mm]	2.4	2.4	2.4	2.4
Height of Sediment bed [mm]	1.21	1.54	1.74	1.94
Particle number: silt	463	1740	2597	3472
Particle number: sand	18	18	18	18
Particle Properties				
Normal stiffness [N/m]	$1x10^8$	$1x10^8$	$1x10^8$	$1x10^8$
Shear stiffness [N/m]	$1x10^8$	$1x10^8$	$1x10^8$	$1x10^8$
Density ρ [kg/m³]	2650	2650	2650	2650
Diameter [µm]: sand	600	600	600	600
Diameter [µm]: silt	80	80	80	80
Particle friction $\mu(P)$	0.5	0.5	0.5	0.5

Fluid Model	Experiment - S	Experiment - M	Experiment - L	Experiment - XL
Length [mm]	1.8	1.8	1.8	1.8
Width [mm]	1.8	1.8	1.8	1.8
Height [mm]	2.4	2.4	2.4	2.4
Height of the water column [mm]	1.21 - 2.4	1.54 - 2.4	1.74 - 2.4	1.94 - 2.4
Boundary inflow velocity U [cm/s]	10, 15, 20, 25 and 30			
Fluid Properties				
Density ρ_f [kg/m³]	1000	1000	1000	1000
Pore pressure ψ [mbar]	250	250	250	250
Saturation φ [%]	100	100	100	100

Table 4.2: Flow velocities.

Boundary inflow velocity U [cm/s]	Surface velocity u_* [cm/s]	Velocity in silt layer [cm/s]	Velocity in sand bed [cm/s]
Experiment - S			
10	8.3	7.5	2.1
15	12.3	10.4	2.5
20	15.9	14.8	4.2
25	19.5	18.4	4.9
30	24.5	21.2	5.4
Experiment - M			
10	7.6	7.2	1
15	11.5	9.5	2.2
20	15.5	12.4	2.6
25	19.2	15.8	3.4
30	23.6	18.4	4
Experiment - L			
10	5.2	4.8	0.8
15	12.1	7.2	2.1
20	14.8	9.8	2.2
25	17.3	12.4	2.4
30	20	14.2	3.3
Experiment - XL			
10	7.4	4.2	1.1
15	11.4	5.8	1.8
20	14.8	7	2.1
25	17.6	10.1	2.2
30	22.2	12.2	2.5

Table 4.3: Transport rates.

Boundary inflow velocity velocity U [cm/s]	**Experiment - S** [%]	**Experiment - M** [%]		**Experiment - L** [%]		**Experiment - XL** [%]	
	top	**top**	**base**	**top**	**base**	**top**	**base**
10	67.93	69.95	7.58	67	2.46	68.93	0.25
15	76.66	82.76	17.6	84.5	12.98	87.01	2.47
20	85.4	89.11	26.65	89	16.5	91.53	5.19
25	86.5	92.57	33	91	17.49	94.92	9.38
30	89.78	94.06	34.56	92.5	24.63	96.02	14.07

Table 4.4: Porosity measurements extracted at a U = 20 cm/s boundary inflow velocity.

Modeliteration steps	**Experiment - S** [%]	**Experiment - M** [%]		**Experiment - L** [%]		**Experiment - XL** [%]	
	top	**top**	**base**	**top**	**base**	**top**	**base**
1	53.0	67.3	51.9	67.8	52.0	69.1	52.0
2	52.8	67.2	51.8	67.5	52.0	68.9	52.0
3	52.6	66.8	51.8	67.2	51.9	68.5	51.9
4	52.5	66.2	51.5	66.6	51.9	68.1	51.9
5	52.5	65.7	51.5	66.0	51.7	67.9	51.9
6	52.1	65.2	51.4	65.1	51.6	67.6	51.8
7	51.5	64.6	51.3	64.2	51.6	66.9	51.7
8	51.4	63.9	50.9	63.3	51.4	65.6	51.7
9	51.2	63.6	50.8	62.7	51.2	64.7	51.7
10	51.4	62.9	50.5	62.2	51.0	64.2	51.3
11	51.2	62.8	50.4	61.9	50.9	63.4	51.1
12	51.3	62.3	50.4	61.7	50.8	63.1	51.0
13	51.3	62.0	50.2	61.1	50.6	62.5	50.9
14	51.5	61.3	50.0	60.8	50.5	62.5	50.9
15	51.8	60.7	50.0	60.3	50.2	62.7	50.7
16	52.0	60.2	50.2	59.3	50.0	62.5	50.7
17	52.2	59.7	49.9	59.1	49.9	61.4	50.6
18	52.2	59.4	49.8	58.4	50.1	61.0	50.5
19	52.2	59.1	49.6	57.6	50.0	60.4	50.3
20	51.8	58.6	49.3	57.7	50.1	60.1	50.1
21	51.3	58.3	49.2	57.4	49.7	59.2	50.2
22	51.5	58.2	49.0	56.8	49.3	58.8	50.2
23	51.4	58.0	48.9	56.9	49.2	58.4	50.4
24	51.6	58.2	48.7	56.7	49.2	58.5	50.1
25	51.4	57.5	48.6	56.1	48.8	58.1	50.1
26	51.8	57.3	48.2	55.7	48.6	57.7	49.8
27	52.1	57.1	48.1	55.7	48.6	57.0	49.7
28	52.0	56.7	48.0	55.4	48.5	56.9	49.6
29	52.2	56.5	48.1	54.9	48.4	56.5	49.4
30	52.3	56.3	48.0	54.7	47.9	56.4	49.4
31	52.0	55.4	48.0	54.5	47.8	56.0	49.0
32	52.2	55.3	47.8	54.3	47.6	55.6	48.9
33	52.3	54.5	47.9	54.2	47.5	54.9	48.7
34	52.5	54.1	48.0	54.0	47.5	54.5	48.5
35	52.2	53.6	47.7	53.8	47.4	53.8	48.4
36	52.2	52.9	47.6	53.8	47.4	53.2	48.5
37	52.3	52.4	47.4	53.8	47.2	52.7	48.4
38	51.9	51.7	47.2	53.5	47.2	52.6	48.3
39	52.0	51.5	47.1	52.8	47.2	52.3	48.2
40	52.3	51.0	47.1	52.4	47.1	52.2	48.1

Chapter V

HOW IS MIXED SEDIMENT PROTECTED FROM EROSION? USING A NUMERICAL APPROACH

Gerhard Bartzke and Katrin Huhn

MARUM – Center for Marine Environmental Sciences, University of Bremen, Leobener Straße, D-28359 Bremen, Germany

Abstract

Within aquatic environments, an increase of the erosion behavior of sediment towards higher threshold conditions and hence sediment bed stabilization is controlled by: (1) biostabilization, (2) cohesion and (3) texture induced structures. However, the understanding of the processes influencing (3) texture induced bed stabilization, whereby fine particles prevent erosion by encompassing coarser grains like a cage, is limited. This conceptual model was postulated based on analogue flume tank experiments in combination with theoretical assumptions. Due to technical restrictions e.g. limited resolution of these laboratory techniques, it is not possible to directly quantify the physical processes acting during bed stabilization at the sediment-water interface and in the interior of sediment beds. Consequently, numerical simulations are required to gain a deeper insight into the effect of texture related caging structures and to validate of previous conceptual models.

We developed a high resolution, 3D numerical 'flume tank' model adopting the general settings of analogue experiments. Therein, a Finite Difference Model (FDM) was coupled with a Distinct Element Model (DEM). The major aim was to investigate the physical processes occurring during the initiation of motion at the surface of mixed sediment beds under different boundary inflow velocities. Four suites of experiments were designed, whereby numerical fine 'silty' particles were mixed with increasing amounts into of a coarse 'sand' matrix to simulate mixed 'sediment beds' (starting with a pure sand bed Experiment 1 = 0, Experiment 2 = 500, Experiment 3 = 800 to a fully saturated sand silt bed Experiment 4 = 2182 particles). All numerical 'sediment beds' were tested for their erosion behavior at predefined boundary inflow velocities (U = 10, 15, 20, 25 and 30 cm/s). We measured the inflow behavior, transport rates, and porosity differences during fluid streaming. The experiments showed that with increasing the fine fraction textural caging structures developed between sand pores. This caused a blocked inflow into the sediment bed, and hence, protected the sediment bed from erosion, and ultimately, reduced the flow available to entrain particles located in the deeper parts of a bed.

Keywords: sediment stability, inflow blocking, mixed sediments; textural caging; DEM; FDM;

5.1 Introduction

Sediment transport within aquatic environments is the process whereby sediment particles are transported essentially horizontally from one place to another with an independent fluid (Allen, 1970). Some classical studies of e.g. Shields (1936), Hjulstroem (1939) or Bagnold (1941) fundamentally influenced the modern understanding of the interaction between fluids and sediment particles. Additionally, numerous studies within aquatic environments have shown that the threshold beyond which particles move is reached when the instantaneous fluid force (F_F) is larger than the resistant force (F_R) of the grain, which is related to the ratio of the particle weight (F_G), the particle angle of repose (φ), the lift force (F_L), and the drag force (F_D) (e.g., (Allen, 1970; Rijn, 2007; Soulsby, 1997)). According to this relationship, to understand the processes that cause this initiation of sediment transport, and to identify specific critical threshold values, researchers have commonly focused on the transport behavior of homogeneous sediment beds of the same grain size class under differing flow conditions. This approach has been undertaken in various studies using analogue techniques (e.g., (Shields, 1936; Soulsby, 1997; Whitehouse et al., 2000) such as laboratory flume studies (e.g., (Black and Paterson, 1997) or *in situ* field studies (Soulsby, 1997)). However, studies testing e.g. mixed sediment bed compositions (Torfs, 1997; Tucker, 1981) revealed that additional parameters that modify the erosion characteristics of mixed sediment beds shift the theoretical initial sediment threshold towards higher regimes, thus causing sediment bed stabilization (Whitehouse et al., 2000).

Today, it is widely accepted that the erosion resistance of a sediment bed is controlled by biostabilization (Whitehouse et al., 2000), cohesion (Sutherland, 1987), and textural induced caging structures (van Ledden et al., (2004) and Hir et al., (2008)). In particular, the entrainment characteristics of mixed sediment beds can be altered by texture induced caging structures, which develop when fine particles are mixed into a coarse matrix, whereby the fine particles encompass coarse grains as a cage (Whitehouse et al., 2000). This phenomenon has been shown in various studies, e.g. Whitehouse (2000), Torfs (1997), van Ledden et al., (2004) and Hir et al., (2008) on mud (i.e., cohesive clay and sand) using laboratory based analog flume studies. Mitchener and Torfs (1996) observed a similar effect when fine clays are mixed into a sand bed. They concluded that the generation of a cage-like network encompassing the sand grains increases the density of the matrix and the additional cohesive forces bind the clay particles and raise the erosion resistance. This was also observed in various experiments, e.g. Panagiotopoulos et al., (1997), Wiberg and Smith (1987), and Torfs et al. (2000), which showed that sediment stability is increased by clay in-filled pockets within the sand bed. These observations support the conceptual model by Panagiotopoulos et al., (1997) that bed stabilization occurs when clay particles are mixed into sand causing the fine clay fraction to surround the coarser sand grains.

In the past, this textural caging effect has been mainly investigated in the context of clay-sand mixtures. The effect would therefore also be expected with other fine fractions, e.g. silt, which are very common in many sandy coastal environments. However, until now this has not been considered. Accordingly, extensive analogue flume experiments could be undertaken to examine the effect with silt, similar to previous works, but specific quantification of the textural effects on the grain scale level at sediment-fluid interface can not be extracted from such laboratory studies. The spatial and temporal evolution of caging structures in mixed sand and silt beds cannot be examined due to spatial restrictions and limitations of the sensors of traditional analogue flume techniques. Hence, there is a need for validation of caging effects in mixed silt-sand beds using other techniques that allow the investigation of textural related physical processes.

Numerical models are tools that can satisfy this need. Most of the numerical approaches are excellent tools for a simulation of the hydrodynamic drivers and subsequent sediment transport (e.g. Delft 3D, WL Delft Hydraulics). However, most of these models are limited in their ability to quantify textural effects and inflow processes within the sediment bed. As there is need to focus on textural changes in sediment beds and their influence on sediment stabilization, we developed a new modeling approach that allows for the simulation of the initiation of motion in mixed sediment beds under different flow conditions.

Two independent numerical simulation techniques were coupled, (1) the Finite Difference Method (FDM) and (2) the Distinct Element Method (DEM) for simulation of sediment transport processes in aquatic environments. The major aim was to study the evolution of caging structures in mixed sediment beds and their influence on sediment stability. The FDM model simulates the inflow conditions and velocities and, simultaneously, the DEM model simulates the numerical ‘sediment’ bed. This 3D model parameterized general settings of laboratory flume tanks. In order to quantify the effect of a mixed sediment bed on the erosion behavior and bed stabilization, four suites of experiments were designed.

A coarse ‘sand’ bed was generated and mixed with fine ‘silt’ particles. The number of silt particles was varied in the experiments by mixing increasing amounts of smaller numerical ‘silt’ particles into the coarse sand matrix, starting with a pure sand bed (Experiment 1 = 0 silt particles) to a fully saturated sand silt bed (Experiment 2 = 500 silt particles, Experiment 3 = 800 silt particles and Experiment 4 = 2182 silt particles). For the quantification of bed stabilization by textural caging, fluid profiles, transport distances and porosity variations were extracted from the models at the sediment surface and in the deeper parts of the bed. All beds were tested under predefined, constant boundary inflow velocities using values of U = 10 cm/s, 15 cm/s, 20 cm/s, 25 cm/s, and 30 cm/s. These flow velocities, as well as ‘sediment’ configurations, were chosen to mimic the environment of tidal sand flats (Allen, 1970).

Analyses of these experiments indicated, that texture induced bed stabilization is influencing the inflow characteristics into a mixed sediment bed and subsequently reduces the inflow properties (i.e. the shear stress in the interior of the sediment beds) with increasing fine amounts and the increase of packing density. This confirmed the theoretical assumptions developed based on previous flume tank experiments and in-situ measurements. In addition, our experiments provide further information that the 'silt' cages block the inflow into the deeper horizons of the bed through pore space plugging. This process influences the inflow characteristics and, subsequently, reduces the shear stress conditions with increasing fine content, thus, increasing the bed stability. It was also found that these processes also contributed to increases in the particle packing density of the bed. Consequently, we postulate that textural caging effects could be another major player in mixed sediment beds that can shift the initial sediment threshold towards higher regimens. In this way, smaller fractions fill the pore spaces between the larger particles, and protect the coarse fraction by blocking the inflow into the sediment preventing the bed from re-erosion. The resultant higher bed stability suggests that higher flow velocities would be required to erode the deeper, coarser horizons.

This new model approach provides a deeper insight in to the mechanics and physical processes that occur during bed failure evolution on a grain scaled level.

5.2 Methods

A high resolution 3D numerical flume tank was developed for the quantification of the physical processes at the surface of mixed sediment beds in aquatic environments. In order to simulate sediment transport by a moving fluid, we combined two independent numerical simulation techniques: the Finite Difference Method (FDM) and the Distinct Element Method (DEM). Therein, the FDM model calculates the flow conditions (Fluid model, Figure 5.1) and the DEM model simulates the 'sediment' matrix (Sediment matrix model, Figure 5.1). Both models were coupled via an Input Output routine, which will be described in section 5.2.1.

The 3D FDM Fluid model was generated using the commercial software FLAC 3D (Fast Ligurian Analysis of Continua; (Itasca, 2004b). This technique is based on the spatial discretization of the study domain into a grid of a finite number of three dimensional rectangular polyhedral elements (Figure 5.1 (Itasca, 2004b)). The software allows the assignment of physical material properties (i.e. fluid parameters) to each cell in the grid (e.g. fluid density and viscosity) in order to mimic natural conditions. In addition, boundary conditions (e.g. boundary inflow velocities and fluid sources) were designated to the model. Consequently, the FDM model calculates flow velocities in each grid cell based on the applied boundary conditions and approximations of the differential flow equations through numerical differentiation at defined time steps (Itasca, 2004b).

At the same time, a DEM model was used to mimic ‘sediment beds’ numerically. These were simulated as a particle assembly consisting of multiple, ideal and spherical particles (i.e. numerical ‘silt’ and ‘sand’ grains (Figure 5.1)). The software, (PFC 3D, (Particle Flow Code; (Itasca, 2004a)), is based on the DEM theory by Cundall and Strack (1979), which describes the mechanical behavior of particle assemblages based on physical contact laws. In order to mimic natural conditions, physical properties such as density, friction and hardness were assigned to each particle (Table 5.1). Similar to FDM, boundary conditions must be designated (e.g. gravity and ball acceleration). The resultant particle assemblages, or the ‘sediment body’, respectively, are deformable by these applied forces. Consequently, DEM allows the simulation of sediment particles, sediment particle interactions, internal structures, and also porosities. Thus, the method simulates the physical behavior of the particle assemblages during deformation processes, such as the initiation of motion of single spherical grains driven by defined boundary conditions (e.g. fluid forcing (Figure 5.1)).

A more detailed review of the involved algorithms of the FDM and DEM exceeds the scope of this paper. A complete description of the numerical procedure of the FDM code can be found e.g., in Itasca (2004a). Further descriptions of the numerical DEM code can be found in e.g., Cundall and Hart (1989), Cundall and Strack (1979, 1983), Itasca (Itasca, 2004a), and Kock and Huhn (2007).

Please note that hereafter, the term ‘grains’, as well as ‘sediment’ will be used, regardless of whether the context is related to numerical or real grains. The same applies to sand and silt, respectively.

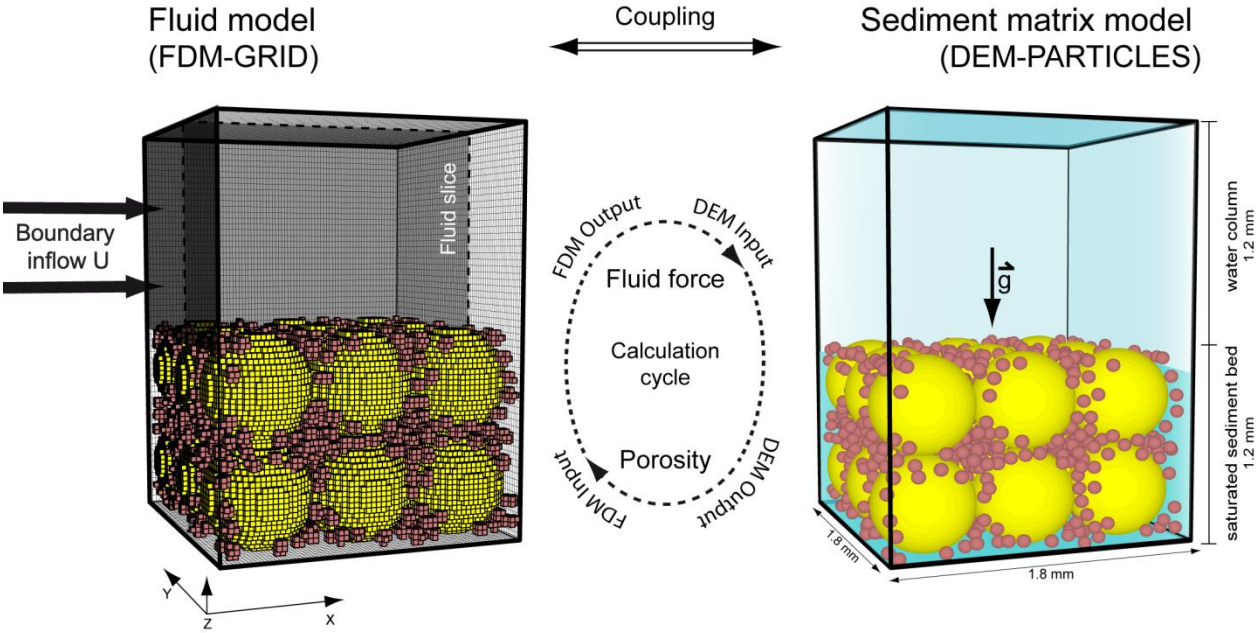

Figure 5.1: Sketch of the coupled Sediment matrix model (DEM - discrete elements method) and the Fluid model (FDM - finite difference method). In the Fluid model the location of the vertical cross section (Fluid slice) is shown which is presented in Figure 5.3 and 5.4.

5.2.1 Model configuration

Mixed numeric sediment beds were generated in order to quantify the influence of fine particles mixed into a coarse matrix with respect to erosion behavior, inflow properties, and bed stability. In the following, all sediment beds were exposed to a range of boundary inflow velocities.

For simulation of fluid motion and particle transport with the 3D numerical flume tank, both the DEM and the FDM models had identical dimensions (1.8 x 1.8 x 2.4 mm), geometries, material properties as well as boundary conditions (Figure 5.1).

At the beginning of the simulation, the grain or sediment model was generated in order to mimic an isolated section of a sediment surface in a flume tank on the grain-scale level. In order to mimic this sediment bed numerically, a sample box was generated with the dimensions of 1.8 mm x 1.8 mm, and 1.2 mm in height, which was filled with the numerical sediment. Therein, five stiff un-deformable box walls were created (Table 5.1).

For the generation of the mixed sediment beds, two end members were used as a simplified treatment of fine grains (i.e., numerical silt (D_{50} = 0.08 mm)) and coarse particles (i.e., numerical sand (D_{50} = 0.6mm)). Initially, numeric sediment beds were generated of a coarse-grained sand fraction with a constant height (1.2 mm, Figure 5.2). The coarse fraction was composed of 18 spherical sand particles deposited in a cubic assembly under applied gravity, always filling half of the box (Figure 5.1and 5.2). This geometry having the largest pore volume compared to that of a randomly packed bed was chosen as the aim was to investigate processes that occur in the pore-space between the sand particles. All sand particles were fixed to ensure open pockets enabling quantification of the erosion behavior of the mixed bed in more detail. Physical properties (density, friction, normal stiffness, and shear stiffness (Table 5.1)) were assigned to each particle to mimic the natural properties of coastal sands.

In the next step, finer silt was mixed into the coarse sand matrix. The number of silt particles was varied in the experiments by mixing increasing amounts of smaller silt grains into the coarse sand matrix (Experiment 2 = 500, Experiment 3 = 800, and Experiment 4 = 2182). In each experiment the grains were randomly distributed across the entire box. Physical properties were also assigned to each silt particle with respect to natural conditions (Table 5.1). Additionally, in order to ensure statistically significant results one pure sand experiment (Experiment 1 = 0) without any silt was generated.

For the simulation of a flow field, the Fluid model was generated by using the FDM model (Figure 5.1). The spatial extensions of this Fluid model were assigned identical dimensions to the Sediment matrix model. In order to simulate flow fields in highest resolution, the FDM grid was discretized into 288,000 elements (60x60x80 in X, Y and Z directions) with a uniform axes length of 0.03 mm (Figure 5.1). Hence, the smallest DEM grains were represented by at least 6 elements to ensure stable coupling between FDM

– DEM model (see below). The corresponding fluid properties were applied to the Fluid model (Table 5.1) to simulate natural coastal conditions based on the literature (Allen, 1970; Eisbacher, 1996) and to exclude any scalar discrepancies. The entire box model was flooded to generate a fully saturated sediment bed.

Coupling of both models was undertaken after generation of the above described initial model configurations. In the first step, all information from the sediment matrix, such as the spatial parameters x, y, and z coordinates and the radii of all particles, were sent from the DEM to the FDM model. Based on these data representing the grain distribution within the DEM model, the FDM grid elements are defined as either fluid cells or sediment cells. The resulting FDM model grid consists of elements where fluid streaming was allowed (fluid zones) or not allowed (solid matrix zones).

After the grid was classified, a constant boundary inflow above the fully saturated bed field was applied in X-direction at the left box wall and outflow boundary condition at the right box wall (Figure 5.1). Starting with these initial stable conditions, a constant stream in the positive X-direction above the sediment bed evolved. All flow velocities were calculated from cell to cell throughout the whole model (in the water column and the saturated matrix area) based on the initial porosity distribution. After the flow field reached stable conditions, all flow velocities were extracted. These flow velocities were transformed into forces according to the Stokes velocity law (Miller et al., 1977). These fluid forces were sent to the sediment matrix model at their corresponding X,-Y, and Z coordinates and applied to their positioned particles. The velocity parameters then served as boundary conditions for the Sediment matrix model. Based on this forcing, new particle contact forces and the resulting particle displacements were calculated in the DEM model. If the added fluid forces were larger than the resisting force of the particles, the particle contacts broke up and the grains were transported (Cundall and Strack, 1979). This caused new porosities within the DEM model and new particle configurations, respectively. Hence, sediment transport and / or grain re-assembly was initiated. In the cases of grains that were eroded from the matrix, they were transported by the stream. The resultant new porosities (Sediment matrix model) were sent back to the Fluid model and, subsequently, a re-meshing of the FDM model grid was initiated starting a new calculation cycle.

The calculation cycle between both models was repeated until constant flow and transport conditions were reached. For consistency, each model was coupled 40 times to ensure that the results were statistically stable and analyzable. Hence, high resolution information about, e.g., particle distribution, porosity, texture, and fluid velocities at the sediment surface as well as in the interior of the sediment matrix was available in space and time.

The applied boundary inflow velocities were increased stepwise from U = 10 cm/s, in 5 cm/s increments to 30 cm/s to mimic the environment of tidal sand flats (Allen, 1970).

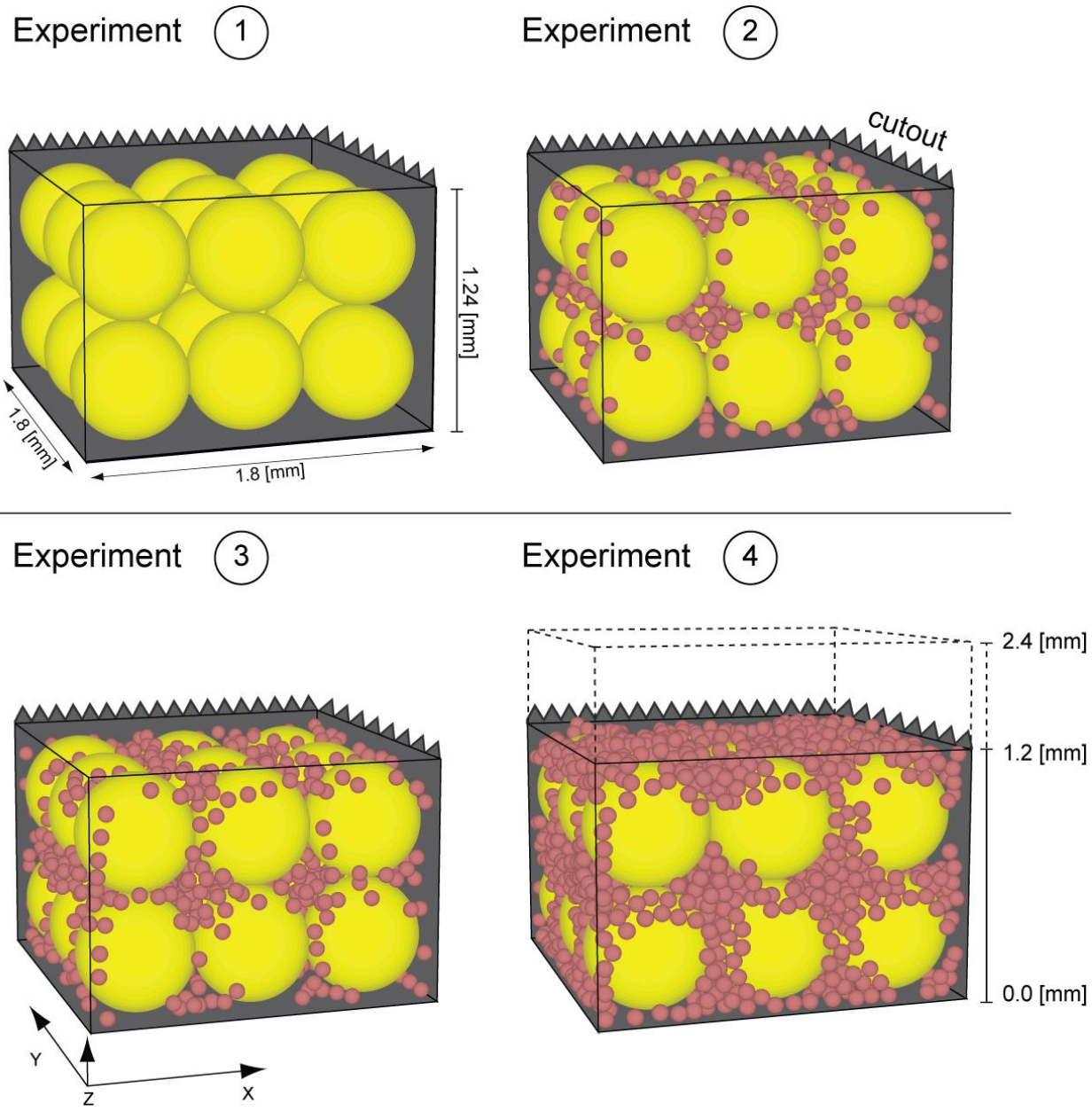

Figure 5.2: Schematic sketch of the four suits of experiments cutting out the sediment matrixes out of the DEM models 1 - 4. Silt (brown particles) has been mixed into a sand bed (yellow particles). The number of silt particles was increased incrementally ranging from: Experiment 1) 0 silt particles, Experiment 2) 500 silt particles, Experiment 3) 800 silt particles, to Experiment 4) 2185 silt particles.

5.2.2 Measurements and data statistics

To quantify the influence of mixed sediment beds on the erosion behavior, we analyzed variations in fluid velocities, particle positions, and particle displacement at each time step. All data was processed using programmed routines in FLAC 3D, PFC 3D, and Matlab 2011 environments. These analyses revealed high resolution data of velocities in the flow field, transport distances and porosity changes in the sediment bed.

5.2.2.1 Fluid profiles

Vertical slices in the X-Z direction were extracted from the Fluid model, after reaching steady state flow conditions, to monitor the velocities in the water column as well as the velocity differences at the sediment-water interface and within the sediment bed. This section intersected the entire box at the location Y = 0.006 mm (Figure 5.1and 5.3). An example is shown for Experiment 3, in Figure 5.3A and B. This data allows for a monitoring of along stream variations through the whole Fluid model. Due to the large amount of data (288,000 velocities at 4e10 times steps and 40 model runs per each experimental setting), single 2D vertical fluid profiles were extracted that allowed for a direct comparison of the four Experiments (1 – 4) at different boundary inflow velocities and a better visualization of our modeling results. These fluid profiles were processed at four positions. Exemplarily locations were chosen to intersect the pore space between the sand particles as we were aiming to extract as much flow data as possible along the vertical cross sections (Figure 5.4). In the cases where the velocity profile intersected a particle (i.e. cell with no flow data), the velocity profile was interpolated using a cubic spline function (Mathworks, 2011). Therein, a linear regression analysis was undertaken. Following extraction, a complete velocity profile was obtained including the water column and the complete height of the fully saturated sediment bed. This profile was based on the results of 40 model iteration steps ensuring statistically significant results.

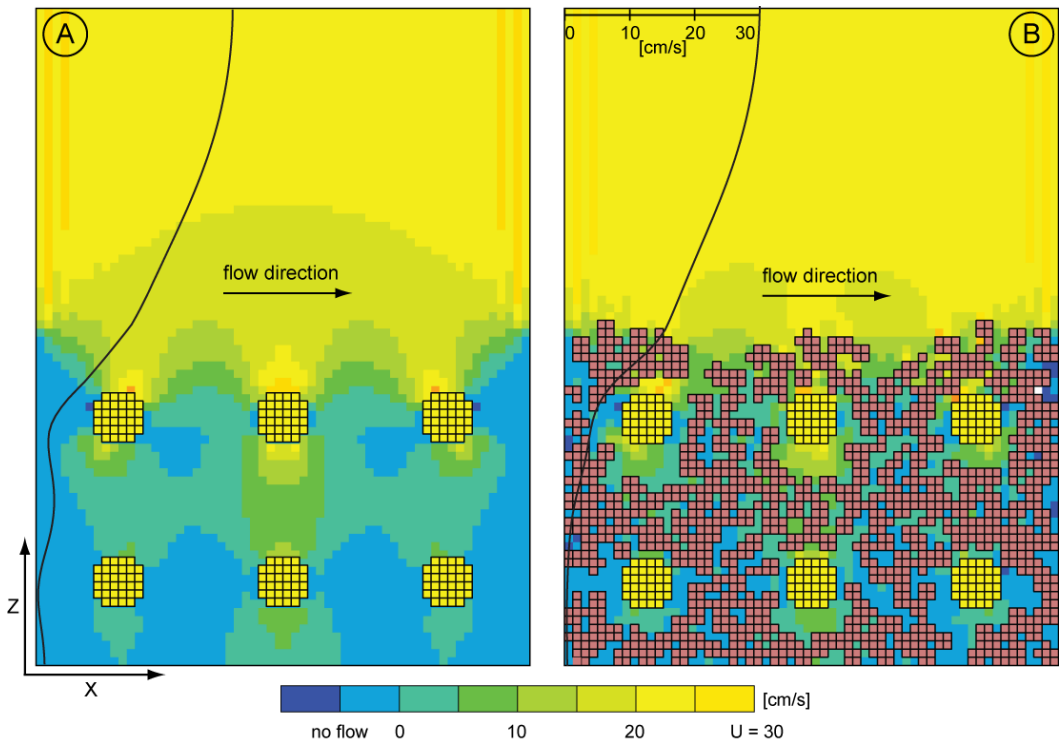

Figure 5.3: A) and B) represent flow velocities along vertical slices through the Fluid model from Experiment – 1 and Experiment 4 at a U = 30 cm/s boundary inflow velocity after reaching steady state conditions. The locations of these vertical slices are shown in Figure 5.1 in the FDM grid X-Z slice at Y = 0.6mm. Silt and sand zones have been colored to brown and yellow, respectively (porosity = zero, no flow). A single vertical fluid profile measured at the position of X = 0.6 mm and Y = 0.6 mm is shown as example of the profiles plotted in Figure 5.4.

5.2.2.2 Transport distances and porosities

Due to large data volumes, as with the fluid profiles (e.g., 2,182 particle positions at 4e10 calculation steps at 5 predefined boundary inflow velocities and 40 model runs), the total transport distance of singles grains was calculated within each Sediment matrix model as the difference between the initial and the final position after reaching steady state flow conditions. For further analyses, only particles transported a distance exceeding their own radius, were considered. This criterion represented the assumed threshold for particle transport in all experiments. Particle transport and porosity changes were extracted from a horizontal volume at interior of the sediment bed (0.45 mm $\leq z \leq$ 0.65 mm; Base Slice in Figure 5.5). A similar procedure was undertaken for the uppermost sediment portion (1.1 mm $\leq z \leq$ top of sediment bed; Top Slice in Figure 5.5). To make these data comparable between the Experiments (1 – 4), which contain differing quantities of silt particles, the ratio of transported particles was calculated.

The porosities (Φ) were also quantified in the two analytical sections (Top Slice and Bottom Slice in Figure 5.5). In each slice, the porosity was calculated by determining the ratio between the total particle volumes (V_T) and the bulk volume of the void space (V_V). In the cases of particles bisected by the designated boundary of the analytical sections grains, lying outside this given area, was subtracted using a spherical cap formulation (Harris and Stöcker, 1998). Consequently, the volume of the remaining hemispheres was considered in the total particle volume calculation (V_T). In order to present fluctuations in the porosity measurements in the mixed compositions the larger sand grains were not considered in our porosity calculations which would decrease the offset to 20 %. The data presented represents a statistically significant average from 40 model runs of each experimental setting.

5.3 Results

In order to quantify the erosion behavior of a fine fraction mixed into a coarse matrix four numerical experiments were undertaken (Figure 5.2). The silt content was increased incrementally (Experiment 1, 2, 3 and 4) and tested under the predefined boundary inflow velocities (U = 10, 15, 20, 25, and 30 cm/s). Fluid profiles, transport distances, as well as porosities were extracted and analyzed as explained above.

5.3.1 Flow properties and fluid profiles

All experiments showed a constant flow pattern above the sediment surface in the X – direction at all tested boundary inflow velocities, which indicates uniform flows over the beds (Figure 5.3 and 5.4). In addition, all experiments showed that in the vicinity of the sediment bed a layer evolved where flow velocities decreased logarithmically towards the sediment - water interface. For example, the vertical velocity profile of the Experiment 2 (extracted at U = 30 cm/s boundary inflow velocity) showed a decline from 30 cm/s boundary inflow velocity to 17 cm/s towards the lowermost 1.25 mm above the bed (Figure 5.4 and Table 5.2). Furthermore, a significant decrease in the flow velocities occurred just below the

sediment surface in the uppermost part of the sediment beds in all experiments. However, the magnitudes of the velocities in the sediment bed increased to a lesser extent compared to flow velocities measured in the water column (Table 5.2). Additionally, it was observed in all experiments that the flow velocities measured in the sediment beds increased when the boundary inflow velocities increased.

This general vertical fluid profile was modified by applied boundary inflow velocities and number of silt particles mixed into the bed.

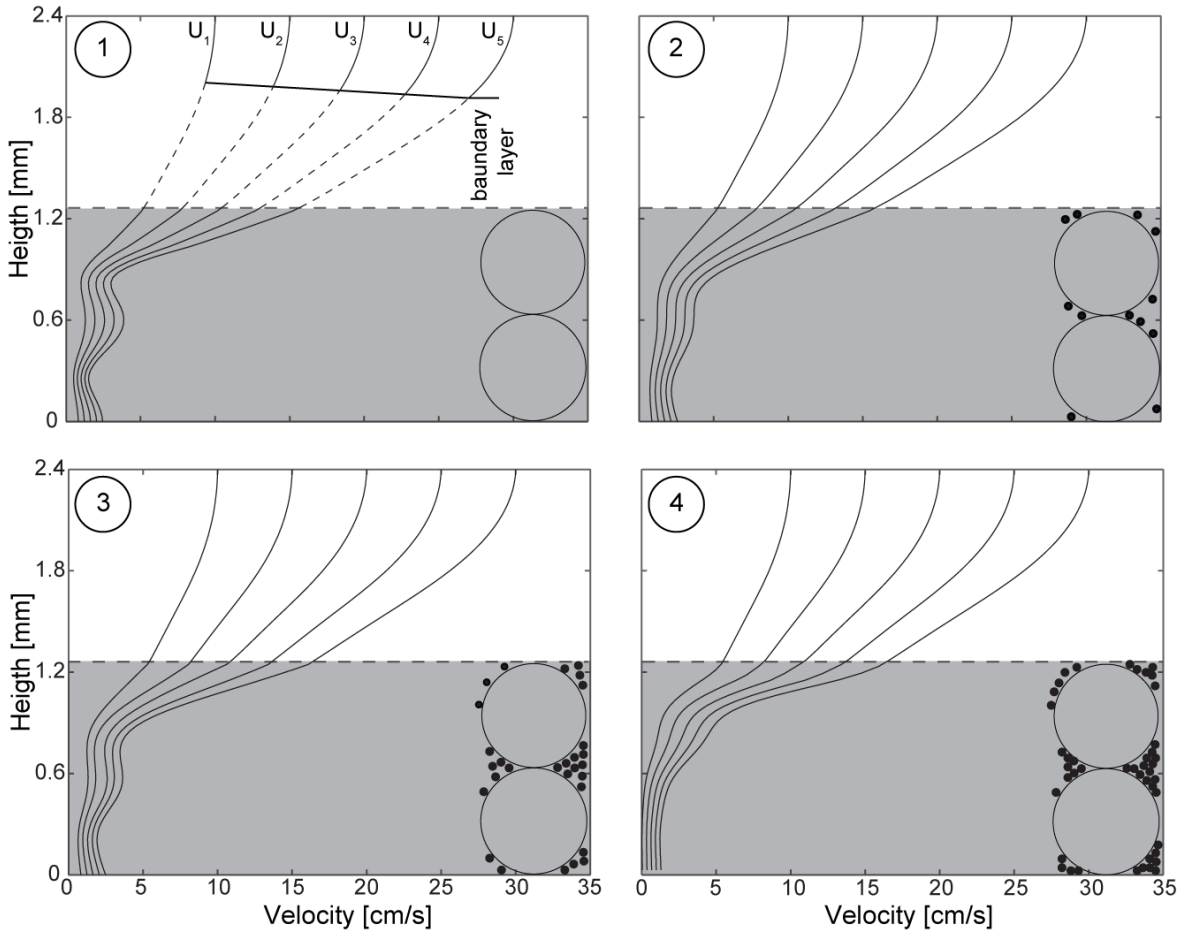

Figure 5.4: Fluid profiles derived from all experiments, sliced at 0.003 mm Y-direction, at all tested flow speeds (U = 10, 15, 20, 25, and 30 cm/s). The sediment bed was colored in light and dark gray.

The results showed that in case of the pure sand sediment bed (Experiment 1) the flow velocities consistently decreased, showing a deep inflow into the deeper parts of the sediment bed (Figure 5.4). Additionally, a slight increase of the flow speeds, indicated by two maxima, was measured between the larger sand grains, e.g., 4.8 cm/s at U = 30 cm/s in case of the Experiment 1 (Figure 5.3).

In contrast to this flow pattern, the maxima in the flow profiles disappear and showed a smoother profile shape with increasing silt contents in the beds (compare Experiments 2, 3 and 4 in Figure 5.4). When comparing the fluid profile measured within Experiment 2, the measurements showed a significant

velocity decrease within the upper part of the bed (17 cm/s - 3.5 cm/s; Table 5.2). A similar trend of decreasing flow velocities with respect to the introduced silt content was also observed from the results of the high concentration runs of Experiment 3 - 4 at 30 cm/s boundary inflow velocity (Table 5.2). In particular, Experiment 4 showed the largest flow decrease whereby the fluid velocities decreased already in direction towards the sediment surface (17 cm/s - 5 cm/s; Table 5.2) and reached zero flow conditions at the bottom of the sediment box. Additionally, it was shown that with increasing silt content the transition point to decreasing flow speeds migrated to a higher point in the profile (compare Experiments 2, 3 and 4 in Figure 5.4). For example in case of the high silt concentrated Experiment 4 the flow velocities approached towards zero just below the sediment surface.

In summary, the velocities decreased significantly with increasing silt concentrations in the beds. This transition is evident from the velocity profiles of the zero and low silt concentrated experiments characterized by a deep inflow and tow maxima, whereas with increasing silt amounts the transition point towards decreasing flow velocities migrated to the sediment surface. This indicated a blocked inflow with increasing silt contents mixed into the bed.

5.3.2 Sediment transport

Our results showed that in all experiments silt particle transport at the sediment surface was initiated immediately at a velocity of 10 cm/s. The number of grains transported at the sediment surface remained relatively constant throughout all experiments (Table 5.3). In all experiments the transport rates measured of the sediment top indicated higher transport distances with increasing boundary inflow velocities (Top Slice in Figure 5.5). Values ranged from 85 % transport at U = 10 cm/s at the beginning, to 90 % at 30 cm/s at the end of fluid streaming for all experiments (Figure 5.5 A and Table 5.3). In contrast, in case of the high silt concentrated Experiment 4, the number of particle transport was much lower, 18 % transport at U = 10, to 50 % at 30 cm/s.

In the deeper parts of the beds, the transport of particles declined with depth, but similar to the top slice the number of transported particles increased with increasing velocity from 20 % in the case of U = 10 cm/s to 42 – 59 % at U = 30 cm/s i.e., Experiments 2 - 3 (Base Slice in Figure 5.5A). Grain transport numbers indicate that more particles were transported at the sediment surface when lower silt contents were mixed into the bed and the flow velocity was higher. However, the measurements showed that in case of the high silt concentrated Experiment 4 no particles were transported in the deeper parts of the bed, at all tested flow speeds (Base Slice in Figure 5.5A).

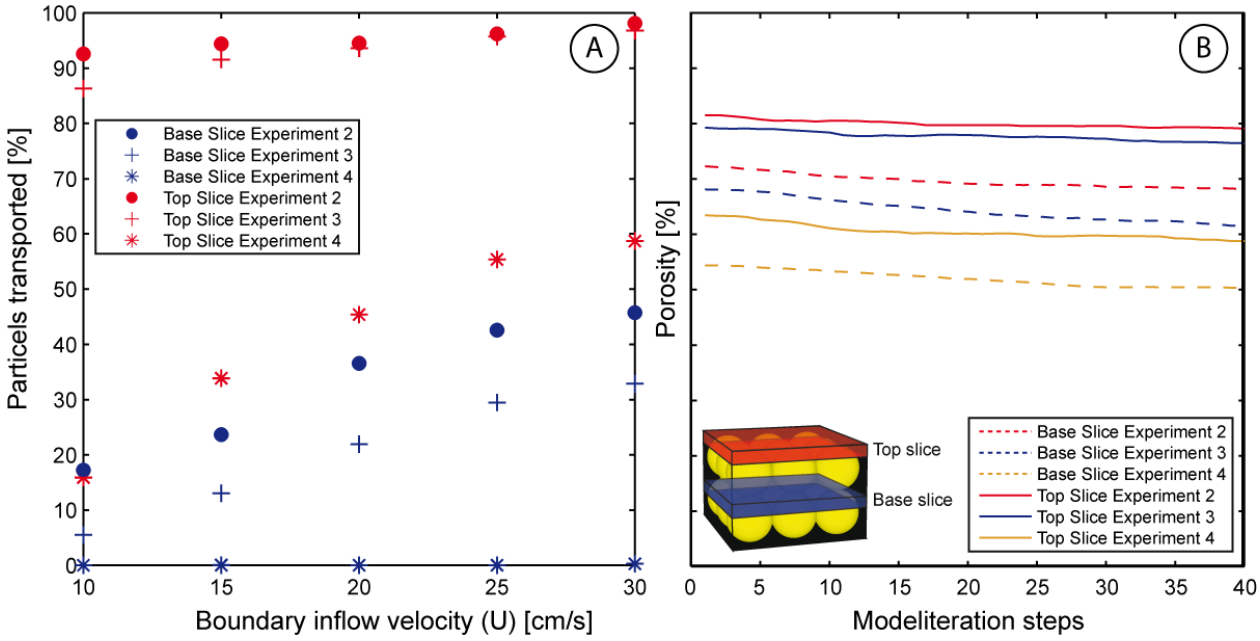

Figure 5.5: A) Mean transport distance of the transported silt particles normalized to the absolute amount of silt at increasing boundary inflow velocities of Experiment 1, 2 and 3. The red box show the transport distances at the top – surface of the sediment bed, whereas the blue box characterizes the transport distances at interior of the sediment bed. B) Porosity measurements derived from U = 30 cm/s boundary inflow velocity. Extracted from the top - surface and from the bottom of the sediment beds.

5.3.3 Porosity differences

Based on the zero silt amounts in Experiment 1, porosity was always 100 %. Therefore, only values from the Experiments 2 to 4 were processed (Figure 5.5 B and Table 5.4). All values were compared for all boundary inflow conditions, but only those from U = 30 cm/s are presented here as an example case to highlight general observations. For analyses, porosities were extracted following the onset of stable flow conditions in the water column and sediment bed. For consistency, porosity extraction was always undertaken at time step 4e10.

The offset of porosity values increased with increasing silt contents in the bed, where for example almost similar values were measured at the top and the base of Experiment 2, but a higher difference of the porosity values was measured at the top and the base of Experiment 4.

In addition, the porosity measurements of Experiments 2 to 4 indicated that the porosities at the top of the bed surface were generally higher compared to those at the base (Figure 5.5B). The top slice showed a stronger porosity decrease with depth compared to those derived at the base slice in the interior of the bed. So, with increasing fluid streaming time, porosity values revealed two different trends. The porosity values extracted from the sediment surface showed a strong decrease, with values that ranged from 70 % to 55 %. In contrast, porosities extracted from the base slice decreased to a lesser extent (54 % to 43 %, in Figure 5.5B) and were almost uniform with respect to fluid streaming time. Consequently, the top slice measurements showed a stronger porosity decrease with depth compared to those derived at the interior of

the sediments beds, whereby Experiment 4 for example showed the lowest constant porosity values at depth.

5.4 Discussion

The results showed that our new numerical approach reproducing a 3D numerical flume tank was capable of simulating sediment transport processes of mixed sediment beds. Four suites of experiments were designed (Experiment 1 - 4; Figure 5.2), whereby numerical fine silt particles were mixed incrementally into a coarse sand matrix to simulate mixed sediment beds. All numerical mixed sediment beds were tested for their erosion behavior at predefined boundary inflow velocities (U = 10, 15, 20, 25, and 30 cm/s). We were able to process high resolution 3D flow velocity data, particle transport rates, and porosity changes for the quantification of the physical processes occurring in the water column, at the sediment surface, and in the interior of the sediment beds.

It was identified that with increasing silt content mixed into the beds, the inflow into the sediment bed decreased. This resulted in a decreasing transport potential with depth (Figure 5.5A). Consequently, a relatively small amount of fine silt mixed into the sand bed changed the sediment texture, the fluid inflow and hence the threshold conditions into the deeper parts of the bed. The above findings verify the hypothesis that the generation of cage-like structures is a major player in bed stabilization (Figure 5.3). We observed that cages were created by finer silt particles which were originally mixed into a coarse sand matrix, and subsequently filled the pore spaces between the sand grains. Hence, these cage-like structures increase the bed stability significantly in mixed sediment beds. This observation was also supported by high resolution porosity measurements enabled by our new simulations, which show a decrease in porosity that was larger at the bed surface, but also apparent at depth.

Detailed analyses of our numerical results revealed that the fluid profiles decreased logarithmically from the water column towards the sediment surface (Figure 5.4), which corresponds to data recorded during field campaigns, as well as in laboratory experiments, e.g., ADCP, ADV data (Wright et al., 1999). Furthermore, this logarithmic velocity decrease indicates that a boundary layer developed above the sediment surface. With increasing boundary inflow velocities the boundary layer became compressed with a larger velocity profile gradient (Figure 5.4), which agrees with prior studies using analogue techniques to measure the boundary layer development above sediment beds (Munson et al., 2002; Peterson et al., 1989). However, with increasing silt contents mixed into the matrix, the flow velocities measured at the sediment surface (u_*) were in the same range for all Experiments 1 - 4 (Table 5.3; Figure 5.4). This finding corresponds with the boundary layer development theory (Leeder, 1999) that suggests that the surface velocities (u_*) are independent of bed roughness at similar free stream velocities. Smaller variations in the flow velocities may have been related to the local irregularities in surface roughness caused by the unique particle distributions at the surface of each experiment. Additionally, it was shown

that erosion of the silt particles was initiated and perpetuated within the logarithmic boundary layer. This corresponds with previous studies, that suggest that sediment transport of particles (< 200 µm) occurs in the boundary layer (Leeder, 1999).

In deeper parts of the mixed beds, the simulations showed that with increasing silt contents in the beds the inflow depth into the sediment bed and the overall flow velocity decreased as indicated by the transition of the turning point and the shift to an increasingly steep convex flow velocity profile shape (1 – 4; Figure 5.4). This indicates that the amount of silt mixed into the beds controls the flow profile in the sediment bed, and hence, the flow environment required to entrain particles in the deeper parts of the bed. This finding demonstrates the significant influence of silt concentration on bed stabilization, which is the focus of our study.

The particle transport measurements showed that sediment transport at the surface in each experiment was initiated at 10 cm/s. This finding corresponds to the Shields criterion for initiation of sediment motion for the grain diameter tested (Shields, 1936; Soulsby, 1997). Similarity in transport rates at the sediment surface of all experiments indicates that erosion conditions at the sediment surface (Figure 5.5A) were comparable as would be expected from the consistent flow velocities measured at the sediment surface in all experiments (Figure 5.4 and Table 5.2). However Experiment 4 showed the lowest amounts of particle transport at the surface of the bed. This showing could be related to the high silt content, in the bed where more silt particles are in contact which increases the threshold conditions and significantly decreases the transport potential.

However, in the deeper parts of the sediment beds particle transport decreased with increasing silt contents in the beds (Table 5.4), a trend that corresponded to the fluid measurements (Figure 5.4). The model results showed an inflow decrease with increasing silt contents, indicating that with increasing silt contents the erosion threshold velocities decreased with depth and successively lost their ability to transport particles. Based on this, we postulate that there may also be a decrease in particle washout and, subsequently, less sorting effects. As shown by the particle transport measurements, higher numbers of particles were eroded at the sediment surface due to higher flow velocities at the sediment surface (Figure 5.5A).

The occurrence of decreased flow velocities and particle transport rates with depth is also supported by the porosity measurements. The strong decrease in the porosity values at the sediment surface is related to the high particle transport rates (Figure 5.5B) and indicates a high compaction rate at the sediment surface (Figure 5.5B) caused by migration of the particles into the deeper parts of the bed. However, the porosity values in the deeper parts of the bed showed only a moderate decrease with increasing silt contents towards deeper parts of the sediment beds, which corresponds with the lower particle transport rates, and

thus, indicating lower compaction rates in the deeper parts of the bed. The high values of Experiment 2 indicated a washout of particles, whereas the increase of the values of Experiment 4 indicated compaction.

Traditionally, for the investigation of sediment erosion and transport phenomena analogue techniques (laboratory flume tanks or *in-situ* experiments) are used. However, direct comparison and therewith validation of our data with field/lab data was difficult as the quantification of flow velocities, transport rates and porosity changes in the interior of a sediment bed is highly limited using analogue techniques (Komar, 2007). Analogue tools are typically used for measuring flow speeds at the sediment surface and are limited in their ability to measure flow speeds in high resolution on micro scale level due to the low resolution of the sensors. For example, flow data measured by ADV (e.g., Sontec Micro ADV) above a flat sand bed allowed for measurement of the flow speeds to only 0.3 mm above the sediment bed (Bartzke et al., unpublished data). However, in order to quantify processes in sediment beds, other studies used analogue techniques, such as x-rays of the sediment bed (Mitchener and Torfs, 1996; Whitehouse et al., 2000) for fluid flow quantification, or colored particles to measure transport rates (Komar, 2007; Leeder, 1999). These studies serve as a basis for our new conceptual model of bed stabilization.
As these *in-situ* techniques are limited in their ability to quantify the dynamical processes of the highest resolution during fluid streaming, our experiments represent a new step forward for overcoming the limitations of the quantification of flow velocities, particle transport changes, and porosity changes that occur in the direct vicinity of the sediment surface and in the mixed sediment beds.

5.4.2 Conceptual model and sediment bed stabilization

As a result of the detailed analysis of the fluid behavior and particle transport as well as porosity changes, a quantification of the effect of texture induced caging structures on the bed stability was possible. This effect was already postulated for clay–sand sediments by various authors e.g. (Hir et al., 2008; Mitchener and Torfs, 1996; Panagiotopoulos et al., 1997; van Ledden et al., 2004; Whitehouse et al., 2000). These researchers assumed that cohesive clay network structures, surrounding the coarser sand grains caused the development of caging structures which increase the erosion resistance. This conceptual model is based on analogue flume experiments and was introduced in more detail by (Panagiotopoulos et al., 1997). They concluded that in sediment beds composed of coarse sand particles, all particles are more or less connected to each other, indicating a relatively easy erosion of the bed. After mixing fine clay particles into the matrix of the coarse sand bed the authors suggested that increase in the bed stability occurred through the development of cage-like structures around the sand particles. However, the theory and the quantification of bed internal processes are extremely difficult by analogue flume studies and could not be verified due to limitations of analogue studies (Komar, 2007).

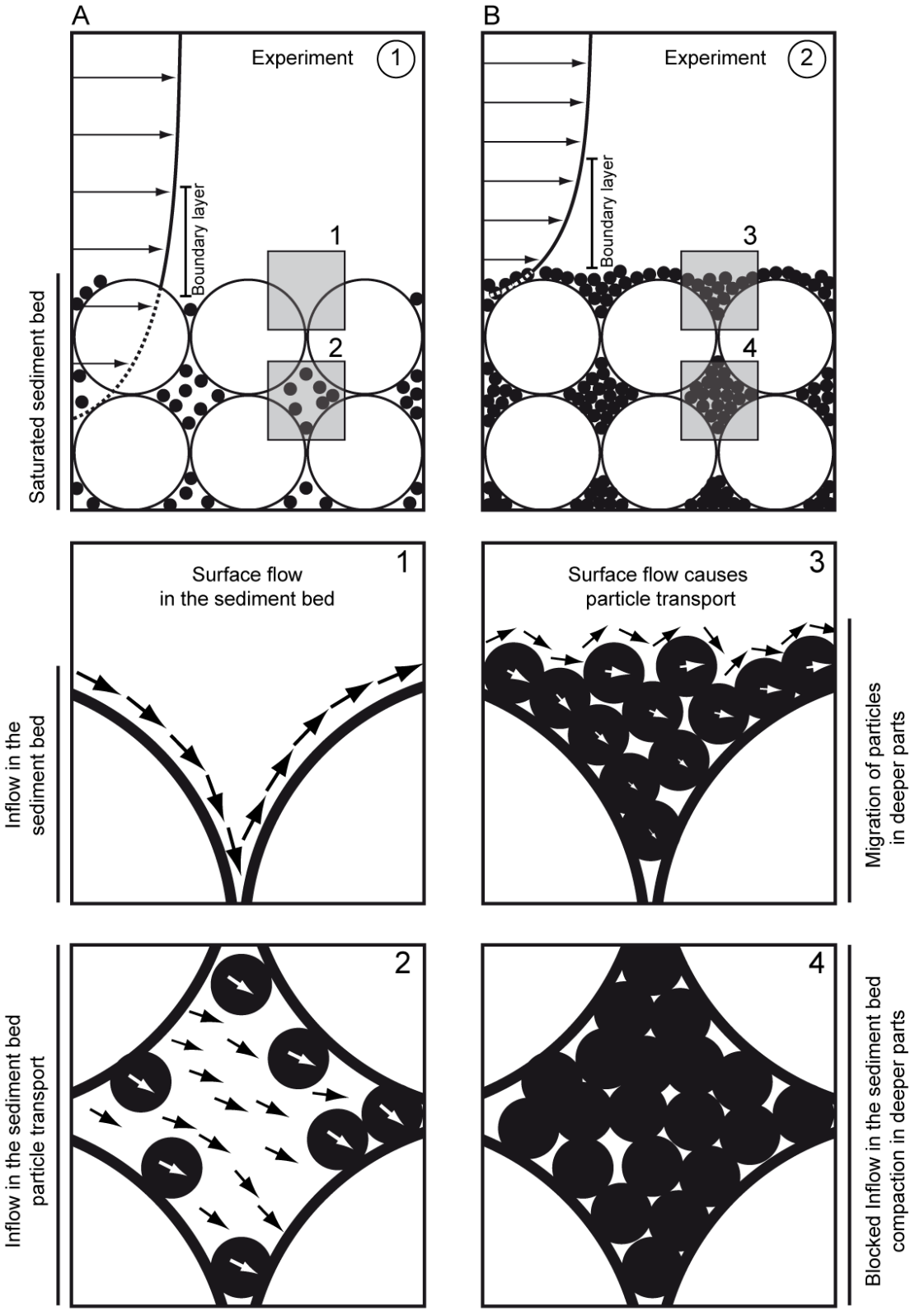

Figure 5.6: Concept model illustration the processes of the low silt concentrated Experiment 2, and the high silt concentrated Experiment 4.

Based on these previous analogue flume studies e.g. (Hir et al., 2008; Mitchener and Torfs, 1996; Panagiotopoulos et al., 1997; van Ledden et al., 2004; Whitehouse et al., 2000) our numerical results quantified the generation of textural caging structures and their potential for increasing the bed stability of mixed sediment beds. We adapted the previous theoretical model in clay-sand sediments to develop a new conceptual model on the patterns of texture induced bed stabilization in silt-sand mixed beds (Figure 5.6). The conceptual model shows two cases, one where a low silt content (Experiment 2, Figure 5.6A), and one where a high silt content (Experiment 4, Figure 5.6B) was incorporated into a sand matrix (see Figure 5.6C and 5.6D for a close-up view). Our model results highlight an improved understanding of the mechanisms for the generation of caging structures and bed stabilization by inflow blockage and internal compaction, which act to increase the erosion resistance of coarse particles mixed with increasing fine contents. To the best of our knowledge, this is the first study that directly simulates the generation of textural caging structures and their influence on changes in inflow velocities, particle transport rates, and porosities in mixed sediment beds.

As shown by the fluid profiles in all experiments (Figure 5.4), a bed boundary layer developed, which corresponds to the boundary layer theory (Munson et al., 2002; Peterson et al., 1989). This boundary layer is illustrated by the flow vectors in Figure 5.6. At the top of the bed, the flow infiltrated and entrained the particles there (Figure 5.6), which was also shown by the decreasing inflow rates into the deeper parts of the mixed beds (compare with section 5.3.1).

The results showed that with increasing silt contents in the bed, inflow decreased (Figure 5.3 and 5.4). For example in the case of a pure sand bed (Experiment 1; Figure 5.6A), it was shown that the fluid migrates through the pore space of the coarse fraction and flows through the whole sediment bed allowing erosion of the coarse particles (Figure 5.6C). In case of high silt concentrated bed (Experiment 4; Figure 5.6B), the fluid flow infiltrated the sediment bed (compare fluid velocities of the Experiment 2 and 4); however, due to the additional silt contents in the pore space and the development of caging structures surrounding the coarse grains (Figure 5.3), the flow did not penetrate into the deeper parts of the bed. This resulted in a decrease in fluid velocities and thus to reduced transport potential in the deeper horizons of the bed (i.e. blocked inflow).

The experiments also showed that a downward directed bed internal flow developed (arrows in Figure 5.6B and 5.6D) causing particle transport into the deeper parts (Figure 5.6). This process led to an increasing compaction rate with depth (compare section 5.3.2 and 5.3.3) as shown by the significant decline in porosity values and the decreasing transport distances in deeper parts of the coarse matrix. This suggests that the presence of fine particles mixed into a coarse matrix increases the erosion resistance through the process of inflow blockage and internal texture induced compaction. Therein, the threshold velocities are lowered in the interior of the sediment bed and the entrainment of coarser particles located

in the deeper parts of the bed is prevented, which together contribute to an increased stability of the whole sediment bed (Figure 5.6).

In summary, following former studies and pre-existing conceptual models on the key role of textural induced sediment stabilization, our results confirm the theory of texture induced bed stabilization for mixed sediment beds. Our new model approach confirms that sediments beds are stabilized through the generation of cage-like structures or rather an inflow protection caused by pore space filling and/or porosity decrease (Figure 5.6), brought about by the mixing of fine silt particles in the pore spaces of the coarse sand fractions. Therefore, bed stabilization in mixed sediment beds is induced by the development of a protective silt horizon filling the pore space that blocks the inflow and results in increased erosion resistance of particles located in the deeper parts of the bed.

5.5 Conclusions and outlook

To investigate the effect of fine particles mixed into a coarse sediment bed on bed stability and hence on the inflow behavior and threshold conditions, we used a 3D high resolution numerical flume tank. Using this approach, we were able to quantify processes controlling texture induced bed stabilization caused by the development of cage-like structures in a mixed sediment bed. Four suites of experiments were designed generating a coarse matrix (i.e., numerical sand) and mixing increasing quantities of numerical silt to establish mixed sediment beds.

All numerical sediment samples were tested for erosion resistance and bed stability with respect to predefined boundary inflow velocities. The experiments showed that with mixing silt in increasing quantities, the inflow into the sediment bed decreased, causing a reduced inflow, and hence, a decrease in erosion potential in the deeper parts of the bed.

Measurements in the mixtures showed lower transport rates in the deeper parts of the beds compared to those at the sediment surface. Further is was observed that the measured transport rates were lowered in the deeper parts of the bed as compared to those at the sediment surface in cases with a higher silt content.

Porosity measurements in the beds showed that with an increase in silt contents, compaction was also increased. Therefore, we conclude that silt mixed in sufficient quantities into a coarse matrix can cause an inflow blockage into the sediment bed, thereby increasing the sediment stability. Furthermore, the effect of texture induced caging structures caused structural compaction towards deeper parts of the beds and a complete blockage of the flow, which protected the underneath lying coarser fractions and increased the stability of the bed under higher flow regimes.

There are however, some limitations to this study, such as the difficulty in generating larger sediment beds or multiple grain spectra due to an extreme calculation effort, e.g. an exponential increase in calculation

time even on faster supercomputers. Regardless, this new approach allowed for the development of an improved conceptual model through the testing of a general hypothesis. Following, the analogue history, future research will focus on multiple particle spectra and density compositions, as well as the implementation of cohesive clay aggregates e.g., through the stacking of elongated particles to quantify cohesion related bed stability processes (Kock and Huhn, 2007). It is anticipated that these added model features will assist in improved quantification of internal threshold conditions, further explain internal grain entrainment and allow for the development of sediment bed forms within the continuum. In order to increase the complexity of our models, we are also aiming to implement more complex flow conditions and also a larger amount of particles in the numerical sediments beds. Therefore we will use faster supercomputers.

5.6 Acknowledgments

This work has been funded through the DFG-International Research Training Group INTERCOAST.
We thank Lina Podszun, Jannis Kuhlmann, Bryna Flaim, Melanie Schäfer, Linda Wenk, Firoz Badesab, and the INTERCOAST research student Antonia Ruppel and Leonard Rossmann for discussion and comments on the manuscript.

5.7 References

Allen, J.R.L., 1970, Physical processes of sedimentation: London, Unwin University Books, 248 p.

Bagnold, R.A., 1941, The Physics of Blown Sand and Desert Dunes: London, Chapman & Hall.

Black, K., and Paterson, D.M., 1997, Measurement of the erosion potential of cohesive marine sediment: A review of current in situ technology: J. Mar Environ. Eng, v. 4, p. 43-83.

Coleman, S., E. , and Eling, B., 2000, Sand wavelets in laminar open-channel flows: Journal of Hydraulic research, v. 38, p. 331-338.

Cundall, P.A., and Hart, R.D., 1989, Numerical modeling of discontinua, *in* Mustoe GGW., Henriksen M., and H-P., H., eds., In Keynote address in Proceedings of the 1st US conference on discrete element methods Golden Colorado, CSM Press, p. 1–17.

Cundall, P.A., and Strack, O.D.L., 1979, A discrete numerical model for granular assemblies: Geotechniqe, v. 29, p. 47-65.

Cundall, P.A., and Strack, O.D.L., 1983, Modeling of microscopicmechanisms in granularmaterial: Proceedings of the US-Japan Seminar on New Models and Constitutive Relations in The Mechanics of Granular Materials, p. 137-149.

Cunningham, E., 1910, On the velocity of steady fall of spherical particles through fluid medium: Proceedings of the Royal Society of London, Series A, Containing Papers of a Mathematical and Physical Character, v. 83(563), p. 357-365.

Eisbacher, G.H., 1996, Einführung in die Tektonik: Stuttgart, Spektrum Akademischer Verlag; Thieme; Enke, 374 p.

Harris, J., and Stöcker, H., 1998, Handbook of Mathematics and Computational Science: New York, Springer, 1028 p.

Hir, P.L., Cann, P., Waeles, B., Jestin, H., and Bassoullet, P., 2008, Chapter 11 Erodibility of natural sediments: experiments on sand/mud mixtures from laboratory and field erosion tests, *in* Tetsuya Kusuda, H.Y.J.S., and Joseph, Z.G., eds., Proceedings in Marine Science, Volume Volume 9, Elsevier, p. 137-153.

Hjulstroem, F., 1939, Transport of detritus by moving water recent marine sediments, *in* Trask, P.D., ed., Recent Marine Sediments; a symposium, Tulsa Oklakoma: American Association of Petroleum Geologists: New York, London, T.Murby & Co., Reprinted 1968 by Dover Publications p. 3-31.

Itasca, 2004a, PFC 3D 3.1 Manual: Minneapolis, Itasca Consulting Group, Inc.

Itasca, 2004b, FLAC 3D 3.1 Manual: Minneapolis, Itasca Consulting Group, Inc.

Kock, I., and Huhn, K., 2007, Influence of particle shape on the frictional strength of sediments — A numerical case study: Sedimentary Geology, v. 196, p. 217-233.

Komar, P.D., 2007, Chapter 1 The Entrainment, Transport and Sorting of Heavy Minerals by Waves and Currents, *in* Maria, A.M., and David, T.W., eds., Developments in Sedimentology, Volume Volume 58, Elsevier, p. 3-48.

Leeder, M.R., 1999 Sedimentology and Sedimentary Basins: From Turbulence to Tectonics Oxford, Blackwell Science, 608 p.

Mitchener, H., and Torfs, H., 1996, Erosion of mud/sand mixtures: Coastal Engineering, v. 29, p. 1-25.

Panagiotopoulos, I., Voulgaris, G., and Collins, M.B., 1997, The influence of clay on the threshold of movement of fine sandy beds: Coastal Engineering, v. 32, p. 19-43.

Rijn, L.C.v., 2007, Unified view of sediment transport by currents and waves. I: Initiation of motion, bed roughness, and bed-load transport: Journal of hydraulic engineering, v. 133, p. 649-667.

Schlichting, H., and Klaus, G., 2004, Boundary-layer theory: Berlin-Heidelberg, Springer, 811 p.

Shields, A., 1936, Anwendung der Ähnlichkeitsmechanik und der Turbulenz- forschung auf die Geschiebebewegung: Mitteilungen der Preußischen Versuchsanstalt für Wasserbau und Schiffbau, v. NW 87.

Soulsby, R., 1997, Dynamics of Marine Sands. A Manual for Practical Applications: London, Thomas Telford Publishing.

Sutherland, A., 1987, Static armour layers by selective erosion, *in* Thorne, C.R., Bathurst, J.C., and Hey, R.D., ed., Sediment Transport in Gravel-Bed Rivers: London, Wiley, p. 141-169.

Torfs, H., 1997, Erosion of mixed cohesive/non cohesive sediments in uniform flow: Cohesive Sediments, p. 245-252.

Torfs, H., Jiang, J., and Mehta, A.J., 2000, Assessment of the erodibility of fine/coarse sediment mixtures, *in* William, H.M., and Ashish, J.M., eds., Proceedings in Marine Science, Volume Volume 3, Elsevier, p. 109-123.

Tucker, M.E., 1981, Sedimentary Petrology: Oxford, Blackwell Scientific Publications, 252 p.

van Ledden, M., van Kesteren, W.G.M., and Winterwerp, J.C., 2004, A conceptual framework for the erosion behaviour of sand-mud mixtures: Continental Shelf Research, v. 24, p. 1-11.

Whitehouse, R., Soulsby, R., Roberts, W., and Mitchener, H., 2000, Dynamics of estuarine muds. A manual for practical applications: London, Thomas Telford Publishing, 210 p.

Wiberg, P.L., and Smith, J.D., 1987, Calculations of the Critical Shear Stress for Motion of Uniform and Heterogenious Sediments: Water Resources Research, v. 23, p. 1471-1480.

Wright, J., Colling, A., and Park, D., 1999, Waves, Tides and Shallow-Water Processes: Oxford, Butterworth Heinemann.

Table 5.1: Properties and configurations of the numerical experiments.

Particle properties				
Particle Properties	**Exp. 1**	**Exp. 2**	**Exp. 3**	**Exp. 4**
Diameter [µm]: sand	600	600	600	600
Diameter [µm]: silt	80	80	80	80
Particle number: sand	18	18	18	18
Particle number: silt	0	600	800	2185
Normal stiffness [N/m]	$1x10^8$	$1x10^8$	$1x10^8$	$1x10^8$
Shear stiffness [N/m]	$1x10^8$	$1x10^8$	$1x10^8$	$1x10^8$
Density ρ [kg/m³]	2650	2650	2650	2650
Friction µ	0.5	0.5	0.5	0.5

Fluid properties				
Fluid properties	**Exp. 1**	**Exp. 2**	**Exp. 3**	**Exp. 4**
Fluid density ρ [kg/m³]	1000	1000	1000	1000
Pore pressure ψ [mbar]	250	250	250	250
Fluid saturation φ [%]	100	100	100	100
Boundary inflow velocity U [cm/s]	10, 15, 20, 25 and 30			

Table 5.2: Flow velocities.

Flow velocities		
Boundary inflow velocity U [cm/s]	**Surface velocity [cm/s]**	**Bed velocity [cm/s]**
Exp. 1		
10	5.8	1.6
15	7.8	2.4
20	11.4	3.2
25	14.5	4.0
30	18.0	4.8
Exp. 2		
10	7.6	1.0
15	11.5	2.2
20	15.5	2.6
25	19.2	3.4
30	23.6	4.0
Exp. 3		
10	5.2	0.8
15	12.1	2.1
20	14.8	2.2
25	17.3	2.4
30	20.0	3.3
Exp. 4		
10	7.4	1.1
15	11.4	1.8
20	14.8	2.1
25	17.6	2.2
30	22.2	2.5

Table 5.3: Transport rates.

Transport rates [%]								
Velocity [cm/s]	**Exp.1**		**Exp.2**		**Exp.3**		**Exp.4**	
	top	**base**	**top**	**base**	**top**	**base**	**top**	**base**
10	Not measured		92.59	17.20	86.31	5.47	15.89	0
15	Not measured		94.44	23.65	91.57	13.01	33.84	0
20	Not measured		94.54	36.55	93.61	21.91	45.38	0
25	Not measured		96.22	42.55	95.74	29.45	55.38	0
30	Not measured		98.14	45.74	96.84	32.87	58.71	0.23

Table 5.4: Porosity measurements extracted at a U = 20 cm/s boundary inflow velocity.

Porosity [%]				
Velocity [cm/s]	**Exp. 1**			
	top		**base**	
	Start	End	Start	End
10	100		100	
15	100		100	
20	100		100	
25	100		100	
30	100		100	
	Exp. 2			
	top		**base**	
	Start	End	Start	End
10	81.5	80	72.4	68.9
15	81.5	79.8	72.4	68.6
20	81.5	79.6	72.4	68.4
25	81.5	79.3	72.4	68.2
30	81.5	79.1	72.4	68.0
	Exp. 3			
	top		**base**	
	Start	End	Start	End
10	80.0	78.1	68.2	63.2
15	80.0	77.5	68.2	62.8
20	80.0	77.2	68.2	62.6
25	80.0	76.5	68.2	62.2
30	80.0	76.0	68.2	61.9
	Exp. 4			
	top		**base**	
	Start	End	Start	End
10	63.2	60.0	54.5	51.5
15	63.2	59.5	54.5	50.2
20	63.2	59.0	54.5	50.0
25	63.2	58.5	54.5	49.8
30	63.2	58.0	54.5	49.6

Chapter VI

A NUMERICAL APPROACH TO QUANTYFY SELECTIVE SORTING OF HEAVY - MINERAL ASSEMBLAGES

Gerhard Bartzke and Katrin Huhn

MARUM – Center for Marine Environmental Sciences, University of Bremen, Leobener Straße, D-28359 Bremen, Germany

Abstract

The enrichment of heavy minerals causing placer formation has been explained as selective grain entrainment using laboratory experiments. However, the validation, in particular, the quantification of grading processes in the sediment bed is difficult using such techniques. For quantification of selective grain entrainment, we used a 3D high resolution numerical 'flume tank' based on a coupled Finite Difference Method (FDM) and Discrete Element Method (DEM) model. For the quantification of processes occurring at the bed surface and in the interior we designed four suites of experiments: (1) deposition of a single 'quartz' grain on top of a 'magnetite' bed, and (2 – 4) deposition of the 'quartz' grain at depths with respect to the bed. All samples were tested at flow velocities ranging from 10 – 30 cm/s. Further measurement routines, such as fluid profiles, transport distances, and coordination numbers (nearest neighbors) were extracted. The results showed that an exposed light mineral is entrained more easily than a heavy mineral grain. In contrast, with increasing burial depth, erosion resistance of the light mineral increased. We conclude that for placer formation, higher flow velocities (e.g., storm events) are needed to 'wash-out' the lighter fractions in the deeper part of a sediment bed.

6.1 Introduction

Heavy minerals (e.g., Magnetite, Ilmenite, Zircon and Garnet) play an important role in the mineral industry due to their high economic value. In general, such heavy minerals differ from light minerals (e.g., Feldspar and Quartz) based on mineralogical composition, grain size, and also in hydrodynamic susceptibility according to their differing densities (e.g., 4 - 6 g/cm³ for heavy minerals and 2.5 - 2.8 g/cm³ for light minerals). Due to their higher densities, heavy minerals are more resistant to erosion by flowing water (Komar, 1987). Therefore, the light mineral fractions can be 'washed-out' more easily due to differing density-related threshold conditions. This process of hydrodynamic sorting, understood as selective grain entrainment, can lead to the formation of heavy mineral placers (Komar, 2007). The position and distribution of such placers is interesting for the industry, because they are easier to mine. So within the marine environment beach placer deposits are very common, where heavy minerals can be found in high concentrations. These are defined as deposits of residual or detrital mineral grains in which a valuable mineral has been concentrated by a natural process (Komar, 1987; Peterson et al., 1989).

Prior studies, attempted to determine the formation of placers by the process of selective grain entrainment used analogue, mechanical models (e.g., flume tanks). Here, research focused on interaction between fluid forces and resulting particle motion by testing a variety of particle mixtures differing in grain size, density, and weight. An excellent review of these experiments can be found in Komar (2007). However, it is difficult to validate the process of selective grain entrainment on exposed or buried light minerals in a heavy mineral bed (Komar, 2007). Hence there is a clear lack in knowledge about the role of sediment texture or granular skeleton besides hydrodynamic forcing on heavy mineral enrichment, and placer formation (Komar, 2007). In consequence, further studies are required, for a better understanding of mineral enrichment processes, and to develop conceptual models dealing with 'wash-out' processes on a grain-scale level. Additionally, this information will improve numerical simulations, to simulate the physical processes controlling selective sorting at the surface and in the interior of a sediment bed. This can assist in the detection of heavy mineral accumulations and can concurrently reduce expensive and time consuming exploration activities for mining heavy mineral placers in the marine environment.

Our study shows the quantification of the physical processes controlling selective grain entrainment to understand the formation of heavy mineral placers. Therefore, a 3D numerical model approach was designed by coupling two simulation techniques – the Finite Difference Method (FDM) with the Discrete Element Method (DEM). This 3D model parameterized general settings of laboratory flume tanks to investigate selective grain entrainment as the main factor for heavy mineral accumulation. In order to quantify the 'wash-out' processes, four suites of experiments were designed, wherein different grades of exposure of light minerals within a heavy mineral bed were tested under different flow velocities: starting with an exposed 'quartz' grain (Experiment 1, z = 0.4 mm) deposited on top of a 'magnetite' bed, and ending with a fully buried 'quartz' grain (Experiment 4, z = 0.2 mm). Hence, exposure (z) is defined as the distance of the 'quartz' grain to the model base (Table 6.1). Analyses of these experiments indicated that the erosion resistance of the light fraction increases with burial depth, which is caused by a decreased inflow to the 'magnetite' bed. Therefore, it should be considered that the quantity of 'washed-out' light minerals, located in deeper parts of a sediment bed, might also contribute to the enrichment of heavier minerals in a placer. The resultant higher erosion thresholds of the buried lighter fractions suggest that their entrainment would be more likely in high energy flow events, such as during episodically occurring extreme storm events.

6.2 Numerical methods

We developed a high resolution, 3D numerical 'flume tank' (Figure 6.1) for the simulation of light and heavy mineral transport through a fluid. Therefore, we coupled a FDM model with a DEM model by an input - output routine. These are two independent numerical simulation techniques, wherein the FDM simulation creates the flow conditions and flow velocities (fluid model) and the DEM model simulates the

'sediment' matrix (sediment matrix model, Figure 6.1). The 3D FDM fluid model was generated using the commercial software (FLAC3D, Itasca). It is based on the spatial discretization of the study domain by a finite number of three-dimensional, rectangular, polyhedral elements. These elements can be assigned with broad physical property spectra e.g., fluid density, pore pressure, and flow velocities, to mimic natural conditions. Hence, this FDM model calculates fluid forces and solves the differential flow equations by partial integration in defined time steps based on given boundary conditions e.g., inflow velocity. Simultaneously, we used the PFC 3D software (Itasca, 2004), which is based on the DEM theory by Cundall and Strack (1978), to simulate the 'sediment' matrix. This granular model consists of ideal spherical particles which interact according to physical contact laws. Hence, these granular assemblages mimic the 'sediment' bed (i.e. numerical 'magnetite' and 'quartz' grains), in particular the internal structure and porosity. DEM enables to investigate the mechanical behavior, deformation processes and hence, the 'sediment' grain interactions caused by applied, defined boundary conditions, e.g. fluid forcing (Figure 6.1). Physical properties are assigned adopting natural conditions, such as e.g., grain density, friction, and stiffness. For a detailed review of PFC and FLAC refer to Itasca, 2004.

In order to couple both models, the fluid model and the sediment matrix model have identical geometries, dimensions, material properties, as well as boundary conditions (Figure 6.1). Initially, the grain or 'sediment' model was generated. The spatial parameters of this sediment matrix model (x, y, z coordinates and the particle radii) were then sent to the FDM model. Based on these data representing the grain distribution in the DEM model, the fluid model is discretized into a high resolution finite difference grid wherein each grain is represented by at least 8 elements. The resulting FDM model consists of elements, where fluid streaming was either allowed (fluid zones) or not allowed (particle / solid matrix zones). Therefore, the FDM model and the DEM model, showed identical porosity distributions within the 'sediment' filled areas (compare 'sediment' beds in Figure 6.1).

After the 'sediment' bed was generated (Figure 6.1), a flow field streaming into X-direction was initiated above the bed, by an inflow boundary condition in the FDM model. In the following step, all flow velocities were calculated based on the initial porosity distribution. After the flow field reached stable conditions, all fluid forces were extracted around each element and sent to the sediment matrix model to be assigned to all particles at their corresponding X-Y and Z coordinates. If the added fluid forces are larger than the resisting force of the particles and their inter-particle friction respectively, the particle contacts break up and the grains are transported (Cundall and Strack, 1978). Hence, 'sediment' transport was initiated at the sediment matrix model, which caused new porosities within the DEM model. Those were sent back to the fluid model, and subsequently a re-meshing of the FDM model grid was initiated. This calculation cycle between both models was repeated until constant flow and transport conditions were reached. Hence, high resolution information about e.g., particle distribution, porosity, texture, and fluid velocities at the 'sediment' surface as well as in the interior of the 'sediment' matrix are capable in

space and time. This approach yields a deeper insight into grain-fluid interactions on a micro-scale level and provides a fundamental understanding of physical processes occurring during selective grain entrainment.

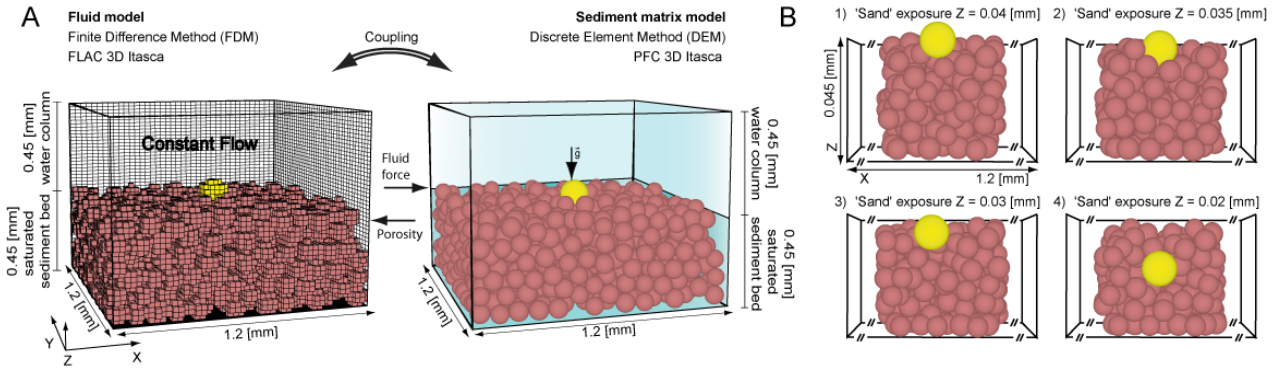

Figure 6.1: A) Schematic of the coupled fluid model (FDM) and sediment matrix model (DEM) for simulation of particle transport by a fluid. B) Experimental setup, 'quartz' deposited on top or within a 'magnetite' bed at increasing the particle depths or respectively reducing the exposure (z).

6.2.1 Experimental setup

Both the FDM and DEM models had identical dimensions (1.2 x 1.2 x 0.45 mm), which were designed to isolate a micro-scale section of the sediment surface from a laboratory flume tank, to focus on the quantification of the physical processes controlling selective grain entrainment at the surface and in the interior of the 'sediment' bed. The grain sizes, and physical properties of all grains, as well as the flow velocities, were chosen to ensure conditions known from natural environments of heavy mineral placers (Allen 1970; Table 6.1). Therefore, two end-members of heavy- and light-mineral fractions, which are significantly differing in their hydrodynamic and physical properties (Table 6.1), were tested as a simplified 'sediment' bed of smaller, heavier, numerical 'magnetite' grains (D_{50} = 0.08 mm, ρ_m = 5.6 g/cm³) and larger numerical 'quartz' grains (D_{50} = 0.14 mm, ρ_q = 2.65 g/cm³,). Within all DEM model experiments the 'sediment' bed consisted of 1000 'magnetite' particles, which were randomly distributed and deposited under applied gravity into the numerical 'sediment' box (Figure 6.1B). Here, the generated 'magnetite' bed filled always half of the box. To validate the effect of selective grain entrainment and the influence of exposure (i.e. z = distance from the 'quartz' grain to the box base) between of light/larger and heavy/smaller minerals under different flow velocities, we designed four suites of experiments: 1) a single 'quartz' grain was deposited on top of a heavy 'magnetite' bed (z = 0.45 mm; Experiment 1; Figure 6.1B). In order to reach a deeper burial position of the 'quartz' grain within the 'magnetite' bed, i.e. Experiment 2 - 4 (Figure 6.1B), we removed 'magnetite' particles out of the matrix at those locations where 'quartz' grains should be embedded. Then we deposited the single 'quartz' grain there (Figure 6.1B).

Starting from these initial stable conditions, a constant free-stream in positive X-direction above the fully saturated 'sediment' bed was calculated at the beginning of each model run in all FDM models (grid

space: 48 x 48 x 40 elements). To investigate the erosional behavior, flow velocities were stepwise increased, ranging from 10, 15, 20, 25 to 30 cm/s, within each Experiment 1 - 4. These flow velocities were chosen to mimic the environment of tidal sand flats (Leeder, 1999).

In order to validate the effect of selective entrainment within all experiments, we extracted fluid profiles, coordination numbers, and transport distances from the fluid and sediment matrix models (Figure 6.2). To quantify changes in the flow field above and in the 'magnetite' bed, we generated X-Z slices (fluid profile slice in Figure 6.2), which were sliced exemplarily at 0.06 mm (Y-direction) through the fluid model. The exact flow velocities were extracted from each cell and are illustrated as a contour plot (Figure 6.2). Furthermore, we processed single fluid profiles to highlight velocity differences in more detail. Within the sediment matrix model we recorded the exact position and speed of the 'quartz' grain, and all 'magnetite' grains, to compare and quantify both 'quartz' and 'magnetite' transport. Therefore, particle transport was defined as a transport distance greater than the radius of each individual particle. Furthermore, we measured the coordination numbers of the 'quartz' grain and the nearest 'magnetite' neighbors.

In addition, we compared the ratio of exposure, and coordination number with respect to transport distance, to understand the relationship between the transport distances of the light minerals, the burial depth of 'quartz' grain, and the coordination number (Figure 6.3).

6.3 Results and discussion

All experiments showed that a continuous free stream developed above the 'sediment', which decreased from the top of the water column (0.9 mm in height) towards the 'sediment' surface (0.45 mm height) in a logarithmic shape (Figure 6.2, fluid profiles). Towards the deeper parts of the 'magnetite' bed the flow velocity was further decreased in all experiments and ranged from 12 to 2 cm/s. Considering the results from all experiments in terms of the exposure of the 'quartz' particle, it was observed that the deeper the position of the particle within the 'magnetite' bed, the lower the surrounding fluid flow. In addition, it was shown that at a 30 cm/s free stream velocity, the 'quartz' particle in Experiment 1, was encountered to higher flow velocities as compared to the buried 'quartz' grain. Further, the flow velocity above the 'quartz' particle in Experiment 1 was higher as compared below, whereas the flow velocities of the deeper buried case of Experiment 4, were more constant above and below the particle.

The model results showed that transport speeds seem to depend on the 'quartz' particle exposure (see speed vectors in the top view slice of Figure 6.2). Within all models 'sediment' transport at the surface was imitated at 10 cm/s for 'quartz' and 15 cm/s for 'magnetite'. Therein, the most exposed 'quartz' particle of Experiment 1 was transported with fastest speeds at 3 cm/s, compared to the deepest positioned particle of Experiment 4, which was transported at relatively low speeds (~0.2 cm/s). This corresponds to the findings of the velocity profiles, where the flow velocities decreased with increasing depth (top view slice in Figure 6.2). In addition, it was observed that in Experiment 1, the exposed 'quartz' grain was

transported faster as the ‘magnetite’ particles of the bed. In contrast, the experiments with deeper embedded ‘quartz’ particles (Experiment 3 and 4) showed that the heavy mineral fractions were transported at higher speeds than the buried ‘quartz’ grain.

To quantify the individual transport distance of the ‘quartz’ particles differing in exposure, in relation to their nearest adjacent ‘magnetite’ neighbors (coordination number), we compared Experiments 1 - 4 for 30 cm/s in more detail (Figure 6.3). It was observed that the exposed ‘quartz’ grain was transported a greater distance (Experiment 1, 0.19 mm total distance) than the embedded ‘quartz’ grains of Experiments 2 - 4 (Figure 6.3; Experiment 2, 0.07 mm, Experiment 3, 0.03 mm and Experiment 4, 0.002 mm total distance). This finding was also confirmed by the coordination number measurements, where the ‘quartz’ grain of Experiment 1 showed 4 contacts and the deeper buried grain of Experiment 4 had 7 contacts. In comparing the ratio of exposure, and coordination number to the transport distance it was shown that an increase of burial depth of the particle in the ‘magnetite’ bed caused an increase of coordination number and subsequently a lowering in the transport distance (Figure 6.3).

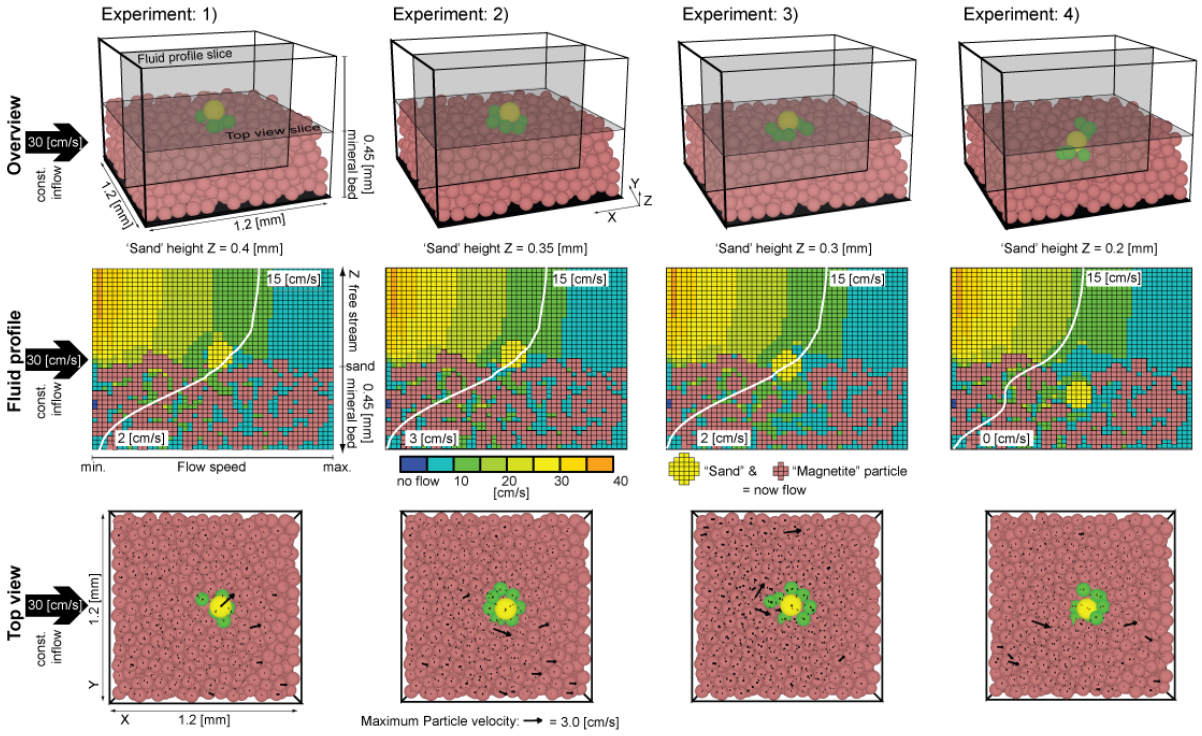

Figure 6.2: Overview of the processed experiments, at 30 cm/s flow velocity, showing the fluid profiles (fluid profile slice), transport velocities and coordination numbers (top view slice).

Our 3D numerical ‘flume box’ experiments are capable to quantify selective grain entrainment and ‘wash-out’ processes, which cause heavy mineral placer formation. The experiments showed that the enrichment of heavy minerals by the ‘washing-out’ of light minerals is controlled by the exposure of the light ‘quartz’ grains. It was identified, that a single ‘quartz’ grain deposited on top of a ‘magnetite’ bed was transported

preferentially due to their lower density over the bed (Figure 6.3). By decreasing the exposure of a ‘quartz’ grains with respect to the ‘magnetite’ bed it was validated that the deeper buried ‘quartz’ minerals were not, or to a minor extend transported. This finding for exposed grains in our study corroborate, those from previous laboratory flume experiments (Komar 2007), which showed that heavy minerals, especially magnetite, are harder to entrain as the pure quartz fraction. However, the quantification of selective grain entrainment by those analogue models was limited in their validation of the processes occurring in the sediment bed, and hence in their ability of measuring the transport of buried grains (Komar, 2007).

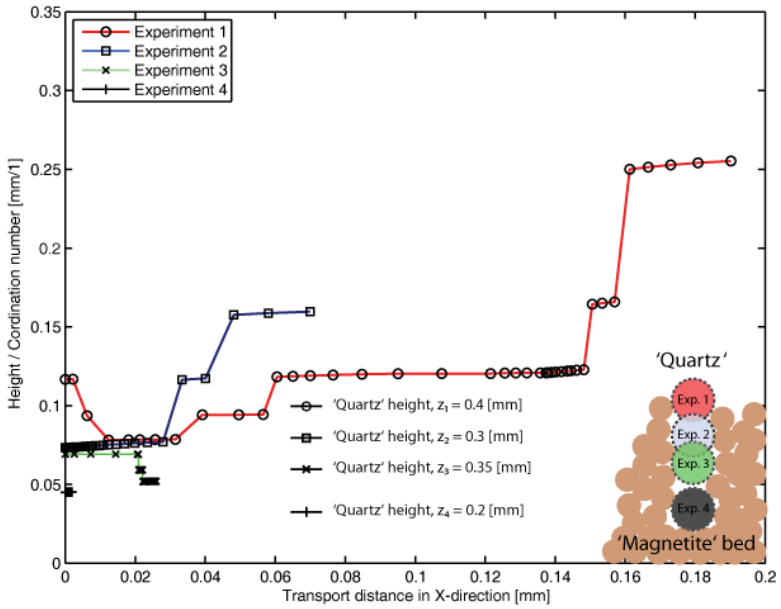

Figure 6.3: Processed transport distances in x-direction of all experiments with respect to ‘quartz’ exposure and coordination number.

In analyzing the flow properties in interior of the ‘sediment’ bed numerically, a decrease of the flow velocities was shown, and hence, decreasing threshold velocities with depth. In addition, coordination number measurements indicated that ‘quartz’ particles located deeper in the bed were surrounded by more ‘magnetite’ neighbors, which mechanically prevented the ‘quartz’ grain from moving. In addition, the increase in coordination number implicates that more particle contacts have to break up to ‘wash-out’ the larger lighter minerals. This indicates that much higher flow velocities are required to ‘wash-out’ particles located in the deeper parts of a ‘magnetite’ bed, which causes the accumulation of heavy minerals in placer deposits. Such extreme velocities, influencing deeper depth levels in the ‘sediment’ bed, could occur during cyclic storm events. In this case, the deeper buried sediments are perfused with higher flow velocities, effecting a higher potential to ‘wash-out’ quartz fractions located in deeper parts of the bed (Leeder, 1999). We hypotheses that only such an extreme event is able to ‘wash-out’ all light fractions with respect to the heavy mineral fraction, which possibly causes the establishment of a pure placer

deposit. However, a detailed quantification of this effect influencing selective grain entrainment requires further investigations testing multiple grain spectra and heavy mineral compositions.

6.4 Conclusion

A new high resolution 3D numerical model approach to simulate particle transport by fluid forcing has been developed. Hence, it is possible by this numerical 'flume tank' to quantify the physical processes of selective sorting of heavy and light minerals fractions and explains the formation of placers with high economical values. Through our experiments it was validated that selective grain entrainment is causing a 'wash-out' of the light minerals above a heavy mineral deposit at the sediment-water interface, which is directly linked to grain exposure. By decreasing the burial depth of light minerals i.e. 'quartz' within the heavy mineral bed i.e. 'magnetite', it was quantified that the exposure has an important influence on the threshold conditions and therefore, on the erosion resistance of the light minerals. This is caused by a reduced flow velocity reaching the light minerals located deeper in the bed, which prevents a 'wash-out'. This coincides that the greater the number of heavy mineral neighbors, the greater the required velocity for transport. We conclude that higher flow velocities are required, such as those caused by cyclic storm events, to 'wash-out' light mineral fractions in the deeper parts of the bed, which cause an enrichment of heavy minerals and the formation of placer deposits. Based on that, extreme events have to be taken into account particular in large scaled sediment transport models to study evolution of heavy mineral placer deposits.

Our numerical approach can be used as a prototype characterizing selective grain entrainment at the sediment-water interface, but also for quantification of processes acting in the sediment bed, which may be useful to the heavy mineral industry.

6.5 Acknowledgements

This work has been funded through the DFG-International Research Training Group INTERCOAST. We thank L. Podszun, L. Rossmann, B. Flaim, M. Schäfer, J. Kuhlmann, L.Wenk, and L. Torbahn.

6.6 References

Allen, J.R.L. 1970. *Physical processes of sedimentation*. Unwin University Books, London.

Cundall, P.A. and O.D.L., Strack, 1979. "A discrete numerical model for granular assemblies." *Géotechnique*. 29(1): 47-65.

Itasca 2004. *PFC 3D 3.1 Manual*. Itasca Consulting Group, Inc., Minneapolis.

Itasca 2004. *FLAC 3D 3.1 Manual*. Itasca Consulting Group, Inc., Minneapolis.

Leeder, M.R. 1999. *Sedimentology and sedimentary basins: From turbulence to tectonics*. 3rd ed., Blackwell Science, Oxford.

Komar, P.D. 1987. "Selective grain entrainment by a current from a bed of mixed sizes: A reanalysis." *J. Sediment. Petrol.* 57(2): 203-211.

Komar, P. D. 2007. "The entrainment, transport and sorting of heavy minerals by waves and currents." In M.A. Mange, and D.T. Wright (Ed.), *Heavy minerals in use*, pp. 3-48. Elsevier, Amsterdam.

Peterson, C. D., P. D. Komar and K. F. Scheidegger. 1989. "Distriburion, Geometry, and Origin of heavy mineral placer deposits on oregon beaches." *J. Sediment. Petrol*. 56(1): 67-77.

Table 6.1: Properties and configurations of the numerical experiments.

Particle properties

Properties	Exp. 1	Exp. 2	Exp. 3	Exp. 4
'Quartz' diameter D_{50} [mm]	0.14	0.14	0.14	0.14
'Magnetite' diameter D_{50} [mm]	0.08	0.08	0.08	0.08
Particle number: 'quartz'	1	1	1	1
Particle number: 'magnetite'	1000	1000	980	975
Normal stiffness [N/m]	$1x10^8$	$1x10^8$	$1x10^8$	$1x10^8$
Shear stiffness [N/m]	$1x10^8$	$1x10^8$	$1x10^8$	$1x10^8$
Density ρ_s 'quartz' [kg/m³]	2650	2650	2650	2650
Density ρ_m 'magnetite' [kg/m³]	5640	5640	5640	5640
'Quartz' friction μ_s	0.5	0.5	0.5	0.5
'Mineral' friction μ_m	2	2	2	2
'Quartz' exposure z [mm]	0.4	0.35	0.3	0.2

Fluid properties

Fluid properties	Exp. 1	Exp. 2	Exp. 3	Exp. 4
Fluid density ρ_f [kg/m³]	1000	1000	1000	1000
Pore pressure ψ [mbar]	250	250	250	250
Fluid saturation φ [%]	100	100	100	100
Fluid velocity u [cm/s]	10, 15, 20, 25 and 30			

Chapter VII

SELECTIVE TRANSPORT AND FRACTIONATION OF MAGNETIC PARTICLES IN A TRANSIENT COASTAL ENVIRONMENT (TAURANGA HARBOUR AND BAY OF PLENTY, NEW ZEALAND)

Firoz Badesab, Gerhard Bartzke, Tilo von Dobeneck and Katrin Huhn

MARUM – Center for Marine Environmental Sciences and Faculty of Geosciences, University of Bremen, Germany

Abstract

Heavy (magnetic & non-magnetic) minerals are found concentrated by natural processes in many fluvial, estuarine, coastal and shelf environments with a potential to form economic placer deposits. Understanding the processes of heavy mineral transport and enrichment is prerequisite to interpret sediment magnetic properties in terms of hydro- and sediment dynamics. In this study, rock magnetic and sedimentological laboratory measurements with numerical 3D discrete element models were combined to investigate differential grain entrainment and transport rates of magnetic minerals in a range of coastal environments (riverbed, mouth, estuary, beach and near-shore). Rock magnetic measurements showed that distribution shapes, population sizes and grain-size offsets of bulk and magnetic mineral fractions hold information on the transport conditions and enrichment process in each depositional environment. A downstream decrease in magnetite grain size and an increase in magnetite concentration was observed from riverine (source) to marine (sink) environments. Lower flow velocities permit differential settling of light and heavy mineral grains creating heavy mineral enriched zones in estuarine settings, while lighter minerals are washed out further into the sea. Numerical model results showed that higher heavy mineral concentrations in the bed increased the erosion rate and enhancing heavy mineral enrichment. In beach environments where sediments contained light and heavy mineral grains of equivalent grain sizes, the bed was found to be more stable with negligible amount of erosion compared to other bed compositions. Heavy mineral transport rates calculated for four different bed compositions showed that increasing heavy mineral content in the bed decreased the transport rate. There is always a lag in transport between light and heavy minerals which increases with higher heavy mineral concentration in all tested bed compositions. The results of laboratory experiments were validated by numerical models and showed good agreement. This study demonstrates that the presented approach bears the potential to investigate heavy mineral enrichment processes in a wide range of sedimentary settings.

Keywords: Environmental magnetism, magnetic minerals, grain size distributions, numerical modeling (DEM - FDM), enrichment, transport

7.1 Introduction

Enrichment of heavy minerals in coastal environments has been well studied by numerous workers (Badesab et al., 2012; Bryan et al., 2007; Frihy and Komar, 1991; Hughes et al., 2000; Komar and Wang, 1984; Li and Komar, 1992). Magnetic and non-magnetic heavy mineral grains in sands mainly fall within the finer fraction of the total sediment population. Compared to lighter minerals such as quartz and feldspar, they possess different hydrodynamic properties due to their contrasting densities, sizes and shapes. It is well known that heavy minerals are more difficult to transport or entrain by currents in the flowing water than lighter minerals (Komar and Wang, 1984; Li and Komar, 1992; Slingerland, 1977). Due to their higher settling velocity and smaller grain sizes they tend to settle quickly and accumulate in the sediment bed forming lag deposits enriched in heavy minerals. Lighter minerals are selectively removed from the bed and transported further downstream depending onto the flow regime. The transport of heavy mineral grains in the sediment bed occurs mostly as bedload (movement on the bed) or by saltation (sliding and bouncing) rather than in suspension. Selective transport, settling, entrainment and burial plays an important role in concentrating heavy minerals in coastal environments (Frihy and Dewidar, 2003; Komar and Wang, 1984; Slingerland, 1977). These processes are schematically illustrated in Figure 7.1. During entrainment, the sediment grains moving out of the bed and entering the flow are carried along and deposited where the flow energy decreases.

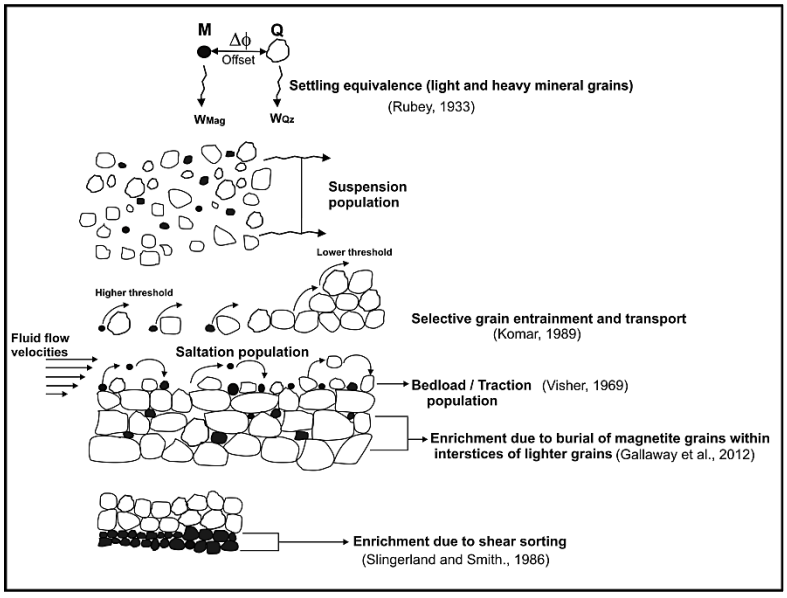

Figure 7.1: Conceptual model illustrating the entrainment, enrichment and transport processes of light and heavy minerals grains.

A recent study by Gallaway et al., (2012) highlighted the importance of burial mechanisms in the formation of heavy mineral enrichments in the swash zone. They found that magnetic minerals get rapidly buried and sheltered within the interstices of larger and lighter mineral grains under the influence of gravitation and therefore require much higher energies for their entrainment. Differential entrainment and

transport also produces variability in the enrichment patterns and grain-size distributions of heavy minerals. Furthermore, studies by Badesab et al., (2012) showed that differential rates in entrainment and transport of heavy and lighter mineral grains in combination with localized surf zone processes and littoral drift lead to the formation of coast parallel magnetite enrichment belts off a mesotidal estuarine lagoon. The grain size distribution characteristics of these coastal sediment bodies reflect their small scale transport processes. As more complex coastal morphologies, varying rates of sediment input and localized hydrodynamics also produce more complex grain size distribution patterns.

Many researchers attempted to characterize depositional processes and environments based on grain-size distribution of sediments (Gao and Collins, 1992; Inman, 1949; McLaren, 1981; Moss, 1962). The statistical parameters mean, dispersion, skewness and kurtosis were mostly used to investigate the effects of sediment transport on grain size distributions, but also to characterize the depositional environments (Mason and Folk, 1958; McLaren, 1981; Pettijohn. J. et al., 1972). Visher (1969) described a method to determine the modes of sediment transport by analyzing the log-normal probability curves of cumulative grain size distributions. The sieved grain size distribution data was plotted against normal probability percentage scale. His method was based on the hypothesis that each grain-size mode could be linked to particular type of sediment transport. Straight lines connecting several points of a given grain size distribution were used to subdivide the grain-size spectrum according to the various transport modes traction (bedload), saltation (mix load) and suspension (wash load) (McQuivey and Keefer, 1969).

Settling velocities of different mineral grains play a key role in enrichment processes. The differences in the densities and the turbulence of the flow determine the settling behavior of mineral grains. Grains with lower settling velocities experience more time in the flow and are carried further by turbulent eddies compared to grain with higher settling velocities (Allen, 1970). Many researchers investigated the sorting of heavy and light mineral grains during transport and deposition in function of their different settling velocities. According to concept of hydraulic equivalence developed by (Rubey, 1933), smaller and denser grains such as magnetite will have the same settling velocity compared to larger and light quartz grains in any given conditions. (Baba and Komar, 1981) determined the settling velocities of heavy minerals and quartz sand grains with spherical shapes. They showed that differences in the settling rates of heavy minerals mostly occur due to the grain sphericity and asymmetries. The application of this concept in our present study has been described in detail in the methods chapter.

Magnetic minerals are abundant in coastal environments and are found concentrated in association with other heavy minerals as lag deposits in fluvial, estuarine, beach and nearshore regions. They have been widely used as a markers to provide information on sediment source, transport, deposition, identifying the areas of erosion and accretion, to assess heavy metal pollution and to examine hydrodynamic conditions in coastal regions (Bloemendal et al., 1992; Booth et al., 2005; Cioppa et al., 2010; Maher et al., 2009;

Oldfield and Yu, 1994; Razjigaeva and Naumova, 1992; Robinson et al., 1995; Wheeler et al., 1999; Zhang et al., 2007).

Magnetic measurements are fast, cost-effective and help to characterize the sediment in terms of their concentration, mineralogy and grain size (Booth et al., 2005; Lees and Pethick, 1995; Oldfield and Yu, 1994; Walden et al., 1997). Magnetic mineral grain-size distributions can be easily quantified by sieving the total sediment and measuring the magnetic susceptibility of each sieve fraction, which is not much influenced by particle size. Thus it is possible to compare bulk sediment grain-size distribution against magnetite grain-size distribution, a strategy which is promising to demonstrate differences in the transport modes of light and heavy mineral grains.

So far environmental magnetic studies on coastal sediments were mainly focused on mapping the spatial distribution of magnetic minerals, examining the sediment sorting mechanism, estimating the cross-shore and longshore transport and detecting burial mechanism of magnetic minerals in coastal sediments (Cioppa et al., 2010; Gallaway et al., 2012; Hatfield et al., 2010; Zhang et al., 2007).

The role of density and grain size on the transport dynamics and fractionation of magnetic minerals in coastal environments has not yet received enough attention. The motivation for the present study was based on the findings of Badesab et al., (2012) who used the environmental magnetic approach to investigate the mechanism of magnetite enrichment in estuarine, nearshore and inner shelf region of Tauranga Harbour.

Prior studies traditionally used analogue, laboratory based techniques (i.e. flume tanks) as well as field investigations, to determine the physical processes causing selective grain entrainment and, hence, placer enrichment (Komar, 2007).Therefore, researchers focused on the relation of fluid forces causing particle motion by testing a variety of sediment samples differing in sediment composition, grain size, and density. Their findings were presented as conceptual models based on experimental results and theoretical assumptions. A recent overview of these experiments can be found in Komar et al., (2007). However, these analogue techniques are limited in their ability, e.g., due to low resolution within the sensor range, the measurement of sediment erosion in the direct vicinity of the sediment surface and in the interior of the bed on a grain scaled level is limited by using such techniques. Consequently, it is extremely difficult to identify and quantify the physical processes causing selective grain entrainment from flume experiments. In particular the quantification of the processes occurring at the sediment water interface (Komar, 2007), and in the deeper parts of the bed (Bartzke and Huhn, 2012) is limited.

Numerical simulations are therefore required to clarify, and in particular, to quantify heavy mineral entrainment and enrichment processes. A high resolution 3D numerical modeling approach was used by coupling two simulation techniques – the Finite Difference Method (FDM) with the Discrete Element Method (DEM). This 3D high resolution model parameterizes general settings of analogue laboratory flume tanks to investigate the physical properties controlling heavy mineral accumulation (Bartzke and

Huhn, 2012). This technique allows the detection of heavy mineral accumulations and can concurrently reduce expensive and time consuming exploration activities for mining heavy mineral placers in the marine environment.

The aims of the present study are to:

1. analyze and compare the grain size and magnetite distribution curves of sediments to investigate the transport modes, entrainment and deposition of lighter and heavier (magnetic) mineral grains in fluvial, riverine, estuarine, beach and nearshore sands within a single field setting of Tauranga Harbour, and
2. use a 3D high resolution numerical flume tank model to quantity the influence of flow velocities on numerical "sediment" bed in terms of density, grain sizes (offset), and light and magnetic mineral concentration on selective entrainment.

7.1.2 Study area

The study area chosen is a mesotidal estuarine lagoon located on the Bay of Plenty coast on the North Island of New Zealand (Figure 7.2).

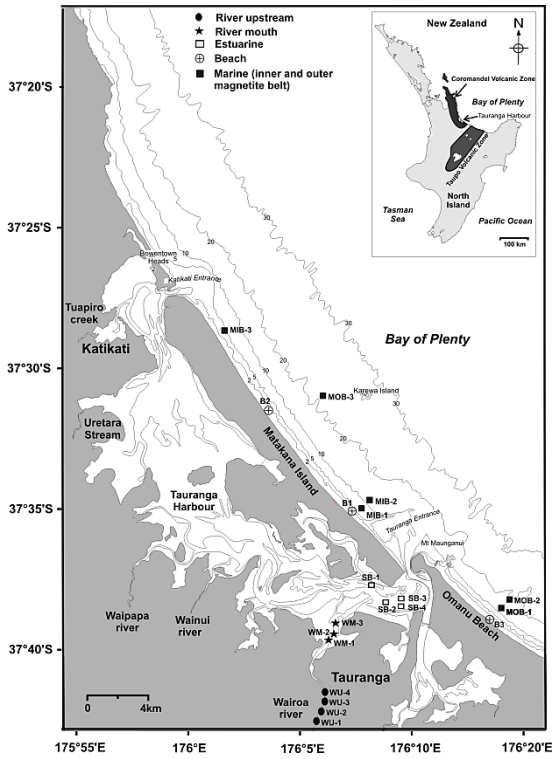

Figure 7.2: Location of study area and sediment sampling sites covering Wairoa river upstream, mouth, estuarine (southern basin of Tauranga Harbour), Beach (Matakana) and marine (off Tauranga Harbour) region in Bay of Plenty, New Zealand.

Tauranga Harbour has an area of 851 km^2 and is bounded by two Holocene barrier tombolos (Bowentown at the northwestern and Mt Maunganui at the southeastern end) and a 24 km long barrier island (Matakana Island). Tidal currents dominate both the northern and southern inlet of Tauranga Harbour. At the southern inlet there is a mean tidal range of 1.4 m and mean annual significant wave height of 0.5 m (De Lange, 1991; Krüger and Healy, 2006). The Taupo Volcanic zone (TVZ) and Coromandel Volcanic zone (CVZ) provide the main sediment supply to the Bay of Plenty coast. The majority of sediments reaching the southern basin of Tauranga Harbour are delivered by the Wairoa River, which is the main source of freshwater to the basin with a mean flow of 17.6 $m^3 s^{-1}$. The sedimentation load is approximately 28,000 tonnes annually which constitutes around 42 % of the total riverine load entering the lagoon. Most of the sediments within the harbour are transported through two tidal channels (Western and Cutter) before they move out of the lagoon and are deposited along Matakana Beach. The regional geology and wave climate has been described in detail by Badesab et al. (2012).

7.2 Methods

7.2.1 Sample Collection and laboratory measurements

25 sediment samples representing fluvial (Wairoa River), estuarine (Tauranga Harbour), beach (Matakana Island) and nearshore environments (inner and outer magnetite enrichment belts) were sieved into 17 fractions including <10, 10, 20, 32, 40, 63, 90, 125, 180, 250, 355, 500, 710, 1000, 1400, 2000 and 2800 µm. The fluvial, riverine and beach samples were collected using a clean plastic shovel to retrieve the top few centimeters of sediment by hand while the estuarine and nearshore samples were retrieved using a Van Veen grab sampler during sediment sampling surveys in February 2010 onboard coastal research vessel *Tai Rangahau*, University of Waikato, Hamilton, New Zealand. Each fraction was weighed to determine the total grain size distribution. Magnetic susceptibility measurements were carried on these sieve fractions using a KLY-2 Kappabridge to estimate their ferrimagnetic mineral concentration. The magnetite-equivalent distribution curves were generated by multiplying the bulk weight percentages with these magnetic susceptibility data. The grain size statistical parameters (mean, dispersion and skewness) were calculated following the moments method of Krumbein and Pettijohn (1938).

7.2.2 Background

7.2.2.1 Calculation of offset in mean grain sizes of light (quartz) and heavy (magnetite) minerals

The transport and deposition of individual mineral grains depends on their respective settling velocities and the intensity of the fluid flow. The difference in densities and grain sizes of mineral grains creates differential rates of movement and settling of sediments. According to the settling equivalence concept of Rubey (1933), the mean grain size of the magnetite is smaller compared to mean grain size of quartz grains and both grains have similar settling velocities in any given hydraulic condition. Baba & Komar (1981) measured the settling velocities in suites of quartz and heavy mineral grains. From these curves, it is possible to determine the settling equivalences of lighter (quartz) and heavier (magnetite) minerals by plotting a horizontal line of constant velocity passing through their respective curves. The points of intersection on each curve on phi scale would represent their individual mean grain sizes. Our work is based on the hypothesis that the difference in their mean grain sizes (offset) reflects the individual grain settling behavior, hydrodynamic and depositional environment.

According to Stokes law, the settling velocity (W_S) of a grain is given by:

$$W_S = \frac{2(\rho_g - \rho_f)g}{9\mu} r^2 \qquad (1)$$

where ρ_g and ρ_f are grain and fluid densities, g is the acceleration due to gravity, r is the radius of the grains and μ is the dynamic viscosity. We now assume a magnetite and a quartz grain

$$W_{mag} = \frac{2(\rho_{mag} - \rho_{H_2O})g}{9\mu} r_{mag}^2 \quad (2)$$

$$W_{Qz} = \frac{2(\rho_{Qz} - \rho_{H_2O})g}{9\mu} r_{Qz}^2 \quad (3)$$

where ρ_{mag} = 5.2 g/cm³, ρ_{Qz} = 2.65 g/cm³ and ρ_{H_2O} = 1g/cm³

If the grains are in settling equivalence (Rubey, 1933), i.e W_{mag} = W_{Qz}, then equation is solved as follows:

$$\frac{2(\rho_{Mag} - \rho_{H_2O})g}{9\mu} r_{Mag}{}^2 = \frac{2(\rho_{Qz} - \rho_{H_2O})g}{9\mu} r_{Qz}{}^2 \quad (4)$$

$$\frac{r_{Mag}{}^2}{r_{Qz}{}^2} = \frac{(\rho_{Qz} - \rho_{H_2O})}{(\rho_{Mag} - \rho_{H_2O})} \quad (5)$$

$$\log_2 \frac{r_{Mag}}{r_{Qz}} = \log_2 \left[\frac{(\rho_{Mag} - \rho_{H_2O})}{(\rho_{Qz} - \rho_{H_2O})} \right]^{1/2} \quad (6)$$

In the logarithmic scale, Φ corresponds to a constant size offset of magnetite and quartz grains given as

$$\Delta\Phi = -\log_2 d_{Mag} + \log_2 d_{Qz} = -\log_2 \frac{d_{Mag}}{d_{Qz}} = \log_2 \sqrt{\frac{(\rho_{Mag} - \rho_{H_2O})}{(\rho_{Qz} - \rho_{H_2O})}} = 1.432 \quad (7)$$

7.2.3 Numerical methods

For the quantification of the influence of increasing amounts of heavy minerals in sediment beds on sediment erosion behavior and placer enrichment at the sediment water – interface and in the interior of the sediment bed a high resolution 3D numerical ‘flume tank’ was used (Figure 7.3). In order to simulate sediment transport by a moving fluid, we combined two independent numerical simulation techniques, the Finite Difference Method (FDM) and the Distinct Element Method (DEM). Therein, the FDM model

calculates the flow conditions (Fluid model, Figure 7.3) and the DEM model simulates the 'sediment' matrix (Sediment matrix model, Figure 7.3). Both were coupled via an Input Output routine which will be described in section 7.3.4.

The 3D FDM Fluid model was generated using the commercial software FLAC 3D (Fast Ligurian Analysis of Continua; (Itasca, 2004b)). This technique is based on the spatial discretization of the study domain into a grid of a finite number of three dimensional rectangular polyhedral elements (Figure 7.3 (Itasca, 2004b)). The software allows the assignment of physical material properties, i.e. fluid parameters, to each cell in the grid, e.g., fluid density, viscosity etc. in order to mimic natural conditions. In addition, boundary conditions, e.g., inflow velocities and fluid sources, have to be applied to the model. Consequently, this FDM model calculates flow velocities in each grid cell driven by applied boundary conditions. Therefore the differential flow equations are approximated by numerical differentiation in defined time steps (Itasca, 2004b).

At the same time, a DEM model was used to mimic 'sediment beds' numerically. These were simulated as a particle assembly consisting of multiple, ideal and spherical particles, i.e., numerical 'quartz' and 'magnetite' grains (Figure 7.3). The software, i.e., PFC 3D, (Particle Flow Code; (Itasca, 2004a)), is based on the DEM theory by Cundall and Strack (1979) which describes the mechanical behavior of particle assemblages based on physical contact laws. In order to mimic natural conditions, physical properties such as density, friction or hardness were assigned to each particle (Table 7.3). Similar to FDM model, boundary conditions have to be defined e.g., gravity, ball acceleration etc.. The resultant particle assemblages or the 'sediment body', respectively, are deformable by these applied forces. Consequently, DEM model allows the simulation of sediment particles, sediment particle interactions, internal structures, and also porosities. Thus, the method simulates the physical behavior of the particle assemblages during deformation processes, e.g., the initiation of motion of single spherical grains driven by defined boundary conditions, e.g. fluid forcing (Figure 7.3).

A more detailed review of the involved algorithms of the FDM and DEM exceeds the scope of this paper. A complete description of the numerical procedure of the FDM code can be found e.g., in Itasca (2004a). Further descriptions of the numerical DEM code can be found in e.g., Cundall and Hart (1989), Cundall and Strack (1979, 1983), Itasca (Itasca, 2004a), and Kock and Huhn (2007). Please note that in the following the term grains as well as sediment will be used, interchangeably whether the context is related to numerical or real grains at the same time. The same applies to quartz and magnetite respectively.

7.2.3.1 Model configuration

Numerical sediment beds (Figure 7.4) consisting of various amounts of heavy and light particles were generated to quantify of the physical processes controlling selective grain entrainment with respect to erosion behavior. In the following all sediment beds were exposed to a range of flow velocities. For

simulation of fluid motion and particle transport with the 3D numerical flume tank, both the DEM and the FDM models had identical dimensions (1.8 x 0.9 x 1.2 mm), geometries, material properties as well as boundary conditions (Figure 7.3). At the beginning of the simulation, the grain or sediment model was generated, isolating a micro-scale section of the sediment surface, from a sediment bed. In order to mimic a sediment bed numerically, a sample box was generated with the dimensions of 1.8 mm x 0.9 mm, and 1.2 mm in height, to be filled with the numerical sediment. Therein, 5 stiff un-deformable box walls were created (Table 7.3).

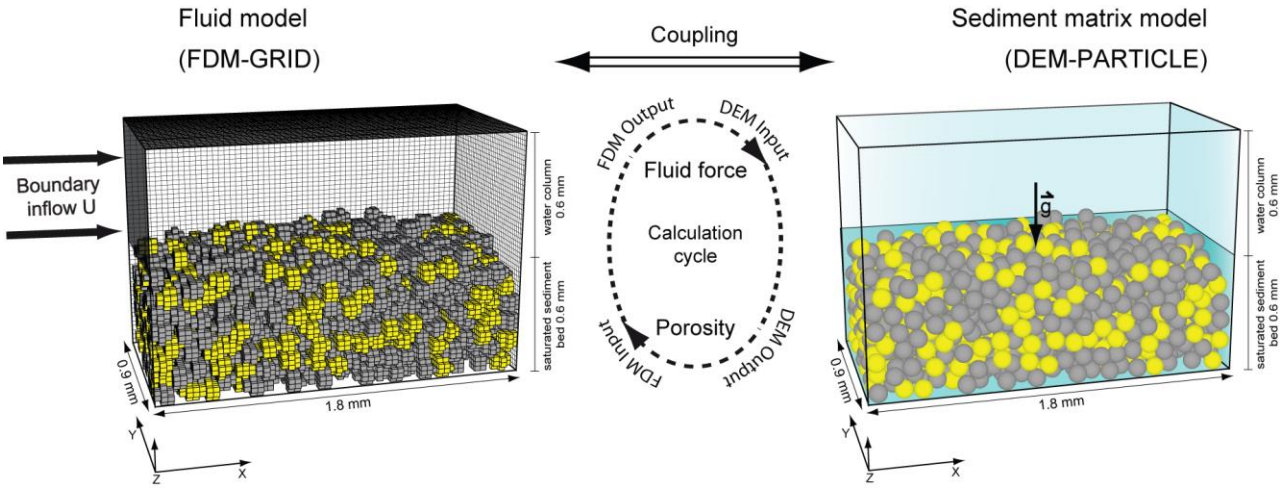

Figure 7.3: Sketch of the coupled Sediment matrix model (DEM - discrete elements method) and the Fluid model (FDM - finite difference method).

For the generation of the sediment beds (Figure 7.4), two end members were used as a simplified treatment of, heavier, numerical magnetite grains ($\rho m = 5.1$ g/cm³) and lighter i.e., numerical quartz grains ($\rho q = 2.6$ g/cm³). In order to quantify the influence of increasing heavy mineral contents of heavy minerals on sediment erosion, three numeric sediment beds were generated. These were composed of randomly distributed heavy magnetite and light quartz particles in the same grain size (D50 = 0.09 mm) and filled always half of the box (Figure 7.4). Within each experiment, the amount of quartz with respect to magnetite particles in the bed was changed: Experiment 1) 70 % magnetite and 30 % quartz (i.e., 889 magnetite and 381 quartz particles), Experiment 2) 30 % magnetite and 70 % quartz (i.e. 381 magnetite and 885 quartz particles), and in Experiment 3) 50 % magnetite and 50 % quartz (i.e. 635 magnetite and 635 quartz particles). For the quantification of grain size related effects in heavy and light mineral sediment beds one sediment bed (Experiment 4) was created by using magnetite (D50 = 0.09 mm) and larger numerical quartz grains (D50 = 0.128 mm). In this case 50 % magnetite and 50 % quartz (i.e. 350 magnetite and 350 quartz particles) were deposited into the box. Please note that all grains in the experiments were deposited under gravity and randomly distributed in the entire box. This ensures natural depositional conditions and packing. Physical properties, i.e. density, friction, normal stiffness, and shear stiffness were assigned to each particle with respect to natural conditions (Table 7.3).

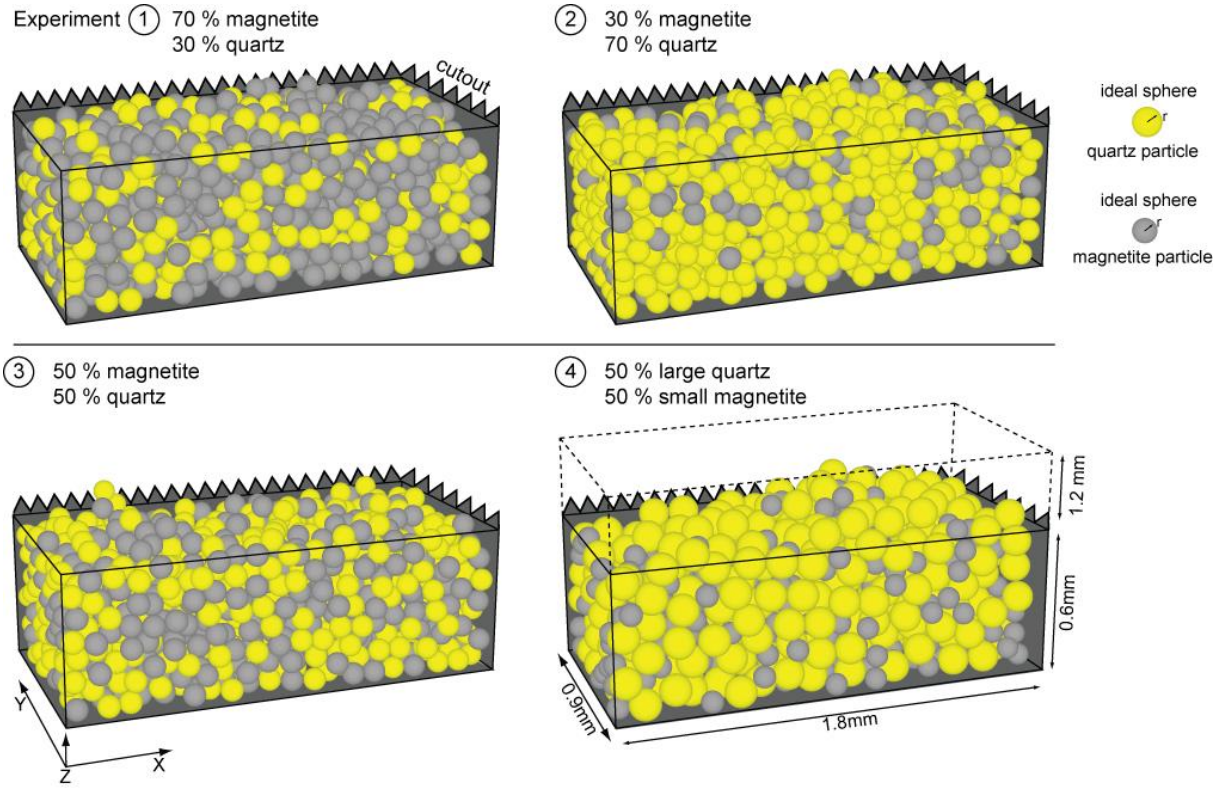

Figure 7.4: Four types of numerical sediment beds: Magnetite (gray particles) and quartz (yellow particles) were deposited under applied gravity into a sample box. The number of magnetite and quartz particles was variable and ranged from: Experiment 1) 889 magnetite and 381 quartz particles, Experiment 2) 381 magnetite and 885 quartz particles, and in Experiment 3) 635 magnetite and 635 quartz particles. In Experiment 4) the grain size of the quartz particles was increased therefore 350 magnetite and 350quartz particles were deposited.

For the simulation of a flow field the Fluid model was generated by using the FDM model (Figure 7.3). The spatial extensions of this Fluid model were chosen with identical dimensions as the Sediment matrix model. In order to simulate flow fields in highest resolution, the FDM grid was discretized into 288.000 elements (60x60x80 in X, Y and Z directions) with a uniform axes length of 0.025 mm (Figure 7.3). Hence, the smallest DEM grains are represented by at least 8 elements to ensure stable coupling between the FDM – DEM model. The corresponding fluid properties were applied to the Fluid model (Table 7.3) to simulate natural coastal conditions based on the literature (Allen, 1970) and to exclude any scalar discrepancies. The entire box model is flooded generating a fully saturated sediment bed.

Coupling of both models was undertaken after generation of these initial model configurations. In the first step, all information about from the sediment matrix, e.g. the spatial parameters x, y, and z coordinates and the radii of all particles, were sent from the DEM to the FDM model. Based on these data representing the grain distribution within the DEM model, the FDM grid elements are defined as either fluid cells or sediment cells. The resulting FDM model grid consists of elements where fluid streaming was allowed (fluid zones) or not allowed (solid matrix zones). After the grid was classified, a constant inflow above the

fully saturated bed field was applied in x-direction at left box wall (Figure 7.3). Starting with these initial stable conditions, a constant stream in positive x-direction above the sediment bed evolved. All flow velocities were calculated from cell to cell throughout the whole model (in the water column and the saturated matrix area) based on the initial porosity distribution. After the flow field reached stable conditions, all flow velocities were extracted. These flow velocities were transformed into forces according to the Stokes velocity law. These fluid forces were sent to the sediment matrix model at their corresponding X-Y and Z coordinates and applied to their corresponding particles. These velocity parameters serve now as boundary conditions for the Sediment matrix model. Based on this forcing, new particle contact forces and resulting particle displacements are calculated in the DEM model. If the added fluid forces are larger than the resisting force of the particles, the particle contacts break up and the grains are transported (Cundall and Strack, 1979).This caused new porosities within the DEM model and new particle configurations respectively. Hence, sediment transport and / or grain re-assembling is initiated. In cases grains are eroded from the matrix they are transported by the stream. The resultant new porosities (Sediment matrix model) were sent back to the Fluid model, and subsequently a re-meshing of the FDM model grid was initiated and a new calculation cycle starts.

This calculation cycle between both models was repeated until constant flow and transport conditions were reached. Whereby each model was coupled 140 times to ensure that the results were statistically stable and analyzable. Hence, high resolution information about, e.g., particle distribution, porosity, texture, and fluid velocities at the sediment surface as well as in the interior of the sediment matrix is available in space and time. The applied boundary flow velocities were stepwise increased from U = 10 cm/s, 20 cm/s, 30 cm/s, and 40 cm/s.

7.2.3.2 Measurements and data statistics

To quantify the influence of increasing amounts of heavy minerals in sediment beds on sediment erosion behavior and placer enrichment we analyzed variations of particle positions and particle displacements at each time step in horizontal and vertical directions. All data has been processed using programmed routines in FLAC 3D, PFC 3D, and Matlab 2011 environments. These analyses revealed high resolution data of the particle transport distances in the sediment bed.

7.2.3.3 Transport distances

The total transport distance of singles grains was calculated within each Sediment matrix model as the difference between the initial and the final position after reaching steady state flow conditions. For further analyses only particles were considered which exceeded their own radius, which is considered as threshold for transport. Particle transport changes were extracted from a horizontal volume at the interface between sand and silt (0 mm $\leq z \leq$ 0.3 mm; Base Slice in Figure 7.8). A similar procedure was processed for the

uppermost sediment portion (0.4 mm ≤ z ≤ top of sediment bed; Top Slice in Figure 7.8). In addition particle transport changes were extracted from a vertical volume (0 mm ≤ x ≤ 0.4 mm; vertical box in Figure 7.9). For comparison, the individual transport distances of magnetite and quartz particles were calculated the separately. Hence, the amount of transported quartz and magnetite particles was plotted as a percent in a horizontal bar plot.

7.4 Results

7.4.1 Analysis and comparison of bulk sediment grain size and magnetite distribution curves (log probability & cumulative) of representative samples from various depositional environments

The samples collected from various depositional environments including river upstream and mouth (Wairoa River), estuarine (Tauranga Harbour), Beach (Matakana Beach) and Marine inner and outer magnetite enrichment belt (off Tauranga harbour, Bay of Plenty) sediments were analyzed to gain information on the grain settling, transport and enrichment mechanism. Here the distribution curves of each sedimentary environment are described separately. Figure 7.5 shows the comparison of log probability curves of bulk sediment and magnetite distributions of representative samples.

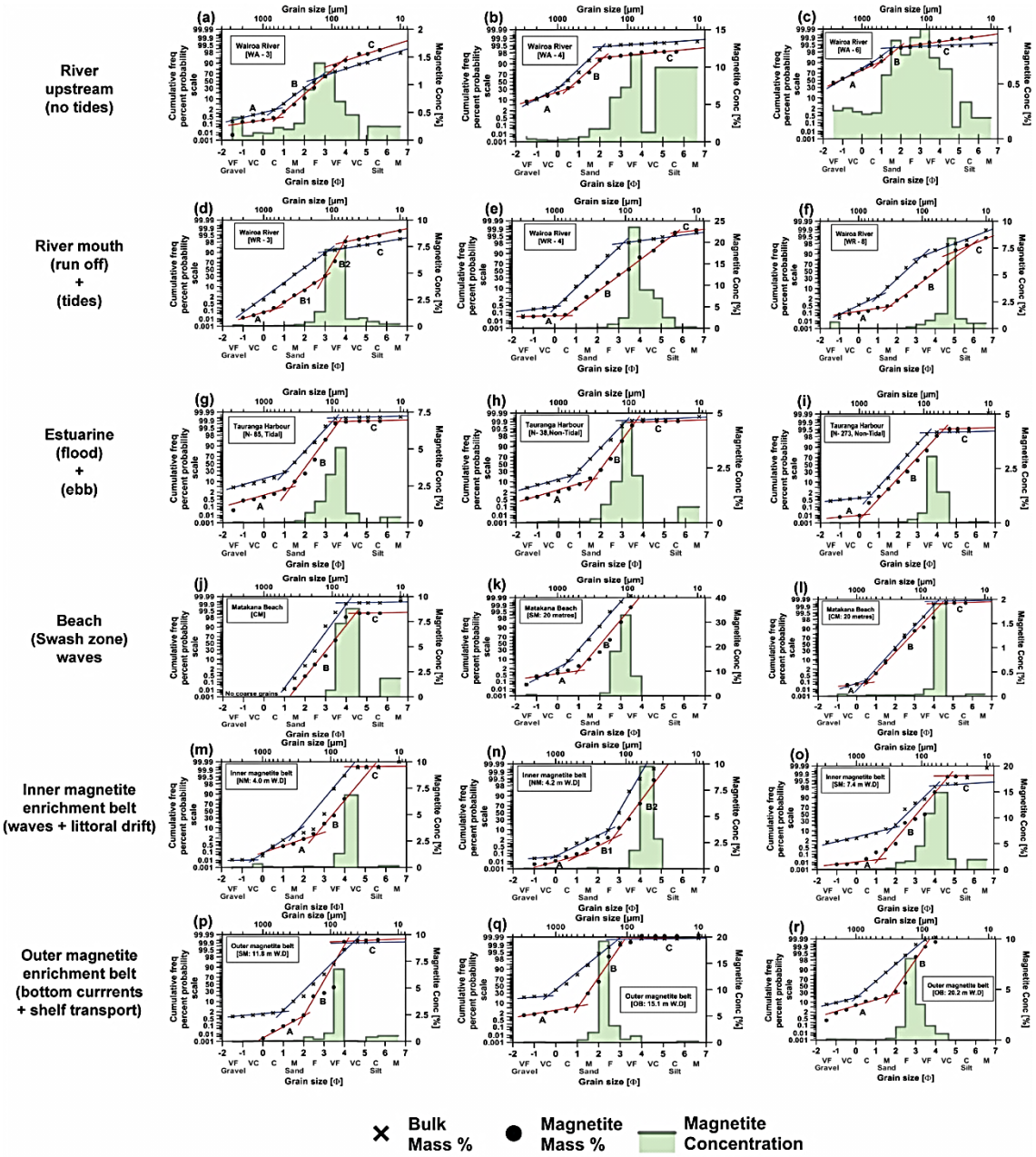

Figure 7.5: Examples of log probability curves for bulk sediment and magnetite fraction of representative samples from various depositional environments. I) Wairoa River upstream, II) Wairoa River mouth, III) Estuarine (Tauranga Harbour), IV) Beach (Matakana Beach), V) Marine: Inner magnetite enrichment belt and VI) Outer magnetite enrichment belt off Tauranga Harbour.

7.4.1.1 Wairoa River upstream

Examples of distribution curves for bulk sediment and magnetite grain size of samples from river upstream are shown in Figure 7.5 (a-c). The log probability curves for the representative samples indicate that sediments were mainly transported as two major population a) saltation and b) suspension as indicated in Figure 7.5 (a-c). The distribution shows well sorted saltation and suspension population developed within narrow range of total distribution.

The traction population has a size range from -2.0 to 0.5 phi with a truncation point at 0.5 phi. The break between traction (bedload) and saltation is mostly found at 0.5 phi, which is mainly in coarse sand. The percentage of saltation and suspension population of magnetite grains are in the range from (59.0 - 62.5 %) and (0.85 – 39 %) respectively (Table 7.1). The break between saltation and suspension population is between 2 – 3 phi fine sand range, except sample WA-6 which does not possess traction population. The distribution of magnetite in river upstream and mouth samples are similar. The cumulative distribution curve shows that the magnetite is mostly concentrated with the range of very fine - fine – medium sand size with highest values in fine sand size grains Figure 7.6 (a-c). The offset between the bulk sediment and magnetite distribution ranges between 0.1 – 0.6 phi (Table 7.2).

7.4.1.2 Wairoa River mouth

Three distribution curves for bulk sediment and magnetite grain size of river mouth samples are shown in Figure 7.5 (d-f). The log probability curves shows that mode of transport was similar to that of upstream samples i.e. two major population saltation and suspension, with saltation population being dominant. The distribution shows moderately sorted saltation and suspension population developed within narrow range of total distribution. The traction population has a grain size ranges from -2.0 to 1.5 phi with a truncation point at 1.5 phi. The break between traction (bedload) and saltation population varies in the range between 0.5 – 1.5 phi, which represents mainly medium - coarse sand. The percentage of saltation and suspension population of magnetite grains are in the range from (68.2 – 99.65 %) and (0.2 – 5.3 %) respectively (Table 7.1). The break between saltation and suspension population is between 0.5 – 5.5 phi, i.e. coarse silt – coarse sand range. The cumulative distribution curves shows that the magnetite is mostly concentrated with the range of very fine sand size Figure 7.6 (d-f). The offset between the bulk sediment and magnetite distribution is highest compared to rest of the environments and ranges between 1.3 –1.9 phi (Table 7.2).

7.4.1.3 Estuarine (tidal & non tidal channel)

Examples of distribution curves for bulk sediment and magnetite grain size of samples from estuary are shown in Figure 7.5 (g-i). The log probability curves for the representative samples indicate that sediments were as transported as all three populations (traction, saltation and suspension). The distribution shows well sorted saltation and suspension population developed within broad range of total distribution, compared to traction population. The traction population has a size ranges from -1.5 to 1.5 phi with a truncation point at 1.5 phi, except one sample which has much smaller truncation (0.0 phi) compared to other samples. The break between traction (bedload) and saltation population are in the range of 0.5 – 4 phi. The percentage of traction, saltation and suspension population of magnetite grains are in the range from (0.005 – 11.4 %), (87.7 – 98.1%) and (0.25 – 1.6%), respectively (Table 7.1). The break between

saltation and suspension population is between 1.5 – 4 phi. The cumulative distribution curves shows that the magnetite is equally distributed within the range of very coarse silt – very fine sand Figure 7.6 (g-i). The offset between the bulk sediment and magnetite distribution ranges between 0.4 – 1.4 phi (Table 7.2).

7.4.1.4 Matakana Beach

The distribution curves for the bulk sediment samples form Matakana Beach are illustrated in Figure 7.5 (j-l). The log probability curves indicate that sediments were mainly transported as two major population saltation and suspension with hardly any traction population. The distribution shows well sorted saltation and suspension population. The traction population was lacking from the total distribution. The percentage of saltation and suspension population of magnetite grains are in the range from (98.2 – 99.86 %) and (0.01 – 0.9 %) respectively, with suspension population being dominant (Table 7.1). The break between saltation and suspension population is between 1.5 – 4.5 phi i.e. very coarse silt – medium sand range. The cumulative distribution curves shows that the magnetite is mostly concentrated within the range of very coarse silt fraction Figure 7.5 (j-l). The offset between the bulk sediment and magnetite distribution ranges between 0.7 –1.0 phi (Table 7.2). Interestingly, a zero offset in one of the beach sample was observed (Figure 7.6i).

7.4.1.5 Marine (inner and outer magnetite enrichment belt)

Examples of distribution curves for bulk sediment and magnetite grain size of samples from inner and outer magnetite enrichment belts are shown in Figure 7.5 (m-r). The log probability curves for the inner belt samples indicate that sediments were transported mainly as saltation population with minor load transported as traction and suspension population. The saltation population has a size ranges from 0 to 3.5 phi with a truncation point at 1.5 phi. The break between traction and saltation population are in the range of 1 to 4 phi. The percentage of traction, saltation and suspension population of magnetite grains are in the range of (0.025 – 1.95 %), (2.9 – 97.9%) and (0.01 – 4.7%), respectively (Table 7.1). The cumulative distribution curves show that the magnetite is distributed with the range of very coarse silt – very fine sand Figure 7.6 (m-o). The offset between the bulk sediment and magnetite distribution ranges between 0.5 – 1.2 phi (Table 7.2).

The curves for the outer belt samples showed that sediments are mostly transported as traction and saltation population with minor amount of load as suspension population (Figure 7.6 p-r). The percentage of traction, saltation and suspension population are in the range of (0.99 – 19.8 %), (79.9 – 98.9%) and (0.05 – 0.09 %), respectively (Table 7.1). The cumulative distribution curves shows that the magnetite is contained in the range of very fine to fine sand. There appears to be a shift in the magnetite distribution in all three samples varying between very fine – fine sand Figure 7.6. (m-o). The offset varies between 0.4 – 1.3 phi.

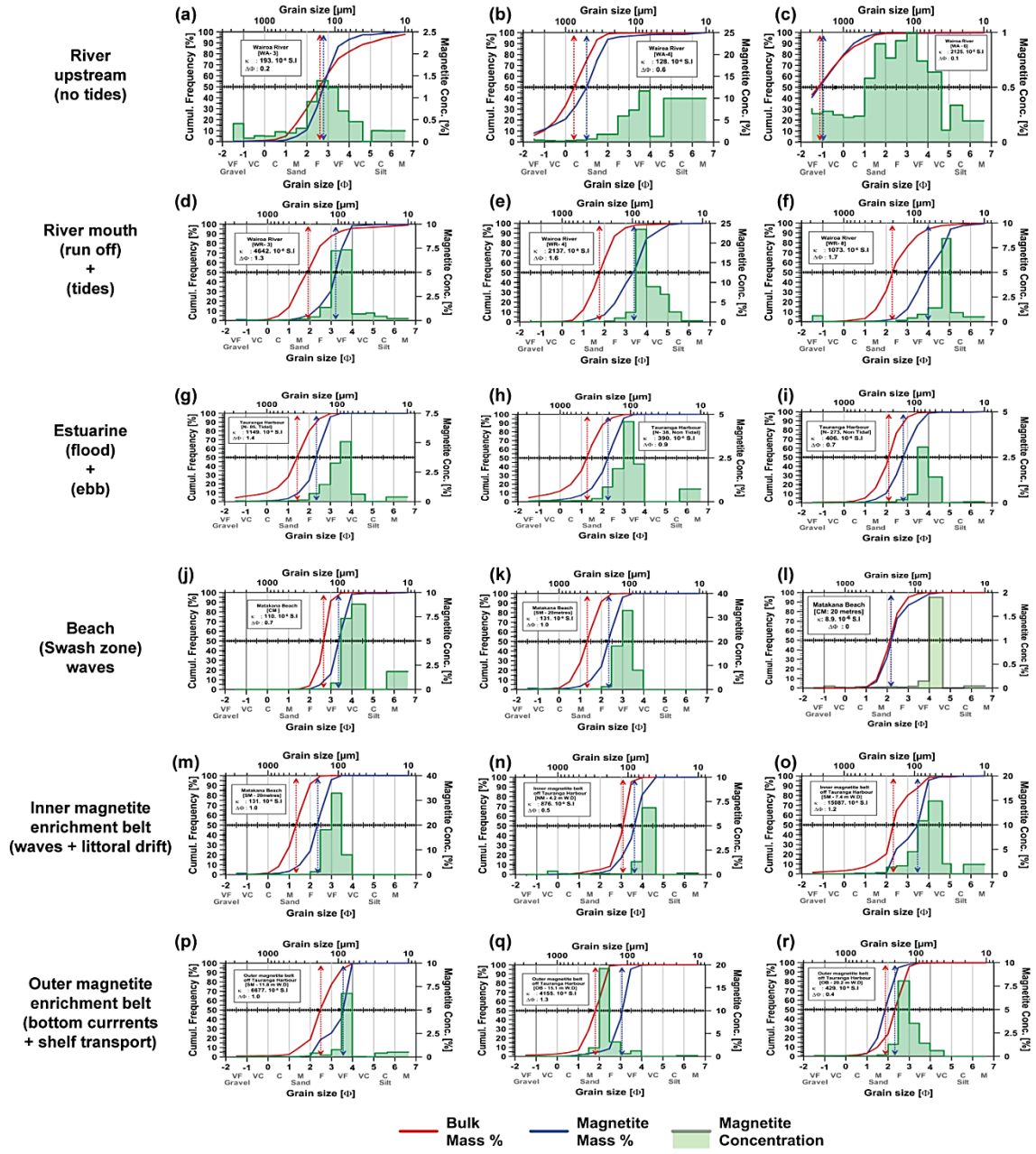

Figure 7.6: Cumulative curves for bulk and magnetite distribution of samples from range of depositional environment. The black dots in the plot represent the mean grain size of bulk & magnetite fraction calculated using mathematical method proposed by Krumbein and Pettijohn, (1938).

7.4.2 Distribution of the statistical parameters

Statistical parameters calculated from grain size distribution provide information on the energies of the depositional environments. The statistical parameters (mean, dispersion, and skewness) of river upstream, mouth, estuary, beach and marine samples were analyzed (Figure 7.7). Table 7.3 provides details on the statistical parameters used in the study. Overall the mean grain size of magnetite ranges between 1.0 – 4.0 phi scale i.e. (very coarse silt – medium sand). Figure 7.7a shows the plot of mean grain size for different depositional environments. We observed a trend in increase in mean grain size (phi) of magnetite grains in the samples originating from Wairoa river mouth to marine sands. Marine sands seem to possess finer size magnetite grains and have highest bulk magnetite content; upstream riverbed sediments are coarsest and show lower magnetite concentrations. Figure 7.7b shows the bivariate scatter plot of skewness versus mean grain size. This parameter mainly shows the asymmetry of the probability distribution in bulk sediment and magnetite grain size distribution. The bulk sediment grain size distribution appears to be more positively skewed with marine sample had highest skewness compared to magnetite grain size distributions.

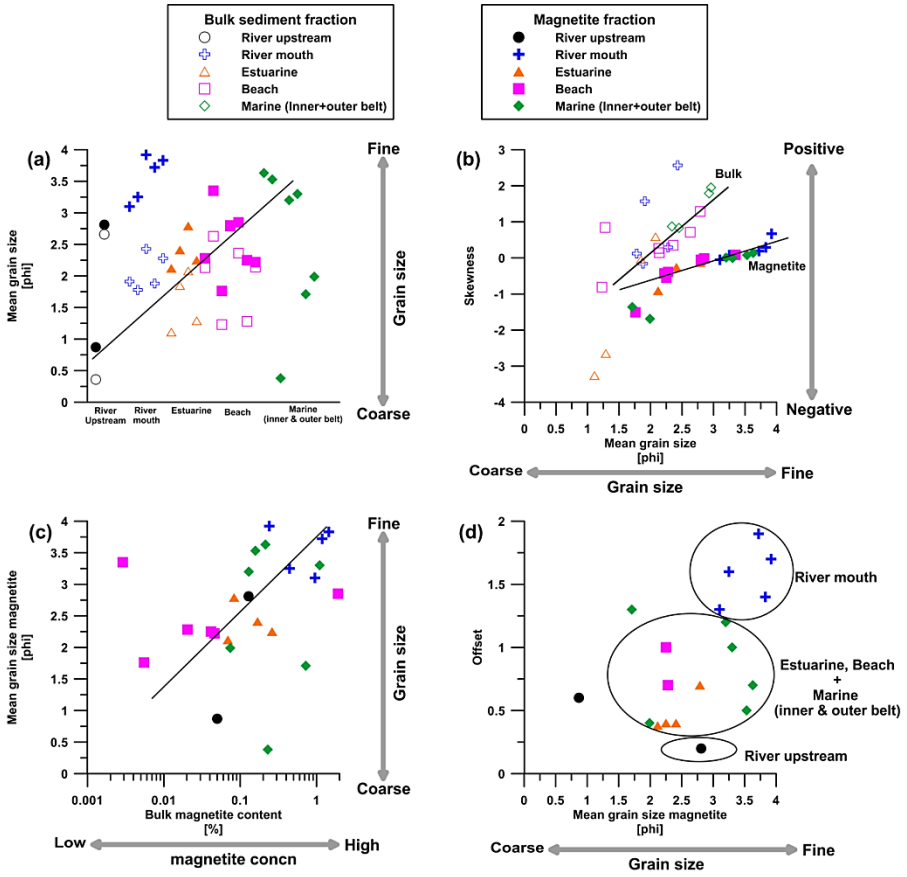

Figure 7.7: Bivariate scatter plot of statistical parameters (mean, skewness, offset) and magnetic parameters (bulk magnetite content) for sample from various environments.

Previous studies have shown that various depositional environments could be characterized based on distribution of their statistical parameters. For example magnetite rich sands from Wairoa River mouth showed finer grain sizes (3.2 – 4.0, phi scale, i.e. very coarse silt – very fine sand) and larger offset in grain sizes between as compared to the upstream samples (1.0 – 2.8 , fine - medium sand) which had lower offsets although similar grain size. It was observed that the river mouth samples are much finer and possesses higher offset samples compared to river upstream samples. Magnetite grains from estuarine, and marine sand (inner and outer) had mixed grain sizes ranging between 2.2- 3.7 phi scale i.e. very fine – fine sand (Figure 7.7d). Estuarine, beach and marine sands falls into one group. It seems to be possible to characterize the environments based on their offset and mean grain sizes into three groups a) river mouth samples which possesses a higher offset (1.25 – 2) and finer grain sizes, b) estuarine, beach and marine samples: intermediate having average offset (0.2 - 1.1) and c) Wairoa river upstream samples having lowest offset i.e. 0.1 phi (Figure 7.7d).

7.4.3 Results of the numerical simulations

For the quantification of influence of increasing amounts of heavy minerals in sediment beds on sediment erosion, and hence, placer enrichment four suites of numerical sediment beds were tested on their erosion behavior under predefined boundary inflow velocities (U = 10 cm/s, 20 cm/s, 30 cm/s and 40 cm/s). Therefore, three numerical sediment beds of randomly distributed mixtures containing heavy magnetite and light quartz particles of the similar grain size were generated (Table 7.4). Therein, the amount of magnetite with respect to quartz particles in the sediment beds was changed in each experiment (Experiment 1 - 3). In addition, Experiment 4 was created of magnetite and larger quartz grains (Table 7.4) for the quantification of grain size related effects occurring in heavy and light mineral composed sediment beds. The extracted amounts of transported particles horizontal and vertical of each Experiment are presented in Table 7.4 and 7.5. The results derived at 30 cm/s flow speed are presented as an example case in the Figure 7.8 and 7.9.

7.4.3.1 Horizontal and vertical transport rates

Comparing the horizontal transport rates of all analyzed experiments, the results showed that particle transport in x-direction was initiated at 10 cm/s. The amount of particle transport distances extracted from the top of all processed experiments at 30 cm/s flow speeds, showed generally higher amounts of quartz transport with respect to the decreasing magnetite contents in the beds (Figure 7.8).

In particularly, when comparing the results of the low, high, and medium quartz content experiments i.e., Experiment 1, 2 and 3, quartz transport increased. Therefore, the sediment bed of Experiment 1 (low quartz content) showed the lowest amounts of quartz particle transport and Experiment 2 (high quartz content) showed the highest amount of quartz particle transport. Values ranged from 6.60E-05 m

(Experiment 1) to 1.71E-04 m (Experiment 2) at 30 cm/s flow speed. Consequently, transport rates of magnetite particles extracted at the sediment surface was generally lower as compared to those of the quartz minerals. Therefore, sediment transport at the surface of the bed is clearly related to the amount of heavier magnetite particles in the sediment beds.

The amount of particle transport in the deeper parts of the bed differs to those measured at the sediment surface. Consequently, lower amounts of quartz and magnetite transport with increasing quartz content in the beds were shown. However, similar to the measurements derived from the top of the sediment bed the results showed that more quartz was transported as compared to magnetite. An increase of magnetite transport was observed, when comparing the amount of particle transport extracted in the deeper parts of the sediment bed of Experiment 1 (low quartz content) with those of Experiment 2 (high quartz content). The corresponding values of magnetite transport ranged from 2.51E-05 m (Experiment 1) to 6.68E-05 m (Experiment 2) at 30 cm/s flow speed. It is interesting to note that Experiment 1 having the lowest quartz content showed the lowest amounts of quartz transport towards depth. Whereby, quartz transport, within the higher quartz concentrated Experiment 2 and Experiment 3 increase with depth. In addition, Experiment 4, which was composed of magnetite and larger numerical quartz grains, followed the trend described in Experiment 1. Consequently, higher amounts of quartz particles were transported at the top of the sediment bed as compared to magnetite particles. Similar to Experiment 1 quartz transport was higher at the sediment surface and in the deeper parts of the bed.

The vertical transport rates extracted from all experiments at 30 cm/s flow speeds are presented in Figure 7.9. The results showed different transport distances in vertical direction with respect to the quantity of magnetite and quartz particles mixed into the bed. When comparing the results of the low, high and medium quartz content experiments, quartz transport increased and magnetite transport decreased with increasing quartz contents in the beds. Values of quartz transport ranged from -1.70E-05 m (Experiment 1) to -5.76E-05 m (Experiment 3), at 30 cm/s flow speed. Consequently, the results show that in case of the low quartz concentrated bed, magnetite was transported faster into the deeper parts of the bed compared to quartz. However, with increasing quartz content in the bed this trend is decreasing. The results of Experiment 4 showed an equivalent trend to Experiment1, wherein more of magnetite particles were transported into the deeper parts of the bed as compared to quartz particles.

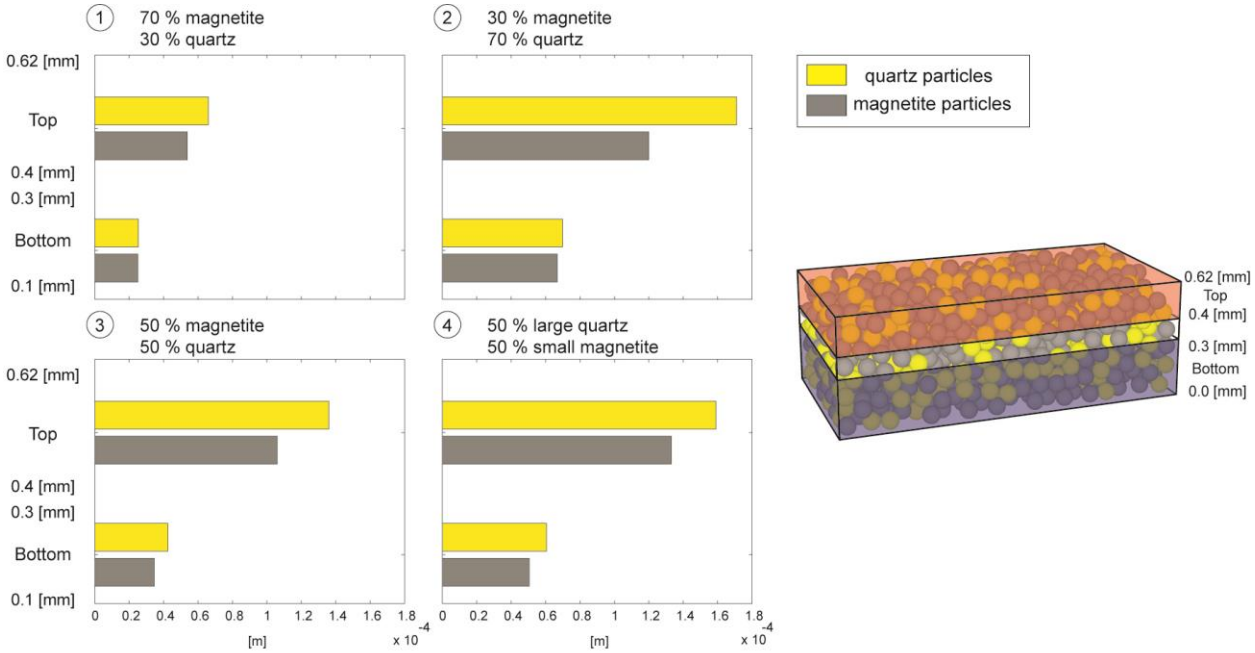

Figure 7.8: Horizontal particle transport extracted from the top and the bottom of the numerical sediment beds. The transport rates of quartz particles are illustrated in yellow color, whereas the transport rates of the magnetite particles are illustrated in gray colors. All presented transport distances were extracted at 30 cm/s boundary inflow velocity.

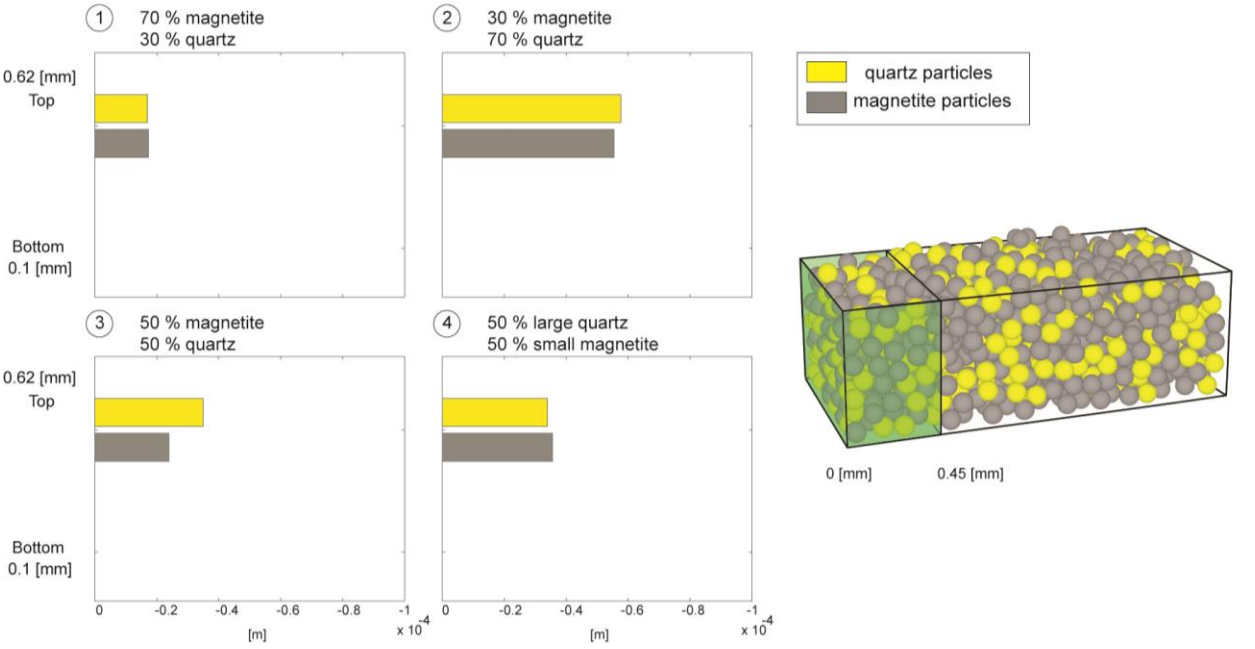

Figure 7.9: Vertical amount of particles transported in the numerical sediment beds. Transported quartz particles are illustrated in yellow color, whereas transported magnetite particles are illustrated in gray colors. All data was extracted at 30 cm/s flow speed.

7.5 Discussion

7.5.1 Interpretation and comparisons of log-probability distribution curves of bulk and magnetite grains and its implications for characterizing sediment transport and depositional environment

Generally, the grain size distributions of sediments composed of two or more populations are produced due to variable energy and transport conditions. Visher (1969) plotted cumulative distribution on log probability scale to relate the modes of each grain size to the various transport modes and depositional processes. He demonstrated that the truncation points for traction, saltation and suspension population provides information on depositional environment including sources and energy conditions. Thus the transport and deposition of magnetite grains in any of the environment depends on the dynamics of the flow conditions. Consequently, in any given flow conditions the magnetite grains will be transported as traction, saltation or suspension population over the bed and depending upon the energy conditions. It is generally observed that the magnetite grains being smaller in size and denser tends to settle faster on the bed as compared with coarser (lighter) minerals. In the present study, the three modes of transport for magnetite fraction and bulk sediment fraction for the samples representing various depositional environments are studied in detail. The magnetite distribution curves were generated from bulk sediment distribution curves by measurement of magnetic susceptibility on each sieved fractions. Around 22 representative distribution curves (log-probability and cumulative percent) of bulk sediment and magnetite properties (size, shapes of the curves and percentage of each grain size population) have been interpreted and compared to gain information on enrichment of magnetite in variable hydrodynamic environments (Figure 7.5 and 7.6). The distribution curves for magnetite in majority of the samples from different depositional environments showed that magnetite grains are mainly transported as bedload and also saltation with minor load moving as traction and suspension population (Figure 7.5 and 7.6). The variability in mean grain size and dispersion of magnetite grains from different environments suggest that it is more likely that a small portion of magnetite grains moving within grain layer populations (saltation or suspension). Further, they tend to fall on to the bed and remain deposited followed by burial resulting in formation of enrichment zones. The following sections describe the relation of magnetite grain transport (size, shape and percentage) and hydrodynamic environments. (a) river upstream, (b) river mouth, (c) estuarine (d) beach and (e) marine.

7.5.1.1 Wairoa River upstream and mouth

In river upstream environment, the flow is unidirectional and sediments transport is mostly dependent on intensities of currents velocities. Hence, the whole sediment load is carried downstream as one major population i.e. predominantly as suspension load. As soon as the flow velocities are reduced, the heavy mineral grains within the bulk sediment composition settle down and are deposited in the river bed. So, heavy minerals being finer and denser sink into the bed and form heavy mineral enriched zones. In

general, river sediments are coarser as compared to the beach sediments. This is understood due to its proximity to the source. Mostly the coarser grains population moves as traction (rolling & sliding). In the studied upstream samples it was observed that the sediment were mainly transported as saltation and suspension population which suggests that high energies in the flow carried the sediment load in this two populations and therefore traction population is not much clearly visible and lacks in few samples.

The similarity in log probability plots of magnetite distribution for Wairoa River upstream and mouth samples suggests that the magnetite grains are mainly in fine-medium grain size range. Although the higher magnetite concentration was found to occur in very fine sand, saltation population was dominant (Figure 7.5 a-c). The Wairoa River upstream samples had lowest offset compared to samples from other environments. This suggests that higher energies in the river upstream enhance the transport of magnetite grains rather than settling. As observed in most of the magnetite distribution curves, highest concentration was found to occur in very fine sand ranges in the river upstream samples and also possessed lowest mean grain size (coarsest) and highest dispersion. Whereas the river mouth samples showed highest mean grain sizes (finer) and low (consistent) dispersion (Table 7.2). This could be explained through the continuous inflow of sediments in mixed grain sizes into river due to the proximity of the source rocks. It is also possible that variability in current intensities of river run offs which would transport the magnetite grains mainly as saltation population together with the bulk sediment load. The truncation point of the saltation population is variable and found to occur between 0.5 to 4.0 phi i.e. very fine to coarse sand (Figure 7.5 d-f). This is probably due to fluctuations occurring within the flow. This causes the magnetite grains within river environment to move out of the traction (bedload) population and enters the saltation mode during its transport. The curves for samples (WA- 4 & WA -6) seem to lack the traction population. This could be attributed to sudden changes in the flow velocities within the river run off (Figure 7.5 a-c). The bulk sediment grain size distribution of river upstream samples appears to be similar to that of river mouth samples. They mainly contain low amount of traction population i.e. from 0.03 – 0.48 %. The truncation points in the river mouth samples is much different than upstream samples, this is possibly due to the interaction of tides and river run offs (currents) at the Wairoa river mouth, which generates the grain size distribution curves of various shapes and percentages.

7.5.1.2 Estuarine environment

In estuaries, due to intense interaction between waves and tidal currents grain size distribution curves of different sizes, shapes and populations are produced. The distribution curves for the samples from estuary appear to be different compared to other environments (Figure 7.5 g-i). The samples were well sorted and showed three distinct populations. Magnetite distributions in different fractions are similar to other samples. These samples represent tidal and non-tidal channel environment within the estuary in water depths of 4 – 10 m but flow energy (tides) are able to drag or lift the magnetite grain fraction into saltation

and suspension. Most of this population comes from sediment load brought by Wairoa River and delivered to the southern basin of Tauranga Harbour. The tidal channel sample showed that the saltation population has a range between 1.0 to 3 phi and its truncation point is at 1.5 (Figure 7.5g), while the non-tidal channel sample has range between 0.0 to 4.0 phi and its truncation point is at 0.5 phi (Figure 7.5i). Within tidal channel, traction population for this samples showed well sorted three distinct populations and possesses wide range (-1.5 to 1.5) phi and also higher percentage (0.005 to 11.4 %) compared to distributions from other environments. This could be due to the strong interaction of the traction population with high bottom current flow velocities within tidal channels. The higher percentages of the traction population within estuarine samples suggests that the transport of magnetite is mainly driven by bottom current velocities produced due to bi-direction flows generated as a result of ebb and flood currents / tides.

7.5.1.3 Beach samples

Analysis of log probability curves on beach samples showed that the magnetite is mostly transported as saltation population and has highest mean grain size (2.2–3.3 phi) i.e. very fine – fine sand (Figure 7.5 j-l). The lowest offset between the grain sizes of the bulk and magnetite grains could be attributed to the similarity in their grain sizes. For example in sample (CM–20m), the offset is nearly zero, this suggests that the magnetite grains mostly remain deposited along with other lighter grains and only higher energy events such as storm surges could entrain or transport this grains from the bed (Figure 7.6j–l). The traction population in this sample is very low and lacks in a few samples, since this coarse grain sizes are not available in the depositional environment. In the beach environment, especially in the swash zone where the grains move back and forth through crests and troughs, but finally remain in the same position which is termed as null point for the particular grain size. The minerals possessing grain size higher than null point size are transported seawards and the smaller ones are moved towards the shore. Therefore such mechanism causes the heavy mineral grains to remain on beach as a lag deposit which lacks the tail of coarser grain size fraction.

In beach and nearshore environment the transport of sediment is controlled by longshore transport / littoral drift and surf generated waves. The sediments of different grain sizes are suspended and mixed together and hence settling of grains onto the bed takes place depending on the individual grain properties. Higher energies generated by waves and longshore currents tend to sort the mineral grains according to their individual grain hydraulic properties. The waves throw the sediment into suspension and then the currents move those seawards. Thus beach or nearshore sand are better sorted than river sand and could sometimes results in accumulation of the heavy minerals as lag deposits.

7.5.1.4 Nearshore marine environment (inner and outer magnetite belt)

Figure 7.5 (m-o) illustrates the magnetite distribution for marine samples mostly covering nearshore region which includes surf zone. Higher energies in this region tend to produce higher suspension population. The bulk susceptibility of sediment was much higher compared to other samples (Figure 7.6 m-o).The samples were moderately sorted in three populations with saltation being dominant (98.2 – 99.86 %). It appears that the percentage of saltation population is highly dependent on wave energies in surf zone. In this zone, higher energy generated due to breaking of incoming waves causes large amount of sediment (light & heavy mineral grains) to move into suspension and hence the mixing between two population occurs. Magnetite grains being finer and denser mostly remain as saltation population and settle down quickly onto the bed during low energy conditions, while the lighter mineral grains are transported seaward by currents. The break between the traction and saltation population is in the range between 2 – 2.5 phi i.e. very fine – fine sand (Figure 7.6 m-o). This could be attributed to transport of magnetite grains in both the cycles (crest & trough) of the waves and then deposition during low energy condition.

In the samples from outer belts (inner shelf) the break between the traction and saltation population for bulk sediments and magnetite grains varies and is mostly in the range between – 0.5 to 1.0 phi (coarse – very coarse sand) and 1.0 to 2 phi (medium - fine sand) respectively. This mostly indicates the calm energy conditions and nature of sediment in this region. The sediments in inner shelf off Tauranga Harbour are mainly medium-coarse grained relict lag deposits of Pleistocene age that were reworked during the last glacial (Bradshaw et al., 1994; Krüger and Healy, 2006; Michels and Healy, 1999). Therefore such conditions favor deposition of the grain although there is a difference in the settling of light and heavy (magnetite) minerals. It is possible that the magnetite grains (inner and outer belt) smaller than 4 phi are usually in suspension and are transported seawards unless the sediment input exceeds the transport energy.

7.5.2 Numerical models and implications for understanding grain entrainment and transport

In estuaries, sediment transport is controlled by the hydrodynamics which is dependent on the combined interaction of river runoff, tides (ebb and flood), and also waves. The sediments in this environment were well sorted and mostly transported as bedload, saltation, and suspension. In addition the magnetic grains were much finer and found to be concentrated in higher amounts as compared to the Wairoa River upstream. This could be due to the influence of bidirectional currents in the estuary generated by tides (ebb & flood) that causes better sorting of the sediments, and hence, selective deposition of individual heavy mineral grains. Within the beach environment, the transport and entrainment is controlled by winnowing and waves (swash zone). In this region, once the grains are in the suspension, they move back and forward due to periodicity of the waves. So finally, after certain interval the grains which were in

suspension settle down and are found to remain in the same position, which is termed as null point. In our study area, we found that the sediments on the beach (dunes and the swash zone sediments of Matakana beach) were mainly composed of heavy and light grains in similar sizes and the offset was almost zero. This reflects the characteristics of a depositional environment, wherein the grains seemed to be deposited in the bed without any further transport or entrainment. This suggests that much higher energies are required for their movement for example periodic storm surges. This phenomenon was observed by a recent numerical modeling study on selective grain entrainment (Bartzke and Huhn, 2012). We hypothesized that the numerical Experiment 4 consisting of sediment bed of coarser lighter quartz and magnetite grains represents the initial beach conditions when sediment supply to the beach would have been sufficiently rich in coarse light and fine heavy grains (Figure 7.7 and 7.11). There appears to be higher washout of the quartz grains in this bed configuration as previously observed in flume studies (Komar, 2007). Furthermore, Experiment 3 represents the present conditions of the beach and it was found that increase in magnetite content considerably reduces or even inhibits the movement of the grains within the bed. This in turn reduces the rates of erosion resulting in stabilization of bed (Figure 7.7 and 7.11). This findings reveals that it is not always true that not only the coarser particles provides shielding to the fine heavy mineral fraction (Komar, 2007). Therefore we hypothesize that the past conditions on the beach was much different (eroding) compared with present (stabilizing). One could imagine that the bed becomes more stabilized if the present conditions persist. Past, present and future conditions of the beach evolution based on these findings are presented in a conceptual diagram (Figure 7.11 A, B, C).

Within the marine environments including nearshore and shelf region, a recent study by (Badesab et al., 2012) off Tauranga Harbour identified two coast parallel magnetite enrichment belt. They found that highly energetic conditions generated due to surf zone processes in the nearshore region caused well sorting of heavy minerals resulting in the formation of magnetite rich zones in the region, while the outer belt was mainly composed of relict reworked sediments. The samples analysed from the inner belt showed a well-defined grain size distribution and the highest magnetite enrichment in the fine fraction. Therefore, it can be concluded that higher energies caused by waves (surfzone), littoral drift, tides play a key role in the formation of this belt. In the outer belt sample, i.e., inner shelf, the sediment is transported either as a traction or saltation population. It is possible that due to the presence of lower energy regime induced only by bottom currents and much lower sediment input, inhibited the sorting of mineral grains which mostly remained accumulated in this region.

7.5.3 Conceptual model explaining magnetite enrichment and transport

Here we summarize our findings based on the laboratory and numerical experiments in a conceptual model, which explains the mechanisms of magnetite enrichment in sedimentary environments ranging from fluvial to marine settings (Figure 7.10 and 7.11).

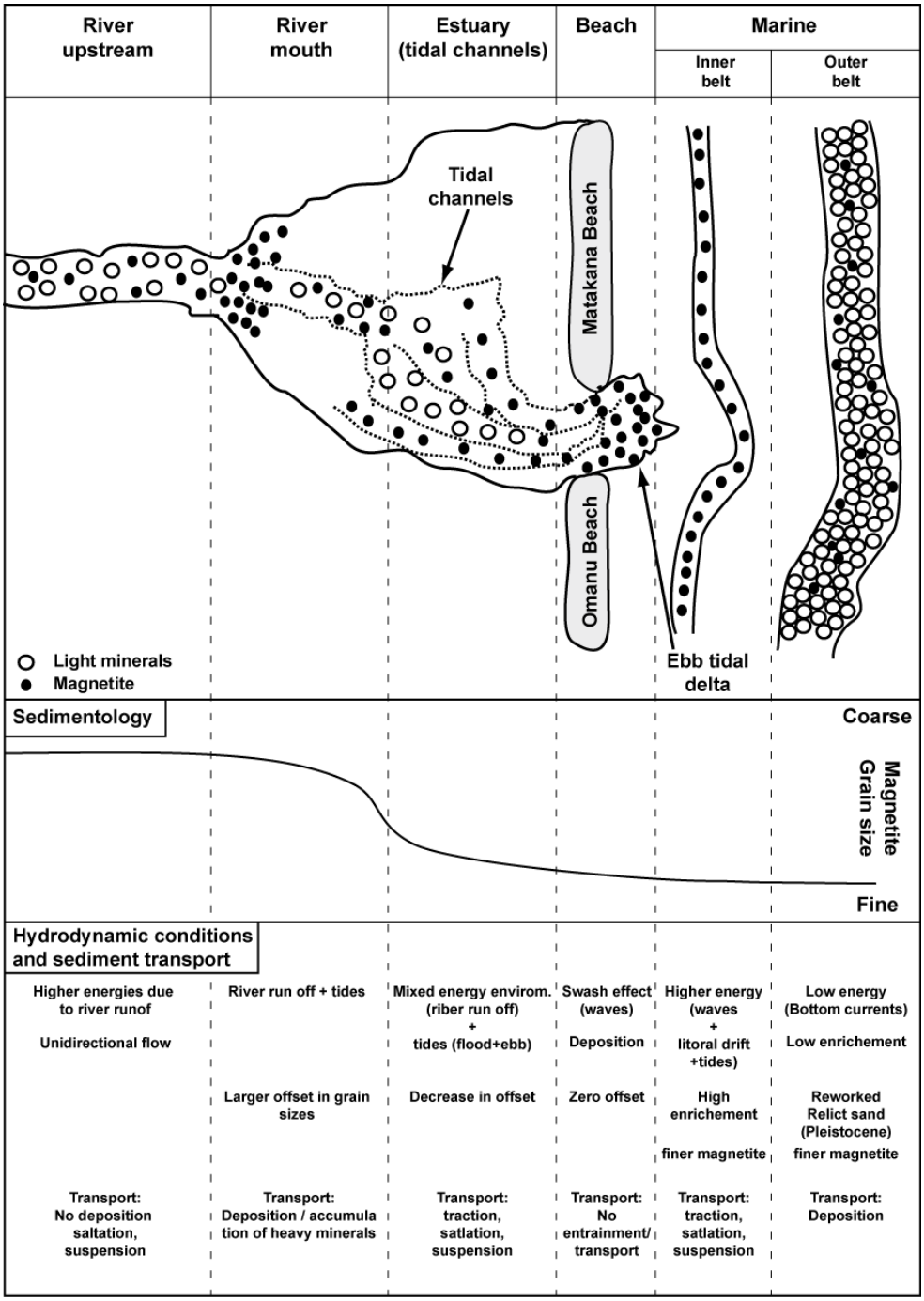

Figure 7.10: Conceptual model summarizing the findings from the laboratory measurements and numerical models.

Therefore, we describe the enrichment processes of magnetite occurring in six different sub-environments i.e., river upstream, river mouth, estuary, beach, marine (near shore and inner shelf). In the river upstream the majority of the sediment was transported as saltation and suspension load. This could be due to the association of high current velocities within the uni-directional river flow, which limited the sediment accumulation and deposition in the riverbed, even though the sediment influx from the proximal source was higher. Within the river mouth, magnetite grains were coarser and had a higher concentration as compared to the river upstream. Additional sediment input brought from the river runoff (Wairoa River, Figure 7.3) and the presence of a lower energy environment favored magnetite accumulation rather than transport, which resulted in higher deposition of magnetite grains onto the bed forming enriched layers. In all environments, a general trend of decrease in grain size of magnetite was observed. In addition the sediments from the river mouth had coarser magnetite grains and higher concentration, while the sediments in the marine region were much finer although the concentrations were similar.

Prior studies have shown that the grain size of sediment decreases and becomes finer with increasing transport distance from source to sink due to abrasion and collision caused during transport. This concept supports and explains our findings wherein we observed a decrease in magnetite grain size in samples originating from river mouth (source, coarser) to marine environment (finer, sink; Figure 7.10). Even though the river mouth, beach and marine (outer belt) environments showed distinct magnetite distributions in terms of their grain sizes and also the concentration, highest amounts of magnetite were seen to be concentrated at the river mouth. The beach environment showed intermediate and the outer belt showed lowest magnetite concentrations. The enrichment in the river mouths is possibly caused due to proximity to the source area. As the sediments are transported away from the source i.e. to more distal areas (estuarine, marine), the magnetite concentration in the bed also decreased. Hence, the numerical models representing this three sub environments were developed to validate the effect of magnetite enrichment within this environments: 1) river mouth: Experiment 1 (70 % magnetite & 30 % quartz), 2) beach: Experiment 2 (50 % magnetite & 50 % quartz), 3) Marine: outer belt: Experiment: 3 (30 % magnetite & 70 % quartz). Our present study showed that in beach environment, the heavy mineral grains provide shielding to lighter mineral grains reducing the rate of erosion and this seems to be true only in a bed consisting of sediments with equivalent grain sizes (see Experiment 3: Figure 7.8 and 7.9).

In general, our combined study based on laboratory analysis and interpretation of magnetite and bulk sediment distribution curves, statistical methods and 3D high resolution numerical modeling results has provided deep insights into the fundamental mechanism of transport and settling dynamics of magnetite in wide range of depositional environments.

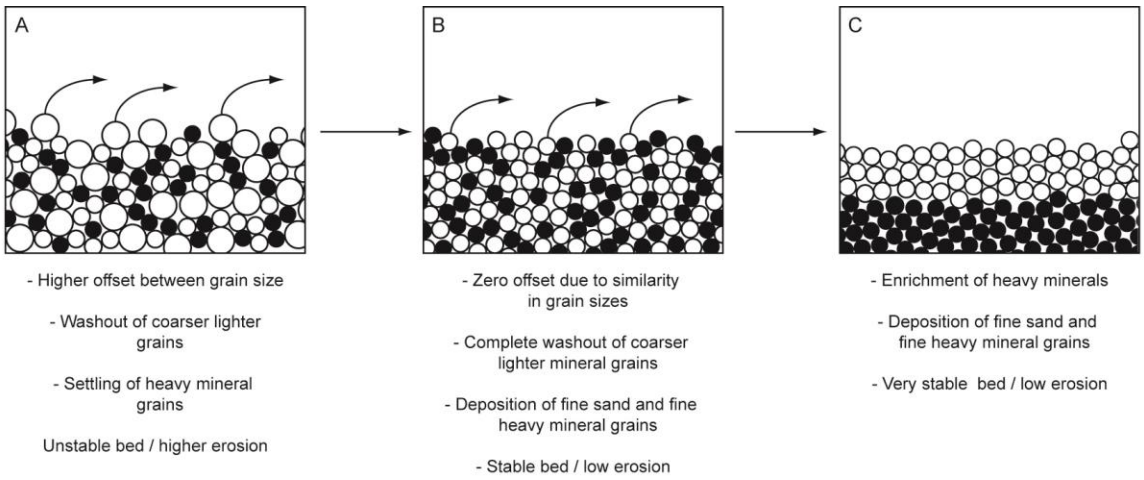

Figure 7.11: Schematic illustration showing the evolution of the Matakana Beach. A) Past conditions of the beach, containing a mixture of fine and coarse light minerals and fine and heavy minerals. B) Present conditions showing wash out of the coarser lighter mineral and leaving behind the fine sand and fine magnetite behind, in turn increasing the stability of the bed C) Predicted future conditions showing the bed enriched with heavy minerals with a negligible amount of erosion.

7.6 Conclusion

The distribution curves of bulk sediment and magnetite grains describe the enrichment and transport processes of magnetite occurring in six different sub-environments i.e., river upstream, river mouth, estuary, beach, marine (near shore and inner shelf). These were analyzed and compared to interpret the transport, deposition, enrichment processes of magnetite and light mineral grain in six sedimentary environments.

The differences in shapes of distribution curves, percentage of each population, offset in grain sizes of bulk and magnetite fraction reflects the variability in grain transport, settling and entrainment dynamics and depositional conditions in each environment.

Magnetite was mostly found in the very fine – fine sand fraction of the total sediment population and highest concentration was found in samples from river mouth and marine environment (inner). Although the majority of the bulk sediments were transported as saltation population, the heavy mineral grains being finer and denser settled down quickly and were trapped between the larger coarser (lighter) grains as the energy of the flow decreases.

The numerical models run to quantify the laboratory findings of three distinct sedimentary environments i.e. river mouth, beach and marine (outer). The results validated the observed processes of magnetite enrichment as observed from laboratory findings. Further it was found that sediments bed consisting of light and heavy mineral grains of equal sizes is highly stabilized as compared to other beds possessing sediments with unequal grain size distributions.

We demonstrate that our present approach of using combined laboratory analysis and numerical modeling possesses potential to investigate the dynamics of magnetic minerals and enrichment processes at grain scale level and could be further applied to any other setting.

7.7 Acknowledgements

This work was supported by Deutsche Forschungsgemeinschaft (DFG) through a joint International Research Training Group (Bremen–Waikato) INTERCOAST and MARUM, Center for Marine Environmental Sciences at the University of Bremen, Germany. We would like to thank Liane Brück, Dirk Immenga, Ruggero Capperucci, Serena Fraccascia, Sebastien Boulay and Christopher Daly for providing help during sediment sampling expeditions. The authors would like to thank Lina Podszun, Jannis Kuhlmann, Linda Wenk and INTERCOAST research students Rike Vöppel, Steffen Wiers, Max Kluger for providing assistance with numerical modeling and laboratory work.

7.8 References

Allen, J. R. L., 1970, Physical processes of sedimentation, London, Unwin University Books, 248 p.:

Baba, J., and Komar, P. D., 1981, Measurements and analysis of settling velocities of natural quartz sand grains: Journal of Sedimentary Petrology, v. 51, no. 631.

Badesab, F. K., T. v. Dobeneck, K. R. Bryan., H. Müller., R. M. Briggs , and Kwoll, T. F. a. E., 2012, Formation of magnetite-enriched zones in and offshore of a mesotidal estuarine lagoon: An environmental magnetic study of Tauranga Harbour and Bay of Plenty New Zealand: Geochemistry, Geophysics, Geosystems, v. 13, no. 6.

Bartzke, G., and Huhn, K., Numerical Approach to Quantify Selective Sorting of Heavy Minerals, *in* Proceedings EST 2012, Houston, 2012, Volume Special Volume, p. in rev.

Bloemendal, J., King, J. W., Hall, F. R., and Doh, S. J., 1992, Rock Magnetism of Late Neogene and Pleistocene Deep-Sea Sediments: Relationship to Sediment Source, Diagenetic Processes, and Sediment Lithology: J. Geophys. Res., v. 97, no. B4, p. 4361-4375.

Booth, C. A., Walden, J., Neal, A., and Smith, J. P., 2005, Use of mineral magnetic concentration data as a particle size proxy: A case study using marine, estuarine and fluvial sediments in the Carmarthen Bay area, South Wales, U.K: Science of The Total Environment, v. 347, no. 1–3, p. 241-253.

Bradshaw, B. E., Healy, T. R., Nelson, C. S., Dell, P. M., and de Lange, W. P., 1994, Holocene sediment lithofacies and dispersal systems on a storm-dominated, back-arc shelf margin: The east Coromandel coast, New Zealand: Marine Geology, v. 119, no. 1–2, p. 75-98.

Bryan, K. R., Robinson, A., and Briggs, R. M., 2007, Spatial and temporal variability of titanomagnetite placer deposits on a predominantly black sand beach: Marine Geology, v. 236, no. 1–2, p. 45-59.

Cioppa, M. T., Porter, N. J., Trenhaile, A. S., Igokwe, B., and Vickers, J., 2010, Beach sediment magnetism and sources: Lake Erie, Ontario, Canada: Journal of Great Lakes Research, v. 36, no. 4, p. 674-685.

Cundall, P. A., and Hart, R. D., Numerical modeling of discontinua, *in* Proceedings In Keynote address in Proceedings of the 1st US conference on discrete element methods Golden Colorado, 1989, CSM Press, p. 1–17.

Cundall, P. A., and Strack, O. D. L., 1979, A discrete numerical model for granular assemblies: Geotechniqe, v. 29, no. 1, p. 47-65.

-, 1983, Modeling of microscopicmechanisms in granularmaterial: Proceedings of the US-Japan Seminar on New Models and Constitutive Relations in The Mechanics of Granular Materials, p. 137-149.

De Lange, W. P., 1991, Wave climate for No 1 Reach, Port of Tauranga, Tauranga Harbour report, Port of Tauranga Ltd., Hamilton, New Zealand.: University of Waikato, New Zealand.

Frihy, O. E., and Dewidar, K. M., 2003, Patterns of erosion/sedimentation, heavy mineral concentration and grain size to interpret boundaries of littoral sub-cells of the Nile Delta, Egypt: Marine Geology, v. 199, no. 1–2, p. 27-43.

Frihy, O. E., and Komar, P. D., 1991, Patterns of beach-sand sorting and shoreline erosion on the Nile Delta: Journal of Sedimentary Research, v. 61, no. 4, p. 544-550.

Gallaway, E., Trenhaile, A. S., Cioppa, M. T., and Hatfield, R. G., 2012, Magnetic mineral transport and sorting in the swash-zone: northern Lake Erie, Canada: Sedimentology, v. 59, no. 6, p. 1718-1734.

Gao, S., and Collins, M., 1992, Net sediment transport patterns inferred from grain-size trends, based upon definition of "transport vectors": Sedimentary Geology, v. 81, no. 1–2, p. 47-60.

Hatfield, R. G., Cioppa, M. T., and Trenhaile, A. S., 2010, Sediment sorting and beach erosion along a coastal foreland: Magnetic measurements in Point Pelee National Park, Ontario, Canada: Sedimentary Geology, v. 231, no. 3–4, p. 63-73.

Hughes, M. G., Keene, J. B., and Joseph, R. G., 2000, Hydraulic Sorting of Heavy-Mineral Grains by Swash on a Medium-Sand Beach: Journal of Sedimentary Research, v. 70, no. 5, p. 994-1004.

Inman, D. L., 1949, Sorting of sediment in light of fluvial mechanics: Journal of Sedimentary Petrology, no. 19, p. 51-70.

Itasca, 2004a, PFC 3D 3.1 Manual, Minneapolis, Itasca Consulting Group, Inc.

-, 2004b, FLAC 3D 3.1 Manual, Minneapolis, Itasca Consulting Group, Inc.

Kock, I., and Huhn, K., 2007, Influence of particle shape on the frictional strength of sediments — A numerical case study: Sedimentary Geology, v. 196, no. 1–4, p. 217-233.

Komar, P. D., 2007, Chapter 1 The Entrainment, Transport and Sorting of Heavy Minerals by Waves and Currents, *in* Maria, A. M., and David, T. W., eds., Developments in Sedimentology, Volume Volume 58, Elsevier, p. 3-48.

Komar, P. D., and Wang, C., 1984, Processes of selective grain transport and the formation of placers on beaches: The Journal of Geology, v. 92, no. 6, p. 637–655.
Krüger, J. C., and Healy, T. R., 2006, Mapping the Morphology of a Dredged Ebb Tidal Delta, Tauranga Harbour, New Zealand: Journal of Coastal Research, v. 22, no. 3, p. 720-727.
Krumbein, W. C., and Pettijohn, F. J., 1938, Manual of Sedimentary Petrography New York, Appleton-Century, 549 p.:
Lees, J. A., and Pethick, J. S., 1995, Problems associated with quantitative magnetic sourcing of sediments of the scarborough to mablethorpe coast, Northeast England, U.K: Earth Surface Processes and Landforms, v. 20, no. 9, p. 795-806.
Li, M. Z., and Komar, P. D., 1992, Longshore grain sorting and beach placer formation adjacent to the Columbia River: Journal of Sedimentary Research, v. 62, no. 3, p. 429-441.
Maher, B. A., Watkins, S. J., Brunskill, G., Alexander, J., and Fielding, C. R., 2009, Sediment provenance in a tropical fluvial and marine context by magnetic 'fingerprinting' of transportable sand fractions: Sedimentology, v. 56, no. 3, p. 841-861.
Mason, C. C., and Folk, R. L., 1958, Differentiation of beach, dune, and aeolian flat environments by size analysis, Mustang Island, Texas: Journal of Sedimentary Research, v. 28, no. 2, p. 211-226.
McLaren, P., 1981, An interpretation of trends in grain size measures: Journal of Sedimentary Research, v. 51, no. 2, p. 611-624.
McQuivey, R., S, and Keefer, T. N., 1969, The relation of magnetite over ripples.
Michels, K. H., and Healy, T. R., 1999, Evaluation of an Inner Shelf Site off Tauranga Harbour, New Zealand, for Disposal of Muddy-Sandy Dredged Sediments: Journal of Coastal Research, v. 15, no. 3, p. 830-838.
Moss, A. J., 1962, The physical nature of common sandy and pebbly deposits. Part II: American Journal Science, v. 260, p. 337 – 373.
Oldfield, F., and Yu, L., 1994, The influence of particle size variations on the magnetic properties of sediments from the north-eastern Irish Sea: Sedimentology, v. 41, no. 6, p. 1093-1108.
Pettijohn. J., Potter, P. E., and Ever, R. a., 1972, Sand and sandstone, New York, Springer-Ver- lag, .
Razjigaeva, N. G., and Naumova, V. V., 1992, Trace element composition of detrital magnetite from coastal sediments of northwestern Japan Sea for provenance study: Journal of Sedimentary Research, v. 62, no. 5, p. 802-809.
Robinson, S. G., Maslin, M. A., and McCave, I. N., 1995, Magnetic Susceptibility Variations in Upper Pleistocene Deep-Sea Sediments of the NE Atlantic: Implications for Ice Rafting and Paleocirculation at the Last Glacial Maximum: Paleoceanography, v. 10, no. 2, p. 221-250.
Rubey, W. W., 1933, The size distribution of heavy minerals within a water-laid sandstone: Journal of Sedimentary Research, v. 3, no. 1, p. 3-29.
Slingerland, R. L., 1977, The effects of entrainment on the hydraulic equivalence relationships of light and heavy minerals in sands: Journal of Sedimentary Research, v. 47, no. 2, p. 753-770.
Visher, G. S., 1969, Grain size distributions and depositional process: Journal of Sedimentary Petrology, v. 39, no. 3, p. 1074-1106.
Walden, J., Slattery, M. C., and Burt, T. P., 1997, Use of mineral magnetic measurements to fingerprint suspended sediment sources: approaches and techniques for data analysis: Journal of Hydrology, v. 202, no. 1–4, p. 353-372.
Wheeler, A. J., Oldfield, F., and Orford, J. D., 1999, Depositional and post-depositional controls on magnetic signals from saltmarshes on the north-west coast of Ireland: Sedimentology, v. 46, no. 3, p. 545-558.
Zhang, W., Yu, L., Lu, M., Hutchinson, S. M., and Feng, H., 2007, Magnetic approach to normalizing heavy metal concentrations for particle size effects in intertidal sediments in the Yangtze Estuary, China: Environmental Pollution, v. 147, no. 1, p. 238-244.

Table 7.1: Percentages of population (traction, saltation & suspension) and grain size ranges calculated from magnetite distribution curves of samples from various depositional environments.

Depositional Environment	Traction population		Saltation population		Suspension population	
	%	Phi range	%	Phi range	%	Phi range
River upstream (Wairoa River)	0.3 - 2.3	-2.0 to 0.5	58.6 - 62.5	0.5 to 3.0	0.85 - 39	3.0 to 5.5
River mouth (Wairoa River)	0.03 - 0.48	-2.0 to 1.5	68.2 - 99.6	1.5 to 5.0	0.2 - 5.3	5.0 to 7.0
Estuarine (Tauranga Harbour)	0.005 - 11.4	-1.5 to 1.5	87.7 - 98.1	1.5 to 4.0	0.25 - 1.6	4.0 to 5.5
Beach (Matakana Beach)	0.06 - 1.3	0.5 to 1.5	98.2 - 99.8	1.5 to 4.5	0.01 - 0.9	4.5 to 5.5
Marine - nearshore (Inner magnetite enrichment belt)	0.025 - 1.95	-1.0 to 2.5	2.9 - 97.9	2.5 to 4.4	0.01 - 4.7	4.5 to 5.5
Marine – inner shelf (Outer magnetite enrichment belt)	0.99 - 19.8	-1.5 to 2.0	79.9 - 98.9	2.0 to 4.0	0.05 - 0.09	4.0 to 6.5

Table 7.2: Details of magnetic and statistical parameters (Krumbein & Pettijohn, 1938) of analyzed samples.

Sample Details	Bulk magnetite content [%]	Mean grain size Bulk fraction [Φ]	Dispersion [Bulk fraction]	Mean grain size Magnetite fraction [Φ]	Dispersion [Magnetite Fraction]	Offset in grain size [ΔΦ]
			Wairoa River upstream			
WU-4	0.049	0.36	1.76	0.87	2.52	0.6
WU-3	0.12	2.66	1.54	2.81	2.17	0.2
WU-6	0.83	-0.46	2.47	-0.67	3.84	0.1
			Wairoa River mouth			
WM-3	0.95	1.91	1.04	3.1	0.66	1.3
WM-4	0.44	1.78	0.74	3.25	0.88	1.6
WM-8	0.24	2.43	1.1	3.92	1.21	1.7
WM-12	1.19	1.88	0.83	3.72	0.97	1.9
WM-13	1.44	2.28	1.1	3.83	0.95	1.4
			Estuarine (Tauranga Harbour)			
SB-1	0.069	1.11	1.2	2.12	1.24	0.9
SB-2	0.16	1.85	0.53	2.41	0.93	0.4
SB-3	0.083	2.08	0.75	2.79	0.76	0.7
SB-4	0.26	1.29	1.09	2.25	1.04	1.4
			Beach (Matakana Beach)			
B1	0.02	2.2	0.56	2.22	1.05	0.7
B2	0.0029	2.63	0.79	3.35	0.55	1
B3	0.0055	1.23	0.8	1.76	1.73	0
			Marine (Inner magnetite enrichment belt)			
MIB - 1	0.21	2.93	1.13	3.63	0.26	1
MIB - 2	0.15	2.96	1.17	3.53	0.24	0.5
MIB - 3	0.12	2.34	1.06	3.2	0.7	1.2
			Marine(Outer magnetite enrichment belt)			
MOB - 1	1.1	2.45	0.94	3.3	0.63	1
MOB - 2	0.72	0.27	1.81	1.71	1.52	1.3
MOB - 3	0.074	0.65	2.65	1.99	1.47	0.4

Table 7.3: Properties and configurations of the numerical experiments.

Particle properties				
Properties	Exp. 1	Exp. 2	Exp. 3	Exp. 4
Diameter [µm]: quartz	90	90	90	128.8
Diameter [µm]: magnetite	90	90	90	90
Particle number: quartz	381	889	635	350
Particle number: magnetite	889	381	635	350
Normal stiffness [N/m]	$1x10^8$	$1x10^8$	$1x10^8$	$1x10^8$
Shear stiffness [N/m]	$1x10^8$	$1x10^8$	$1x10^8$	$1x10^8$
Density ρ quartz [kg/m³]	2600	2600	2600	2600
Density ρ magnetite [kg/m³]	5140	5140	5140	5140
Quartz friction µ	0.5	0.5	0.5	0.5
Magnetite friction µ	2	2	2	2
Fluid properties				
Fluid properties	Exp. 1	Exp. 2	Exp. 3	Exp. 4
Fluid density ρ [kg/m³]	1000	1000	1000	1000
Pore pressure [mbar]	250	250	250	250
Fluid saturation [%]	100	100	100	100
Boundary inflow velocity U [cm/s]	10, 20, 30 and 40			

Table 7.4: Transported particles in horizontal direction.

Experiment 1				
Flow speed [m/s]	Quartz transport [m] (Top)	Magnetite transport [m] (Top)	Quartz transport [m] (Base)	Magnetite transport [m] (Base)
0.1	3.55E-05	2.37E-05	1.55E-05	1.01E-05
0.2	5.93E-05	3.90E-05	1.93E-05	1.93E-05
0.3	6.60E-05	5.38E-05	2.53E-05	2.51E-05
0.4	7.82E-05	6.72E-05	3.32E-05	3.10E-05

Experiment 2				
Flow speed [m/s]	Quartz transport [m] (Top)	Magnetite transport [m] (Top)	Quartz transport [m] (Base)	Magnetite transport [m] (Base)
0.1	8.45E-05	6.09E-05	3.62E-05	4.14E-05
0.2	1.24E-04	8.85E-05	5.37E-05	5.02E-05
0.3	1.71E-04	1.20E-04	6.98E-05	6.68E-05
0.4	2.14E-04	1.44E-04	8.13E-05	7.78E-05

Experiment 3				
Flow speed [m/s]	Quartz transport [m] (Top)	Magnetite transport [m] (Top)	Quartz transport [m] (Base)	Magnetite transport [m] (Base)
0.1	6.01E-05	4.12E-05	1.63E-05	2.09E-05
0.2	8.07E-05	6.50E-05	3.41E-05	2.56E-05
0.3	1.36E-04	1.06E-04	4.24E-05	3.46E-05
0.4	1.42E-04	1.20E-04	4.30E-05	4.05E-05

Experiment 4				
Flow speed [m/s]	Quartz transport [m] (Top)	Magnetite transport [m] (Top)	Quartz transport [m] (Base)	Magnetite transport [m] (Base)
0.1	7.10E-05	5.25E-05	2.37E-05	2.59E-05
0.2	1.20E-04	1.10E-04	7.15E-05	4.10E-05
0.3	1.59E-04	1.33E-04	6.05E-05	5.05E-05
0.4	1.96E-04	1.45E-04	1.01E-04	7.63E-05

Table 7.5: Transported particles in vertical direction.

	Experiment 1	
Flow speed [m/s]	Quartz transport [m]	Magnetite transport [m]
0.1	-7.98E-06	-8.01E-06
0.2	-1.26E-05	-1.30E-05
0.3	-1.70E-05	-1.73E-05
0.4	-2.00E-05	-2.10E-05

	Experiment 2	
Flow speed [m/s]	Quartz transport [m]	Magnetite transport [m]
0.1	-2.80E-05	-3.01E-05
0.2	-4.45E-05	-4.06E-05
0.3	-5.76E-05	-5.54E-05
0.4	-6.29E-05	-6.10E-05

	Experiment 3	
Flow speed [m/s]	Quartz transport [m]	Magnetite transport [m]
0.1	-1.83E-05	-1.20E-05
0.2	-2.26E-05	-1.48E-05
0.3	-3.50E-05	-2.39E-05
0.4	-4.53E-05	-3.70E-05

	Experiment 4	
Flow speed [m/s]	Quartz transport [m]	Magnetite transport [m]
0.1	-1.71E-05	-1.75E-05
0.2	-2.76E-05	-2.81E-05
0.3	-3.39E-05	-3.56E-05
0.4	-3.53E-05	-4.11E-05

Chapter VIII - Conclusions and Outlook

The results presented in the previous chapters showed that sediment transport processes are highly sensitive over a broad spectrum of physical parameters (see Chapter II; sections 2.3 and 2.5). In particular, it was shown that texture related sediment stabilization and density related differences in sediment beds shift the initial threshold conditions towards higher flow regimes, hence, increasing the bed stability.

In the following text, the conclusions of each Chapter are described. The individual thesis objectives and conclusions of each study comprising Chapters III-VII are detailed within this structure.

In **Chapter III** the following research questions were addressed:

- How does a fine fraction (silt) influence the erosion behavior of a sand bed?
- How do different current velocities influence the sediment stabilization and re-mobilization of a sand bed ?
- What factor causes sediment stabilization in silt and sand beds?

Chapter III focused on the effects of non-cohesive silt and sand grains on sediment bed erosion resistance. The research conducted in this study identified that bed stability is increased when a coarse sand bed is treated with a relatively small amount of fine silt particles. These findings were identified using an analogue (laboratory based) flume tank and led to the formulation of the hypothesis that textural caging structures increase the bed stability, whereby fine silt particles incorporate into the pore space between the coarser sand grains. It was postulated that through the generation of textural caging structures, the inflow into the sediment bed is blocked (i.e. pore space blocking), hence, increasing bed stability and shifting threshold conditions to a higher flow regime. In comparison to previous studies focusing on clay and sand mixtures, it was found that lower silt content is required to increase the bed stability than previously understood. This result could have a significant application in terms of dredging and draining questions.

Further research focusing on the better visualization of the bed stabilization process would improve the findings reported here. Enhanced visualization of the processes occurring in the sediment bed could be achieved by injecting dye into the bed, e.g., by a syringe, in order to follow the infiltration pathways of the fluid. This approach could help to detect and quantify (e.g., by video analysis) flow directions in the bed. Additionally, X-rays of the sediment during fluid streaming could provide a better impression of the pores pace blocking effect. Similar to the approach used by Mitchener and Torfs (1996), samples from the flume could be analyzed using electron microscopy to identify caging structures. The finding that relatively

small amounts of silt can stabilize a sediment bed could be tested in a field campaign (e.g., release of silt from a vessel), with a potential application for stabilization disposed dredged material mounds.

Chapter IV & V focused on the validation of the hypothesis of bed stabilization by textural caging structures, which was proposed in Chapter III. The following questions were addressed with respect to graded sediment beds (Chapter IV) and mixed sediment beds (Chapter V):

- How do textural caging structures increase bed stability on a grain-scale level?
- How do textural caging structures control sediment stability in graded and mixed sediment beds?

As the quantification of the processes occurring in the direct vicinity of the sediment water interface and in the interior of a sediment bed can only be measured to a limited extent by analogue methods, a 3D high resolution numerical models (Chapters IV and V) were used in order to quantify and validate the hypothesis of pore space plugging proposed in Chapter III.

The experiments presented in both chapters showed that fine silt particles, either deposited on or mixed into the coarser matrix, infiltrated the pore space between larger sand particles. Inflow blocking in graded sediment beds was identified at the silt layering, whereas in the case of the mixed beds silt blocked the inflow in the entire bed. This generation of textural caging structures caused the deflection of the flow field and, therefore, a lower erosion potential for entrainment of the coarser sand grains, which was shown by direct fluid measurements in the numerical sediment beds.

The studies presented in **Chapter VI & VII** focused on the effect of density variations in sediment beds and their effect on threshold conditions and the erosion behavior of sediment beds. Therein, the following research question was addressed:

- How do density-related effects influence the erosion behavior of sediment beds?

In order to answer this research question, Chapters VI and VII focused on the quantification of density-related the effects on the erosion characteristics of sediment beds using a 3D high resolution numerical model. By testing different numerical sediment compositions it was possible to quantify the process of selective grain entrainment, which has been identified by previous researchers, using analogue flume tank approaches or field instigations. The 3D numerical model allowed for validation of the theory that light minerals are washed out of the bed faster than the denser heavier mineral grains. This finding indicates

that placer deposits (accumulations of heavy mineral grains) are generated by selective grain entrainment. The model results also showed that higher threshold velocities are required to entrain the heavy minerals grains, and that quartz rich and magnetite poor beds are much more susceptible to erosion compared to quartz poor and heavy mineral rich compositions.

Future research should focus on added effects of multiple particle spectra and density compositions, as well cohesive clay aggregates, e.g., through the stacking of elongated particles (Kock and Huhn, 2007). It is anticipated that that these added model features will improve the quantification of internal threshold conditions, further explaining selective grain entrainment and allowing for the development of sediment bed forms within the continuum. In order to increase the complexity of the models, it is also suggested that more complex flow conditions and a larger amount of particles be implemented using faster supercomputers. Further experiments of the armouring effect would enhance the results presented in this thesis. Finally, the introduction of cohesive properties into the model code would be helpful for analysis of sediment erosion of clay-rich sediment beds.

This thesis provides significant innovations for ongoing research in the field of sediment transport. The finding that bed stabilization is highly sensitive to small silt concentrations could be a useful tool for the dredging and sea-bed structure industry in order to stabilize dumped sediment at the seafloor. The validation of the hypothesis that textural caging structures influence bed stabilization by 3D numerical models provides significant implications for the prediction of sediment erosion. Moreover, the showing that the quantity of fluid inflow into a sediment bed controls the initial erosion conditions of sediment beds allows a better understanding of previous conceptual models and theoretical approaches from analogue experiments. Also, the influence of grain density differences on the erosion behavior of sediment beds shows implications on the prediction of sediment transport processes.
Therefore, the presented 3D models could help to predict the position and distribution of heavy minerals placers for the heavy mineral industry. Assuming that technology keeps evolving, it will be possible to implement these findings by the use of faster supercomputers into large scale numerical models. Consequently, large scaled models, such as Delft 3D or ROMS (Lesser et al., 2004; Shchepetkin and McWilliams, 2004), could be able to simulate sediment transport at the direct vicinity of a sediment bed, but would also be capable to predict sediment transport processes without empirical sediment transport equations (Lesser et al., 2004; Rijn, 2007). Therefore, the models presented in this thesis show a new step in the evolution of sediment transport models to predict sediment transport on a large scale level.

References

Allen, J.R.L., 1970, Physical processes of sedimentation: London, Unwin University Books, 248 p.

Allen, J.R.L., 1982, Sedimentary structures, *in* John, R.L.A., ed., Developments in Sedimentology, Volume Volume 30, Part A, Elsevier, p. 593.

Alvarez-Hernandez, E.M., 1990, The influence of cohesion on sediment movement in channels of circular cross-section, New Castle upon Tyne, UK.

Amos, C.L., Grant, J., Daborn, G.R., and Black, K., 1992, Sea Carousel--A benthic, annular flume: Estuarine, Coastal and Shelf Science, v. 34, p. 557-577.

Baba, J., and Komar, P.D., 1981, Measurements and analysis of settling velocities of natural quartz sand grains: Journal of Sedimentary Petrology, v. 51.

Badesab, F.K., T. v. Dobeneck, K. R. Bryan., H. Müller., R. M. Briggs , and Kwoll, T.F.a.E., 2012, Formation of magnetite-enriched zones in and offshore of a mesotidal estuarine lagoon: An environmental magnetic study of Tauranga Harbour and Bay of Plenty New Zealand: Geochemistry, Geophysics, Geosystems, v. 13.

Bagnold, R.A., 1941, The Physics of Blown Sand and Desert Dunes: London, Chapman & Hall.

Bartzke, G., and Huhn, K., 2012, Numerical Approach to Quantify Selective Sorting of Heavy Minerals, EST 2012, Volume Special Volume: Houston, p. in rev.

Black, K., and Paterson, D.M., 1997, Measurement of the erosion potential of cohesive marine sediment: A review of current in situ technology: J. Mar Environ. Eng, v. 4, p. 43-83.

Bloemendal, J., King, J.W., Hall, F.R., and Doh, S.J., 1992, Rock Magnetism of Late Neogene and Pleistocene Deep-Sea Sediments: Relationship to Sediment Source, Diagenetic Processes, and Sediment Lithology: J. Geophys. Res., v. 97, p. 4361-4375.

Blumberg, A.F., and Mellor, G.L., 1999, A description of a three-dimensional coastal ocean model, *in* Heaps, N.S., ed., Three Dimensional Coastal Ocean Models, American Geophysical Union.

Booth, C.A., Walden, J., Neal, A., and Smith, J.P., 2005, Use of mineral magnetic concentration data as a particle size proxy: A case study using marine, estuarine and fluvial sediments in the Carmarthen Bay area, South Wales, U.K: Science of The Total Environment, v. 347, p. 241-253.

Bradshaw, B.E., Healy, T.R., Nelson, C.S., Dell, P.M., and de Lange, W.P., 1994, Holocene sediment lithofacies and dispersal systems on a storm-dominated, back-arc shelf margin: The east Coromandel coast, New Zealand: Marine Geology, v. 119, p. 75-98.

Bryan, K.R., Robinson, A., and Briggs, R.M., 2007, Spatial and temporal variability of titanomagnetite placer deposits on a predominantly black sand beach: Marine Geology, v. 236, p. 45-59.

Cioppa, M.T., Porter, N.J., Trenhaile, A.S., Igokwe, B., and Vickers, J., 2010, Beach sediment magnetism and sources: Lake Erie, Ontario, Canada: Journal of Great Lakes Research, v. 36, p. 674-685.

Cundall, P.A., and Hart, R.D., 1989, Numerical modeling of discontinua, *in* Mustoe GGW., Henriksen M., and H-P., H., eds., In Keynote address in Proceedings of the 1st US conference on discrete element methods Golden Colorado, CSM Press, p. 1–17.

Cundall, P.A., and Strack, O.D.L., 1979, A discrete numerical model for granular assemblies: Geotechniqe, v. 29, p. 47-65.

Cundall, P.A., and Strack, O.D.L., 1983, Modeling of microscopicmechanisms in granularmaterial: Proceedings of the US-Japan Seminar on New Models and Constitutive Relations in The Mechanics of Granular Materials, p. 137-149.

De Lange, W.P., 1991, Wave climate for No 1 Reach, Port of Tauranga, Tauranga Harbour report, Port of Tauranga Ltd., Hamilton, New Zealand., University of Waikato, New Zealand.

Dolphin, T.J., and Green, M., 2009 Patterns of wave-orbital speed and skin friction under estuarine (fetch-limited) waves: Jornal of Costal Research, p. 178-182.

Dyer, K.R., 1989, Sediment processes in estuaries: future research requirements: Journal of Geophysical Research, v. 94 (C10), p. 14327-14339.

Dyer, K.R., 1994, Estuarine sediment transport and deposition *in* Pye, K., ed., Sediment Transport and Depositional Processes: Oxford, Blackwell Scientific Publications, p. 193-218.

Eisbacher, G.H., 1996, Einführung in die Tektonik: Stuttgart, Spektrum Akademischer Verlag; Thieme; Enke, 374 p.

Essink, K., 1999, Ecological effects of dumping of dredged sediments; options for management: Journal of Coastal Conservation, v. 5, p. 69-80.

Finelli, C.M., Hart, D.D., and Fonseca, D.M., 1999, Evaluating the spatial resolution of an acoustic doppler velocimeter and the consequences for measuring near-bed flows: Limnol. Oceanogr., v. 44 (7), p. 1793–1801.

Frihy, O.E., and Dewidar, K.M., 2003, Patterns of erosion/sedimentation, heavy mineral concentration and grain size to interpret boundaries of littoral sub-cells of the Nile Delta, Egypt: Marine Geology, v. 199, p. 27-43.

Frihy, O.E., and Komar, P.D., 1991, Patterns of beach-sand sorting and shoreline erosion on the Nile Delta: Journal of Sedimentary Research, v. 61, p. 544-550.

Gallaway, E., Trenhaile, A.S., Cioppa, M.T., and Hatfield, R.G., 2012, Magnetic mineral transport and sorting in the swash-zone: northern Lake Erie, Canada: Sedimentology, v. 59, p. 1718-1734.

Gao, S., and Collins, M., 1992, Net sediment transport patterns inferred from grain-size trends, based upon definition of "transport vectors": Sedimentary Geology, v. 81, p. 47-60.

Green, M.O., and Black, K.P., 1999, Suspended-sediment reference concentration under waves: field observations and critical analysis of two predictive models: Coastal Engineering, v. 38, p. 115-141.

Harris, J., and Stöcker, H., 1998, Handbook of Mathematics and Computational Science: New York, Springer, 1028 p.

Hatfield, R.G., Cioppa, M.T., and Trenhaile, A.S., 2010, Sediment sorting and beach erosion along a coastal foreland: Magnetic measurements in Point Pelee National Park, Ontario, Canada: Sedimentary Geology, v. 231, p. 63-73.

Heald, J., McEwan, I., and Tait, S., 2004, Sediment transport over a flat bed in a unidirectional flow: simulations and validation: Philosophical Transactions of the Royal Society of London. Series A: Mathematical, Physical and Engineering Sciences, v. 362, p. 1973-1986.

Healy, T., 2002, Chapter Fourteen Muddy coasts of mid-latitude oceanic islands on an active plate margin--New Zealand, *in* Terry Healy, Y.W., and Judy-Ann, H., eds., Proceedings in Marine Science, Volume Volume 4, Elsevier, p. 347-374.

Hir, P.L., Cann, P., Waeles, B., Jestin, H., and Bassoullet, P., 2008, Chapter 11 Erodibility of natural sediments: experiments on sand/mud mixtures from laboratory and field erosion tests, *in* Tetsuya Kusuda, H.Y.J.S., and Joseph, Z.G., eds., Proceedings in Marine Science, Volume Volume 9, Elsevier, p. 137-153.

Hir, P.L., Cayoccaa, F., and Waeles, B., 2011, Dynamics of sand and mud mixtures: A multiprocess-based modelling strategy: Continental Shelf Research, v. 31, p. 135-149.

Hjulstroem, F., 1935, Studies in the morphological activity of rivers as illustrated by the River Fyris: Bulletin of the Geological Institute of Uppsala, v. 25, p. 221–527.

Hjulstroem, F., 1939, Transport of detritus by moving water recent marine sediments, *in* Trask, P.D., ed., Recent Marine Sediments; a symposium, Tulsa Oklakoma: American Association of Petroleum Geologists: New York, London, T.Murby & Co., Reprinted 1968 by Dover Publications p. 3-31.

Hodge, R., Richards, K., and Brasington, J., 2007, A physically-based bedload transport model developed for 3-D reach-scale cellular modelling: Geomorphology, v. 90, p. 244-262.

Hughes, M.G., Keene, J.B., and Joseph, R.G., 2000, Hydraulic Sorting of Heavy-Mineral Grains by Swash on a Medium-Sand Beach: Journal of Sedimentary Research, v. 70, p. 994-1004.

Inman, D.L., 1949, Sorting of sediment in light of fluvial mechanics: Journal of Sedimentary Petrology, p. 51-70.

Itasca, 2004a, PFC 3D 3.1 Manual: Minneapolis, Itasca Consulting Group, Inc.

Itasca, 2004b, FLAC 3D 3.1 Manual: Minneapolis, Itasca Consulting Group, Inc.

Jacobs, W., Le Hir, P., Van Kesteren, W., and Cann, P., 2011, Erosion threshold of sand-mud mixtures: Continental Shelf Research, v. 31, p. S14-S25.

Jones, H.F.E., Pilditch, C.A., Bryan, K.R., and Hamilton, D.P., 2011, Effects of infaunal bivalve density and flow speed on clearance rates and near-bed hydrodynamics: Journal of Experimental Marine Biology and Ecology, v. 401, p. 20-28.

Kamphuis, J.W., 1990, Influence of sand or gravel on the erosion of cohesive sediment: Journal of Hydraulic Research, v. 28, p. 43-53.

Karl, D.M., and Novitsky, J.A., 1988, Dynamics of microbial growth in surface layers of a coastal marine sediment ecosystem: Marine Ecology Progress Series, v. 50, p. 169-176.

Kim, S.C., Friedrichs, C.T., Maa, J.P.Y., and Wright, L.D., 2000, Estimating bottomstress in tidal boundary layer from Acoustic Doppler Velocimeter data: J. Hydraul. Eng. Asce, v. 126 (6), p. 399–406.

Klute, A., and Dirksen, C., 1986, Hydraulic conductivity and diffusivity: laboratory methods, *in* Klute, A., ed., Methods of Soil Analysis, Part 1 - Physical and Mineralogical Methods. Agronomy Monograph, Volume 9: Madison, WI., American Society of Agronomy-Soil Science Society of America, p. 687-734.

Kock, I., and Huhn, K., 2007, Influence of particle shape on the frictional strength of sediments — A numerical case study: Sedimentary Geology, v. 196, p. 217-233.

Komar, P.D., 1987, Selective grain entrainment by a current from a bed of mixed sizes: a reanalysis: J. Sediment. Petrol., v. 57(2), p. 203-211.

Komar, P.D., 2007, Chapter 1 The Entrainment, Transport and Sorting of Heavy Minerals by Waves and Currents, *in* Maria, A.M., and David, T.W., eds., Developments in Sedimentology, Volume Volume 58, Elsevier, p. 3-48.

Komar, P.D., and Wang, C., 1984, Processes of selective grain transport and the formation of placers on beaches: The Journal of Geology, v. 92, p. 637–655.

Krüger, J.C., and Healy, T.R., 2006, Mapping the Morphology of a Dredged Ebb Tidal Delta, Tauranga Harbour, New Zealand: Journal of Coastal Research, v. 22, p. 720-727.

Krumbein, W.C., and Pettijohn, F.J., 1938, Manual of Sedimentary Petrography New York, Appleton-Century, 549 p.

Leeder, M.R., 1999, Sedimentology and Sedimentary Basins: From Turbulence to Tectonics Oxford, Blackwell Science, 608 p.

Leeder, M.R., 1999 Sedimentology and Sedimentary Basins: From Turbulence to Tectonics Oxford, Blackwell Science, 608 p.

Lees, J.A., and Pethick, J.S., 1995, Problems associated with quantitative magnetic sourcing of sediments of the scarborough to mablethorpe coast, Northeast England, U.K: Earth Surface Processes and Landforms, v. 20, p. 795-806.

Lesser, G.R., Roelvink, J.A., van Kester, J., and Stelling, G.S., 2004, Development and validation of a three-dimensional morphological model: Coastal Eng., v. 51, p. 883-915.

Leys, V., and Mulligan, R.P., 2011, Modelling Coastal Sediment Transport for Harbour Planning: Selected Case Studies *in* Ginsberg, S.S., ed., Sediment Transport, http://www.intechopen.com/articles/show/title/modelling-coastal-sediment-transport-for-harbour-planning-selected-case-studies.

Li, M.Z., and Komar, P.D., 1992, Longshore grain sorting and beach placer formation adjacent to the Columbia River: Journal of Sedimentary Research, v. 62, p. 429-441.

Maher, B.A., Watkins, S.J., Brunskill, G., Alexander, J., and Fielding, C.R., 2009, Sediment provenance in a tropical fluvial and marine context by magnetic 'fingerprinting' of transportable sand fractions: Sedimentology, v. 56, p. 841-861.

Manning, A.J., Baugh, J.V., Spearman, J.R., and Whitehouse, R.J.S., 2010, Flocculation settling characteristics of mud: sand mixtures: Ocean Dynamics, v. 60, p. 237-253.

Mason, C.C., and Folk, R.L., 1958, Differentiation of beach, dune, and aeolian flat environments by size analysis, Mustang Island, Texas: Journal of Sedimentary Research, v. 28, p. 211-226.

Mc Cave, 1984, Erosion, transport and deposition of fine-grained marine sediments: Geological Society, London, Special Publications, v. 15, p. 35-69.

McLaren, P., 1981, An interpretation of trends in grain size measures: Journal of Sedimentary Research, v. 51, p. 611-624.

McQuivey, R., S, and Keefer, T.N., 1969, The relation of magnetite over ripples, p. 244-247.

Mehta, A.J., and Lee, S.-C., 1994, Problems in linking the threshold condition for the transport of cohesionless and cohesive sediment grain: Journal of Coastal Research, v. 10(1), p. 170-177.

Mehta, A.J., and Parchure, T.M., 2000, Surface erosion of fine-grained sediment revisited, *in* B.W. Flemming, M.T.D., and Liebezeit, G., eds., Proceedings in Marine Science, Volume Volume 2, Elsevier, p. 55-74.

Michels, K.H., and Healy, T.R., 1999, Evaluation of an Inner Shelf Site off Tauranga Harbour, New Zealand, for Disposal of Muddy-Sandy Dredged Sediments: Journal of Coastal Research, v. 15, p. 830-838.

Middleton, V., 2003, Encyclopedia of Sediments and Sedimentary Rocks: Dordrecht, Kluwer Academic, 821 p.
Miller, M.C., McCave, I.N., and Komar, P.D., 1977, Threshold of sediment motion under unidirectional currents: Sedimentology, v. 24, p. 507-527.
Mitchener, H., and Torfs, H., 1996, Erosion of mud/sand mixtures: Coastal Engineering, v. 29, p. 1-25.
Moss, A.J., 1962, The physical nature of common sandy and pebbly deposits. Part II: American Journal Science, v. 260, p. 337 – 373.
Munson, B.R., Rothmayer, A.P., Okiishi, T.H., and Huebsch, W.W., 2002, Fundamentals of Fluid Mechanics, John Wiley and Sons, 816 p.
Murray, W.A., 1977, Erosion of coarse sand-clayey silt mixtures: Journal of Hydraulic Division, v. 103 (HY10), p. 1222-1227.
Oldfield, F., and Yu, L., 1994, The influence of particle size variations on the magnetic properties of sediments from the north-eastern Irish Sea: Sedimentology, v. 41, p. 1093-1108.
Panagiotopoulos, I., Voulgaris, G., and Collins, M.B., 1997, The influence of clay on the threshold of movement of fine sandy beds: Coastal Engineering, v. 32, p. 19-43.
Paterson, D.M., 1994, Biological mediation of sediment erodibility: ecology and physical dynamics: In Cohesive sediments, p. 215-229.
Paterson, D.M., Crawford, R.M., and Little, C., 1990, Subaerial exposure and changes in the stability of intertidal estuarine sediments: Estuarine Coastal and Shelf Science, v. 30, p. 541-556.
Paterson, D.M., and Hagerthey, S.E., 2001, Microphytobenthos in contrasting coastal ecosystems: biology and dynamics: Ecological comparisons of sedimentary shores. Ecological studies, p. 105-125.
Peterson, C.D., P. D. Komar, and Scheidegger, K.F., 1989, Distriburion, Geometry, and Origin of heavy mineral placer deposits on oregon beaches: Journal of Sedimentary Petrolology, v. 56, p. 67-77.
Pettijohn, J., Potter, P.E., and Ever, R.a., 1972, Sand and sandstone: New York, Springer-Verlag.
Pope, N.D., Widdows, J., and Brinsley, M.D., 2006, Estimation of bed shear stress using the turbulent kinetic energy approach--A comparison of annular flume and field data: Continental Shelf Research, v. 26, p. 959-970.
Raudkivi A.J., 1990, Loose boundary hydraulics, Pergamon Oxford
Razjigaeva, N.G., and Naumova, V.V., 1992, Trace element composition of detrital magnetite from coastal sediments of northwestern Japan Sea for provenance study: Journal of Sedimentary Research, v. 62, p. 802-809.
Riethmüller, R., Hakvoort, J.H.M., Heineke, M., Heymann, K., Kühl, H., and Witte, G., 1998, Relating erosion shear stress to tidal flat surface colour: Geological Society, London, Special Publications, v. 139, p. 283-293.
Rijn, L.C.v., 2005, ESTUARINE AND COASTAL SEDIMENTATION PROBLEMS: International Journal of Sediment Research, v. 20, p. 39-51.
Rijn, L.C.v., 2007, Unified view of sediment transport by currents and waves. I: Initiation of motion, bed roughness, and bed-load transport: Journal of hydraulic engineering, v. 133, p. 649-667.
Robinson, S.G., Maslin, M.A., and McCave, I.N., 1995, Magnetic Susceptibility Variations in Upper Pleistocene Deep-Sea Sediments of the NE Atlantic: Implications for Ice Rafting and Paleocirculation at the Last Glacial Maximum: Paleoceanography, v. 10, p. 221-250.
Rubey, W.W., 1933, The size distribution of heavy minerals within a water-laid sandstone: Journal of Sedimentary Research, v. 3, p. 3-29.
Schlichting, H., and Klaus, G., 2004, Boundary-layer theory: Berlin-Heidelberg, Springer, 811 p.
Schmeeckle, M.W., and Nelson, J.M., 2003, Direct numerical simulation of bedload transport using a local, dynamic boundary condition: Sedimentology, v. 50, p. 279-301.
Shchepetkin, A.F., and McWilliams, J.C., 2004, The Regional Oceanic Modeling System: A split-explicit, free-surface, topography-following-coordinate ocean model: Ocean Modelling, v. 9, p. 347-404.
Shields, A., 1936, Anwendung der Ähnlichkeitsmechanik und der Turbulenz- forschung auf die Geschiebebewegung: Mitteilungen der Preußischen Versuchsanstalt für Wasserbau und Schiffbau, v. NW 87.
Slingerland, R.L., 1977, The effects of entrainment on the hydraulic equivalence relationships of light and heavy minerals in sands: Journal of Sedimentary Research, v. 47, p. 753-770.
Soulsby, R., 1997, Dynamics of Marine Sands. A Manual for Practical Applications: London, Thomas Telford Publishing.
Sutherland, A., 1987, Static armour layers by selective erosion, *in* Thorne, C.R., Bathurst, J.C., and Hey, R.D., ed., Sediment Transport in Gravel-Bed Rivers: London, Wiley, p. 141-169.
Thrush, S.F., Hewitt, J.E., Cummings, V.J., Ellis, J.I., Hatton, C., Lohrer, A., and Norkko, A., 2004, Muddy waters: elevating sediment input to coastal and estuarine habitats: Frontiers in Ecology and the Environment, v. 2, p. 299-306.
Tonnon, P.K., van Rijn, L.C., and Walstra, D.J.R., 2007, The morphodynamic modelling of tidal sand waves on the shoreface: Coastal Engineering, v. 54, p. 279-296.
Torfs, H., 1997, Erosion of mixed cohesive/non cohesive sediments in uniform flow: Cohesive Sediments, p. 245-252.
Torfs, H., Jiang, J., and Mehta, A.J., 2000, Assessment of the erodibility of fine/coarse sediment mixtures, *in* William, H.M., and Ashish, J.M., eds., Proceedings in Marine Science, Volume Volume 3, Elsevier, p. 109-123.
Torfs, H., Jiang, J., and Mehta, A.J., 2001, Assessment of the erodibility of fine/coarse sediment mixtures: Coastal and Estuarine Sediment Processes, v. 3, p. 109-123.
Tucker, M.E., 1981, Sedimentary Petrology: Oxford, Blackwell Scientific Publications, 252 p.
van Ledden, M., 2002, A process-based sand-mud model, *in* Johan, C.W., and Cees, K., eds., Proceedings in Marine Science, Volume Volume 5, Elsevier, p. 577-594.
van Ledden, M., van Kesteren, W.G.M., and Winterwerp, J.C., 2004, A conceptual framework for the erosion behaviour of sand-mud mixtures: Continental Shelf Research, v. 24, p. 1-11.
van Maren, D.S., 2007, Grain size and sediment concentration effects on channel patterns of silt-laden rivers: Sedimentary Geology, v. 202, p. 297-316.
van Rijn, L.C., 1993, Principles of sediment transport in rivers, estuaries and coastal seas: Amsterdam, 715 p.
Visher, G.S., 1969, Grain size distributions and depositional process: Journal of Sedimentary Petrology, v. 39, p. 1074-1106.

Walden, J., Slattery, M.C., and Burt, T.P., 1997, Use of mineral magnetic measurements to fingerprint suspended sediment sources: approaches and techniques for data analysis: Journal of Hydrology, v. 202, p. 353-372.

Wheeler, A.J., Oldfield, F., and Orford, J.D., 1999, Depositional and post-depositional controls on magnetic signals from saltmarshes on the north-west coast of Ireland: Sedimentology, v. 46, p. 545-558.

Whitehouse, R., Soulsby, R., Roberts, W., and Mitchener, H., 2000, Dynamics of estuarine muds. A manual for practical applications: London, Thomas Telford Publishing, 210 p.

Wiberg, P.L., and Smith, J.D., 1987, Calculations of the Critical Shear Stress for Motion of Uniform and Heterogenious Sediments: Water Resources Research, v. 23, p. 1471-1480.

Widdows, J., Brinsley, M.D., Bowley, N., and Barrett, C., 1998, A benthic annular flume for in situ measurement of suspension feeding/biodeposition rates and erosion potential of intertidal cohesive sediments: Estuar Coast Shelf, v. Sci 46, p. 27-38

Williamson, H.J., 1991, Tidal transport of mud/sand mixtures - a literature review: Sediment distributions Report, v. SR 286.

Winterwerp, J.C., and Van Kesteren, W.G.M., 2004, Introduction to the physics of cohesive sediment in the marine environment, Elsevier B.V., 466 p.

Wright, J., Colling, A., and Park, D., 1999, Waves, Tides and Shallow-Water Processes: Oxford, Butterworth Heinemann.

Young, R.N., and Southard, J.B., 1978, Erosion of fine-grained marine sediments: Sea-floor and laboratory experiments GSA Bulletin, v. 89, p. 663-672.

Zajac, R., Whitlatch, R., and Thrush, S., 1998, Recolonization and succession in soft-sediment infaunal communities: the spatial scale of controlling factors: Hydrobiologia, v. 375-376.

Zhang, W., Yu, L., Lu, M., Hutchinson, S.M., and Feng, H., 2007, Magnetic approach to normalizing heavy metal concentrations for particle size effects in intertidal sediments in the Yangtze Estuary, China: Environmental Pollution, v. 147, p. 238-244.

Acknowledgements

First of all I want to greatly thank Prof. Dr. Katrin Huhn, for giving me the opportunity to pursue my PhD thesis and all her support provided throughout the last three years.

I also want to thank my co – supervisors Dr. Karin Bryan and Dr. Conrad Pilditch for all their efforts and support at all times.

Special thanks to Lina Podszun and all the members of the group of Modeling of Sedimentary Systems including: Jannis Kuhlmann, Linda Wenk, Melanie Schäfer and Lutz Torbahn. Further, I want to thank the INTERCOAST research students Antonia Ruppel and Leonard Rossmann. I want to thank my computer Hans Dampf, who had a lot to calculate, sorry for that. I am very thankful to all of you; it was a pleasure for me working with you, I always had great fun.

Further, I want to thank Dr. Christian Winter, Dr. Willem de Lange, Dr. Steven Coleman, and Prof. Dr. Burghard Flemming for providing scientific inputs during my doctoral work. Special thanks to the Department of Earth & Ocean Science, University of Waikato. I want to thank, Annette Rodgers and Jacinta Parenzee for providing all the help with the sieving and laboratory analysis.

I also would like to thank Firoz Badesab and Prof. Dr. Tilo von Dobeneck for their collaboration.

I would also like to thank Dr. Rafael Guedes (also known as Burger), Dr. Hannah Jones and Dr. Hazel Needham and Dr. Sören Warnecke for their help during my research stays in New Zealand. Special thanks to Bryna Flaim, Ingo Unterweger and all INTERCOAST students for all the great time and support.
Many thanks to my lady girl.

I greatly want to thank the Deutsche Forschungsgemeinschaft (DFG) for funding my research within the INTERCOAST International Research Training Group during last three years.

Finally, I want to thank my parents Lore and Dr. Gerhard Bartzke, who always supported me. I also want to thank my brothers Alexander and Constantin Bartzke.

Vielen herzlichen Dank Euch allen

This thesis is dedicated to:
Lore and Gerhard Bartzke